DOE/ER/01198-129

TIC

MASTER

THERMAL VACANCIES AND PHASE SEPARATION IN BCC MIXTURES OF HELIUM-3 AND HELIUM-4

BY

BENEDICK ANDREW FRAASS

B.S., Stanford University, 1974
M.S., University of Illinois, 1975

THESIS

Submitted in partial fulfillment of the requirements
for the degree of Doctor of Philosophy in Physics
in the Graduate College of the
University of Illinois at Urbana-Champaign, 1980

Urbana, Illinois

DISTRIBUTION OF THIS DOCUMENT IS UNLIMITED

DISCLAIMER

This report was prepared as an account of work sponsored by an agency of the United States Government. Neither the United States Government nor any agency Thereof, nor any of their employees, makes any warranty, express or implied, or assumes any legal liability or responsibility for the accuracy, completeness, or usefulness of any information, apparatus, product, or process disclosed, or represents that its use would not infringe privately owned rights. Reference herein to any specific commercial product, process, or service by trade name, trademark, manufacturer, or otherwise does not necessarily constitute or imply its endorsement, recommendation, or favoring by the United States Government or any agency thereof. The views and opinions of authors expressed herein do not necessarily state or reflect those of the United States Government or any agency thereof.

DISCLAIMER

Portions of this document may be illegible in electronic image products. Images are produced from the best available original document.

THERMAL VACANCIES AND PHASE SEPARATION IN BCC MIXTURES OF HELIUM-3 AND HELIUM-4

BY

BENEDICK ANDREW FRAASS

B.S., Stanford University, 1974
M.S., University of Illinois, 1975

DISCLAIMER

This book was prepared as an account of work sponsored by an agency of the United States Government. Neither the United States Government nor any agency thereof, nor any of their employees, makes any warranty, express or implied, or assumes any legal liability or responsibility for the accuracy, completeness, or usefulness of any information, apparatus, product, or process disclosed, or represents that its use would not infringe privately owned rights. Reference herein to any specific commercial product, process, or service by trade name, trademark, manufacturer, or otherwise, does not necessarily constitute or imply its endorsement, recommendation, or favoring by the United States Government or any agency thereof. The views and opinions of authors expressed herein do not necessarily state or reflect those of the United States Government or any agency thereof.

THESIS

Submitted in partial fulfillment of the requirements
for the degree of Doctor of Philosophy in Physics
in the Graduate College of the
University of Illinois at Urbana-Champaign, 1980

Urbana, Illinois

DISTRIBUTION OF THIS DOCUMENT IS UNLIMITED

THERMAL VACANCIES AND PHASE SEPARATION IN BCC MIXTURES OF HELIUM-3 AND HELIUM-4

Benedick Andrew Fraass, Ph.D.
Department of Physics
University of Illinois at Urbana-Champaign, 1980

Thermal vacancy concentrations in crystals of ^{3}He-^{4}He mixtures have been determined from accurate measurements of the temperature dependence of the x-ray lattice parameter. A new x-ray diffractometer-position sensitive detector system is used to make measurements of the absolute lattice parameter of the helium crystals with an accuracy of 300 ppm, and measurements of changes in lattice parameter to better than 60 ppm. The phase separation of the concentrated ^{3}He-^{4}He mixtures has been studied in detail with the x-ray measurements.

Vacancy concentrations in crystals with 99%, 51%, 28%, 12%, and 0% ^{3}He have been determined. The vacancy data in the nearly pure ^{3}He crystals confirm previous x-ray results from pure ^{3}He. The first direct measurements of vacancies in pure hcp ^{4}He are reported, along with study of vacancies in bcc ^{4}He. The vacancy concentrations in the 51% and 28% ^{3}He mixed crystals are found to be as large as 5%. Progress is made toward characterization of the detailed temperature dependence of the vacancy concentration in all the crystals. The low temperature x-ray molar volumes of the crystals are determined to better than 0.1%. Vacancy volumes of formation are inferred by several methods.

Phase separation has been studied in mixed crystals with concentrations of 51%, 28%, and 12% ^{3}He and melting pressures between 3.0 and 6.1 MPa.

The phase separation temperatures determined in this work are in general agreement with previous work. The pressure dependence of T_c, the phase separation temperature for a 50% mixture, is found to be linear: dT_c/dP = -34 mdeg/MPa. The x-ray measurements are used to make several comments on the low temperature phase diagram of the helium mixtures.

ACKNOWLEDGEMENTS

I sincerely thank Professor Ralph O. Simmons for his support, guidance, and enthusiasm throughout all stages of this work. I also thank several friends and colleagues who have made direct contributions to this work: R. O. Hilleke, for construction of Version II of the Position Sensitive Detector, for help with computer programming and diffractometer testing, and for assistance during all phases of the experiment; P. R. Granfors, for design and construction of Version I of the Position Sensitive Detector; S. V. Marx, for construction of the Four-Terminal Bridge; and S. N. Ehrlich, for assistance during the data acquisition phase of the experiment. The members of the Materials Research Lab Machine Shop are acknowledged for their construction of the x-ray diffractometer gear drive.

I gratefully acknowledge the friendship and assistance of Dr. D. R. Aadsen, Prof. A. C. Anderson, Dr. D. R. Baer, Dr. P. Chaddah, Dr. J. V. Gates, Dr. S. M. Heald, Dr. A. T. Macrander, Dr. A. E. Pontau, D. H. Riehl, and Dr. E. P. Roth. The interest and support of my parents has been important throughout my educational career. Mrs. Minnie Rindt is thanked for her accurate and neat typing.

Finally, I thank my wife, Wendy, whose support, interest, help, curiosity, patience, and love have made this work possible.

This research was supported by the U.S. Department of Energy under contract EY-76-C-02-1198.

To my parents

TABLE OF CONTENTS

CHAPTER		Page
I.	INTRODUCTION	1
II.	THEORY	12
	A. Mixture Thermodynamics	12
	B. Vacancy Thermodynamics	26
III.	EXPERIMENTAL TECHNIQUES	34
	A. Introduction	34
	B. Cryostat and Dilution Refrigerator	34
	C. High Pressure System	42
	D. Temperature Measurement and Thermometer Calibration	46
	E. Sample Preparation and Analysis	54
	F. Position Sensitive Detector	61
	G. X-ray Diffractometer	73
IV.	DATA	103
	A. Introduction	103
	B. Summary	103
	C. Details and Observations	110
V.	ANALYSIS	186
	A. Vacancies	186
	B. Molar Volumes and Vacancy Volumes of Formation	202
	C. Phase Separation	207
	D. Bcc ^{4}He and Other Analysis	228
VI.	SUMMARY	231
APPENDIX A.	CAPACITIVE STRAIN GAUGE	235
APPENDIX B.	MACHINE LANGUAGE PROGRAMS	240
APPENDIX C.	X-RAY DIFFRACTOMETER INTERFACE SCHEMATICS	249
REFERENCES		272
VITA		279

LIST OF TABLES

TABLE		Page
1.	Mixture concentrations	61
2.	Diffractometer scan types	90
3.	Absolute lattice parameter measurements	104
4.	Low temperature x-ray molar volumes	106
5.	Results of fits to vacancy data	108
6.	Phase separation temperatures	109
7.	Inferred vacancy volumes of formation	205
8.	Values of T_c obtained from Equation II-16 with the present results are compared to the determination of Edwards, *et al.*[35]	211
9.	Phase diagram information obtained from x-ray data in the phase separated region	221
10.	Phase boundaries derived from x-ray data in the phase separated region	223

I. INTRODUCTION

Solid helium is a remarkable subject for study from both theoretical and experimental viewpoints. The basis of this interest is that the quantum-mechanical zero-point energy (ZPE) of solid helium is comparable to its potential energy.[1/] The ZPE is large due to the small masses of ^{3}He and ^{4}He and the weakness of the attractive part of the van der Waals interaction between the atoms. Solid helium is called a quantum crystal[2/] because for it the harmonic approximation, which is the basis of the usual theories of lattice dynamics, breaks down, forcing a quantum-mechanical treatment of the system.

One manifestation of the large ZPE in helium is that the root-mean-square deviation ($\langle u^2\rangle^{1/2}$) of an atom from its lattice site is large: in ^{3}He it can be as large as 1/3 of the near neighbor distance R.[1/] The large excursion of the atom from its lattice site has three results:[3/] (1) neighboring atoms are encountered at distances on the order of their hard core radii, (2) the "small" parameter of classical lattice dynamics, $\langle u^2\rangle^{1/2}/R$, is not small, and (3) neighboring atoms tunnel and exchange lattice sites. Theories of solid helium are therefore forced to acknowledge the non-localized description applicable to the atoms on their lattice sites by describing the atoms with wave functions, which are usually taken to be Gaussian in shape.[2/] This description allows easy visualization of the tunneling and exchange between the atoms. They are seen simply as due to the overlap of the atomic wave functions.

The low temperature phase diagrams of ^{3}He and ^{4}He illustrate both the importance of the ZPE and the wealth of interesting features present in this quantum solid. The pressure-temperature (P-T) phase diagrams for both pure ^{3}He[4-7] and pure ^{4}He[5,8] are shown in Fig. 1. Among the obvious points of interest in this figure are: (1) both ^{3}He and ^{4}He are liquid all the way to zero temperature at low pressures, (2) ^{3}He requires a pressure of 2.9 MPa before it solidifies, while ^{4}He solidifies at 2.5 MPa, (3) both ^{3}He and ^{4}He melting curves have minimums, although that of ^{3}He is much more pronounced, (4) the bcc phase exists from 2.9 MPa to about 10.5 MPa in ^{3}He, while it is only a small (at most 50 mdeg wide) sliver along the melting line in ^{4}He, and (5) liquid ^{4}He becomes superfluid He II at about 2 K. Not shown are the superfluid ^{3}He phases which occur at about 2 mK,[9] the magnetically ordered phase in solid ^{3}He (at $\sim$1.1 mK on the melting line[10]), and the fcc phases of both ^{3}He and ^{4}He which occur at $\sim$100 MPa and 15 K. This wide variety of different phenomena at low temperatures in helium is ample reason for interest in helium.

The bcc phase of ^{3}He has been the focus of much interest in recent years (see reviews of nuclear magnetic resonance (NMR)[3] and thermodynamic[11] experiments). The bcc phase is the least dense, shows the largest effects due to atomic delocalization, and has the largest ZPE of the solid phases of helium. Differences between a quantum solid and classical solids are evident in many properties. The heat capacity of ^{3}He, for example, has many contributions other than the Debye T^3 behavior normally expected in an insulating solid.[11] Among these are a nuclear exchange contribution at low temperatures and the high temperature anomaly due to vacancies.

Figure 1. P-T phase diagrams of pure ^{3}He and pure ^{4}He. The pressure-temperature phase diagrams of both ^{3}He and ^{4}He are plotted. The dashed lines are ^{3}He phase boundaries, while the solid lines are those of ^{4}He. Also shown is the superfluid λ line in ^{4}He. These curves are compiled from the data in references 4-8.

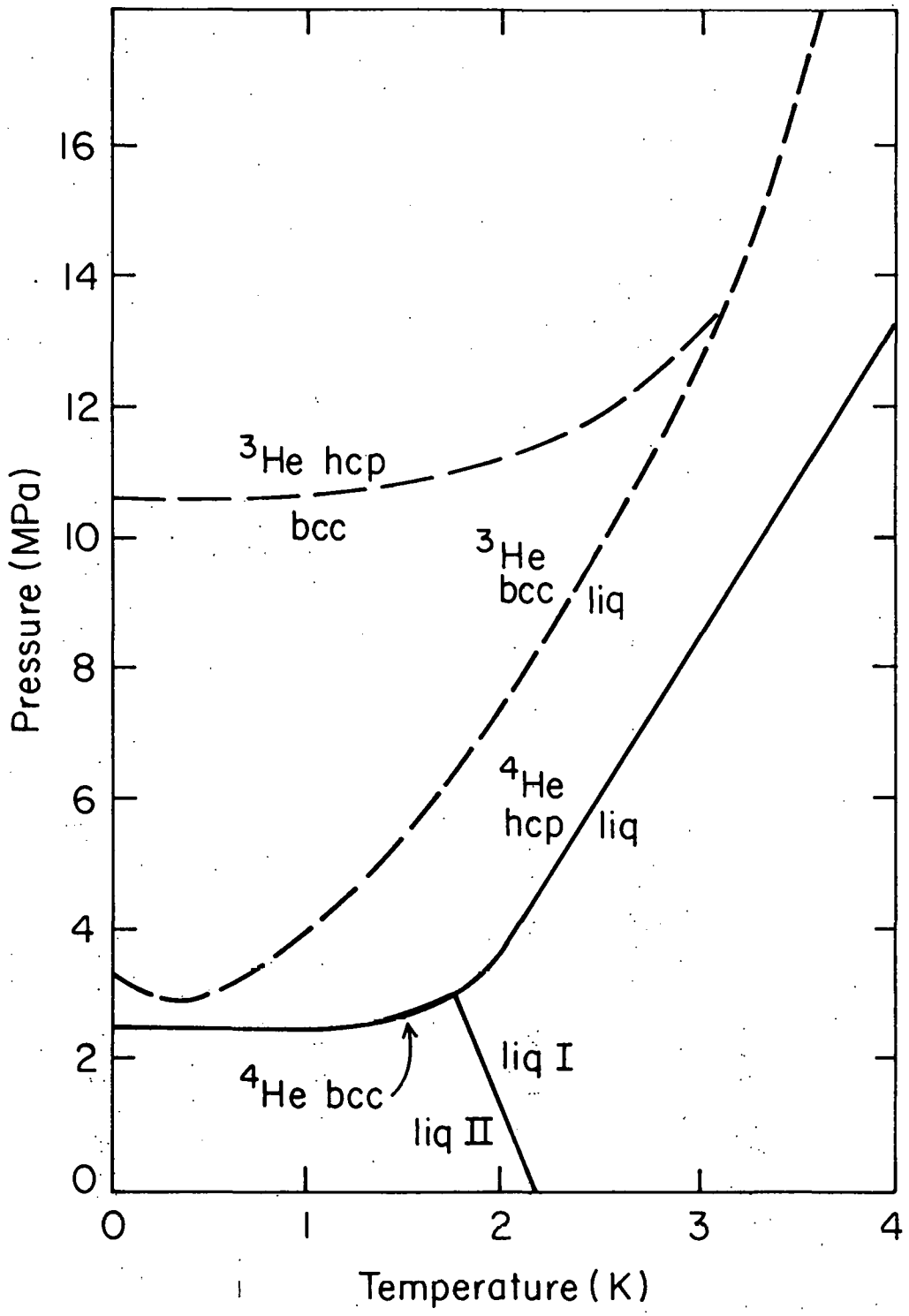
16
14
12
10
8
6
4
2
0
Pressure (MPa)
0
1
2
3
4
Temperature (K)
^{3}He hcp
bcc
^{3}He
bcc
liq
^{4}He
hcp
liq
liq I
^{4}He bcc
liq II

Vacancies have been studied in bcc ^{3}He with heat capacity techniques by many workers.[12-17] Their measurements are sensitive to the model of the normal lattice heat capacity which is used, because the lattice properties of hypothetically perfect quantum solids are not in general known with high accuracy. Vacancies in bcc (and hcp) ^{3}He have also been studied with NMR experiments. The diffusion data of Reich[18] and the T_1 measurements of Sullivan, Deville, and Landesman[19] give activation energies for vacancy motion that are in general agreement with the activation energies obtained in the heat capacity work. Finally, the x-ray measurements of Heald[20] have directly determined the vacancy formation energy in both bcc and hcp ^{3}He. Heald has found that the concentration of vacancies at melting in bcc ^{3}He is about 5×10^{-3}, approximately independent of the molar volume of the sample. The x-ray formation energies are in qualitative agreement with the other determinations in the bcc phase.

The microscopic nature of a vacancy in a quantum solid is an interesting subject for discussion. As mentioned above, there is tunneling and exchange of the atoms in the solid. Thus the vacancies also tunnel through the crystal, since a helium atom situated next to a vacancy has a finite probability of tunneling into the vacancy. This rapid tunneling results in the vacancy having a wave-like character. This excitation, called a delocalized or nonlocalized[21] vacancy or a vacancy wave,[22] is one of the interesting manifestations of quantum mechanics which is present in helium.

The delocalization of the vacancy should cause the vacancy formation energy to widen into a band, in a manner analogous to that of conduction electrons in a solid. Imagine a vacancy and a helium atom which are placed in a lattice, and given an interaction strength t. The energy of the two

possible vacancy states (the vacancy on either of the two lattice sites) is split by the interaction, so that the vacancy energy $\phi = e$ becomes $\phi = e \pm t$. Allowing the vacancy to have z near neighbors would result in $\phi = e \pm zt$. This result for the width of the vacancy band is essentially the same as that from a more detailed calculation,[21] and illustrates the formation of the band.

All the previous vacancy measurements[12-20] have been interpreted in terms of the usual localized vacancies. Attempts have been made to use delocalized vacancies to explain deviations from normal vacancy behavior in heat capacity[13] and x-ray[20] measurements, but have not been successful. The vacancy formation energies obtained in heat capacity[13] and x-ray[20] work also appear to differ from each other, especially at high molar volumes. This disagreement is typical of the situation: it is believed that the problems are connected with delocalization, but they are not explained by the present theories.[21-24]

The original goal of this work was the study of vacancies in bcc ^{4}He. Solid ^{4}He is somewhat simpler than ^{3}He since there are no nuclear spins. Because of the different spin states of the two isotopes, the delocalized vacancies in the two solids are qualitatively different. In ^{4}He, the excitations are waves, with well-defined wave vectors, while at high temperatures in ^{3}He, the vacancies move by diffusion since the random spins destroy the periodicity of the lattice.[22] If the delocalization of vacancies is important, then a qualitative difference in the nature of vacancies in ^{4}He and ^{3}He should yield more understanding of the whole situation.

The present measurements of vacancy concentrations are made with x-ray diffraction using the well-known Simmons and Balluffi method,[25] in

which the concentration of vacancies x_v is given by

$$x_v = 3(\Delta l/l - \Delta a/a) \quad . \qquad (1\text{-}1)$$

$\Delta l/l$ is the change in macroscopic length of the crystal, and $\Delta a/a$ the change in lattice parameter, both with respect to some low temperature reference state in which there are few thermal vacancies present. For experiments which are done at essentially constant macroscopic volume (such as the present one), $\Delta l/l$ is zero, and the vacancy concentration is given directly by the change in lattice parameter. It is impossible, however, to study bcc ^{4}He directly using this technique: the bcc phase does not exist in a large enough temperature range to allow determination of the low temperature reference state necessary for the vacancy measurements.

To overcome this difficulty, the present work in bcc mixtures of ^{3}He and ^{4}He was undertaken. A small amount of ^{3}He added to pure ^{4}He results in an enlarged bcc phase in the solid. This enlargement is shown in Fig. 2, which depicts the low pressure phase diagram for a mixture with 5% ^{3}He (x_3=0.05). These sound velocity data of Vignos and Fairbank[26/] show that even with x_3=0.05, the bcc phase is already much larger than in pure ^{4}He. Through the study of vacancies in ^{3}He-^{4}He mixtures, it is hoped that the behavior of vacancies in pure ^{4}He can be ascertained. Further interest in study of vacancies in helium mixtures is due to the NMR measurements made by Miyoshi, Cotts, Greenberg and Richardson.[27/] They found vacancy activation energies in a 32% mixture (x_3=0.321) that correspond to a vacancy concentration of $\sim$2% at the melting temperature. Further study of this result is clearly of interest. Finally, because the experimental apparatus has been improved considerably since the vacancy measurements of Heald,[20/]

Figure 2. Low Pressure P-T phase diagram for x_3=0.05. The solid lines show the phase boundaries for a mixture with 5% ^{3}He (x_3=0.05). The dashed lines show the pure ^{4}He melting line, λ line, and bcc-hcp transformation. $\lambda_{0.05}$ is the λ transition for x=0.05, and λ_o is the λ line for pure ^{4}He. Note the increase in size of the bcc phase in the mixture compared to that of pure ^{4}He. The melting curve minimum is also made more prominent by the addition of ^{3}He to the ^{4}He.

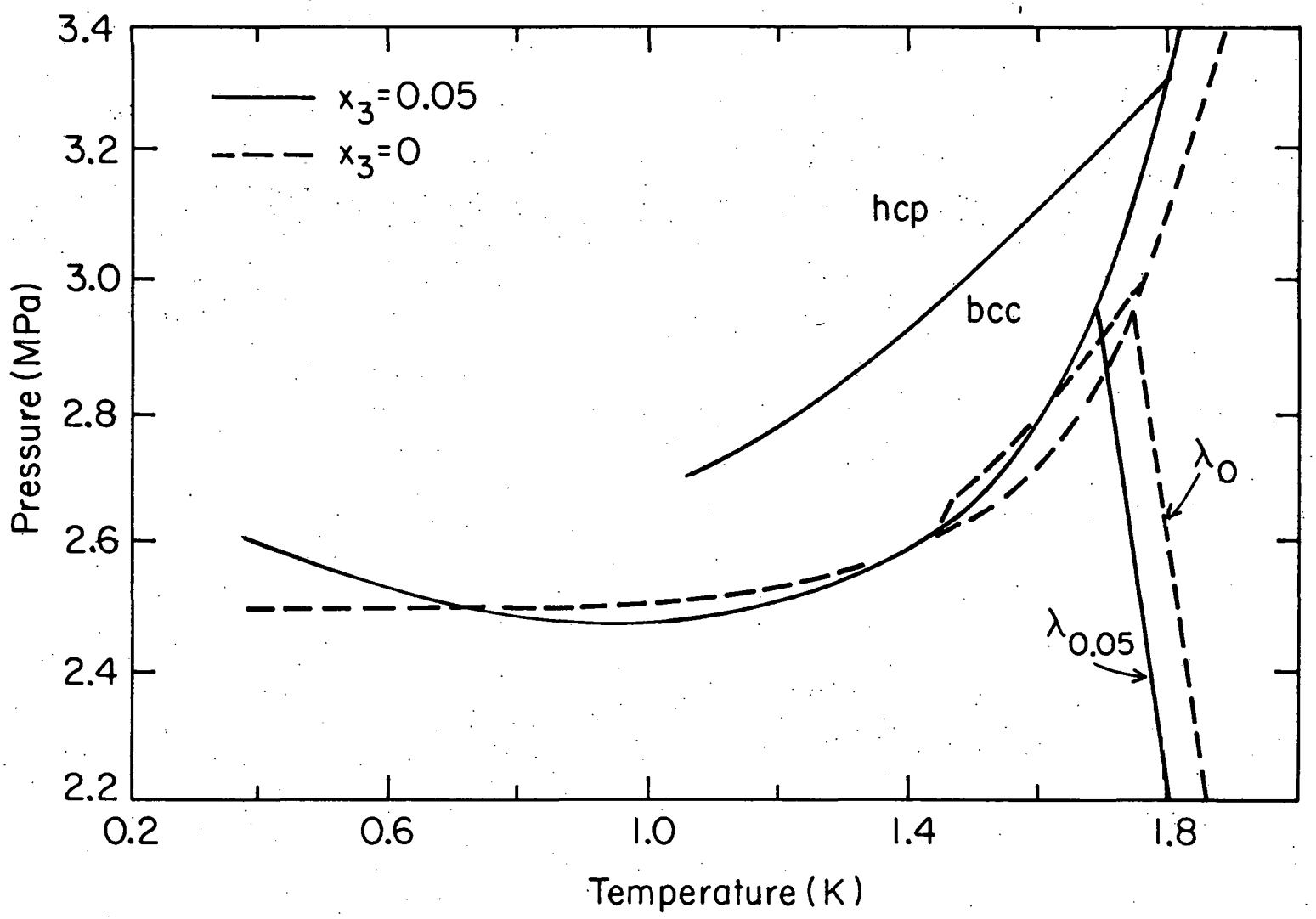
3.4
3.2
3.0
2.8
2.6
2.4
2.2
Pressure (MPa)
0.2
0.6
1.0
1.4
1.8
Temperature (K)
x_3=0.05
x_3=0
hcp
bcc
λ_0
$\lambda_{0.05}$

knowledge of vacancies in ^{3}He, and particularly the effect of delocalization on their behavior, can be improved.

The study of solid helium mixtures also has two benefits unrelated to vacancy knowledge. The state of knowledge of the bcc-hcp transformation in mixtures as a function of ^{3}He concentration (x_3) and pressure (P) is not satisfactory. The P-T phase diagrams published by Vignos and Fairbank,[26] Miyoshi, et al.,[27] Berman and Rogers,[28] and Grigor'ev, Esel'son, and Mikheev[29] do not seem to be self-consistent with respect to the bcc-hcp transformation. The consistency of the various melting curve determinations[26,27,29-33] seems somewhat better. The present experiment is the first to study mixtures with x-ray diffraction. The present work may be able to shed some light on the discrepancies in the phase diagrams mentioned above.

One important feature of the mixture phase diagram that is studied in great detail in this work is phase separation. Phase separation of liquid ^{3}He-^{4}He mixtures is well known.[34] Separation of the solid mixture into ^{3}He-rich and ^{4}He-rich components on cooling below the phase separation temperature (T_{ps}) was first seen by Edwards, McWilliams, and Daunt[15] in 1962. A more complete study by the same authors later in 1962[35] found that T_{ps}=0.38 K for x_3=0.5 and P=3.63 MPa. Later experimental[36-39] and theoretical[40] work has confirmed the existence of phase separation in the solid.

Phase separation is interesting in helium because the atomic tunneling and exchange that are present in solid helium allow the macroscopic separation into two components to proceed on a reasonable time scale. The present investigation is very useful, because it (1) makes the first

microscopic measurements of phase separation in concentrated mixtures, (2) makes these measurements over a much larger pressure range than any previous studies, (3) allows accurate determination of the phase separation temperature T_{ps}, and (4) makes inference of the low temperature phase diagram possible. Phase separation data are also useful because thermodynamic information about the mixture in general can be obtained from the behavior of the solid at phase separation.

The final reason for the present work is that x-ray absolute lattice parameters may now be measured with the present x-ray diffractometer with an accuracy of about 300 ppm. This equipment, in conjunction with the ^3He-^4He dilution refrigerator used in this work, makes absolute lattice parameter measurements possible at temperatures of 0.05 K. This capability is of much use in understanding vacancies in helium, and in the study of phase separation.

II. THEORY

The fact that the substance studied in this work is a mixture of two isotopes is perhaps the dominant factor in the results which are presented in later chapters. A brief summary of thermodynamic results which are relevant to the present study is therefore given here. The mixture thermodynamics then naturally leads to two important points: an explanation of the phase separation which occurs in solid helium mixtures, and a discussion of the interesting low temperature phase diagram of ^3He-^4He mixtures.

The last half of this chapter is devoted to the study of vacancies. A general review of the relevant thermodynamic relations is given for the normal case of non-interacting monovacancies in a homogeneous host crystal. Vacancy contributions to the measured properties of the crystal, such as heat capacity and thermal expansion, are a useful result of this discussion. The section is concluded with short discussions of various complications to the non-interacting monovacancy picture. Included are multiple vacancy aggregates, solute-vacancy binding in the mixtures, and delocalization of vacancies.

A. Mixture Thermodynamics

1. Regular Solution Theory

A general review of the thermodynamics of regular solutions is given below. Solid helium mixtures turn out to be nearly regular solutions, although for reasons far different than the usual explanation of regular

behavior of a solid.[40/] In the discussion that follows, the Helmholtz free energy F is used because most solid helium experiments are done at essentially constant volume. The Gibbs free energy G will be referred to from time to time, in order to make contact with usual thermodynamic treatments. In this chapter, and throughout the rest of this work, all energies will be measured in degrees. Thus entropies are simply numbers. In general molar quantities are used. For clarity in this chapter, the ^{3}He concentration x_3 is sometimes called x.

The free energy of mixing, f^M, is defined as the change in free energy on mixing of two pure substances:

$$f^M = f(V,T,x) - xf(V,T,x=1) - (1-x)f(V,T,x=0) \quad . \qquad \text{(II-1)}$$

There are similar expressions for other quantities, such as the energy of mixing u^M, the entropy of mixing s^M, and the pressure of mixing p^M. The relationships between Gibbs and Helmholtz free energies still hold,[41/] such as

$$f^M = g^M - Pv^M \quad , \qquad \text{(II-2)}$$

where g^M is the Gibbs free energy of mixing, and v^M is the volume of mixing given by

$$v^M = v - xv(x=1) - (1-x)v(x=0) \quad . \qquad \text{(II-3)}$$

An important point is that the usual derivatives are also valid, for example

$$s^M = - (\partial f^M/\partial T)_V \qquad \text{(II-4)}$$

$$p^M = - (\partial f^M/\partial V)_T \quad . \qquad \text{(II-5)}$$

A discussion of the energy of mixing u^M is useful at this point. Consider a helium crystal with Nx ^{3}He atoms and N(1-x) ^{4}He atoms, with a lattice coordination number z (z=8 for the bcc lattice). In this case there are as nearest neighbors $Nzx^2/2$ pairs of ^{3}He atoms, $Nz(1-x)^2/2$ pairs of ^{4}He atoms, and Nzx(1-x) pairs of one ^{3}He and one ^{4}He atom. If the energy of a nearest neighbor pair of atoms is defined to be e_{ij}, where i and j are either 3 or 4 depending on the isotopes of the atoms involved, then $e_{ij}=e_{ji}$. The molar total energy of the crystal due to interatomic interactions is then[42/]

$$u = \left[Nzx^2e_{33}/2 + Nz(1-x)^2e_{44}/2 + Nzx(1-x)e_{34}\right]/N$$

$$= \frac{z}{2}\left[xe_{33} + (1-x)e_{44} + 2x(1-x)\left(e_{34} - \frac{e_{33} + e_{44}}{2}\right)\right] \quad . \qquad \text{(II-6)}$$

Rewriting this equation in terms of the molar energy of mixing u^M, and noting that $u(x=1) = \frac{1}{2}ze_{33}$ and $u(x=0) = \frac{1}{2}ze_{44}$, we have

$$u^M = u - u(x=1) - u(x=0) = zx(1-x)\left(e_{34} - \frac{e_{33} + e_{44}}{2}\right)$$

$$= x(1-x)w \quad . \qquad \text{(II-7)}$$

w is called the interaction energy.

A solution is called ideal if w=0.[43/] Therefore, for an ideal solution $u^M=0$, so that

$$f^M(\text{ideal}) = -T\, s^M(\text{ideal}) = T[x\ln(x) + (1-x)\ln(1-x)] \quad . \qquad \text{(II-8)}$$

A more useful characterization is that of a regular solution, which has $s^M=s^M(\text{ideal})$, but with $w\neq 0$.[44/] The differences between ideal solution properties and those of a regular solution (or in fact any solution) are

usually discussed in terms of excess properties. For example, the excess free energy, f^E, is defined as the deviation from the ideal free energy:

$$f^E = f^M - f^M(\text{ideal}) \quad . \qquad \text{(II-9)}$$

In regular solutions, properties such as the excess energy u^E, excess volume v^E, and excess pressure p^E are identical to the mixing values (u^M, v^M, and p^M) because we have u^M, v^M, and p^M equal to zero in an ideal solution. Thus for a regular solution,

$$f^E = u^M = u^E = x(1-x)w \quad . \qquad \text{(II-10)}$$

The sign of the interaction energy w (or equivalently the sign of u^E) determines the behavior of the system at low temperatures. If $w<0$, then the atoms are more likely to be found next to the other isotope present. This results in ordering or clustering of unlike atoms at low temperatures.[44/] In solid helium $w>0$, and so at low temperatures where entropy effects are small, the free energy is lowered by minimizing the number of pairs of unlike atoms. This is the basic cause of the phenomenon of phase separation.

2. Phase Separation

Before a detailed discussion of phase separation, a qualitative look at several different phase diagrams is useful. In Fig. 3 the relationship between the free energy (F) versus x diagram and the T-x phase diagram are schematically shown for a hypothetical material at three different temperatures.

The simplest of the three diagrams is (b), which shows a single phase region. The mixture is in the solid α-phase everywhere because at $T=T_2$, the free energy F_α is everywhere smaller than F_{liq}. Figure 3(a)

Figure 3. Phase Diagram Examples. Three sample T-x phase diagrams, and their associated free energy F versus x diagrams. (a) shows the liquidus-solidus region of the phase diagrams. At temperature $T=T_1$, the concentration of the liquid present is $x_{liq}=x_B$, while $x_{solid}=x_A$. (b) shows the single phase region with $T=T_2$. The free energy F_α of the solid α-phase is everywhere lower than F_{liq}. (c) shows the solid phase separation at $T=T_3$. Solid in the α-phase at $x=x_E$ can lower its total free energy by separating into two components which have $x=x_C$ and $x=x_D$. The "hump" in F between x_C and x_D is due to the $f^E = x(1-x)w$ term in F, where $w>0$. If $w<0$ then the "hump" in F is inverted, so that phase separation does not occur. x_A and x_B, and x_C and x_D are determined by a line (dots in a and c) drawn tangent to the free energy minimums.

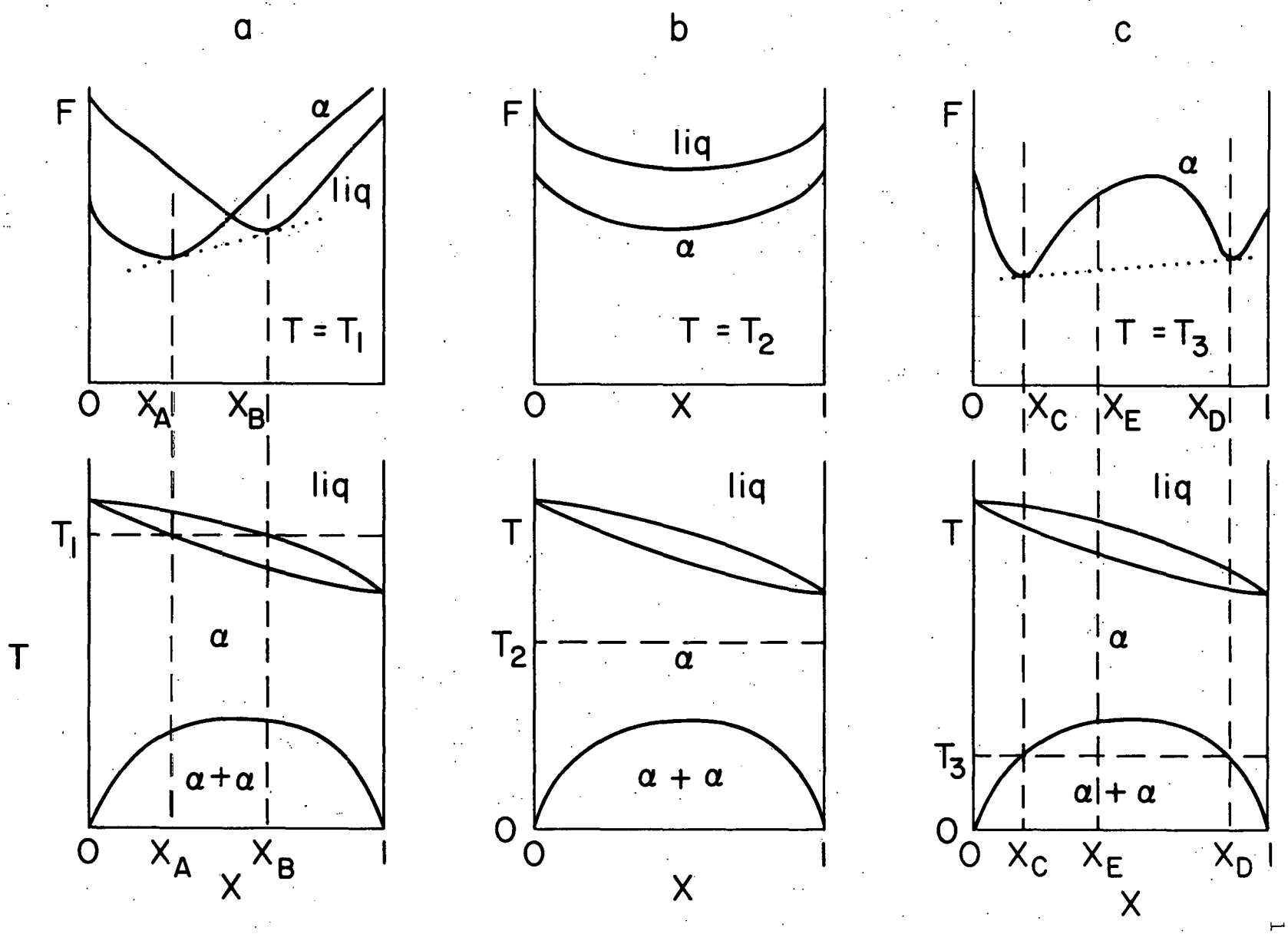
a
b
c
F
α
liq
T = T1
O
XA
XB
T = T2
X
T = T3
XC
XE
XD
T
T1
α
α+α
T2
α + α
T3
X

shows the situation at a higher temperature T_1, where part of the mixture is solid and part is liquid. The two minimums in the F-x picture mean that there is a mixed phase region. At this temperature, any solid in contact with the liquid has a concentration x_A, while the liquid has a concentration x_B. The curves in the T-x picture on which the solid and liquid concentrations (at this temperature T_1) are found are called respectively the solidus and the liquidus. As an example of the use of this T-x diagram, suppose one has a liquid with concentration x_B, which one cools in an attempt to grow a crystal. When the temperature reaches T_1, solid would form. However, the solid would have concentration x_A. On further cooling, the concentration of the liquid present would follow the liquidus curve, and the concentration of the newly grown solid would follow the solidus curve, until the sample was fully solidified. This type of behavior is generally true in other kinds of mixed phase regions.

Phase separation (sometimes called a miscibility gap[44/]) is shown in Fig. 3(c). As can be seen in the F-x diagram, F no longer has a simple shape. The solid solution is unstable between concentrations x_C and x_D. When $x_C<x<x_D$, the solution then separates into two parts, one with $x=x_C$, and the other with $x=x_D$. The two inflection points between x_C and x_D in the F-x diagram are called the spinodes. At concentrations between the spinodes, the mixture spontaneously decomposes, while outside the spinodes, the decomposition must take place by nucleation and growth processes.[44/] A useful approach to the subject of composition fluctuations has been made by Cahn and Hilliard,[45/] but this is clearly beyond the scope of this work.

The temperature of critical mixing, T_c, is the highest temperature at which phase separation occurs. This is determined by finding the

temperature at which the minimum in the free energy f^M becomes flat, i.e.[43/]

$$\partial f^M/\partial x = 0 \qquad \text{(II-11)}$$

and

$$\partial^2 f^M/\partial x^2 = 0 \quad . \qquad \text{(II-12)}$$

The calculation of T_c for a regular mixture is straightforward. For a regular solution we have

$$f^M = u^M - T\, s^M = x(1-x)\, w + T\left[x\ell n(x) + (1-x)\ell n(1-x)\right] \qquad \text{(II-13)}$$

since u^M is given by II-7 and s^M by II-8. Substituting into Equation II-11 yields

$$T_{ps} = w(2x-1)/\ell n(\frac{x}{1-x}) \quad . \qquad \text{(II-14)}$$

This equation gives the phase separation temperature T_{ps} as a function of concentration.

To obtain the relationship between T_c and w, Equation II-12 must be employed. Substituting II-13 into II-12 gives

$$2w/T = \frac{1}{x(1-x)} \quad . \qquad \text{(II-15)}$$

At the maximum of the T_{ps} curve, x=1/2, II-15 gives T_c=w/2. Therefore, the phase separation curve for a regular solution is given by Equation II-14, with $w=2T_c$,

$$T_{ps} = 4T_c(x-1/2)/\ell n(\frac{x}{1-x}) \quad . \qquad \text{(II-16)}$$

This equation describes a curve which is symmetric about x=0.5 and which reaches its peak temperature T_c at x=0.5. T_c is in general a function of volume (or equivalently, a function of pressure).

There are several quantities of experimental interest that can now be discussed. The excess pressure due to phase separation has been measured by Panczyk, et al.[36] In regular solution theory, we have $p^M = p^E$, where p^M is defined in Equation II-5. Using II-9 and

$$p^E = -(\partial f^E/\partial V)_T \qquad \text{(II-17)}$$

we find

$$p^E = -x(1-x)\ (\partial w/\partial V)_T = -x(1-x)2(dT_c/dV) \quad . \qquad \text{(II-18)}$$

The excess pressure p^E is therefore determined by the volume dependence of T_c (and hence w). The excess volume on phase separation can be determined by performing the analogous calculation using the Gibbs excess free energy:[40]

$$v^E = (\partial g^E/\partial P)_T = x(1-x)2(dT_c/dP) \quad . \qquad \text{(II-19)}$$

Mullin[40] has made a quantum mechanical calculation of phase separation effects which is based on a generalization of the Nosanow theory[2,46] of the pure phases of solid helium. His calculation finds

$$v^E = -cx(1-x) \qquad \text{(II-20)}$$

where c=0.4 cm^3/mol. This result is especially important because it has been used in the determination of all helium mixture molar volumes in all previous work. See also Equation IV-1.

The other major result of Mullin's theoretical treatment is that a small deviation from regular solution behavior is found. In particular,

$$g^E(x,P) = x(1-x)[a(P) - b(P)x] \quad . \qquad \text{(II-21)}$$

At 3.63 MPa (the pressure of the Edwards, et al.[35] measurements), a ∿1.0 K,

while $b \sim 0.1$ K. This non-regular behavior should cause the T_{ps}-x curve to be unsymmetric, with the low x part of the curve at higher temperatures than predicted by II-16. The calculation also gives $T_c \sim 0.47$ K, compared to the experimental result $T_c = 0.38$ K of Edwards, et al.[35] at 3.63 MPa. One final result is obtained by comparison of Equations II-19 and II-20. Mullin's theory thus predicts that $dT_c/dP \sim -24$ mdeg/MPa.

3. Phase Diagram of Solid Helium Mixtures

Solid helium is an excellent material with which to study the richness of phase diagrams that are thermodynamically possible: many interesting features are present. As an example, one particular pressure has been chosen, and in this section the helium phase diagram at that pressure will be discussed in some detail. This discussion will serve two purposes: an introduction to the solid phases present in helium mixtures at low temperatures, and an example with which to demonstrate some rules for phase diagram construction.

The Gibbs phase rule is the general rule which is used in the construction of phase diagrams. It can be written as[44]

$$f = r - \phi + 2 \qquad \text{(II-22)}$$

where f is the number of thermodynamic degrees of freedom, r is the number of components in the mixture, and ϕ is the number of phases. As an example, in a binary mixture (r=2), if there is a mixed phase region in which two phases are present (ϕ=2), then f=2. This means that only two degrees of freedom can be varied while keeping the system in the same region of the phase diagram. For example, the pressure and temperature could be varied without changing the phase. A second example is three phases coexisting

in a binary solution. The phase rule then allows the variation of one variable. A univariant line on a T-x phase diagram is such a case.[42] The univariants that are mentioned below are horizontal lines on a T-x diagram because the pressure and temperature are fixed, so that three phases can only coexist on the horizontal univariant line.

The T-x phase diagram for ^3He-^4He mixtures at a pressure of 3.0 MPa, as drawn by Tedrow and Lee,[30] is shown in Fig. 4, along with the measurements[33,35,47-49] on which the diagram is based. This pressure was chosen because of the many interesting features in the diagram, and because this is near the pressure at which some of the present work was done. The first important point to be made is that much of the diagram is uncertain, as there have been no appropriate measurements made along many of the phase boundaries.

The pure ^3He (x=1) and pure ^4He (x=0) behavior in this diagram is easily related to that seen in Fig. 1. ^4He is hcp from above 1.7 K to zero temperature, with only a small sliver of bcc along the melting line. ^3He, on the other hand, is bcc from melting down to its lower melting temperature (G). The liquidus (A) and solidus (B) are shown in Fig. 4, apparently separated by as much as 0.2 deg. The single data point on the solidus, that of Tedrow and Lee,[30] is discussed in Chapter V. Although the difference between the two curves need not be as large as is shown, the phase rule (Eq. II-22) shows that a difference exists, and that this difference goes to zero as the pure substances are approached by changing the concentration. At some pressures, for example at 2.59 MPa,[42] there is a maximum in the liquidus and solidus curves as a function of concentration. At this maximum, the liquidus and solidus curves meet at an

Figure 4. Helium phase diagram at 3.0 MPa. The T-x phase diagram for helium below 1.8 K at P=3.0 MPa is shown here as drawn by Tedrow and Lee.[30/] Several points of interest are noted: A, liquidus curve; B, solidus curve; C, phase separation curve; D, ^{4}bcc-^{4}hcp-^{3}bcc univariant; E, ^{4}hcp-^{3}bcc-^{3}liq univariant; F, ^{3}He upper melting point; G, ^{3}He lower melting point; H, ^{4}He melting point; I, ^{4}He bcc-hcp transition; J, mixed bcc-hcp region. The cross-hatching below the phase separation curve is a reminder that the sample never has a composition x and temperature T which are inside this region. The data points (and experimental methods) shown are: O, Tedrow and Lee[30/] (strain gauge or susceptibility); △ , Vignos and Fairbank[47/] (sound velocity); □ , Le Pair, et al.[48/] (pressure); ● , Baum, et al.[49/] (strain gauge); ■ , Edwards, et al.[35/] (heat capacity) (T_{ps}); ▽ , Zinov'eva[33/] (visual observation).

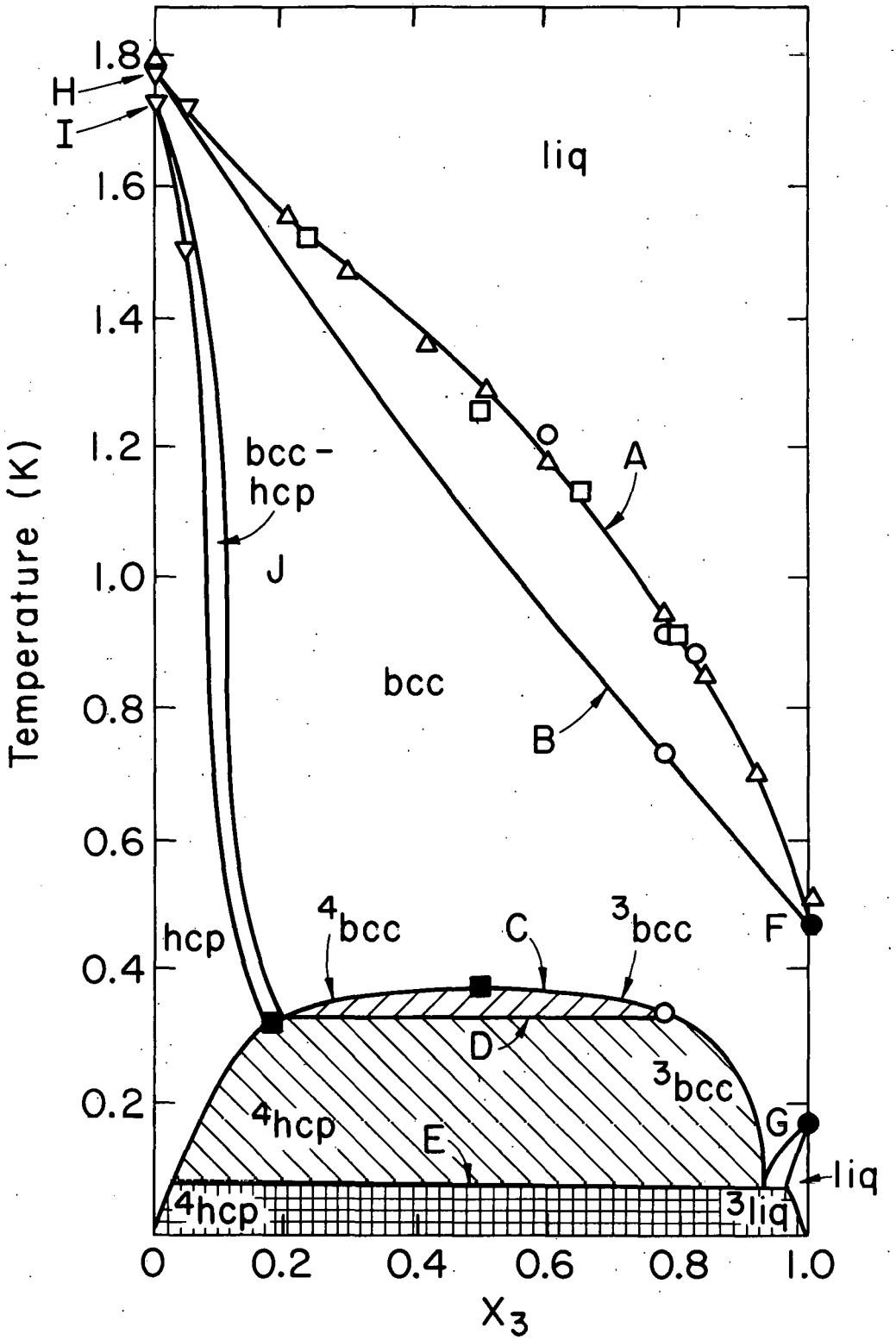
1.8
1.6
1.4
1.2
1.0
0.8
0.6
0.4
0.2
Temperature (K)
H
I
liq
bcc-
hcp
J
A
bcc
B
hcp
4bcc
C
3bcc
F
D
3bcc
4hcp
E
G
liq
4hcp
3liq
0
0.2
0.4
0.6
0.8
1.0
X3

azeotropic point, as they must to satisfy the Gibbs-Konowalow rule.[50/] An azeotropic point is the only point at which a crystal can be grown that has the same concentration as the liquid from which it is grown.

At low concentrations, a mixed hcp-bcc region exists. Again, although this mixed region must exist, there is no condition on its width. The endpoint is not determined either. Although the mixed phase must terminate at a horizontal line (univariant) when it meets the phase separation curve (C), this could occur at any place along the phase separation curve. The data point at which it terminates in Fig. 4 is a heat capacity determination of the phase separation temperature, and has nothing to do with the mixed phase.

The phase separation region in Fig. 4 is shown cross-hatched to reinforce the idea that the mixture never has a composition and temperature which are underneath the curve (C). As a mixture is cooled from the bcc phase, it separates into two components when it reaches the phase separation curve. Each component has the concentration given by the phase separation curve at that particular temperature, as has been described in the last section and Fig. 3. The phase separated region is split into three parts by the two univariant lines (D) and (E). The ^{4}bcc-^{4}hcp-^{3}bcc univariant (D) shows that at that particular temperature, all three of these phases coexist. In this notation, ^{4}bcc means that the ^{4}He-rich component is bcc. At temperatures above this, both the ^{4}He-rich and ^{3}He-rich components are only bcc along the phase separation curve. The univariant (E) shows the coexistence of three phases also: ^{4}hcp-^{3}bcc-^{3}liq. As is shown in the lower right corner of the diagram, the ^{3}liq-^{3}bcc mixed phase must meet the phase separation curve (C) on the horizontal univariant (E) to

satisfy the Gibbs phase rule. The width of the flat (horizontal) part of the phase separation curve that results is not known. It should be reiterated that the relationship of the two univariants (D) and (E) is not fixed by experiment. None of the measurements at those temperatures have determined the hcp-bcc boundaries or the bcc-liquid boundaries at low temperatures.

B. Vacancy Thermodynamics

1. Monovacancy Formation and Contributions to Thermal Properties

The calculation of the equilibrium concentration of vacancies in a homogeneous crystal at constant volume proceeds by minimizing the Helmholtz free energy of the crystal with respect to the number of monovacancies present. The total free energy of the crystal at constant volume, F, is

$$F(V,T) = F^{o}(V,T) + n_v f_v(V,T) - T\ell n(W) \qquad \text{(II-23)}$$

where F^{o} is the free energy of the vacancy-free crystal, n_v is the number of vacancies, N is the number of atoms, f_v is the vacancy free energy of formation, and W is the usual configurational term:

$$W = (N + n_v)!/N!n_v! \quad . \qquad \text{(II-24)}$$

Note that except for differences in notation and emphasis, Eq. II-23 is exactly the result obtained for an ideal solution in Section A-1. (See Equations II-1 and II-8.) By setting $\partial F/\partial n_v = 0$ and using Stirling's formula,[44] the concentration of vacancies x_v is obtained:

$$x_v = \frac{n_v}{N + n_v} = \exp(-f_v/T) = \exp(-e_v/T + s_v) \quad . \qquad \text{(II-25)}$$

The usual thermodynamic relations hold for the vacancy formation parameters:

$$f_v = e_v - Ts_v \tag{II-26}$$

$$s_v = -(\partial f_v/\partial T)_V \tag{II-27}$$

$$p_v = -(\partial f_v/\partial V)_T \quad , \tag{II-28}$$

s_v is the non-configurational entropy of formation of a vacancy. The expression for p_v, the pressure of formation of a vacancy at constant volume, can be easily related to the quantity which is more usually considered, v_p, the volume of formation of a vacancy at constant pressure. Using II-28, we have

$$p_v = -(\partial f_v/\partial V)_T = -(\partial f_v/\partial P)_T(\partial P/\partial V)_T \quad . \tag{II-29}$$

The number of vacancies at any particular temperature and pressure is independent of how they were formed, so

$$g_p = f_v \quad . \tag{II-30}$$

The derivation used to obtain II-25 is analogous to that performed in the constant pressure case to obtain g_p. II-29 may now be simplified, since

$$(\partial g_p/\partial P)_T = v_p \tag{II-31}$$

and the isothermal bulk modulus is defined as

$$B_T = -\frac{1}{V}\left(\frac{\partial V}{\partial P}\right)_T \quad . \tag{II-32}$$

The result is therefore

$$p_v = \frac{v_p}{V} B_T \quad . \tag{II-33}$$

Vacancy contributions to crystal properties can be calculated using the expression for the crystal free energy, Equation II-23.[51/] Starting

with II-23, we have for the energy E

$$E = E^o + n_v e_v \quad . \tag{II-34}$$

The heat capacity of the real crystal $C_v = -(\partial E/\partial T)_V$ is then given by

$$C_v = C_v^{\,o} + n_v\left[(\partial e_v/\partial T)_v + e_v^{\,2}/T^2\right] \quad . \tag{II-35}$$

If the heat capacity of the vacancy-free crystal, $C_v^{\,o}$, is known, then from the experimental heat capacity C_v one can infer information about vacancy formation parameters. This technique has been used on solid helium most recently by Greywall.[13/] In this case, $C_v^{\,o}$ was obtained from the theoretical calculations of de Wette, Nosanow, and Werthamer.[52/]

Vacancy contributions to other properties are calculated analogously.[51/] Several useful results are

$$\chi_T - \chi_T^{\,o} = x_v \frac{v_p}{v_a}\left[-\frac{1}{v_p}\left(\frac{\partial v_p}{\partial P}\right)_T + \frac{v_p}{T}\right] \tag{II-36}$$

$$\alpha - \alpha^o = x_v \frac{v_p}{v_a}\left[\frac{h_p}{T^2} + \frac{1}{v_p}\left(\frac{\partial v_p}{\partial T}\right)_P\right] \tag{II-37}$$

$$V - V^o = n_v v_p \quad . \tag{II-38}$$

Here, χ_T is the isothermal compressibility, α is the coefficient of volume thermal expansion, v_p is the volume of formation, v_a is an atomic volume, and h_p is the enthalpy of formation at constant pressure.

2. Divacancies and Vacancy Clusters

Aside from monovacancies, there may also be aggregates of vacancies present in a real crystal. In a vibrating lattice,[53/] and also on the basis of general strain energy considerations,[44/] the binding energy between two

near neighbor vacancies is expected to be somewhat negative, so that the two monovacancies are bound into a single divacancy. Ignoring the existence of higher order clusters and interactions between divacancies, the derivation of the concentration of divacancies, $x_v^{(2)}$, proceeds exactly as in Section B-1. The result is [54/]

$$x_v^{(j)} = A_j \exp\left[-f_v^{(j)}/T\right] = A_j \exp\left[-e_v^{(j)}/T\right] \exp\left[s_v^{(j)}\right] \qquad \text{(II-39)}$$

where j=2 for divacancies, A_j is a constant geometrical factor that depends on the number of ways the defect can be oriented in the lattice[55/] (A_2=4 for a bcc lattice), and $f_v^{(j)}$, $e_v^{(j)}$, and $s_v^{(j)}$ are the free energy, energy and entropy of formation of the cluster of j vacancies. Equation II-39 is true for larger clusters also.[54/]

The binding energy of the cluster of j vacancies can be defined relative to the monovacancy formation energy $e_v^{(1)}$:

$$e_v^{(j)} = je_v^{(1)} - e_b^{(j)} \quad . \qquad \text{(II-40)}$$

Here, the binding energy of the cluster is $e_b^{(j)}$. The size of $e_b^{(j)}$ determines the effect of the cluster on the system. Using the binding energy $e_b^{(j)}$, the total number of vacant lattice sites in the crystal (ΔN) may be expressed simply:

$$\Delta N/N = x_v^{\text{total}} = \sum_j jx_v^{(j)}$$

$$= \sum_j jA_j (x_v)^j \exp\left[e_b^{(j)}/T\right] \quad . \qquad \text{(II-41)}$$

In this equation, the cluster entropies have been ignored because no general relationship (between $s_v^{(2)}$ and $s_v^{(1)}$ for example) is evident in the measurements that have been made.[54/]

3. Vacancy-Solute Binding

The binding of vacancies to each other is not the only binding possible. Whenever there is a positive binding energy between vacancies and impurities in the crystal, some vacancies will be bound to impurities.[55/] In the case of helium, the possibility of such a binding is shown easily, although there are complications which may overwhelm the following naive argument. At some pressure P (3.0 MPa, for example), the molar volume of ^{3}He is much larger than that of ^{4}He at the same pressure P. This larger molar volume is the result of the smaller mass, and hence larger zero point energy, of ^{3}He.[1/] Therefore, when ^{3}He atoms are present in a lattice of ^{4}He, they will be compressed, raising their energy. A ^{3}He next to a vacancy should have a lower energy, because the vacancy will allow the ^{3}He more room, thus lowering its energy. This naive picture is certainly oversimplified. For example, Locke and Young[56/] have pointed out that formation of this bound state will localize the vacancy, thereby raising its energy. The size of the effect of this localization on the vacancy energy is unclear, because the effect of delocalization itself is not completely understood. See Section B-4 for more discussion of delocalization.

There has been much study of vacancy-impurity binding in dilute metallic solutions.[54/] In the present work, however, the concentrations of solute and solvent are the same order of magnitude. The large number of vacancies present in solid helium prevents any easy limiting case to be studied. The derivation of the equilibrium concentrations of bound vacancy-solute states and free vacancies is straightforward, but very complicated unless approximations are made which are not valid here.

The results of the relevant derivation by Lidiard[57/] are given here to demonstrate the method used. This is just an expansion of the

method used in Section B-1. If there are N solvent atoms, N_i solute atoms, n_v free vacancies, and $N_i p$ solute-vacancy bound states (s-v's), then the free energy of the crystal is

$$F = F^o + n_v f_v + N_i p(f_v - f_b) - T\ell n(W) \qquad \text{(II-42)}$$

where F^o is the free energy of the vacancy-free crystal, f_v is the vacancy formation free energy, f_b is the s-v binding free energy, and W is the configurational term. n_v and p are determined by minimizing the free energy:

$$\partial F/\partial n_v = 0 = \partial F/\partial p \quad . \qquad \text{(II-43)}$$

The difficulty is that W is complicated:

$$W = A \times B \times C \quad . \qquad \text{(II-44)}$$

A is the number of ways of arranging $N_i p$ s-v's on N_s sites:

$$A = \frac{(z)^{N_i p}}{(N_i p)!} \prod_{s=0}^{(N_i p-1)} \left(N + N_i + N_i p + n_v - 2s\right) \qquad \text{(II-45)}$$

where z is the number of near neighbors. B and C are, respectively, the number of ways of putting the $N_i(1-p)$ free solute atoms, and the n_v free vacancies, on the lattice without either having a near neighbor of the other or of the s-v's already on the lattice.

$$B = \frac{(N + N_i(1-p) + n_v)!}{[N_i\ (1-p)]!\ (N + n_v)!} \qquad \text{(II-46)}$$

$$C = \frac{(N - zN_i(1-p) + n_v)!}{[N - zN_i(1-p)]!\ n_v!} \quad . \qquad \text{(II-47)}$$

The difficulty in treating this general case is obvious.

The problem is much simpler in the dilute mixture case. When $x_{solute} < 10^{-3}$, one finds[57] for the total concentration of vacancies

$$x^{tot} = \exp(-f_v/T)\left(1 - zx_{solute} + zx_{solute}\exp(f_b/T)\right) \qquad \text{(II-48)}$$

This result, which was apparently first derived by Lomer,[58] is good only for $x_{solute} < 10^{-3}$, even though it has often been applied to much higher concentration mixtures.[59]

4. Vacancy Delocalization

The delocalization of vacancies in ^{3}He and ^{4}He has been discussed by several workers, including Hetherington,[21,23] Guyer,[22] and Andreev.[60] The motion of vacancies in ^{4}He is generally believed to be wave-like, while the vacancies in ^{3}He move by diffusion. As discussed in Chapter I, the effect of the large tunneling frequencies of the helium atoms in the solid is to cause the vacancy formation energy to split into a band of formation energies. The most detailed calculation of this vacancy band is that of Hetherington,[21] who has used as the basis of his work the Nosanow theory of solid helium.[2,46]

The two main results of this calculation, however, are somewhat in disagreement with experiment. Hetherington calculates the tunneling parameter t, finding a value $t \sim 0.7$ K. This should be compared to the value of t inferred from NMR experiments[18,19,61] which varies from 0.04 to 0.2 K. His result for the minimum vacancy band energy is also too high when compared to experiment. This may be related to the fact that lattice relaxation around the vacancy has been ignored, so that there is a term in his energy which should be Pv_p instead of Pv_a. Inclusion of the correct vacancy

formation volume could significantly lower the energy, since Pv_a is of the order of 10-20 K.

A phenomenological approach to the problem has also been attempted. One method suggested by Hetherington[24/] is the use of an analytical approximation to his calculated density of states for the vacancy band. The use of this function,

$$\rho(E) = N(E-\phi)^4 \exp(-2(E-\phi)/\sigma) \qquad E > \phi$$
$$= 0 \qquad E < \phi \quad , \qquad \text{(II-49)}$$

allows analytical calculations to be performed. Of particular interest in the present work is whether any non-exponential temperature dependence in the vacancy concentration should be visible. As shown by Heald,[20/] use of II-49 gives

$$x_v = F(\sigma,\beta) \exp(-\beta\phi) \qquad \text{(II-50)}$$

where $\beta=1/T$, ϕ is the band minimum, and

$$F(\sigma,\beta) = (1 + \sigma\beta/2)^{-5} \quad . \qquad \text{(II-51)}$$

Precise enough x-ray vacancy measurements should allow measurement of this extra temperature dependence if it is present.

III. EXPERIMENTAL TECHNIQUES

A. Introduction

Following the pioneering x-ray study of vacancies in solid helium by Balzer and Simmons,[62] a great stride was made by Heald with his study of vacancies in bcc ^{3}He.[20] The dilution refrigerator cryostat that he designed, built, and used for that work solved many of the problems associated with the work of Balzer and Simmons. It allows careful crystal preparation and adequate time to perform the delicate vacancy measurements.

Described in detail in this chapter are major improvements to the x-ray diffractometer system. These greatly improve the consistency of the vacancy measurements and also make precise absolute lattice parameter measurements possible. Another improvement was made in the area of temperature measurement, where a new measurement bridge, new thermometers, and new and more complete calibration of those thermometers improve the reliability of the temperature measurements. Also described in this chapter are the operation of the cryostat and dilution refrigerator, crystal growth, and the measurement of the concentration of ^{3}He in the helium mixtures which are the subject of this work.

B. Cryostat and Dilution Refrigerator

The rigid tail cryostat and dilution refrigerator used in this work was designed, built, and described by S. M. Heald.[63] The cryostat is of rigid tail design so that (1) the sample cell stays fixed in space

regardless of the levels of liquid helium or liquid nitrogen in the cryostat, and (2) there are no cryogens in the path of the x-rays. A cross-sectional view is shown in Fig. 5. The dilution refrigerator is based on a simple design given by Anderson.[64/] The refrigerator is shown in Fig. 6, which also shows the present position of the heaters and thermometers. Figure 7 shows the present configuration of the dilution refrigerator pumping system.

Some mention should be made of the numerous low temperature leaks which developed. These included leaks in the sample cell high pressure seal, dilution refrigerator inlet, and exchange gas pumping line, all of which appeared only at 77 K or below. Problems were also caused by cracked welds between the pumping lines and the flanges in the probe (the probe is the dilution refrigerator and its pumping lines, and lifts out of the cryostat). After months of conservative efforts, the problems were solved by remaking all accessible joints on the probe. Soft solder and/or epoxy[65/] were used to fix the cracked welds. These changes necessitated rewiring the cryostat, which helped correct some long-standing problems in that area.

The operation of the refrigerator has been refined, especially since the calibration of the carbon thermometers on the still and the ^{4}He cold plate ("pot"). The starting and normal operation of this dilution refrigerator are now understood. As the ^{3}He-^{4}He mixture is condensed into the refrigerator, the pot temperature warms to about 1.8 K, while the still warms to 1.1 K. As more mixture is forced in, the still begins to act as a ^{3}He refrigerator and starts to cool. This allows the pot to return to its normal operating temperature of about 1.2 K. When enough

Figure 5. Cross-sectional view of the cryostat used in the present work: (A) Upper o-ring plate showing pumping lines for the dilution refrigerator, exchange gas, and ^{4}He pot, along with ports for transfers and electrical leads. (B) Stainless steel bellows to absorb thermal contraction. (C) Nitrogen reservoir vent (fill tube on opposite side) showing o-ring seal and stainless steel bellows to absorb thermal contraction. (D) 10 ℓ gold plated brass liquid nitrogen reservoir. (E) 5 ℓ stainless steel helium reservoir. (F) Main vacuum pumping port. (G) Fiberglass supports. (H) 1 K cold plate. (I) Sample chamber. (J) Beryllium x-ray windows, the outer one is 0.05 cm thick and the inner one is 0.025 cm thick. (K) 0.0012 cm aluminized Mylar x-ray window. (L_1, L_2, L_3) Indium o-rings. (M) Connection for vacuum gauges. (N) Support flange. (O) Removable top plate.

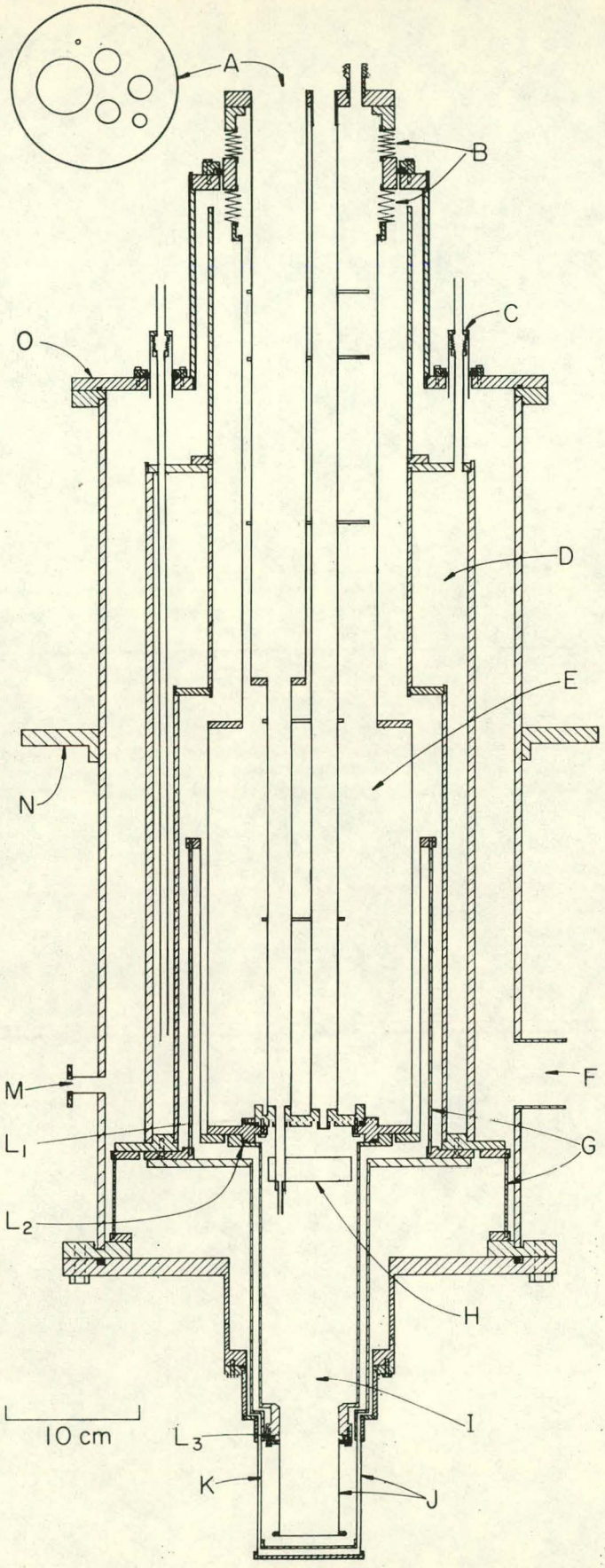
A
B
C
O
D
E
N
M
F
L1
G
L2
H
I
10 cm
L3
K
J

Figure 6. Cross-sectional view of the sample chamber, including the dilution refrigerator: (A) 1 K cold plate ("pot"). (B) Flow impedance. (C) Still. (D) Still thermometer (carbon). (E) Coaxial tube heat exchanger, Inner tube is 0.04 cm o.d. × 0.025 cm i.d. cupronickel, Outer tube is 0.12 cm o.d. × 0.1 cm i.d. cupronickel. (F) Mixing chamber with sintered copper filling. (G) Germanium thermometer (#G15559). (H) 0.0012 cm aluminized Mylar x-ray window. (I) Pot thermometer (carbon). (J) ^{3}He fill line, 0.08 cm o.d. × 0.015 cm i.d. stainless steel. (K) Thermal ground for electrical leads. (L) Graphite support rod. (M) Nylon support for lower ^{3}He fill line consisting of ∿1 m length of 0.04 cm o.d. × 0.025 cm i.d. cupronickel tubing. (N) Carbon resistance thermometers. (O) Control heater. (P) Sample tube. (Q) Gradient heater. (R) Germanium thermometer (#G15678).

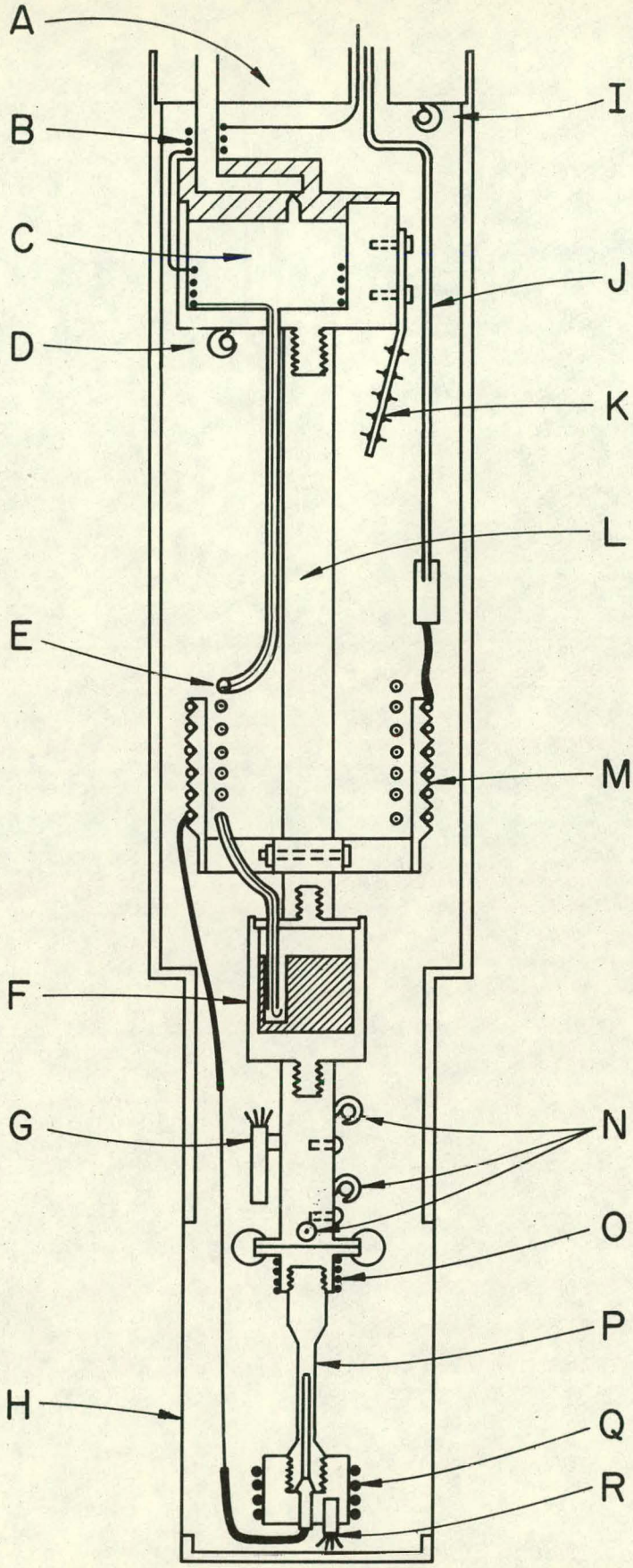
A
B
C
D
E
F
G
H
I
J
K
L
M
N
O
P
Q
R

Figure 7. Dilution refrigerator pumping system. The diffusion pump is a CVC model KS-200 pump. The sealed forepump is a Welch model 1402 KBG. The oil trap is a 2.5 cm tube filled with copper mesh. A dot by a valve indicates that it is open during normal operation. TC1 and TC2 are thermocouple vacuum gauges.

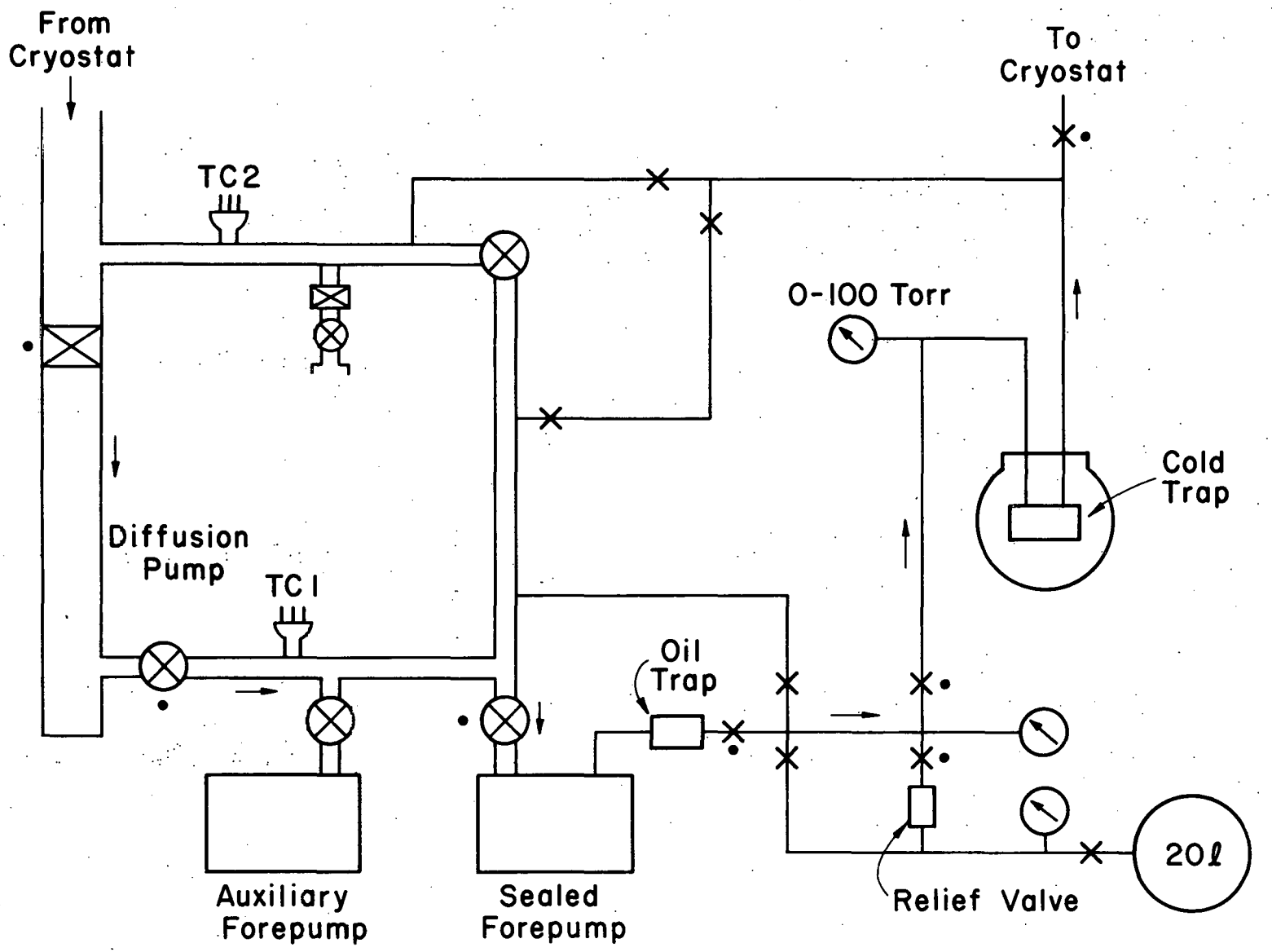
From
Cryostat
To
Cryostat
TC2
0-100 Torr
Cold
Trap
Diffusion
Pump
TC I
Oil
Trap
20ℓ
Relief Valve
Auxiliary
Forepump
Sealed
Forepump

liquid collects in the still, the refrigerator starts. While at low temperatures, the still temperature is maintained at about 0.7 K by the still heater. This heater also allows easy control of the cooling power of the refrigerator.

Temperatures as low as 0.055 K were easily obtained with the refrigerator. However, after two to three weeks of continuous operation the refrigerator becomes plugged. Now that there are calibrated thermometers on the still, pot, and at the bottom of the helium bath, it is clear that hydrogen from the pump oil is mainly responsible. Three actions can help alleviate this problem: (1) replace the molecular sieve in the 77 K cold trap more often, (2) put a more effective oil trap after the sealed forepump in the refrigerator pumping system, and (3) warm the bath and refrigerator above 35 K while pumping out the hydrogen that has collected in the refrigerator.

C. High Pressure System

The high pressure system and Lucite sample cell are basically unchanged from previous work,[20/] although several minor additions have been made. The present configuration of the system is shown in Fig. 8. The basis of the system is the separator, which allows high pressure ^{4}He to pressurize the ^{3}He (or mixture in this case) with a stainless steel bellows arrangement. Changes were made in the system to make the preparation of ^{3}He-^{4}He mixtures and the measurement of their ratio of ^{3}He to ^{4}He possible. Sample preparation and analysis are described in a later section.

The Lucite sample cell, which is shown in the inset of Fig. 8, is similar to those used in the previous work.[20/] One change in the cell

Figure 8. High pressure gas handling system and sample cell. All tubing is 0.16 cm o.d. × 0.025 cm i.d. stainless steel. ^{4}He gauge is Heise model CMM 4526 (0-5000 psia), and ^{3}He gauge is Heise model CM 4527 (0-2000 psia). The metal bellows-sealed separator used to pressurize the ^{3}He is shown schematically. The inset shows the Lucite sample cell. Note the spike of In solder used to minimize crystal rotation. The valves on either side of the separator are electrically operated solenoid valves which prevent over-pressurization of the separator.

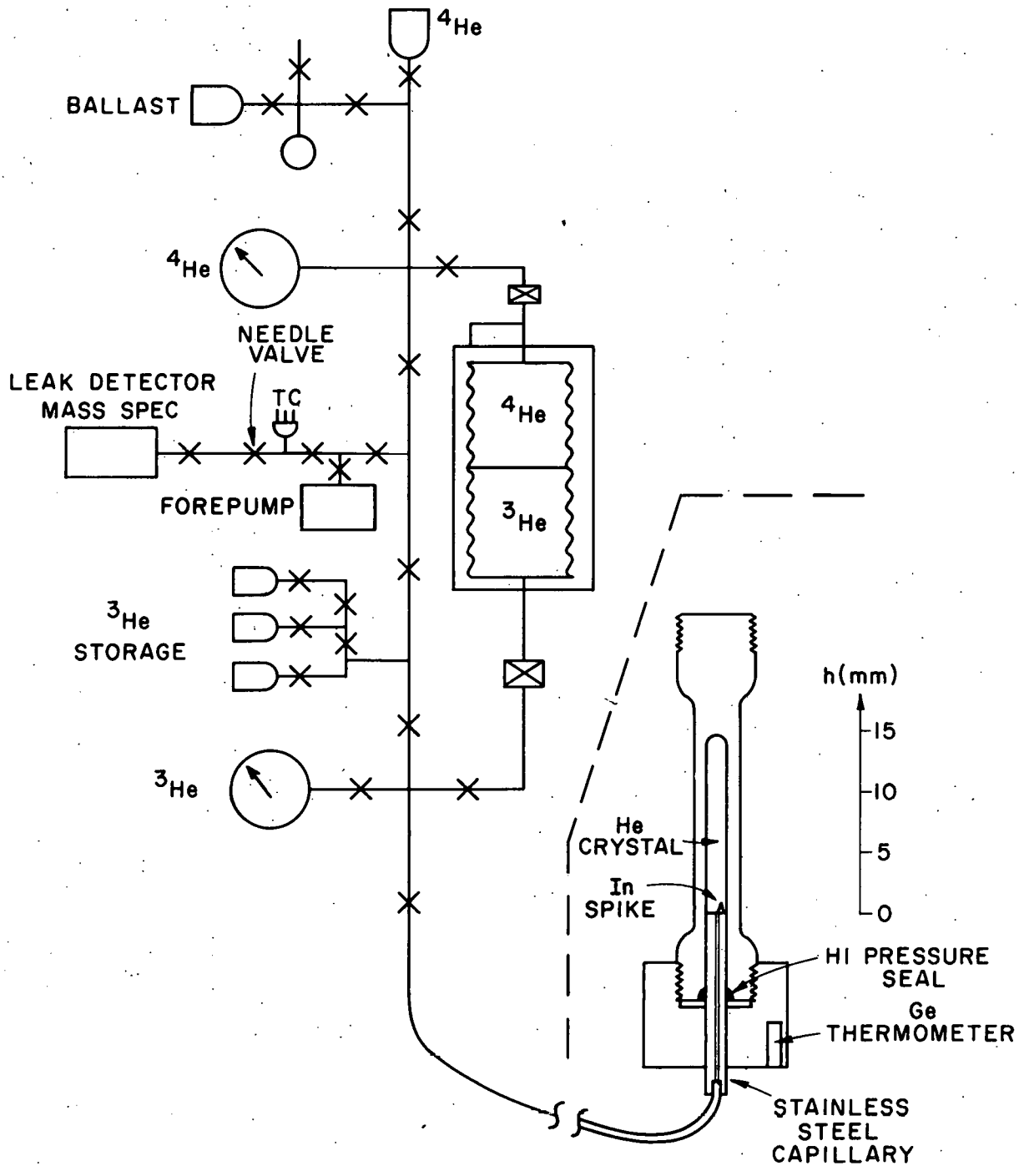
4He
BALLAST
4He
NEEDLE
VALVE
LEAK DETECTOR
MASS SPEC
TC
FOREPUMP
4He
3He
3He
STORAGE
3He
h(mm)
15
10
5
0
He
CRYSTAL
In
SPIKE
HI PRESSURE
SEAL
Ge
THERMOMETER
STAINLESS
STEEL
CAPILLARY

itself is that there are flats on the wide part of the bottom of the cell, and on the nut, so that wrenches may be used to tighten the nut on the cell. This small change has made a significant improvement in the ease with which the sample cell is sealed. The second change was made because the first crystals grown (crystals 1-8) showed an unnerving tendency to rotate in the cylindrical sample cell, sometimes at speeds as high as 1 deg/min. To counter this problem a small (< 1 mm) spike of indium solder was placed on the stainless steel fill line inside the cell. The spike destroys the cylindrical symmetry of the cell and has improved the stability of the crystals. Although the crystals still rotate, especially near the melting temperature, this rotation usually is now measured in hundredths of degrees instead of tens of degrees.

Originally intended to be a major improvement in the capabilities of the system was a capacitive strain gauge mounted on the sample cell. This would make accurate pressure measurements possible during the experiments. It had been found previously[20/] that a large BeCu strain gauge (similar to that used by Straty and Adams[66/]), mounted at the bottom of the sample cell, made crystal growth all but impossible. Therefore, a strain gauge was designed, built, and tested that (1) had small thermal mass, and was made totally of Lucite, so as not to interfere with crystal growth, (2) measured the actual pressure on the crystal, not that at the end of the cell, and (3) did not interfere with the x-ray experiments. Unfortunately, the last characteristic forced the plates of the capacitor to be so small that the gauge was too insensitive to be useful. Details on this attempt are given in Appendix A.

D. Temperature Measurement and Thermometer Calibration

The major change made in the cryostat and its associated electronics has been in the temperature measurement apparatus. A new four-terminal ac resistance bridge is used which eliminates all lead resistances from the measured thermometer resistances. New germanium thermometers are employed which are useful to much lower temperatures than those used previously. The new thermometers are more thoroughly calibrated than before. Several calibration methods have been used, including the use of a NBS Superconducting Fixed Point device. Previously uncalibrated carbon thermometers on various parts of the dilution refrigerator have been calibrated by comparison with a calibrated germanium thermometer, allowing much more effective operational control of the refrigerator.

1. Four-Terminal Bridge

The four-terminal ac resistance bridge used here is a modification of a bridge described by Rubin and Golahny[67] (which itself is a modification of the original version of Ekin and Wagner[68]). A simplified schematic is shown in Fig. 9. One of the most important features of the bridge is the use of low power bipolar input operational amplifiers (opamps),[69] for which batteries may be used as the power supply, thus limiting the 60 Hz pickup by the bridge. A phase sensitive lock-in amplifier is used as the output stage of the detector, as is usual with ac resistance bridges.[67]

Two changes have been made in the bridge design of Rubin and Golahny. The fourth opamp, which was used as a preamplifier, was removed. This preamp caused additional noise, while the gain was unnecessary because the

Figure 9. Four-terminal bridge. The three opamps A_1, A_2, and A_3 are Analog Devices model 153 J. Transformer T_1 is a United Transformer model 0-1, and transformer T_2 is a Triad G-24. The decade resistor is a General Radio model 1433-F. Capacitors C_1 are 110 μf, capacitor C_2 is 6.85 μf, and R_2 is 100 KΩ. The resistance of the germanium thermometer (R_{th}), and the lead resistances (R_{L_i}) are shown separately.

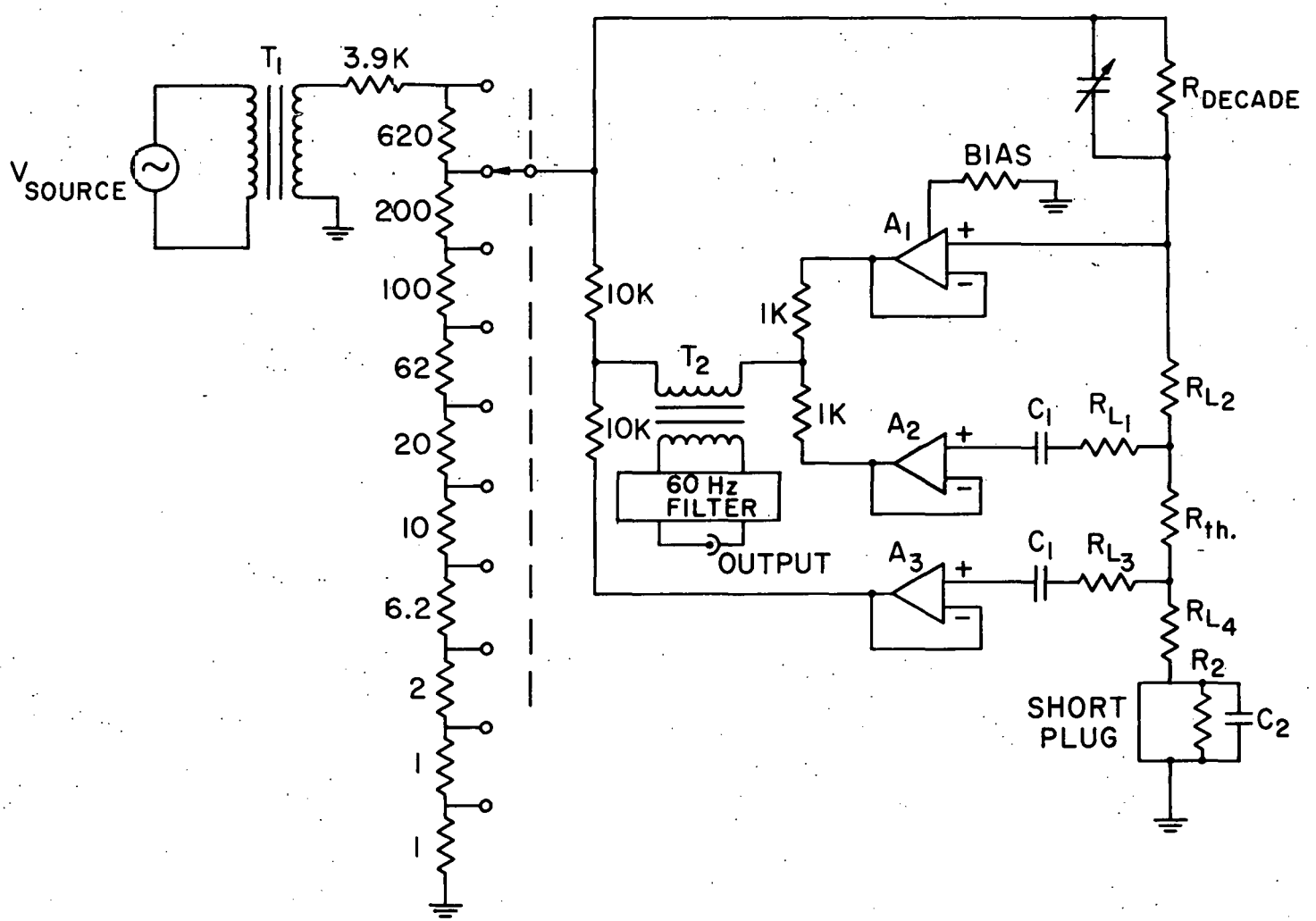
V SOURCE
T1
3.9K
620
200
100
62
20
10
6.2
2
1
1
10K
10K
T2
60 Hz FILTER
OUTPUT
1K
1K
A1
A2
A3
BIAS
R DECADE
C1
C1
RL1
RL3
RL2
Rth.
RL4
R2
C2
SHORT PLUG

lock-in amplifier used[70/] already had adequate sensitivity. The second change was the addition of capacitors C_1 and C_2, resistor R_2, a shorting plug across C_2 and R_2, and the bias adjustment to opamp A_1 (see Fig. 9). The purpose of these additions was to prevent any dc current from flowing through the thermometer. This can cause heating at low temperatures. Experimentally, it was found that with these improvements and the shorting plug removed, there were no overheating problems even at temperatures as low as 0.025 K.

The present four-terminal bridge is much more effective than the three-terminal bridge[20/] that it replaces, especially at low temperatures. Great care was taken to assure that the power level of the signal put through the thermometer was not large enough to cause heating in the thermometer. The usual rule-of-thumb[71/] for the power dissipated in the thermometer is $P(\text{watts}) < (3\times10^{-7})T^{4.5}$. Because the power actually dissipated in the thermometers is not measured, but is calculated, a safety factor of 2 in temperature (a factor of 20 in power) was used here. The attenuation of the signal input is adjusted so that the power dissipated at $T=0.6$ K is 3×10^{-11}W, while that used at 0.025 K is 9×10^{-15}W.

The wide range of input power used has brought an important feature of the bridge to light. The resistance that is measured is a function of the power level used. As the power level gets smaller, the measured resistance goes up: with $P=9\times10^{-15}$W, the error for a 10Ω resistor is 90%, while it is only 6% for resistors between 100 and 10 KΩ. In practice this is just an annoyance. All the thermometers have been calibrated using this bridge at specific power levels between specific temperatures. Therefore the power dependence should not affect the measurements made using this system.

2. Superconducting Fixed Point Device and Bridge

A superconducting fixed point device[72/] was obtained from the National Bureau of Standards, and used to assist in thermometer calibrations. A mutual inductance bridge, from a simple design given by Soulen, Schooley, and Evans,[73/] was used in conjunction with the device. A schematic showing both the device and the bridge is given in Fig. 10. The device and bridge measure the superconducting transitions of lead (7.1999 K), indium (3.4145 K), aluminum (1.1796 K), zinc (0.851 K), and cadmium (0.519 K) reproducibly to ±1 mK.[74/] Note that the temperatures quoted are from the EPT-76 temperature scale.[75/]

The device itself consists of two concentric coils with long, thin cylinders of the five materials inside. A similar set of coils is the basis of the bridge, and thus will be described in detail. The primary is 400 turns of #38 Cu wire (Formvar coated) wound in two layers on a 0.6 cm o.d., 2.5 cm long bakelite cylinder. The secondary is 2000 turns of #40 Cu wire (Formvar coated) wound on a 1.1 cm o.d., 1 cm long bakelite cylinder which fits over the primary. Both coils are covered with GE 7031 varnish. The resistance of the primary is 18.2 Ω, while that of the secondary is 294 Ω.

The reference signal is input, and the output analyzed, by a phase sensitive lock-in amplifier which is operated at 230 Hz. The variable, ten turn 10 KΩ potentiometer in the bridge is used to null the in-phase part of the output signal, while the variable capacitor is used to balance the resistive part. It was found experimentally that the resistive part is so small that the varible capacitor is unnecessary. A

Figure 10. Superconducting fixed point bridge and device. The bridge coils are described in the text. R_{Bal} is a ten turn, 10 K Helipot. The variable capacitor C is effectively zero, and so has been removed from the present version of the bridge.

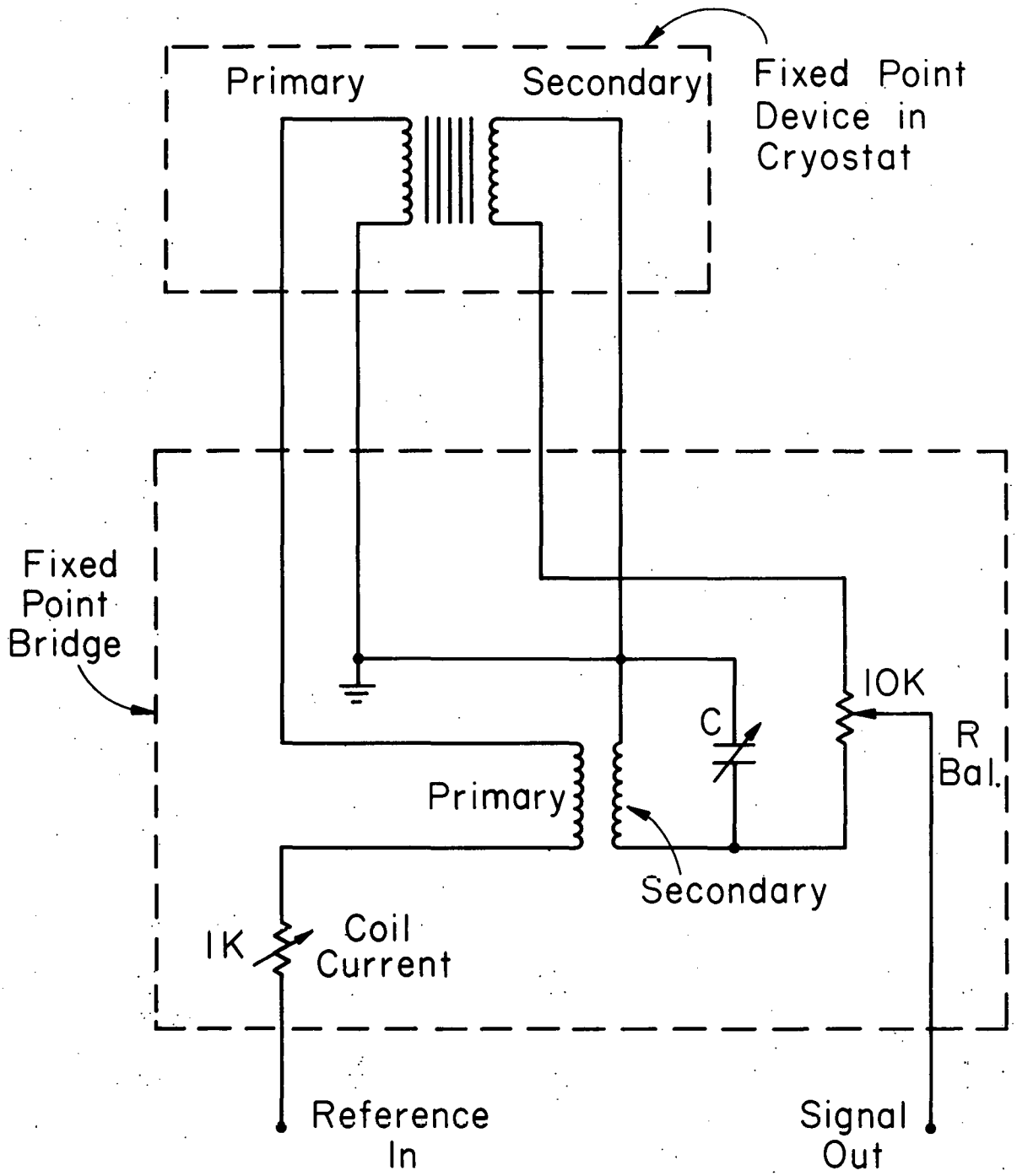
Primary
Secondary
Fixed Point Device in Cryostat
Fixed Point Bridge
C
10K
R Bal.
Primary
Secondary
1K
Coil Current
Reference In
Signal Out

variable resistance is part of the reference input line so that the power input can be easily changed (this is important at low temperatures).

The procedure usually used was to warm(cool) through the superconducting transition in question, and then to cool(warm) back to the center of the deflection of the lock-in due to the transition. The refrigerator was controlled at this temperature, which was operationally defined as the superconducting transition temperature, T_c. The fixed point device was not shielded from stray magnetic fields due to space limitations in the cryostat, and so the actual T_c's were lower than those quoted. The appropriate correction factors are given by Schooley, Soulen, and Evans.[74] They range from 3.2 mdeg for the cadmium T_c to 1.5 mdeg for lead, because the field measured at the cryostat was 3×10^{-5} T.

3. Thermometer Calibration

Several new germanium thermometers, and the previously used germanium and carbon thermometers were calibrated carefully by several different methods. The primary calibration was performed on a new germanium thermometer, G15559,[76] which was calibrated in a separate cryostat against a germanium thermometer which was calibrated against ^{3}He vapor pressure above 1 K, against a CMN magnetic thermometer below 1 K, and checked against a set of NBS fixed points. All temperatures quoted are from the EPT-76 temperature scale.[77]

Calibrations of the other thermometers were determined by comparison with G15559. This calibration was performed by removing the sample cell and replacing it with a copper block in which were mounted four germanium thermometers and the NBS fixed point device. The new calibrations

were consistent with, but more comprehensive than, the old calibrations of C-100A (a carbon thermometer) and G4317, the old calibrated germanium thermometer. They also agree with the temperatures as determined by the fixed point device. The temperature measurements are therefore believed to be accurate to better than 1/2% over the range from 40 mK to 7 K.

E. Sample Preparation and Analysis

Preparation of the ^{3}He-^{4}He mixture to be studied, growth of a crystal adequate for precise x-ray measurements, and the analysis of the concentration of the mixture which was studied are three important facets of the present work. The first is important, though straightforward, because there is no second chance without much expense for new ^{3}He. The second two are crucial. The third part, analysis, is particularly crucial because again there is only one chance to obtain the necessary measurements.

1. Mixture Preparation

The main difficulty in preparation of the mixture was the desire to dilute the ^{3}He with ^{4}He in successive steps, thus using as little ^{3}He as possible. This was accomplished by preparing the new mixture in the ^{3}He gauge and ^{3}He side of the separator shown in Fig. 8, using as its basis the last mixture. This mixing is accomplished easily by letting high pressure ^{4}He ($\sim$13 MPa) rush into the ^{3}He side of the high pressure system. The pressure difference (>7 MPa) assures that there is no contamination of the ^{4}He side with ^{3}He. The difficulty experimentally is that the bellows in the separator expands when the ^{3}He (mixture) pressure increases, thus increasing the volume inside the separator which is available to the mixture.

This problem is avoided by maintaining the piston travel indicator (PTI) in the same place by pressurizing the ^{4}He side of the separator also. Because of the slow response time of the separator, this process takes hours.

After the correct pressure (and thus concentration) was obtained, an attempt was made to improve the homogeneity of the mixture, which was residing both in the separator and the ^{3}He gauge. The separator was compressed so that most of the mixture was forced into the ^{3}He gauge, which then read typically about 8.7 MPa. The separator was then depressurized, and the mixture forced back into the separator, leaving the ^{3}He gauge typically at 2.0 MPa. This prescription was followed once or twice, depending on how much time was available before the cell needed to be pressurized with the new mixture.

2. Crystal Growth

The growth of good quality single crystals is essential to the success of the present x-ray measurements. The crystals must pass stringent tests before they are used for data collection, of which the usual examination of the quality of spots from Laue photographs is only the first. In the previous work,[20/] only crystals that were single over the whole length of the sample cell were acceptable, as the others were found to be unstable. With the development of the new diffractometer drive and position sensitive detector, which are described later, this condition was found to be unnecessary. This is very important: it was also found to be impossible to grow a crystal of a concentrated mixture that was single through the whole cell. Without the new diffractometer system, the present experiment would be impossible. Even with this easing of the quality

requirement, more than 80% of the crystals grown were discarded because of insufficient quality.

The normal method used here for growth of helium crystals, and the results of growth of 110 crystals of pure bcc ^{3}He and pure hcp ^{4}He, have been described by Fraass, Heald, and Simmons.[78/] The crystals are grown slowly from the liquid at constant pressure, since the fill line is kept unplugged until after growth is completed. A plug in the fill line is then formed to keep the crystal at constant volume. The crystals grow from the top down in the cell, because the cold finger of the dilution refrigerator is at the top of the cell. A computer is used to lower the temperature of the cold finger and the top of the cell slowly. A crystal growth curve is obtained by recording the temperature of the germanium thermometer at the bottom of the sample cell as a function of time on a chart recorder. The stated melting temperature is the temperature at which the crystal finishes growing.

Several typical growth curves are shown in Fig. 11, one for each mixture concentration that was studied here. Surprisingly, the curves for each concentration are qualitatively different. The curves for pure ^{4}He and nearly pure ^{3}He (99%) are normal, although the ^{3}He curve shows a small amount of supercooling before growth begins. The important points are that the beginning and finish of growth are obvious, the temperature gradient during growth is fairly small, and the growth time of 0.5 to 2 hours is easily determined. Note the differences in the mixture growth curves. It is nearly impossible to determine the melting temperature of the 51% mixture since there is no clear finish of growth, and the 28% mixture is different only in degree. This is related to the fact that the

Figure 11. Crystal growth curves for several different ^3He concentrations. The five curves (labeled by ^3He concentration) are schematic representations of the temperature of the thermometer at the bottom of the sample cell plotted versus time, as the top of the cell is cooled at a constant rate. The "flat" region in the center of each curve occurs as the crystal grows. The dip seen in the 12% mixture before the growth begins corresponds to supercooling of the liquid. A typical temperature range for the growth curves shown here is about 200 mdeg, while the extent of the time scale is typically 1 to 3 hours.

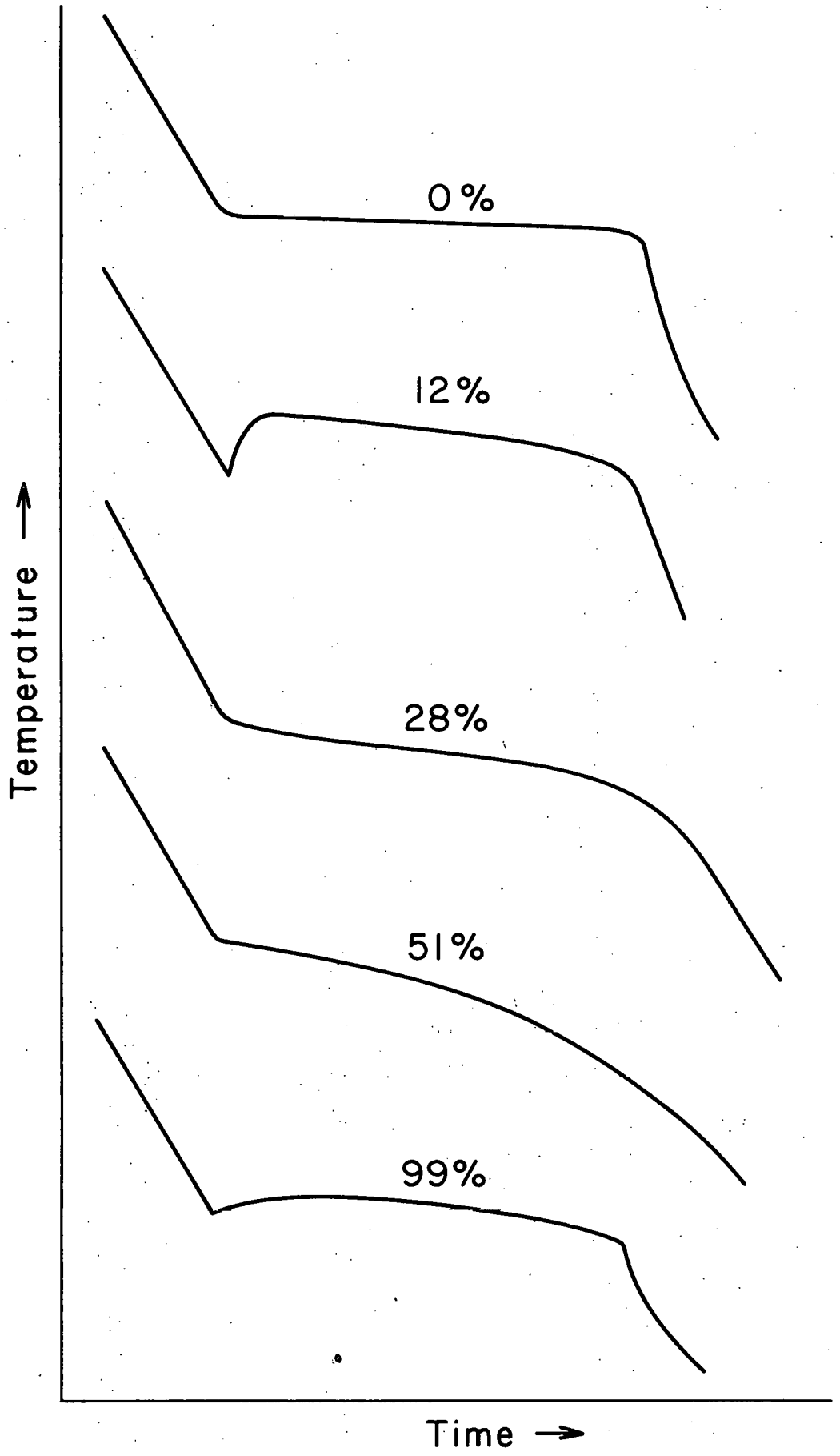
0%
12%
28%
51%
99%
Temperature →
Time →

mixtures are non-azeotropic and thus the crystals do not grow at exactly the same concentration as that of the liquid from which they are grown. The growth curves of the 12% crystals are also interesting: there is always a large amount of supercooling before growth begins, no matter what the cooling rate is. The other interesting point found at this concentration is that the crystals all grow in the same orientation: six in succession were grown in the same orientation, and then three more grew in the same (but different from the previous six) orientation. This behavior has not been seen in any of the other concentrations studied in the present work, or in that of Heald.[20] Similar behavior has been seen by Osgood, et al.[79] in their neutron study of bcc ^{4}He. They saw that all eight of their crystals had an [001] reflection within 5 degrees of the others. In the present study, each of the six crystals had a [110] reflection within one degree of the others.

It had been hoped originally that the melting temperatures, as determined from the growth curves, would be a useful check of the concentration measurements. Unfortunately, there were two problems with this desire. The first is easily seen in Fig. 11: for the concentrated mixtures, the melting temperature is all but impossible to determine. Secondly, the temperatures that were determined from the growth curves were lower than the melting temperatures expected (from published phase diagram data[31-33]) by as much as 0.1 deg. This "disagreement" is due to the difference in the liquidus and solidus curves, as discussed in Chapter II. Most of the P-T melting line data are obtained on the liquidus, while the temperatures obtained from the present growth curves are on the solidus. The point at which growth starts on the growth curve should be on the liquidus. However,

the determination of this temperature from the growth curve is unreliable because there may be a large temperature gradient in the cell, between the thermometer at the bottom, and the top of the cell where the crystal begins growing. Therefore, neither the indicated starting nor finishing temperature obtained from the growth curve is any help in checking the mixture concentration.

3. Sample Concentration Analysis

The concentration of ^{3}He in the mixtures studied here was measured with the mass spectrometer in a Dupont 24-120B Leak Detector. The sensitivity of the spectrometer to ^{3}He and ^{4}He was checked before each set of measurements with ^{3}He and ^{4}He standard leaks,[80/] with sensitivities generally about 2.0×10^{-10} atm cm^3/sec for ^{3}He and 3.0×10^{-10} atm cm^3/sec for ^{4}He. The method used should measure the ratio of the two isotopes to about 500 ppm (0.05%).

The procedure followed during the concentration measurements involves warming the cryostat to 77 K. The warmup is easily accomplished simply by allowing the liquid helium to run out, after which about 24 hours is required before the sample cell warms to 77 K. During this time the separator is used to lower the pressure in the fill line and sample cell, while saving the gas by compressing it into the ^{3}He gauge. At the same time the leak detector is used to pump out the high pressure system, up to the last valve before the fill line. When the cell is near 77 K, the fill line and sample cell are pumped out with the diffusion pump of the leak detector, while the ratio of ^{3}He to ^{4}He that is coming out is measured every minute or two. The gas initially pumped out is from the fill line

only, and so its concentration is not desired. Also not desired is that which is measured after the cell pressure is low because it is sensitive to the vapor pressures of the gas in the cell at 77 K. Only the concentration of the gas pumped out between these two extremes is useful. Because the readings taken at different times during the pumping are somewhat different, the choice of readings which are used to calculate the concentration is the largest contribution to the possible errors in those measurements. The nominal mixtures, concentrations, and estimated uncertainties are given in Table 1.

TABLE 1.--Mixture concentrations. The nominal mixture, measured ^{3}He concentration (x_3), and the uncertainty in x_3 are listed for the various crystals measured in this work.

Nominal Mixture	x_3	Uncertainty	Crystals
0%	0	------	0-14
99%	0.989	0.0005	16-19
51%	0.506	0.012	20-26
28%	0.280	0.005	27-28
12%	0.125	0.015	29-30

F. Position Sensitive Detector

A position sensitive x-ray detector (PSD) was designed and built for use with the newly rebuilt diffractometer (described in the next section). The PSD is a recently-developed type of proportional counter that was first described by Borkowski and Kopp.[81/] From this detector both position and energy information are obtained from each ionizing event. The advantage of this type of detector is obvious: a complete Bragg peak may be

obtained at once, without scanning the detector as is done with the usual scintillation counter. The PSD also allows much flexibility in the diffractometer design and use.

The PSD used here is similar in design to that described by Borkowski and Kopp.[82/] The detector is a gas-filled proportional counter with a very high resistance collector wire. Each ionizing event occurring in the detector causes a current pulse to travel both directions down the collector wire. A comparison of the rise times of the pulses at each end of the wire yields the position of the event which caused the two pulses. As with any proportional counter, the amplitude of the pulses is proportional to the energy of the event.

A schematic drawing of the detector is shown in Fig. 12. The body is Lucite, with a cavity machined into it. The three sides of the cavity have 0.025 mm aluminum foil smoothly fixed to the Lucite with a mixture of a graphite compound[83/] and GE 7031 varnish. Electrical connection to the high voltage supply is made with a wire in a groove at each end of the detector, attached to the foil with silver paint. The Be window on the front of the detector is electrically connected to the foil. A mixture of 90% Ar - 10% CH_4 gas at a pressure of 0.12 MPa above atmospheric pressure is run through the detector at about 6 ml/min.

The collector wire is a 0.025 mm diameter pyrolytic carbon-coated quartz fiber, with a resistivity of 8000 Ω/mm.[84/] The wire is mounted in a guard ring assembly at each end of the detector. The guard rings are very important: a previous version of the detector, without guard rings, showed obvious and important end effects, and also a lack of sensitivity and linearity. The guard rings, shown in Fig. 13, have eliminated these

Figure 12. Position sensitive detector. Both the right and left sides of the PSD are the same. For clarity, they are drawn in this cross-sectional view showing different parts of the design. The 0.25 mm Be window (A) is epoxied into the Lucite frame (B), which is sealed to the body of the detector (D) with an o-ring (C). One of the two gas flow connections (E) is shown, as well as one of the two holes in which the two guard ring assemblies are mounted (G). The grooves for the high voltage wires (F) are shown, as is the 5.1×0.95×0.48 cm cavity (H) which is machined into the Lucite body.

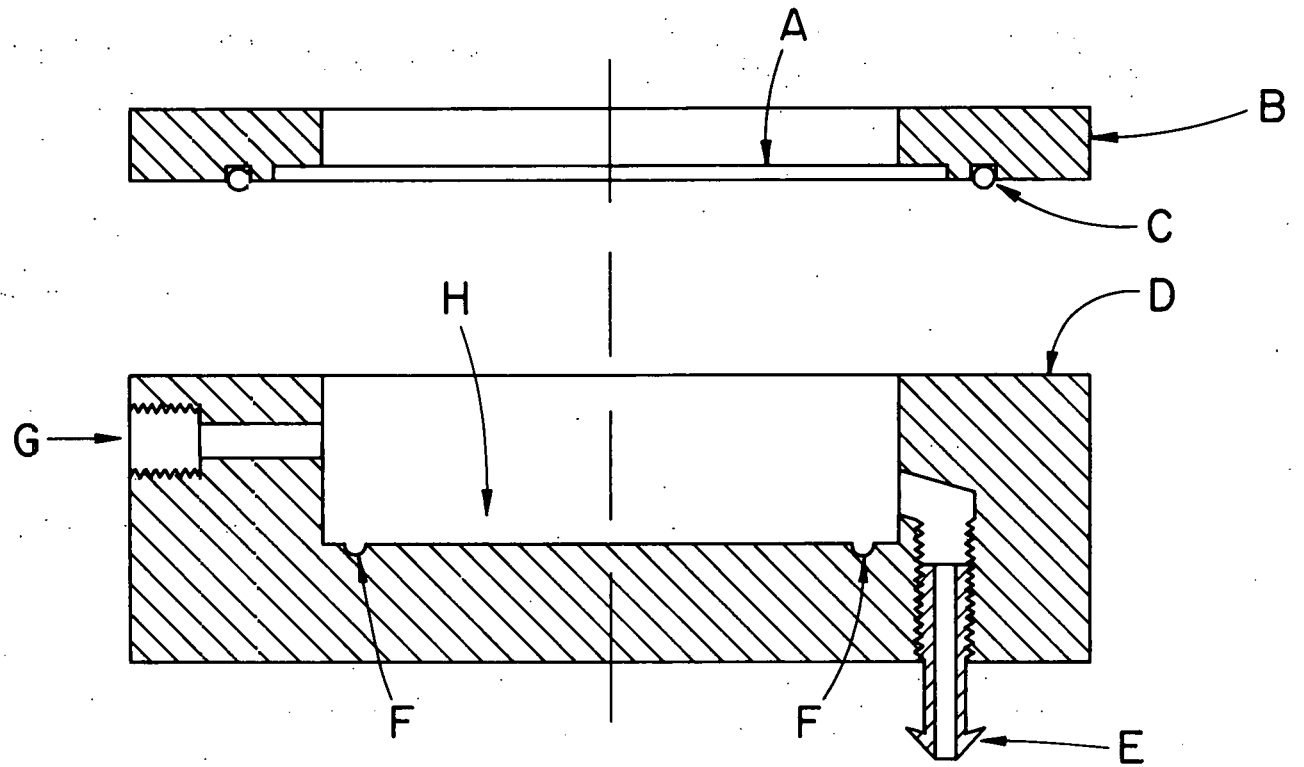
A
B
C
C
H
D
G
F
F
E

Figure 13. Guard ring assembly. The quartz fiber (A) is fastened with epoxy and silver paint (H) inside a 0.4 mm diameter CuNi tube (G), which itself is then epoxied into an insulating Lucite tube (I). The guard ring is a 1.6 mm diameter, 0.1 mm wall CuNi tube (C) which is soldered into a threaded brass piece (D). This piece screws into the body of the detector (B). The fiber assembly slides through the guard ring and is fixed in place and pressure sealed with a rubber o-ring (E) which is tightened with a brass cap (F), to which the guard ring electrical connection is made.

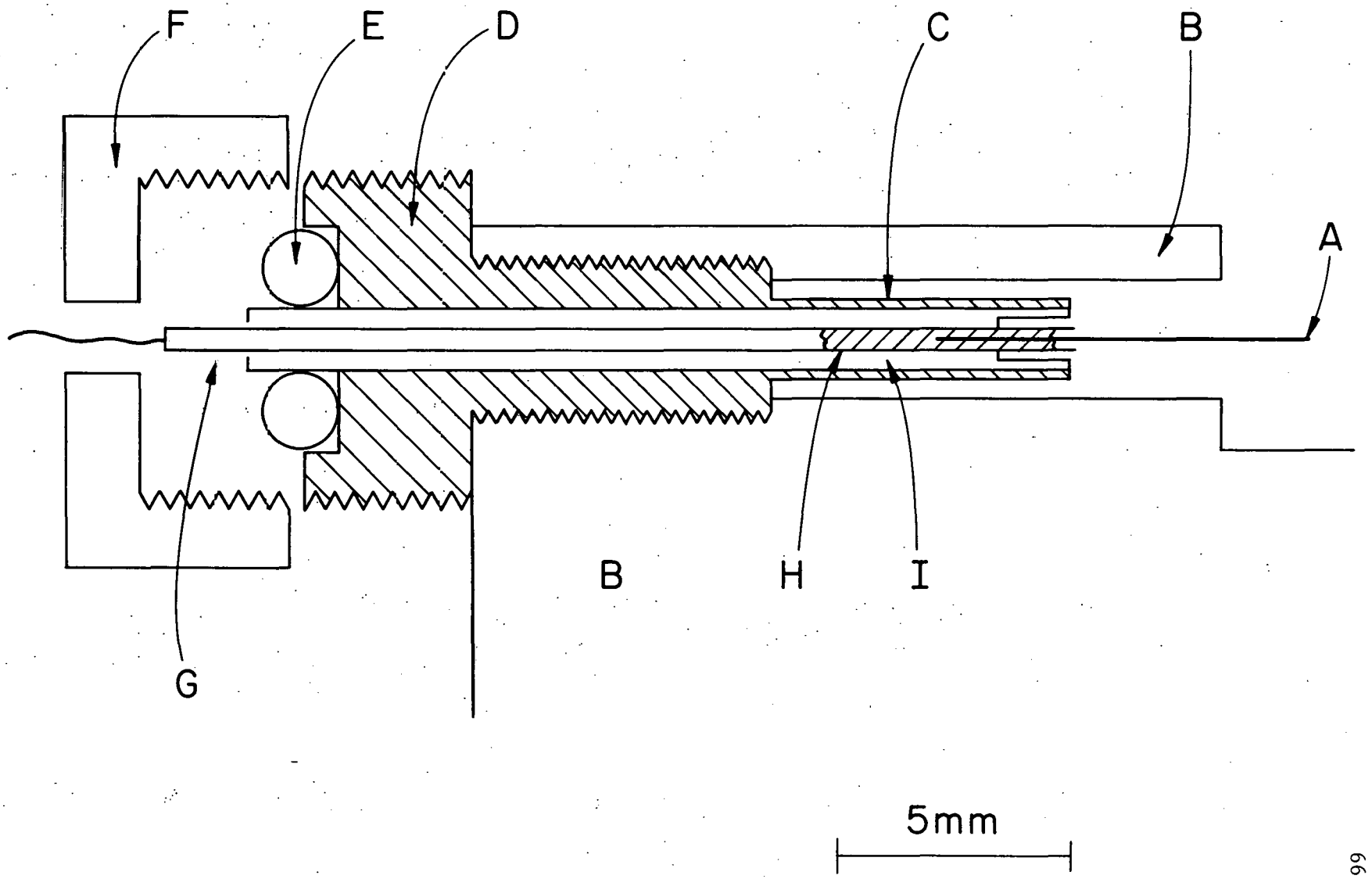
F
E
D
C
B
A
G
B
H
I
5mm

problems. The entire assembly is recessed into the body of the detector in order to minimize the distortion of the electric field near the detector edges. The rings are at ground potential (the wire is near ground) so that leakage currents do not degrade the response of the wire. For additional protection there is a long insulating path between the high voltage and the rings. The purpose of the guard ring design is to allow easy replacement of the fiber. Our experience, and that of others,[85/] has shown that the fiber is very susceptible to damage. In fact, even though very great care was taken in order to prevent this degradation during the present experiment, the detector performance deteriorated noticeably.

One of the advantages of this type of detector over other types of PSD's is the simplicity of the electronics which are required.[86/] A block diagram of the PSD electronics is shown in Fig. 14. Charge-sensitive preamplifiers are mounted immediately adjacent to each end of the wire in the detector, in order to keep the capacitance of the signal leads as small as possible. Each pulse is doubly differentiated by the linear amplifiers, and the times at which the resultant pulses cross zero are detected by the crossover pickoffs (CP's). After time delays in the CP's, the two pulses ("start" and "stop") are fed into the time to amplitude converter (TAC), which converts the time difference to the height of a voltage pulse. This pulse height is then analyzed by the multi-channel analyzer (MCA), which stores the event in a particular channel which corresponds to a position in the detector. The data stored in the MCA are displayed on a cathode ray tube monitor (CRT).

The heights of the pulses from the linear amplifiers are proportional to the energy of the event, and so energy discrimination is possible.

Figure 14. PSD electronics. Shown are the electronics with which the "start" and "stop" pulses from the PSD are analyzed. The preamps are Tennelec model TC 112, the two amplifiers are Tennelec TC 202BLR Linear Amplifiers, and the cross-over pickoffs (CP) are Tennelec model TC 446. Shown also are the Fluke 412B High Voltage Supply (HV), the Canberra 1465A Sum-Invert Amplifier (Sum Amp), the Canberra 1437 Timing Single Channel Analyzer (TSCA), the Tennelec TC 861 Time to Amplitude Converter (TAC), the Tracor-Northern TN-1706 Multichannel Analyzer (MCA), and the Tektronix type 604 monitor (CRT).

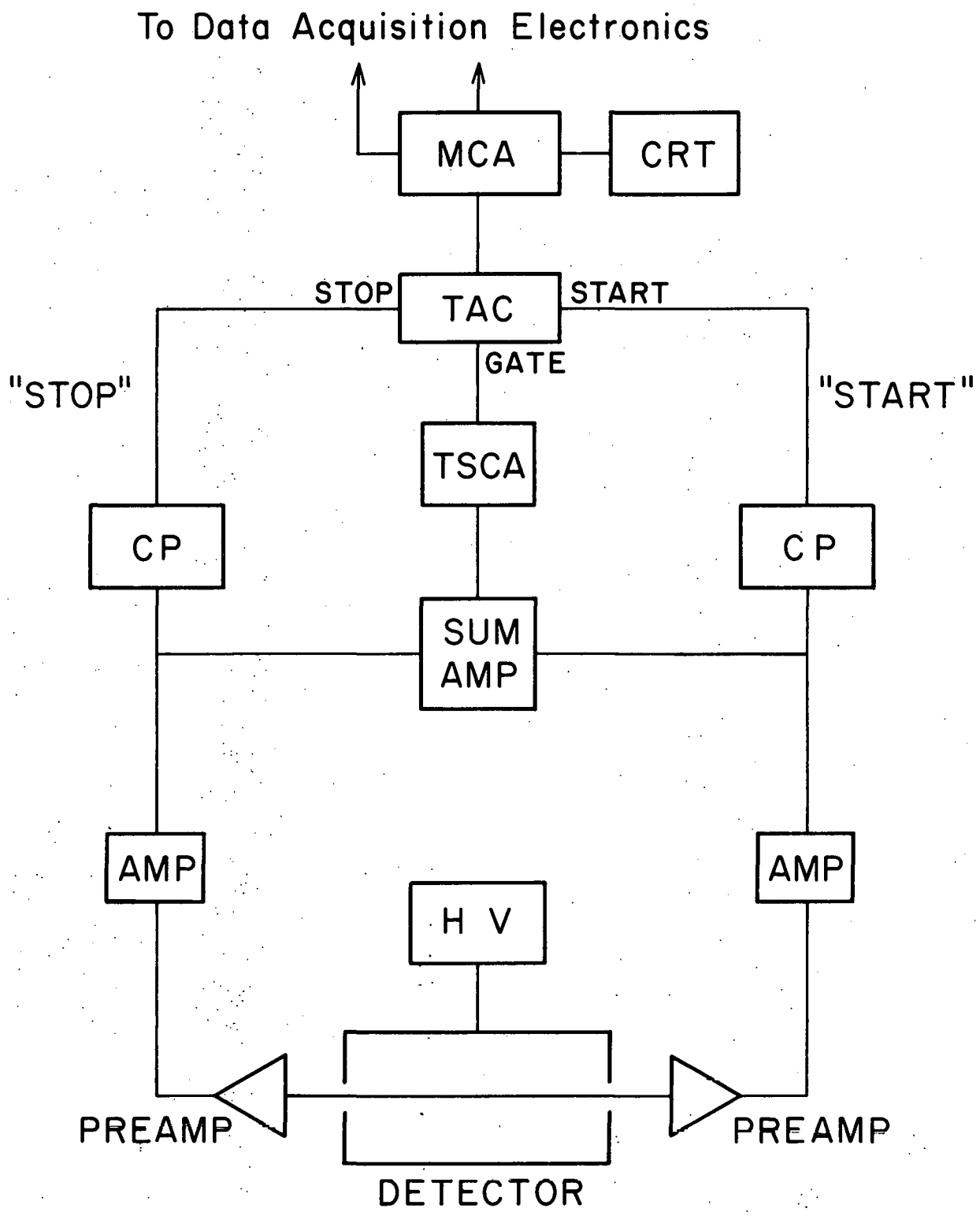
To Data Acquisition Electronics
MCA
CRT
STOP
TAC
START
GATE
"STOP"
"START"
TSCA
CP
CP
SUM
AMP
AMP
AMP
H V
PREAMP
PREAMP
DETECTOR

The "start" and "stop" pulses are added in the sum amplifier (Sum Amp), and the discrimination is performed on the resulting pulse by the timing single channel analyzer (TSCA). If the energy of the sum pulse is within the desired limits, the TSCA gates the TAC, allowing a "start"/"stop" pulse combination to be registered. The discrimination is mildly position-dependent, but this is only bothersome if one wishes to use a small energy window.

It is important that the resolution and linearity of the PSD be well-characterized for its use in the diffractometer system. The usual discussion of PSD resolution involves the full width at half maximum (FWHM) from a well-collimated incident beam. The minimum FWHM of this PSD is 0.5 mm for Cu Kα x-rays. This agrees with that found in other detectors of this type,[87] although smaller FWHM's are possible with different incident radiation.[86,87] However, it is not the width of the peak that is important here, but the reproducibility with which the peak centroid may be determined. Experimentally, we have found that the peak centroids are stable to better than 0.2 MCA channels, which corresponds to 12.5 μm. This is dependent on (1) having enough counts for adequate statistics, (2) correctly handling the background, and (3) a fairly symmetric peak. This sensitivity to peak movement corresponds to a change of lattice parameter of about 60 ppm at a Bragg angle of 15 degrees in the present diffractometer system.

The linearity of the PSD is measured by comparing the peak centroid channel against position as the detector is moved so that the peak moves across the detector. Shown in Fig. 15 are two plots, one of which is distance versus peak centroid channel number. Also shown is the derivative of the distance versus centroid data. The error bar shows the uncertainty

Figure 15. PSD Linearity. Shown plotted is PSD position (•) versus peak centroid channel number. Also shown are the derivatives of those measurements, plotted as channels moved per mm moved (+) versus peak centroid channel number. The error bar on the derivative measurements shows the effect of the uncertainty of the distance measurement (0.01 mm) on the derivative.

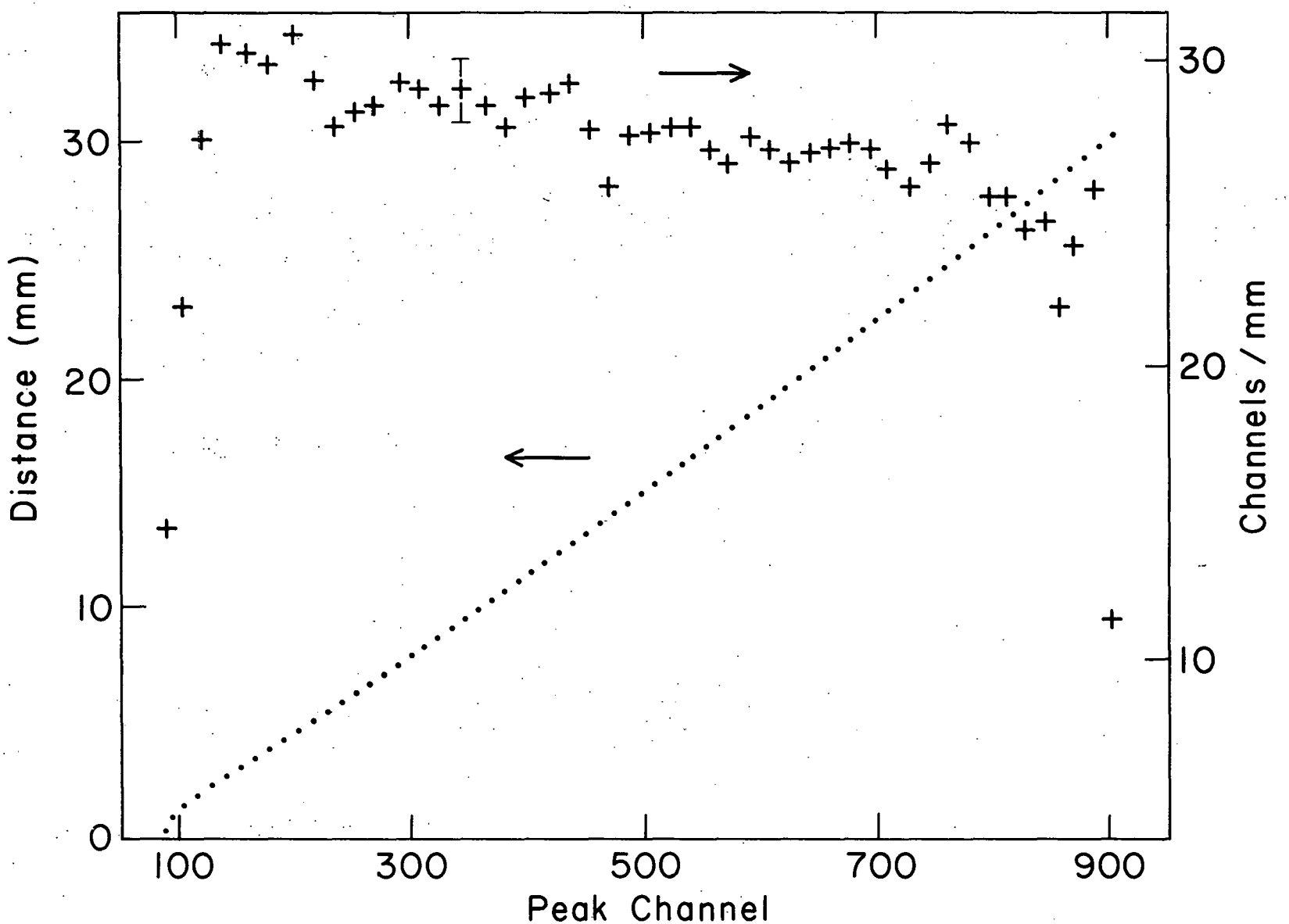
Distance (mm)
0
10
20
30
Channels / mm
10
20
30
100
300
500
700
900
Peak Channel

in the distance measurement, which was 0.01 mm at each position. Apparently all the deviations from the basic linear dependence of this derivative on channel number can be explained by this reading uncertainty. Note that the distance versus peak channel curve shows none of the s-shaped character that other workers have seen.[86]

G. X-ray Diffractometer

The present diffractometer is the third version of a diffractometer originally designed and built in this laboratory by Kabat.[88] The first and second[20] versions were equipped with a θ-θ drive, that is, a drive mechanism which moves the x-ray source and detector at equal speeds in opposite directions. The development of the PSD has made this type of drive unnecessary. This improvement allows the use of a gear drive which makes precise absolute lattice parameter measurements possible.

1. Mechanical Description

A general view of the cryostat and diffractometer is shown in Fig. 16, which also shows the various coordinates used in the following description of the diffractometer. An exploded view of the diffractometer is shown in Fig. 17a-d. Fig. 17a shows the x-y motion. Both the x and y motions are driven by computer-controlled stepping motors. This allows automatic centering of the diffractometer on the sample cell (which is inside the cryostat) to within 0.03 mm. The bottom plate of the x-y motion sits on a commercial elevating table which is made rigid with vertical stainless steel bars and linear ball bushings held in an external frame. This z coordinate is read with a dial indicator. Three screw jacks

Figure 16. Relative positions of the three-circle diffractometer, cryostat, and cryostat support frame. (A) Concrete inertia block. Diffractometer adjustments in angles θ, χ, and ϕ are available. The rectilinear motions X, Y, and Z permit centering of the specimen sample cell in the diffractometer. (B) Cryostat. (C) X-ray tube. (D) Detector.

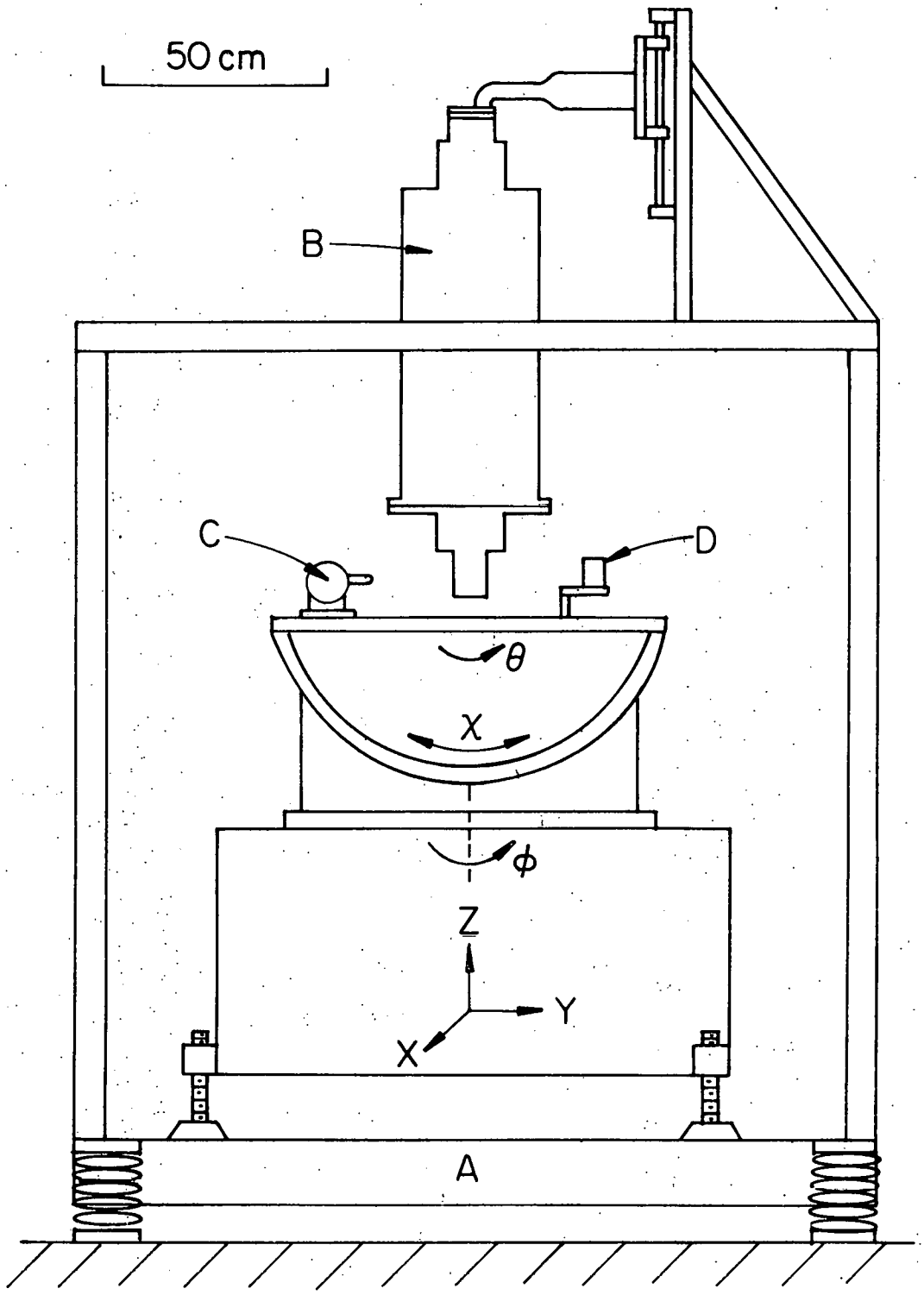
50 cm
B
C
D
θ
χ
φ
Z
Y
X
A

Figure 17a. Diffractometer x-y motion. The x and y motions shown here consist of stainless steel bars sliding inside linear ball bushings. Both motions are driven by computer-controlled stepping motors (I and H), and the motion is measured by dial indicators, which are not shown. The motors are Superior Electric Co. Slo-syn M092-F stepping motors.

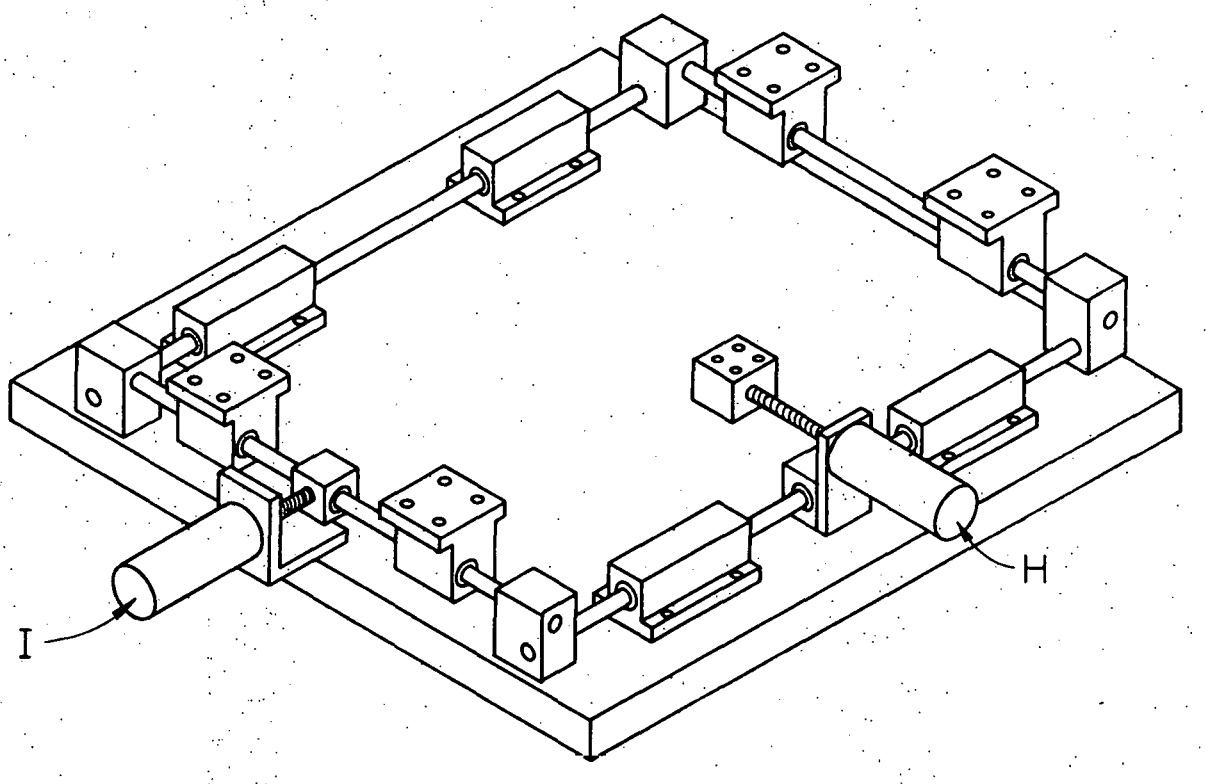
I
H

Figure 17b. Diffractometer ϕ and χ circles. Mounted on a plate above the x-y motion is the 56 cm diameter ϕ circle (G). This circle, which is divided and can be read directly to 5 minutes of arc, rides on a race of balls at the periphery, and is held by a post and ball bearing at the center. On this circle is mounted the χ circle cradle (D). These brass runners have a 40 cm radius, and are the base upon which matching stainless steel runners move with low friction. The declination angle χ is read to $\pm$ 1 minute using a Watts 360° clinometer. The χ circle is moved by the friction of a 1.2 mm diameter braided steel wire on a stainless steel drum (J).

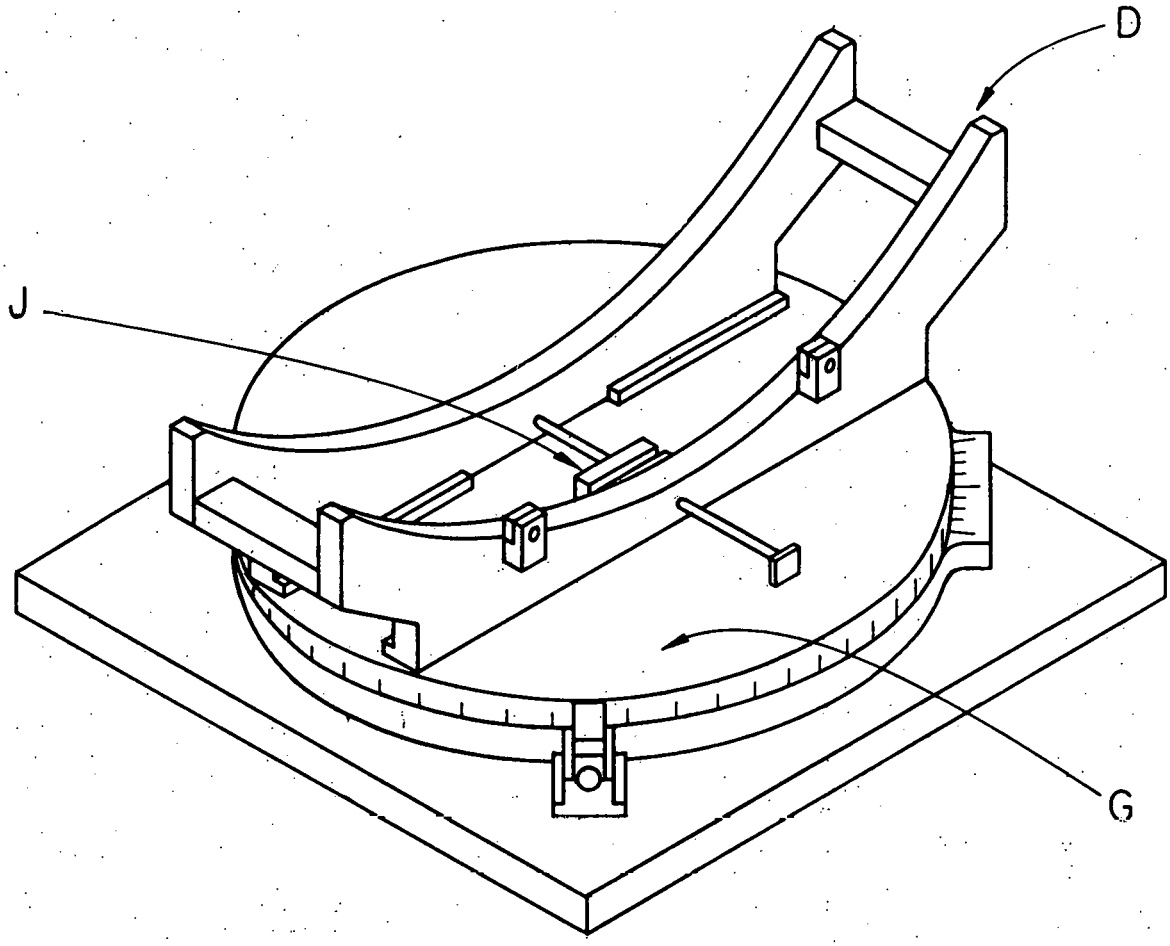
D
J
G

Figure 17c. Diffractometer gear drive. The 384 tooth worm gear (N) is the heart of the drive mechanism. The worm gear can be attached to either of two arms: (O), which can be attached to the θ table, and (C), upon which the PSD is mounted. Each of the arms, and the gear, are supported on the center post by New Departure type H20305 ball bearings. The worm gear is driven by a long gear train, which includes the stepping motor (M), a bevel gear set (L), and the stainless steel worm (F). The worm shaft position is measured by the digital shaft encoder (E). The stepping motor is a Slo-Syn HS-50L, and the encoder is a Datex model C-713-20 shaft encoder. The stainless steel 2:1 bevel gear set is PIC N1-2-S, while the worm shaft is maintained in position by a Bearden SR168SS bearing between the worm and the encoder, and by two opposed Andrews DM-15 Thrust Bearings (K). The bearings which keep the bevel gears in position are Bearden type SR155SS, and SR133SS, one of which is not shown for clarity. Also shown in this figure are the stainless steel χ cradle runners (D). All machined parts except the aluminum bronze worm gear and the brass locks for parts O and C are stainless steel.

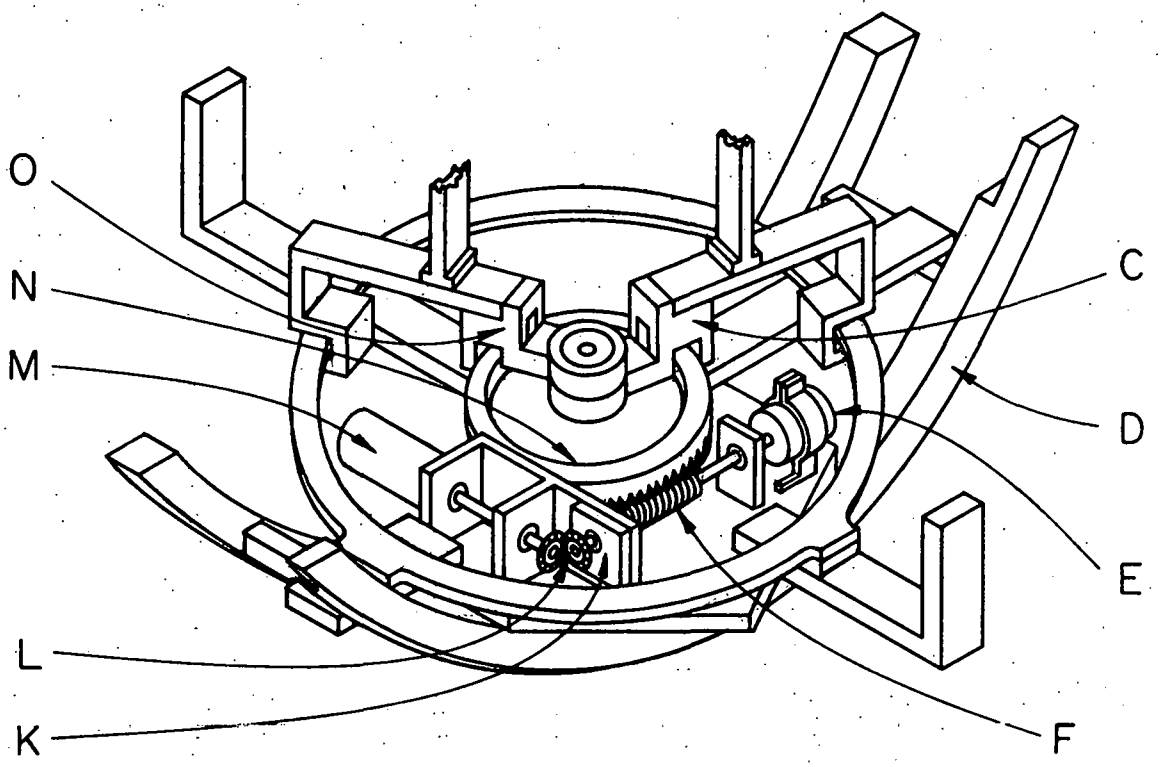
O
N
M
L
K
C
D
E
F

Figure 17d. Diffractometer θ table. The 74 cm diameter θ table (B) is shown here. The table turns on a 50 cm diameter bearing which rests in a stainless steel support attached to the χ cradle. The General Electric CA-8 Cu x-ray tube (S) is mounted on the θ table, as is the 0.10 cm i.d. x-ray collimator (R). The θ table is attached to the worm gear with a lock (Q) when θ table motion is desired. The PSD is mounted on an arm which can also be attached to the worm gear. A lock for preventing θ table motion (P) is also shown.

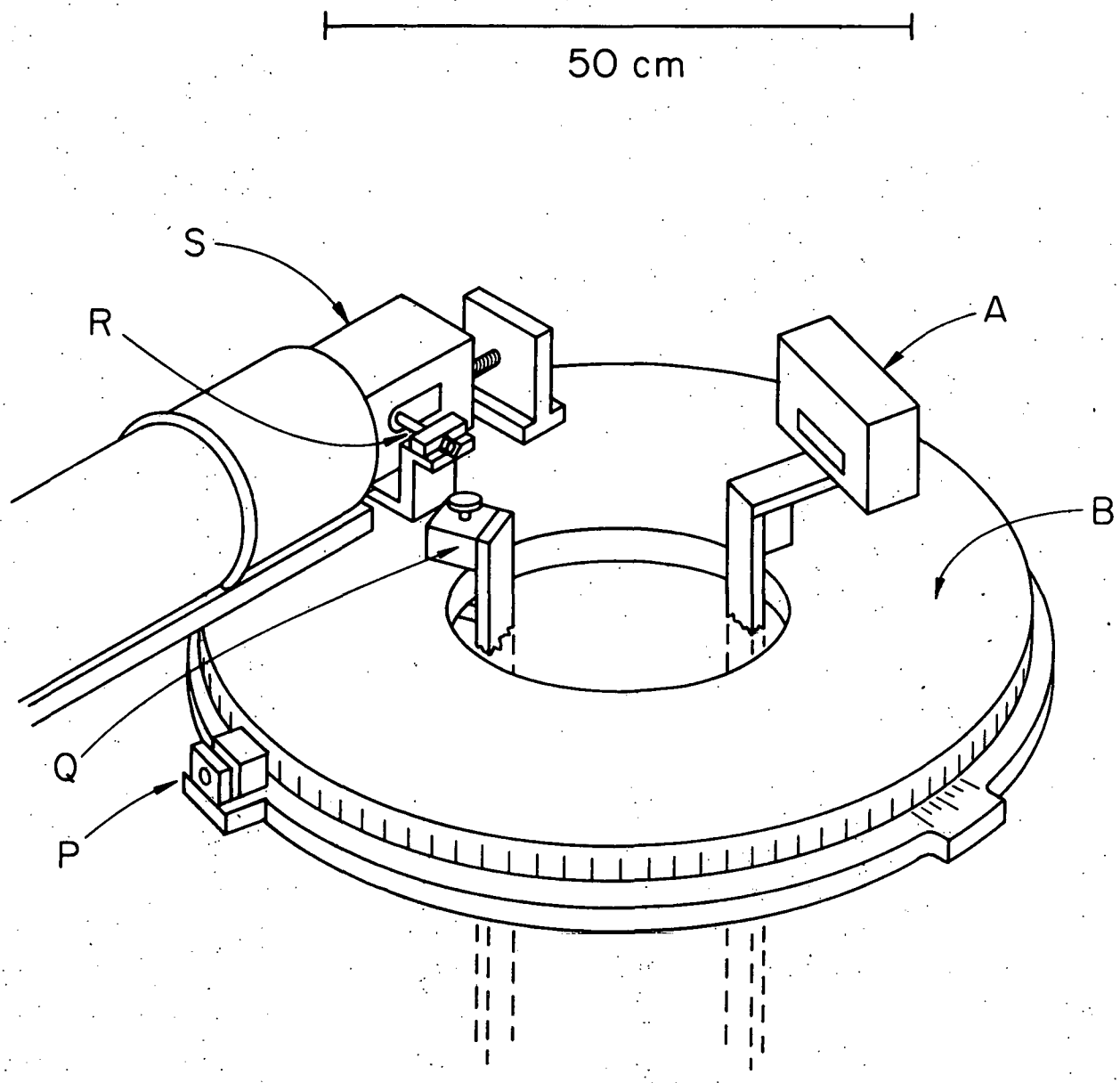
50 cm
S
R
A
B
Q
P

attached to the external frame allow leveling of the whole apparatus. Mounted above the x-y motion is the ϕ circle and χ cradle, which are shown in Fig. 17b .

Shown in Fig. 17c are the runners of the χ circle, upon which is mounted the newly designed gear drive mechanism. A 20 cm diameter worm gear made of aluminum bronze[89/] is the basis of the drive. The gear is supported on a ball bearing at the center post, and a race of balls at the edge. The 384 tooth[90/] worm gear is driven by a 1.3 cm diameter stainless steel worm.[90/] The position of the worm shaft is maintained with a bearing on one side of the worm, while two opposed thrust bearings at the other end of the shaft prevent both lateral and longitudinal motion of the shaft. The worm is driven by a stepping motor which is at a right angle to the worm because of space limitations. This corner is turned with a 2:1 stainless steel bevel gear set. The gears are maintained in position with bearings on each shaft, one of which is not shown in Fig. 17c for reasons of clarity. Also not shown are the Plexiglas shields which protect both sets of gears from dust and other objects.

The final part of the gear train is the digital shaft encoder, which is mounted on the end of the worm shaft. This 100 revolution absolute encoder reads the position of the worm shaft to 0.001 revolutions, which corresponds to 3.4 sec of arc on the worm gear. For comparison, the stepping motor, which gives 200 steps per revolution, moves the worm gear 8.4 sec per step. Although the alignment of the worm with respect to the worm gear is very important, as long as precautions are taken to avoid backlash, the position of the worm gear is correctly measured by the encoder. In practice, it was found that the worm was not correctly centered

when it was cut, and so there is a sine wave variation of the worm gear motion which has as its period one revolution of the worm. This motion was accurately measured, and is automatically corrected by the computer as it reads the shaft encoder position.

The motion of the worm gear must be transmitted to the θ table (on which the x-ray source sits) and/or the PSD (see Fig. 17d). This is accomplished by two "arms" shown in Fig. 17c. These arms are constrained to move only around the θ axis, because they are supported by bearings around the center post, and by a runner arrangement which prevents vertical or "twisting" motion of the arms. The arms can be locked to a "lip" above the gear. These locks slide radially (even when locked) to prevent binding in case of some misalignment, but when locked allow no lateral movement of the arm with respect to the gear. The PSD is mounted on one arm, while the other arm can be clamped to the θ table. This locking arrangement allows the gear to drive the θ table, the PSD, or both. Additional locks are put on the runner on either side of the detector arm to keep the PSD fixed, when that is desired.

The θ table is shown in Fig. 17d. It is a 1.3 cm stainless steel plate, 74 cm in diameter, with a 30 cm hole in the center. The x-ray tube is mounted on the table, as well as the x-ray collimator. The circle is divided and can be read to 5 minutes of arc. It can also be locked to prevent motion.

Alignment of the diffractometer is important. The centers of the ϕ, χ, and θ circles must coincide with the center of the x-ray beam and with the axis of the gear drive. The worm must be aligned so as to minimize backlash, while at the same time preventing any binding of the motion.

With much effort, the diameter of the sphere of confusion due to miscentering of the various circles was reduced to less than 0.15 mm. The accuracy of the motion of the θ table is limited to 4 seconds of arc only by the resolution of the shaft encoder when care is taken with the locks which fasten the gear to the θ table.

2. Computer Control

The electronics with which the diffractometer-PSD system is controlled are shown schematically in Fig. 18. The LSI-11 microcomputer which controls the experiment is interfaced to the laboratory equipment through the "Blox" system developed here at the University of Illinois. Several machine language subroutines have been written for the LSI-11 that allow communication with any particular module in the Blox with one simple Fortran statement. These are listed in Appendix B, with comments and explanations. This system of computer control allows each of several types of scans, and their accompanying analysis, to be performed automatically.

The stepping motor driver is used to step any of the three motors on the diffractometer under computer or manual control. The x and y motors are used when centering the diffractometer on the sample cell, while the θ motor is used to scan the θ table and/or the PSD. Each lock on the diffractometer is equipped with a microswitch. The status of these switches is analyzed by logic in the driver which prevents stepping motor pulses when an incorrect combination of locks is closed. There are also limit switches (with a similar function) on each of the motions. The computer can determine if the motor in use is blocked. Finally, one stepping motor is used in conjunction with the sample temperature controller so that crystals may be grown under computer control.

Figure 18. Diffractometer Computer Control Electronics. The basis of the computer control for the diffractometer is the LSI-11 microcomputer. This is interfaced to the laboratory equipment through the Illinois Blox System. The stepping motor driver allows computer or manual control of all the motors on the diffractometer (x, y, θ), and the motor which is part of the temperature controller (T control). The driver also analyzes microswitches on the various diffractometer locks to prevent undesired movement (logic switches). The interface decodes the information from the shaft encoder, and also allows control of the MCA, and output of the data from the MCA to the LSI-11 at 3000 baud. A separate line directly from the MCA to the Blox (Sca out) carries a pulse for each count (anywhere on the PSD) to a Blox scaler. The x-y plotter is used to plot the data during acquisition, and also during the later analysis. The data are stored on floppy disks, and are later stored on magnetic tape associated with the DEC 2040 computer. The data are transmitted to the 2040 over a phone line (modem), or by directly reading the floppy disks into the computer through a separate LSI-11-floppy disk system directly interfaced to the 2040.

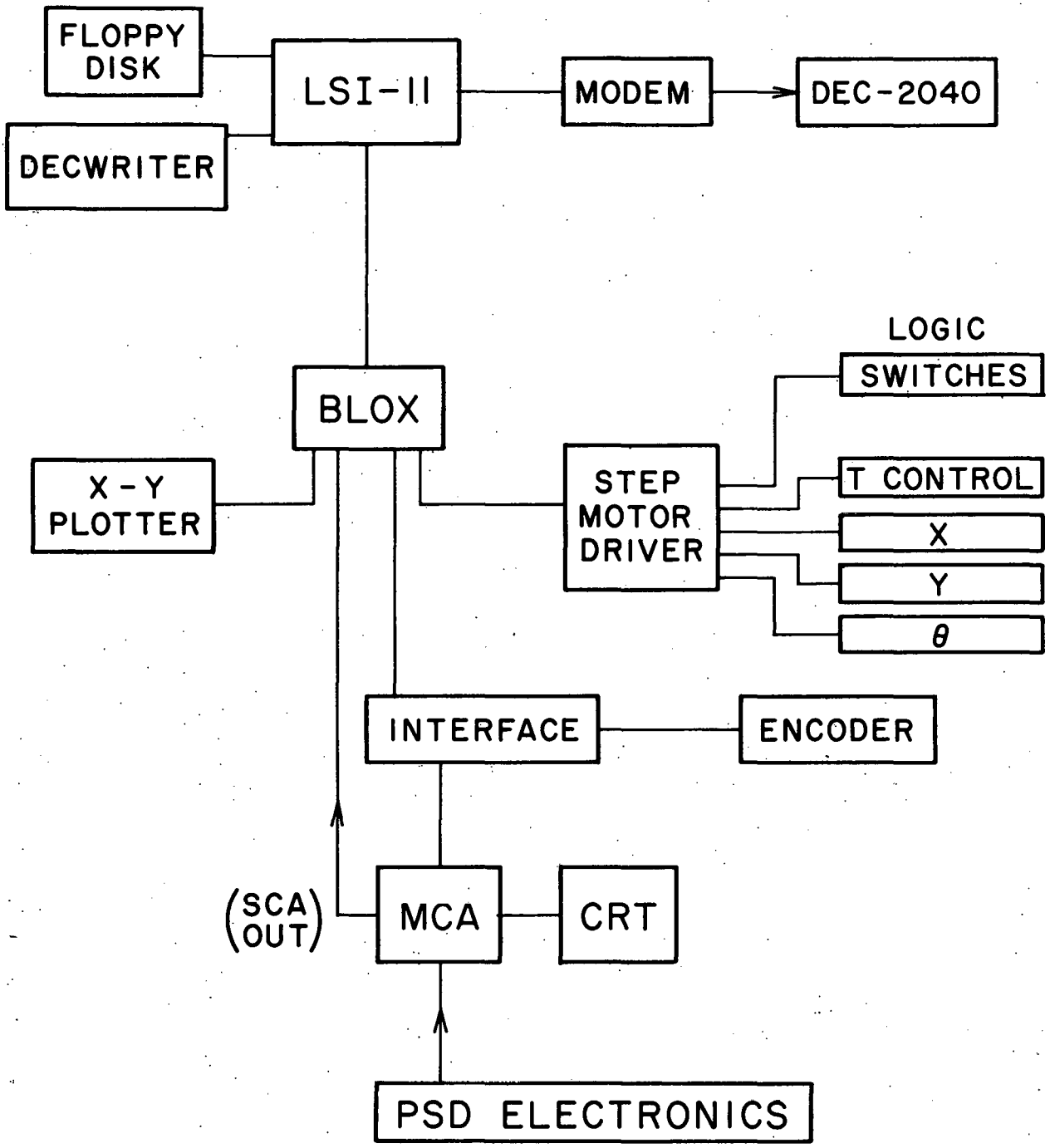
FLOPPY DISK
LSI-11
MODEM
DEC-2040
DECWRITER
LOGIC
SWITCHES
BLOX
X-Y PLOTTER
STEP MOTOR DRIVER
T CONTROL
X
Y
θ
INTERFACE
ENCODER
(SCA OUT)
MCA
CRT
PSD ELECTRONICS

An interface was designed and built which performs several different functions. The MCA is controlled through the interface: functions such as start acquire, stop acquire, start I/O, and stop I/O are initiated by the computer, which can also check the status of these functions. This makes possible great flexibility in the method of data collection. A second section of the interface allows the data from the MCA to be read into the computer at 3000 baud. Detailed computer analysis of the Bragg peaks can thus proceed seconds after the end of the scan. A third section of the interface translates the position information which comes from the shaft encoder in a 28 bit grey code into 6 BCD digits, which are displayed on the front of the interface with LED's, and also stored so that the computer can read the encoder position. Part of this section is also used so that data from a 6 digit frequency meter and 6 digit voltmeter can also be read into the computer (these were used with the strain gauge described in Section III-C and Appendix A). A final section of the interface uses a 12 bit digital to analog converter to display any three digits from the frequency meter on a chart recorder. Functional block diagrams, simplified schematics, and more complete descriptions of the interface are given in Appendix C.

3. Scan Types

The present diffractometer system is used for two separate types of measurements. Absolute lattice parameter measurements ("a") are made with one type of scan. Measurement of the concentration of vacancies present in the crystal ("x_v") is made with several different types of scans, since only knowledge of changes in lattice parameter ("$\Delta a/a$") is

required for these measurements. Vacancy concentrations are obtained by the method of Simmons and Balluffi.[25/] Because the crystal is maintained at essentially constant macroscopic volume in the present work, the Simmons and Balluffi expression for x_v becomes

$$x_v = -3\Delta a/a \qquad \text{(III-1)}$$

where Δa is the change in lattice parameter from some low temperature reference state in which there are few thermal vacancies present and whose lattice parameter is a. The constant volume assumption is valid because a plug of solid helium is used to seal the fill line. Volume changes due to the Lucite cell should be less than 0.01%,[20/] which is about the limit of sensitivity of the present measurements. Information about the different scan types used in the a and x_v measurements is summarized in Table 2.

TABLE 2 .--Diffractometer scan types.

Scan Type	Use	Errors ($\Delta a/a$)	Comments
a	a	200 ppm	More sensitive than 200 ppm to changes in a
PSD	$\Delta a/a$	120 ppm	No mechanical movement Very fast
ω	$\Delta a/a$	60 ppm	Mosaic structure obtained Detector more sensitive $\Delta a/a$ insensitive to crystal rotation $\Delta a/a$ insensitive to crystal quality

The simplest method of measurement of lattice parameter changes (and thus x_v), called PSD scan, uses only the position sensitive capabilities

of the PSD. There is no mechanical movement. The x-ray source is placed at the Bragg angle, and the PSD positioned so that the Bragg peak falls on the detector. The Bragg angle changes as the lattice parameter changes, and the peak moves along the PSD. Although theoretically the source should also be moved as the Bragg angle changes, in practice this is not necessary. The width of the peak due to the mosaic structure of the crystal is about 0.2 degrees, while the Bragg angle changes are less than a fourth of that.

The PSD scan has several advantages over the other scan types. There is no mechanical movement, so that only the PSD linearity and response are important. A second advantage is that the data may be obtained quite rapidly. This is important during melting, for example. Two to three minutes is sufficient time for accumulation of adequate statistics, even for the weak Bragg peaks that are obtained from solid helium. In this context, the 3000 baud output from the MCA to the computer is a necessity. It is the difference between waiting 30 seconds for the output, and the 20 minutes that would be required at 110 baud.

Another type of scan allows measurement of lattice parameter changes to better than 60 ppm. For this measurement, called ω scan, the PSD is fixed to the θ table. The source and PSD are scanned through the Bragg peak. Two types of data are collected during each scan: (1) the total number of counts into the PSD per unit time at each θ table (and hence source) position, and (2) the PSD peak which accumulates in the MCA. The first set of data (called "sca" data) gives the mosaic structure of the crystal and the position in space at which the source is at the Bragg angle. The second set of data ("mca") measures the Bragg angle, independently of the mosaic structure of the crystal. The sum of the changes seen in the "sca" data

plus those seen in the "mca" data gives the Bragg angle change, while the difference of the changes shows how much the crystal has rotated. The tendency of helium crystals to rotate at temperatures near the melting temperature was the cause of much of the instability of the crystals studied by Heald,[20] and the present method of data collection effectively solves that difficulty. All of the vacancy data and lattice parameter changes displayed in the present work were obtained by the ω scan method.

The ω scan has many advantages. Its insensitivity to crystal rotations has already been discussed. The data obtained from the MCA are very insensitive to crystal quality because the mosaic of the crystal is averaged by the scan. Crystal quality and mosaic structure are checked with every scan. This is especially important near melting and below phase separation in the mixtures. Finally, this method is by far the most stable and reproducible. Although the "sca" data are obtained as counts versus encoder position, and so should be limited to the 3.4 sec of arc sensitivity of the encoder, the centroids of the peaks in the sca data are reproducible to about 0.6 sec of arc. This corresponds to about 10 ppm in $\Delta a/a$. The PSD is twice as sensitive when it is fastened to the moving θ table than when stationary. Therefore, lattice parameter changes are measured to better than 60 ppm by this method.

Absolute lattice parameters are measured with a third type of scan, the "a" scan. This scan is somewhat related to the method used by Bond.[91] The data collected here are the same as the "sca" data mentioned above: the total number of counts into the PSD versus the source position. The geometry of the a scan is somewhat complicated, and is illustrated in Fig. 19 . The first step is placement of the source at angular position 1 and

Figure 19. Absolute lattice parameter measurement geometry. The first scan takes place about diffraction vector $\hat{n}_1$, with the x-ray source at angular position 1, and the PSD at position 2. The PSD is then moved by hand to position 4, while the x-rays are scanned accurately to position 3. A second scan is then performed about the diffraction vector $\hat{n}_2$. The difference in angular position between the peak found by the first scan, and that found by the second scan, is twice the Bragg angle θ_B. From θ_B, the lattice parameter is calculated using the Bragg equation.

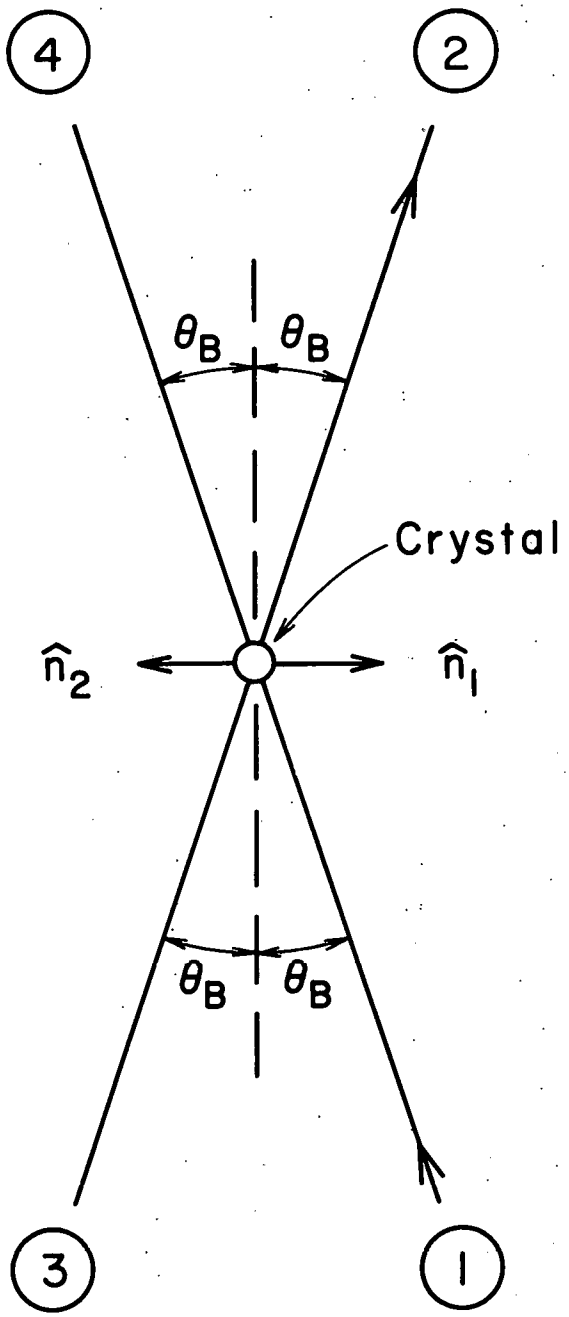
4
2
θ_B
θ_B
Crystal
$\hat{n}_2$
$\hat{n}_1$
θ_B
θ_B
3
1

the PSD at position 2, so that the diffraction is performed about diffraction vector $\hat{n}_1$. The x-ray source is scanned through the Bragg peak, while the PSD remains stationary, since its position sensitive capabilities are unneeded. This scan determines the encoder reading (E_1) at which the source is at the Bragg angle. The PSD is then moved manually to position 4, while the source is accurately scanned to position 3. Another scan is performed here, this time with the diffraction about the diffraction vector $\hat{n}_2$. From this scan is obtained the encoder reading (E_3) at which the source is again at the Bragg angle. The difference between E_1 and E_3 is twice the Bragg angle, from which the lattice parameter is calculated from the Bragg equation. A second set of similar measurements, with the scans in the opposite direction, is made, and the results of the two measurements are averaged to obtain the lattice parameter. This method, which is carefully analyzed in the next section, allows measurement of absolute lattice parameters, generally to better than 200 ppm.

4. Lattice Parameters: Error Analysis and Calibration Measurements

The lattice parameters of single crystals of silicon, lithium fluoride, and sodium chloride have been measured with the present diffractometer system. The purpose was twofold: (1) experimentally to determine possible errors, and (2) to find the angular dependence of the measurements. Diffractometers, especially at low Bragg angles, are susceptible to many kinds of errors which depend on Bragg angle.[92/]

Two kinds of errors which can have a large effect on a diffractometer of this sort are absorption in the specimen and eccentricity error (error in centering the crystal with respect to the various circles of the

diffractometer). With great care, the eccentricity error can probably be reduced to 50 ppm, but in the present work the centering error is responsible for most of the probable errors in the absolute lattice parameter measurements. Errors due to absorption in usual x-ray specimens can be very large, and are discussed in detail below.

In the present work, peak positions (both the "mca" data and the "sca" data) are determined by subtracting from the peak a sloped background, and then calculating the centroid of the top 90% of the peak that remains. This method[93/] minimizes the effect of the difficult-to-determine tails of the peaks on the centroid determination. However, it is important that the peak be fairly symmetric so that consistent results are obtained. The effect of absorption on line shapes and positions of powder lines is discussed by Taylor and Sinclair.[94/] Qualitatively, it is seen that as the product of μ (the absorption coefficient) and r (the crystal diameter) gets larger, the peak shapes are distorted. This causes inconsistent results in the present system.

Aside from the shape problems, absorption also causes a shift in the peak position. This shift, which is a function of Bragg angle, is analyzed by Nelson and Riley.[95/] They found that if lattice parameter results from several reflections are plotted against the function $1/2(\cos^2\theta_B/\sin\theta_B + \cos^2\theta_B/\theta_B)$, then the data lie on a straight line that extrapolates to the correct lattice parameter at $\theta_B = 90°$. In order to check this dependence, lattice parameters of Si, LiF, and NaCℓ were measured. The NaCℓ data are shown in Fig. 20a , while those of Si and LiF are shown in Fig. 20b . Both figures show $(a_{expt}-a_{accepted})/a_{accepted}$ plotted versus the function mentioned above, although the scales of the ordinates are

Figure 20a. Lattice parameter measurements of NaCℓ. Shown plotted is $\Delta a/a_a$ for NaCℓ, where a_a is the accepted value of the lattice parameter for NaCℓ, and Δa is the difference between the value obtained here, and a_a. The different reflections measured are labeled with the appropriate Miller indices, and are plotted against a function of Bragg angle: $F(\theta_B) = 1/2(\cos^2\theta_B/\sin\theta_B + \cos^2\theta_B/\theta_B)$. The line is a guide to the eye only.

b. Lattice parameter measurements of Si and LiF. Results for Si(•) and LiF(x) are shown here, plotted in the same fashion as above, except that the vertical scale is magnified 100x. The error bars show the standard deviations of the various measurements done on the same reflection. The LiF <220> reflection was measured only once, so no error bars are shown. See text for more discussion.

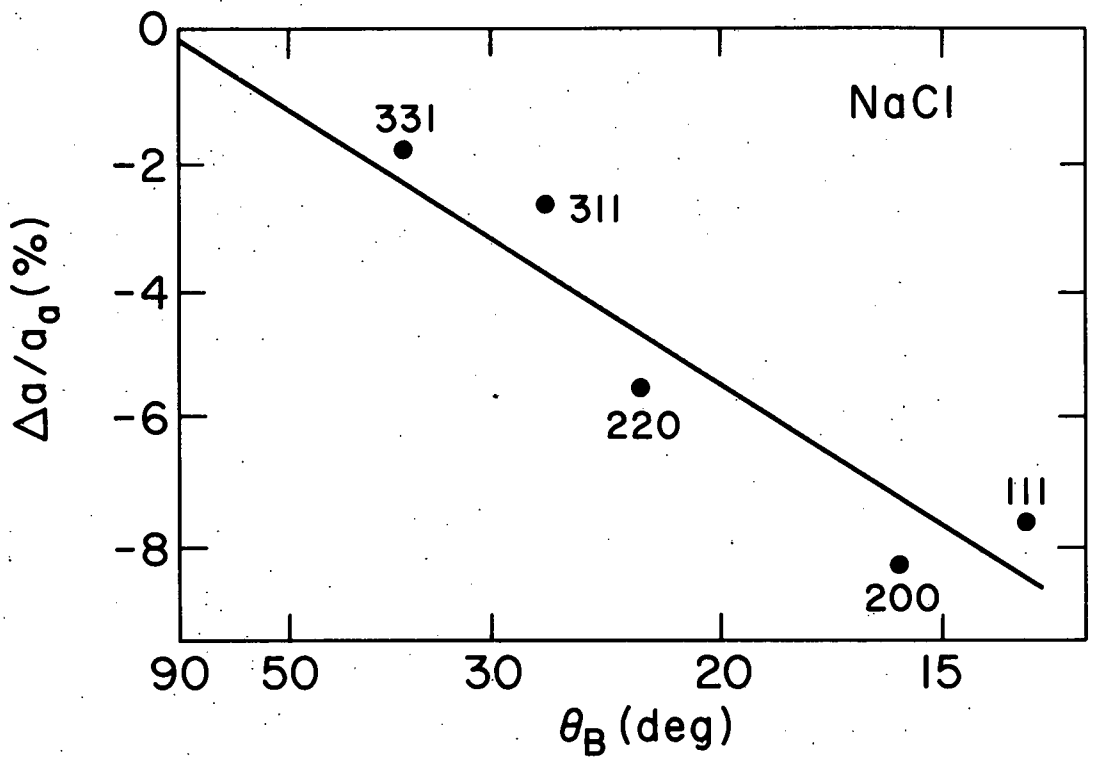
NaCl
331
311
220
111
200
0
-2
-4
-6
-8
Δa/a_a (%)
90
50
30
20
15
θ_B (deg)

a)

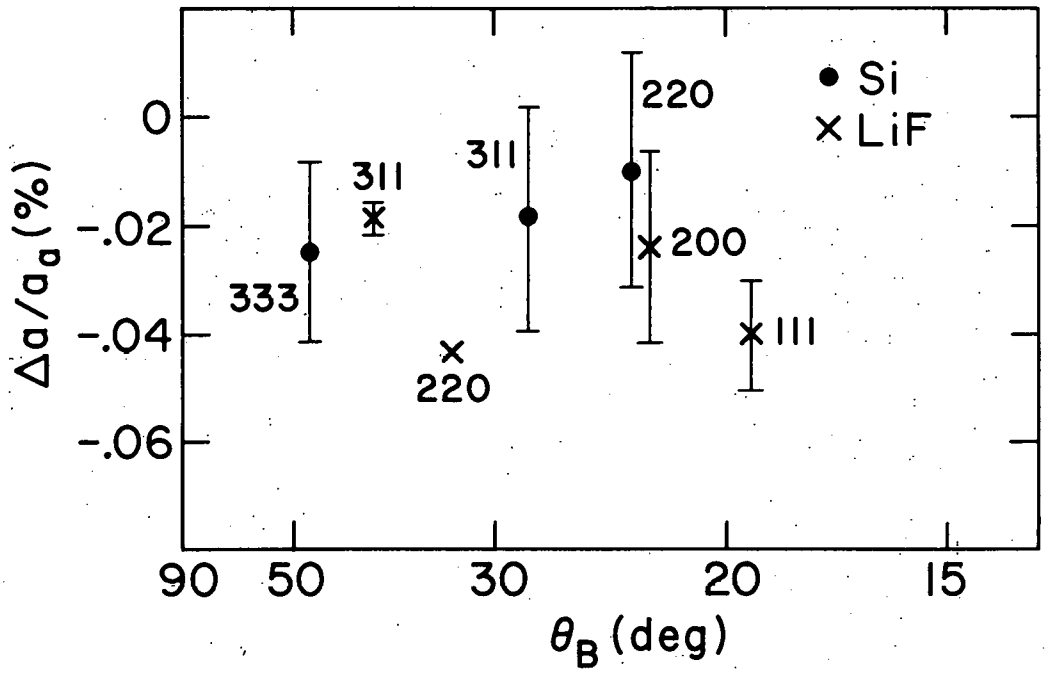
Si
LiF
220
311
311
200
333
111
220
0
-.02
-.04
-.06
Δa/a_a (%)
90
50
30
20
15
θ_B (deg)

b)

different. The accepted value of a used for Si was 5.43101 Å,[96] this being the result of measurements of the same crystal used here by a precise x-ray camera.[97] The single crystal results are more appropriate than the powder results of the International Union of Crystallography Precision Lattice Parameter Project.[98] The number used for LiF was 4.02570 Å at 20° C, this being an average of two values from the literature.[99,100] The accepted value of a used for NaCℓ was 5.63961 Å at 18° C.[101]

The difference between the results displayed in Fig. 20 for NaCℓ, and those for Si and LiF can be understood by looking at the quantity μr mentioned above. For the crystals used in this work, μr was as follows: ∿15.2 for NaCℓ, 5.4 for Si, and 0.93 for LiF. The large absorption in the NaCℓ crystal is the cause of both the slope of the data in Fig. 20a, and the scatter of the data about the line, which is just a guide to the eye. The data for Si and LiF show little or no slope because the absorption in those crystals was much smaller, For the helium crystals studied here, μr is ∿0.005. Therefore, there is no need to worry about the absorption errors.

The error bars shown in Fig. 20b correspond to the standard deviations of the results of the scans done on each reflection. These deviations are about 200 ppm in lattice parameter. This scatter is due mostly to factors inherent in the diffractometer design. The smallest change possible in encoder readings corresponds to 50 ppm in Δa/a, while one step of the stepping motor is about 125 ppm. Crystals can be centered only to about 0.05 mm, which can cause a 200 ppm error in lattice parameter. It is interesting to note that measuring the lattice parameter to 200 ppm

at a Bragg angle of 14° is comparable to an accuracy of 9 ppm at a typical back reflection Bragg angle of 80°, since $\Delta a/a$ is proportional to $\mathrm{ctn}\theta_B$.

Two corrections are made to the data which are due to mechanical difficulties with the diffractometer. The locks between the gear and the x-ray arm, and the arm and the θ table (labeled O and Q in Fig. 17c) flex during motion of the θ table through large angles. This flexing of the θ table lock is measured with a dial indicator, and is at most 80 μm, which corresponds to between 150 and 250 ppm in $\Delta a/a$. The table always lags behind the gear (and the encoder), so the correction is always subtracted from the apparent angle. This same sort of correction must be applied to the lock between the gear and the arm, which unfortunately cannot be fitted with a dial indicator. This second correction of approximately 200 ppm has not been made to the data in Fig. 20b, which explains the fact that the data appear to be about 200 ppm low.

For completeness, a discussion of the usual x-ray corrections is included, although most turn out to be much smaller than the errors which have been discussed above. One possible error is crystal tilt error, which is the result of χ or φ being set incorrectly by an angle Δ. The Bragg equation then becomes[91] $d = m\lambda/(2\cos\Delta\sin\theta')$. In the present work both χ and φ are set to better than 15'. Δ = 15' results in an error of only 10 ppm. The axial divergence error is proportional to the square of the divergence,[91] and here is about 30 ppm. When refraction is included, the Bragg equation becomes[102] $m\lambda = 2d\sin\theta(1-(1-\nu)/\sin^2\theta)$, where $(1-\nu) = 2.7 \times 10^{-6}\lambda^2\rho Z/A$, with λ the wavelength in Å, ρ the density in g/cm^3, Z the number of electrons/atom, and A the atomic number in g/mol. For helium this correction amounts to only 1 ppm. Finally, an expression given by

Segmüeller[103] gives the correction for both the Lorentz and Polarization Factors: $\Delta a_o = \Delta_H^2/8a_o \sin\theta$, where Δ_H is the half width of the reflection. In all cases studied in the present work, this correction was less than 20 ppm. Several other possible errors affecting the vacancy measurements, such as volume changes caused by formation of dislocations, and diffuse x-ray scattering, have been analyzed previously[20] and found to be small enough that they can be neglected. Therefore, it appears that all of the errors mentioned in this paragraph are small enough that they may be ignored in comparison to experimental corrections discussed previously.

The conclusions of the calibration measurements are fourfold. The reproducibility of the lattice parameter measurements is better than 200 ppm. If careful corrections are made for the flexing of x-ray arm locks, then the Si and LiF data are found to agree with the accepted values within 200 ppm. Absorption in the helium crystals is very small, and so there is no need to make corrections to the lattice parameters because of the small Bragg angles involved in these measurements. Finally, due to the somewhat limited reproducibility of the measurements, there is no need to apply further corrections to the lattice parameter measurements.

5. General Procedure

A short description of the method of data collection that was usually used is given below. Crystal growth was followed by at least several hours of annealing with the fill line unplugged. Then as the fill line heaters were turned down, a series of transmission Laue photographs was taken with a Polaroid XR-7 Cassette. These pictures were taken at different heights on the cell, and at different angles (ϕ), until a suitable

reflection was found. The orientation of the crystal was found using the spot and a stereographic projection. The diffractometer was then placed at the angles χ and ϕ determined by the projection. With the PSD placed at approximately the Bragg angle, the θ table (and source) were scanned until the Bragg peak was seen on the PSD.

The correct χ for the reflection was easily found by maximizing the intensity of the spot as a function of χ. Several ω scans were then performed at different heights on the cell to determine the grain structure of the crystal. In the concentrated mixtures, the only useful grain was always at the top of the cell, while for the pure crystals, a single grain usually filled the whole cell. The correct angle ϕ was then determined by performing a lattice parameter measurement. ϕ was adjusted so that the average of the two Bragg peak positions (which are determined during the lattice parameter measurement) agreed with the known zero position of the diffractometer.

Data acquisition then began in earnest. An absolute lattice parameter measurement was usually performed first, at the temperature at which the crystal sat during the above alignment procedures. This was followed by a vacancy run, which consisted of two ω scans at each temperature. Two scans were done to assure that the PSD was not drifting, and that unexpected results were real. The same region of the PSD was used for the ω scans on all the crystals. In some of the earlier crystals, absolute lattice parameter measurements were made again at low temperatures to check the consistency of the vacancy and absolute lattice parameter measurements.

IV. DATA

A. Introduction

Data of several different sorts have been obtained in the present work on solid mixtures of helium. Measurements of the absolute lattice parameters of most of the crystals have been obtained, with an accuracy of about 300 ppm. Measurements of changes in lattice parameter have been made with the ω scan which is discussed in Section III-G-3. These data have made accurate determination of vacancy concentrations possible over a wide range of temperature, pressure, and concentration in ^3He-^4He mixtures. They have also made the determination of low temperature molar volumes of the mixtures possible. Finally, changes in x-ray peak shapes, and lattice parameters allow accurate determination of the phase separation temperatures as a function of pressure and concentration. There are also many other novel and interesting observations which are discussed below.

In Section B, a summary of the results of the various types of measurements is given. The data on each particular specimen, some representative descriptions of various phenomena, and detailed descriptions of the results and observations for each specimen are given in Section C.

B. Summary

The method of lattice parameter measurement has been discussed above, in Chapter III. The results are listed in Table 3. In the crystals

TABLE 3.--Absolute lattice parameter measurements. The estimated uncertainty of the lattice parameter measurements (a) is 300 ppm. Also listed are ^{3}He concentration (x_3), crystal structure, reflection (hkl), melting temperature (T_m), melting pressure (P_m), and the temperature of each a measurement (T). The possible error in P_m is 0.008 MPa, while T is accurate to better than 0.5%. *See the discussion of crystal 13 for its melting temperature and pressure.

Crystal	x_3	Struct.	hkl	T_m(K)	P_m(MPa)	T(K)	a(Å)
13	0	HCP	$10\bar{1}0$	*	*	1.624	3.65996
						0.822	3.66205
						0.921	3.66207
		BCC	110			1.716	4.10252
						1.727	
						1.731	4.09881
						1.751	
14	0	HCP	$10\bar{1}1$	1.798	3.137	1.760	3.64774
						0.947	3.64725
16	0.99	BCC	110	0.561	3.061	0.504	4.34868
						0.280	4.35182
						0.303	4.35440
17	0.99	BCC	110	2.040	7.853	1.961	4.11276
						1.090	4.11505
18	0.99	BCC	110	2.043	7.847	1.989	4.10929
19	0.99	BCC	110	2.017	7.812	1.923	4.11614
						1.161	4.11815
22	0.51	BCC	110	2.01	6.187	1.893	4.10395
23	0.51	BCC	110	1.99	6.187	1.823	4.11090
						1.052	4.11210
24	0.51	BCC	110	1.22	3.220	1.089	4.22903
25	0.51	BCC	110	1.35	3.565	1.246	4.20306
26	0.51	BCC	110	1.33	3.565	1.284	4.20132
27	0.28	BCC	110	1.87	4.681	1.700	4.12644
28	0.28	BCC	110	1.58	3.475	1.352	4.17393
29	0.12	BCC	110	1.701	3.240	1.566	4.12907
						1.562	4.12786
30	0.12	BCC	110	1.656	3.041	1.381	4.14074

of pure ^{4}He, and almost pure ^{3}He (x_3=0.99), measurements were made near melting, and then again at a low temperature, where few thermal vacancies are expected. These measurements were made as a check of the sensitivity of the absolute lattice parameters, as opposed to their absolute accuracy. As can be seen (see for example, crystal 17, Fig. 32), the sensitivity is much better than the 300 ppm accuracy quoted for the lattice parameters. The absolute accuracy of only 300 ppm is largely the result of difficulties in centering the diffractometer on the sample cell. The lattice parameters for crystals 13 through 25 have been corrected for centering errors. The corrections were determined by repeated lattice parameter measurements on crystal 24, with different centering of the diffractometer each time.

The absolute lattice parameter data, in conjunction with the vacancy (change in lattice parameter) measurements, have been used to obtain the molar volumes of the various crystals at low temperatures, MV_o. Lattice parameter determinations of molar volume at various temperatures are corrected for vacancy concentration, and then averaged together. These results are shown in Table 4. The errors quoted for the x-ray molar volumes are the standard deviations of the different measurements. Shown also are the molar volumes obtained from the PVT measurements of Grilly,[4,5,8] using the formula

$$V(x_3,P) = x_3V_3(P) + (1-x_3)V_4(P) + x_3(1-x_3)C \quad , \qquad \text{(IV-1)}$$

where $V_3(P)$ is the molar volume of ^{3}He at pressure P, x_3 is the ^{3}He concentration, $V_4(P)$ is the ^{4}He molar volume, and C is a constant which Mullin[40] has calculated to be -0.4 cm^3/mol. The disagreement between the PVT molar volumes and the x-ray molar volumes is discussed in detail in Chapter V.

TABLE 4.--Low temperature x-ray molar volumes. The x-ray molar volumes (MV_o) are corrected for vacancy content. The molar volumes on the melting line (MV_{PVT}) are obtained from the melting pressure (P_m), the melting line data of Grilly,[4,5,8] and the excess volume of the mixtures calculated by Mullin.[40] The uncertainties shown for MV_o are the standard deviations of the different measurements made. The possible error in MV_o is 900 ppm, which corresponds to 0.019 cm^3/mol. The possible error in MV_{PVT} is about 0.5%, which corresponds to 0.1 cm^3/mol.

Crystal	x_3	T_m(K)	P_m(MPa)	MV_o(cm^3/mol)	MV_{PVT}(cm^3/mol)
14	0	1.798	3.137	20.638±0.014	20.56
16	0.99	0.561	3.061	24.867±0.005	24.70
17	0.99	2.040	7.853	21.000±0.022	20.95
19	0.99	2.017	7.812	21.046±0.014	20.97
23	0.51	1.99	6.187	20.945±0.007	20.43
24	0.51	1.22	3.220	23.443	22.44
26	0.51	1.33	3.565	23.306	22.12
27	0.28	1.87	4.681	21.478	20.54
28	0.28	1.58	3.475	22.327	21.35
29	0.12	1.701	3.240	21.246	20.95
30	0.12	1.656	3.041	21.469	21.10

The low temperature x-ray molar volumes are used for crystal identification throughout this chapter.

The vacancy data are summarized in Table 5. The results of two fits to the data are shown, along with the melting temperature and pressure, and the low temperature molar volume. The first fit is a simple exponential fit using Equation II-25, where s_v is held equal to zero. This is included for comparison with all the previous vacancy data on solid helium, which are not accurate enough to be used to determine more than one fitting parameter. The last two columns in the table list the results of fits in which both e_v and s_v (from Eq. II-25) were allowed to vary. Although the results of this fit are very sensitive to small variations in the data, comparison of this fit with the s_v=0 fit shows clearly that the fit with s_v varying is a better parameterization of the data. The errors quoted for both fits are the probable uncertainties calculated from the fit. Figures showing both fits for each crystal are found in Section C.

Phase separation has also been studied in the present work. The phase separation temperature (T_{ps}) found for each concentration and pressure is listed in Table 6. These transition temperatures were obtained in two different ways. The most obvious method was simply to watch the x-ray peak shape as the crystal was cooled. There is a clearly recognizable change beginning at the phase separation temperature. An example of the peak shape changes is shown in Figs. 41 and 42 for crystal 26. The second method of determination of T_{ps} was equating T_{ps} to the temperature at which the lattice parameter versus temperature curve went through an inflection point. This is an analogy with the method used by Pancyzyk, Scribner, Gonano, and Adams[36/] in their strain gauge study of phase separation. The

TABLE 5.--Results of fits to vacancy data. The results of two exponential fits to the data are given. e_v is the formation energy, and s_v is the apparent formation entropy. In the first fit, s_v=0, while in the second both e_v and s_v are varied. Also listed are the low temperature x-ray molar volume (MV_o), the melting temperature and pressure (T_m and P_m), and the ^{3}He concentration (x_3). The probable errors from the fits are also listed.

Crystal	x_3	MV_o (cm^3/mol)	T_m(K)	P_m(MPa)	e_v(s_v=0)(K)	e_v(K)	s_v
0	0	20.206[a]	1.979	3.710	12.6 ±0.1	27.7 ±0.1	7.8 ±0.1
13	0	20.900	-----[b]	-----[b]	8.6 ±0.1	8.2 ±0.1	-0.2 ±0.1
14	0	20.638	1.798	3.137	10.62±0.05	9.59±0.05	-0.62±0.03
16	0.99	24.867	0.561	3.061	2.6 ±0.1[c]	5.14±0.01[c]	5.30±0.02[c]
					2.6 ±0.5[d]	5.2 ±0.3[d]	4.9 ±0.5[d]
17	0.99	21.000	2.040	7.853	11.9 ±0.3	15.8 ±0.3	2.0 ±0.2
19	0.99	21.046	2.017	7.812	11.1 ±0.4	20.1 ±0.2	4.5 ±0.1
23	0.51	20.945	1.99	6.178	11.8 ±0.6	35.4 ±0.3	12.4 ±0.2
24	0.51	23.443	1.22	3.220	3.8 ±0.1	4.94±0.03	1.02±0.03
26	0.51	23.306	1.32	3.565	4.1 ±0.1	4.40±0.04	0.28±0.03
27	0.28	21.478	1.87	4.681	6.8 ±1.3[e]	27.16±0.02[e]	11.78±0.01[e]
					8.6 ±2.0[f]	37.0 ±0.3[f]	17.2 ±0.2[f]
28	0.28	22.327	1.58	3.475	5.8 ±2.3	15.2 ±0.1	7.3 ±0.1
29	0.12	21.246	1.701	3.240	9.3 ±0.4	16.5 ±0.2	4.7 ±0.1

[a] MV calculated from P_m only

[b] See discussion of crystal 13 for details

[c] Cooling run before melting at low temperature

[d] Warming run after low temperature melting

[e] Cooling run before phase separation

[f] Warming run after phase separation

TABLE 6.--Phase separation temperatures. These temperatures (T_{ps}) were determined from the shape changes in the x-ray peaks, and the inflection points in the lattice parameter versus temperature data. Also listed is the ^{3}He concentration (x_3) and melting pressure (P_m). The quoted uncertainties for T_{ps} are the probable errors in its determination.

Crystal	x_3	P_m(MPa)	T_{ps}(K)
23	0.51	6.178	0.299±0.004
24	0.51	3.220	0.399±0.006
26	0.51	3.565	0.388±0.006
27	0.28	4.681	0.330±0.003
28	0.28	3.475	0.367±0.006
29	0.12	3.240	0.267±0.009
30	0.12	3.041	0.267±0.003

first method is more definite, because the inflection point method is sensitive to the details of the behavior at the phase separation point T_{ps}. This behavior is not always simple, as will be described in the next section.

One quantitative measure of the peak shape changes which are the result of phase separation is the width of the crystal mosaic. This is the width of the peak in the "sca" data described in Section III-G-3. The widths for various crystals are plotted near phase separation in Fig. 21. All the data shown here were obtained on cooling runs. An example of the behavior of the mosaic width on warming back through phase separation is shown in the discussion of crystal 23.

The hcp-bcc transition has been observed in several different circumstances during this work. In crystal 13, which was pure ^{4}He, the transition between the bcc and hcp structures was carefully studied. The transformation of one of the separated phases (below T_{ps}) from bcc to hcp was observed in several of the concentrated mixed crystals. Finally, phenomena which might be associated with the bcc to mixed bcc-hcp phase transformation have been observed in crystals 27, 29, and 30. Details of these observations are given in the next section.

C. Details and Observations

This section contains a detailed description of the data obtained on each specimen. The lattice parameter, vacancy, and phase separation data are plotted, and the measurements described. There are also examples of other characteristics, such as peak shapes and peak widths, which apply to more than one of the crystals. For the vacancy concentration plots and

Figure 21. Crystal mosaic width at phase separation. The width of the crystal mosaic for various crystals is plotted versus temperature near phase separation. This is the width of the "sca" data peak which is discussed in Chapter III. Identification of the various symbols is given in the figure.

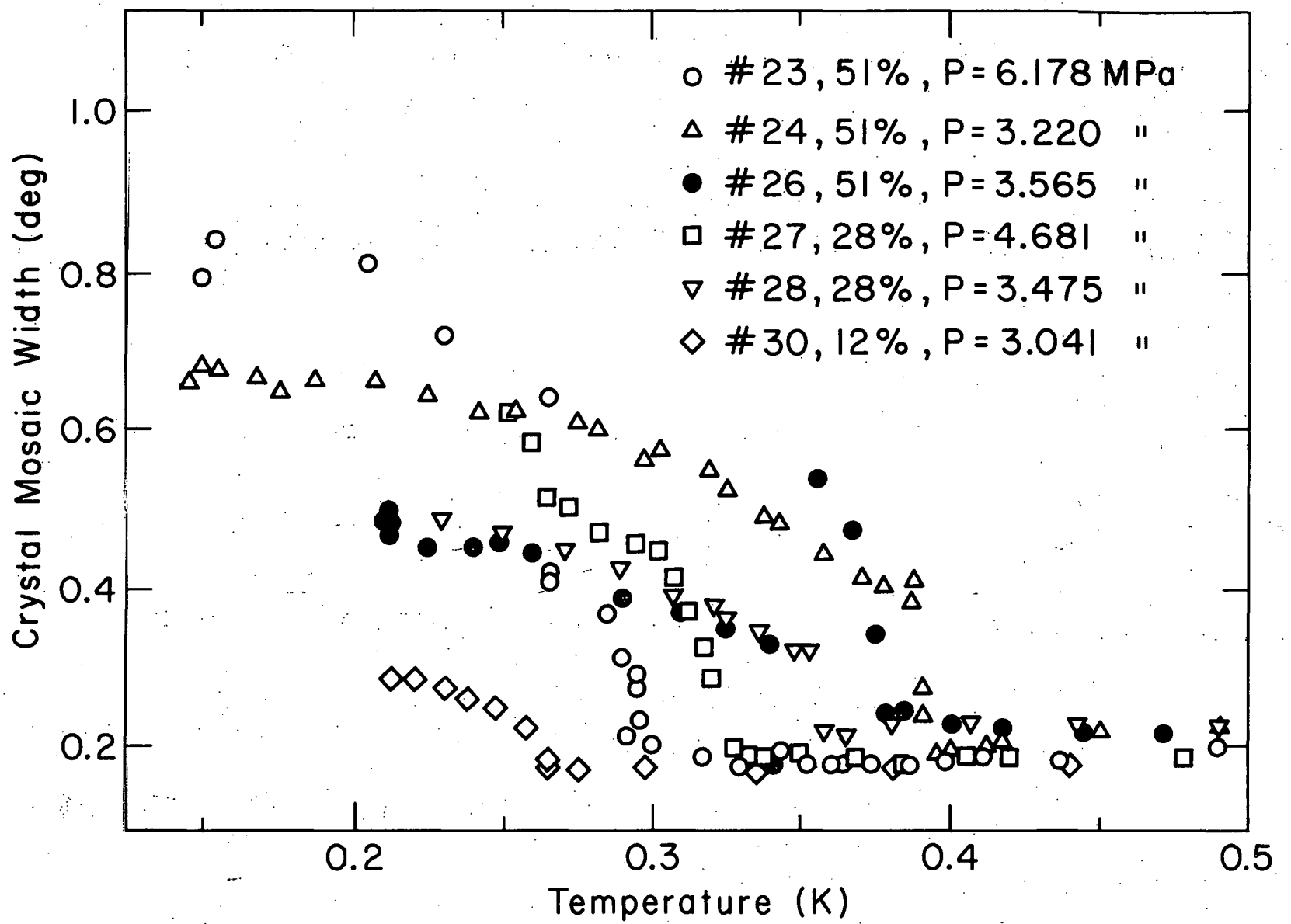
#23, 51%, P = 6.178 MPa
#24, 51%, P = 3.220 "
#26, 51%, P = 3.565 "
#27, 28%, P = 4.681 "
#28, 28%, P = 3.475 "
#30, 12%, P = 3.041 "
Crystal Mosaic Width (deg)
1.0
0.8
0.6
0.4
0.2
0.2
0.3
0.4
0.5
Temperature (K)

fits, all points taken at the same temperature are averaged. On each figure, the crystal is identified by number, low temperature x-ray molar volume (MV_o), melting temperature (T_m), and ^3He concentration (x_3).

1. Crystal 0

The vacancy data which are shown in Fig. 22 were obtained with the θ-θ drive mechanism which was used previously by Heald.[20/] Absolute lattice parameter measurements were not possible with the older version of the diffractometer drive. Unfortunately, the measurements do not extend to a low enough temperature to accurately determine the low temperature reference value of the lattice parameter. This makes the large value of s_v which was obtained somewhat doubtful.

2. Specimens 1-12

Specimens 1 through 12 were prepared in attempts to measure the vacancy content of pure ^4He crystals near a molar volume of 18.8 cm^3/mol. This is the molar volume at which Heald measured vacancies in a pure ^3He crystal.[20/] Unfortunately, it was impossible to obtain any consistent data from any of these specimens. The specimens were very unstable, sometimes rotating in the sample cell at speeds of a degree a minute while the indicated temperature remained constant. After specimen 8, the indium spike was put inside the sample cell to prevent this rotation. It has not been totally effective. Specimens grown after crystal 30, at this same pressure and composition, have rotated more than 20 degrees while at constant temperature. There is some evidence that the temperature of thermometer G15678 at the bottom of the cell seems to fluctuate back and forth a small amount (millidegrees) during the rotation, but there is no definite proof of this.

Figure 22. Crystal 0 vacancy measurements. The data were obtained on cooling with the previous version of the diffractometer used by Heald. The solid line is a least squares fit to Equation II-25 in which both e_v and s_v are varied. The dashed curve is the fit with s_v=0.

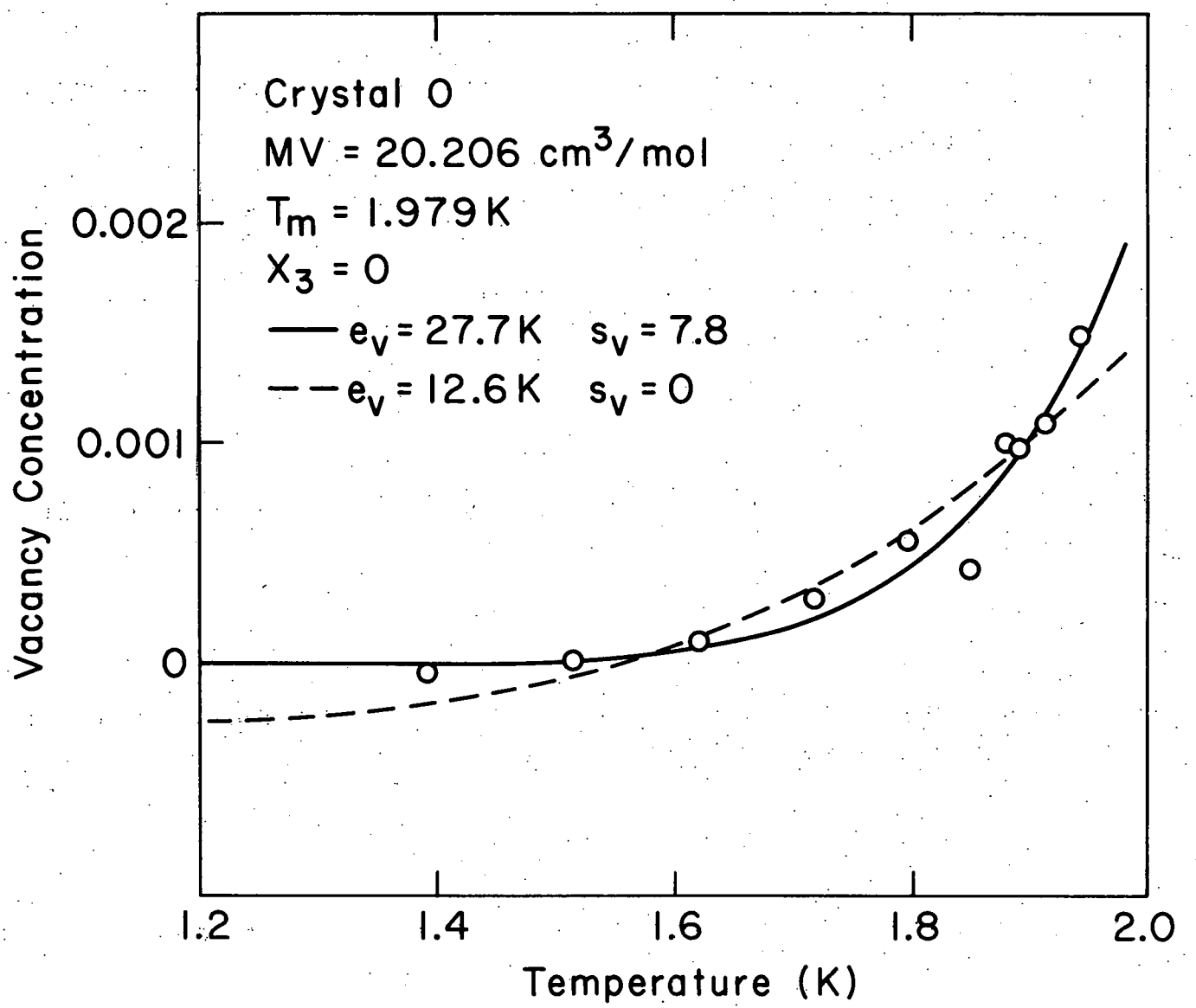
Crystal 0
MV = 20.206 cm³/mol
Tm = 1.979 K
X3 = 0
ev = 27.7 K sv = 7.8
ev = 12.6 K sv = 0
Vacancy Concentration
0.002
0.001
0
1.2
1.4
1.6
1.8
2.0
Temperature (K)

3. Crystal 13

Crystal 13 requires detailed explanation. The crystal was originally grown from pure ^{4}He at a pressure of 3.110 MPa, with a melting temperature of 1.787 K. Apparently the fill line heaters were turned down in such a manner that liquid was trapped in the fill line. During the overnight anneal, a strange warming was seen on the thermometer at the bottom of the sample cell. This was perhaps the pressure equilibration between the higher pressure crystal in the cell, and the lower pressure solid in the fill line which resulted from the solidification of the trapped liquid at constant volume (since the fill line was plugged above the trapped liquid). The result of the above events was that the next morning there was a good single crystal of bcc ^{4}He at 1.735 K.

The data taken in the bcc phase are shown in Fig. 23. The pure bcc phase is seen to extend from 1.70 K to about 1.735 K. At temperatures below 1.70 K, the crystal begins going through the phase transition to a mixed hcp-bcc phase. The Bragg peak disappears as a function of temperature (by losing intensity only, not by changing shape), and it returns as the same function of temperature. There is apparently very little hysteresis in either the lattice parameters or peak shapes. Fig. 24 shows the "mca" peak as the crystal goes from the hcp to the mixed phase. The peak shape behavior at the bcc to mixed transition is the same.

The circles shown in Fig. 23 are from several different warming and cooling runs through the bcc-mixed transition. When the crystal was warmed above 1.735 K, however, the lattice parameter changed irreproducibly. When cooled back below 1.735 K, the lattice parameter again was a reproducible function of temperature. The crosses in Fig. 23 are the data

Figure 23. Crystal 13 bcc phase lattice parameter measurements. The initial lattice parameter changes measured are the circles. The crosses are the measurements made after the crystal was warmed above 1.735 K. The two absolute measurements (x) were made after the study of the hcp phase. The vertical error bars are 300 ppm in lattice parameter although the possible error here is large, as discussed in the text. The horizontal error bars show the temperature change during each of the absolute measurements, since the crystal was then warming with very little temperature control. MV_o is the low temperature x-ray molar volume in the hcp phase. See text for discussion of the melting temperature.

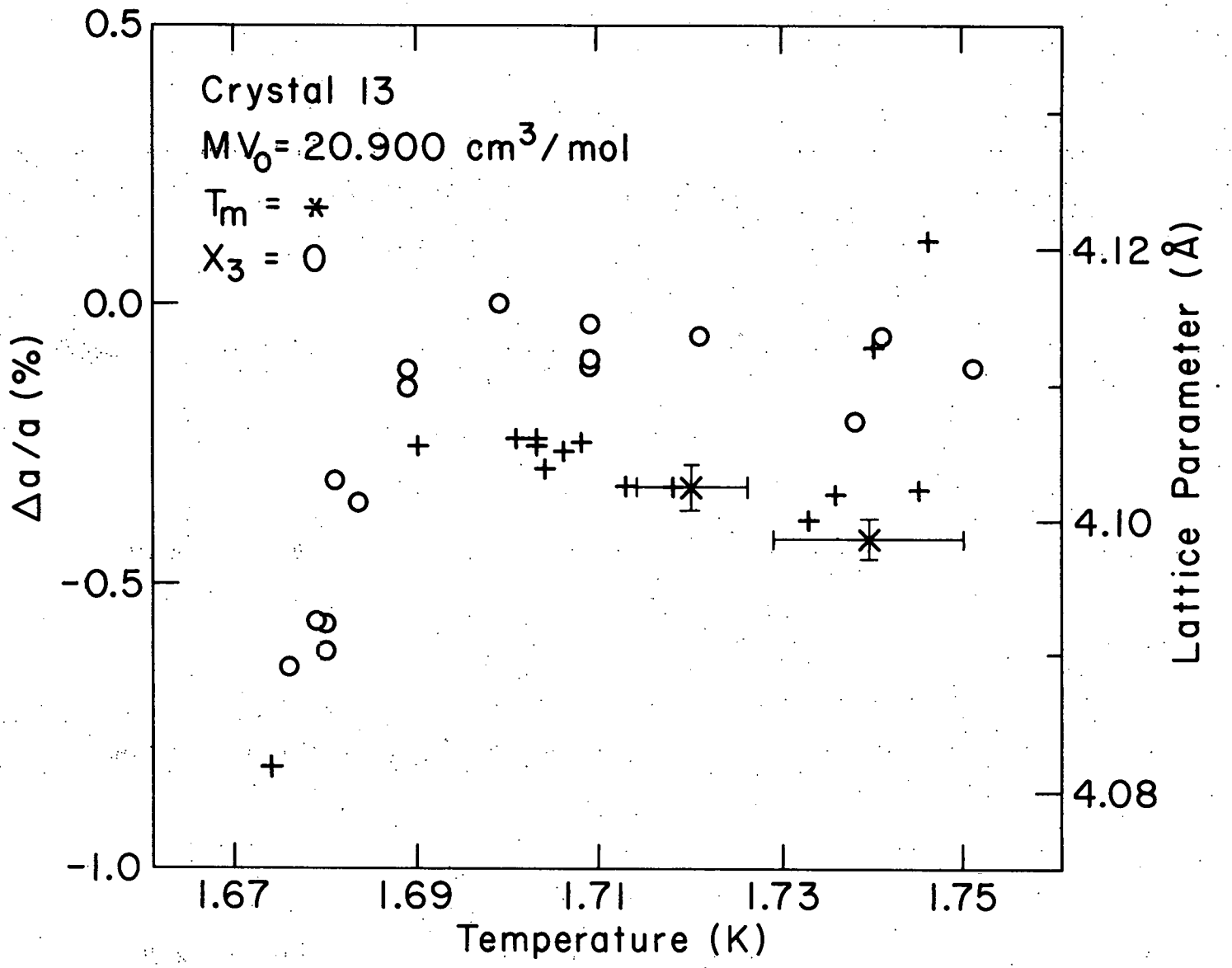
Crystal 13
MV0= 20.900 cm3/mol
Tm = *
X3 = 0
0.5
0.0
-0.5
-1.0
Δa/a (%)
4.12
4.10
4.08
Lattice Parameter (Å)
1.67
1.69
1.71
1.73
1.75
Temperature (K)

Figure 24. Bragg ("mca") peak behavior at the bcc-hcp transition in pure ^{4}He. The Bragg ("mca") peak is shown plotted at three different temperatures as crystal 13 undergoes the hcp to mixed phase transition. The behavior at the bcc to mixed phase transition is exactly the same. The peaks were obtained at the following temperatures: (A) 1.600 K, (B) 1.621 K, and (C) 1.630 K. One degree in Bragg angle corresponds to 101.3 channels on the MCA.

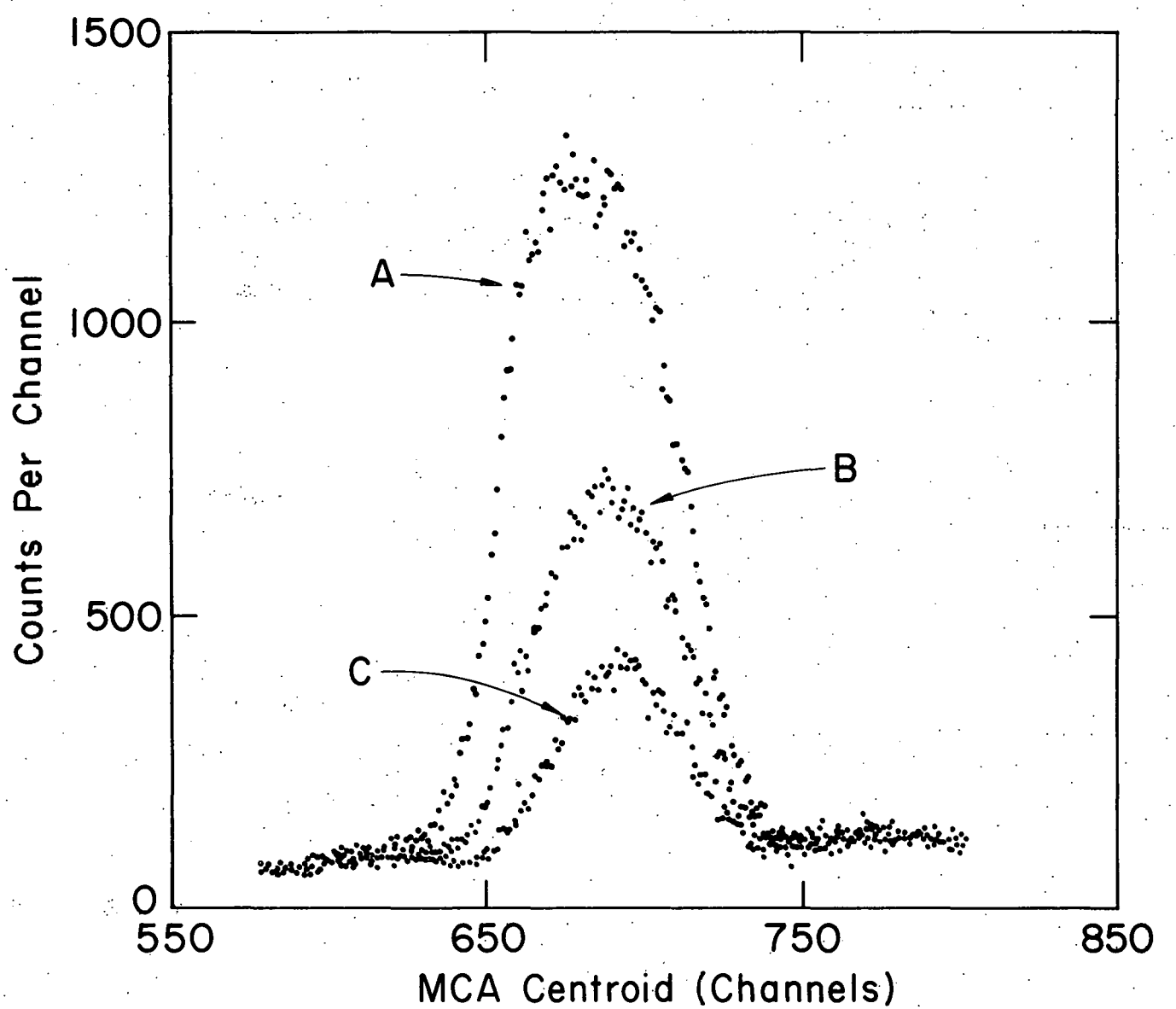
1500
1000
500
0
Counts Per Channel
550
650
750
850
MCA Centroid (Channels)
A
B
C

taken on several runs through the lower transition after being above 1.735 K. Apparently 1.735 K is the melting temperature, above which the plug in the fill line started slipping, allowing the lattice parameters to change. The lattice parameter of the second set of data is lower than that of the first because the external pressure was higher than that of the crystal, so that when the plug slipped, the pressure on the crystal was increased, compressing the lattice.

One very interesting point that should be made is that even in the 35 mdeg temperature range in which the bcc phase exists, vacancy generation is clearly occurring. The change in lattice parameter seen corresponds to a change of vacancy concentration of 4×10^{-3}. This fairly large number of vacancies, and the proof of the ability to make useful measurements in this phase, make further study here useful.

Before leaving the bcc phase, the absolute lattice parameter measurements should be discussed. These measurements, which are shown in Fig. 23, were made after the work done in the hcp phase, on a different (110) reflection than that which was studied before going into the hcp phase. Unfortunately, the dilution refrigerator was in the process of plugging, and so there was little temperature control. The large error bars on the temperatures in Fig. 23 are due to the warming during the measurements. The crystal melted at 1.774 K, but because the fill line was plugged, this is not the actual melting temperature of the crystal. Each of the lattice parameter measurements is the result of scans in only one direction on the diffractometer. They are therefore accurate only to about 500 ppm.

After all the data discussed above (except the lattice parameter measurements) were taken, the crystal was cooled to about 1.62 K. More Laue photographs were taken, revealing a single hcp crystal. A lattice parameter measurement was made on the $(10\bar{1}0)$ reflection, and then the crystal was warmed and cooled through the transition from the hcp to the mixed phase. The Bragg peak disappeared and returned just as it had for the bcc-mixed transition. If the transition to the mixed phase begins when the intensity of the peaks starts decreasing, the mixed phase is found to extend between 1.595 K and 1.70 K.

The data taken in the hcp phase on crystal 13 are shown in Fig. 25. The cooling run (circles) shows a very different behavior near the mixed phase transition than the warming run (crosses). The vacancy data for this crystal, obtained on the cooling run, are pictured in Fig. 26. The determination of s_v from the fit to the data is especially uncertain, since the data stop more than 0.3 deg below the melting temperature.

4. Crystal 14

Crystal 14 was an attempt to get a better measure of the vacancy concentration in the hcp phase of ^{4}He at high molar volume than was obtained with crystal 13. As can be seen in Fig. 27, the problems of crystal 13 were not completely avoided. Figure 27 shows the first cooling run on crystal 14, with two lattice parameter measurements which confirm the unexpected high temperature behavior. The vacancy measurements, shown in Fig. 28, exclude the data above 1.65 K. Further warming and cooling runs, although very inaccurate because of experimental problems, generally show qualitative agreement with the cooling run which is shown in Fig. 28.

Figure 25. Crystal 13 molar volumes determined from lattice parameter measurements. The molar volumes obtained from lattice parameter and $\Delta a/a$ measurements made in the hcp phase on cooling runs (circles), and on warming (crosses) are shown. The absolute lattice parameter measurements (x) are shown with error bars which correspond to 300 ppm in lattice parameter. The absolute lattice parameter at 1.624 K was obtained during the cooling run. The bcc phase molar volumes are also shown. Due to the increased uncertainty in the lattice parameter measurements, the molar volumes in the bcc phase are more uncertain than those in the hcp phase. The error bars which are shown, however, correspond to the usual 300 ppm errors in lattice parameter.

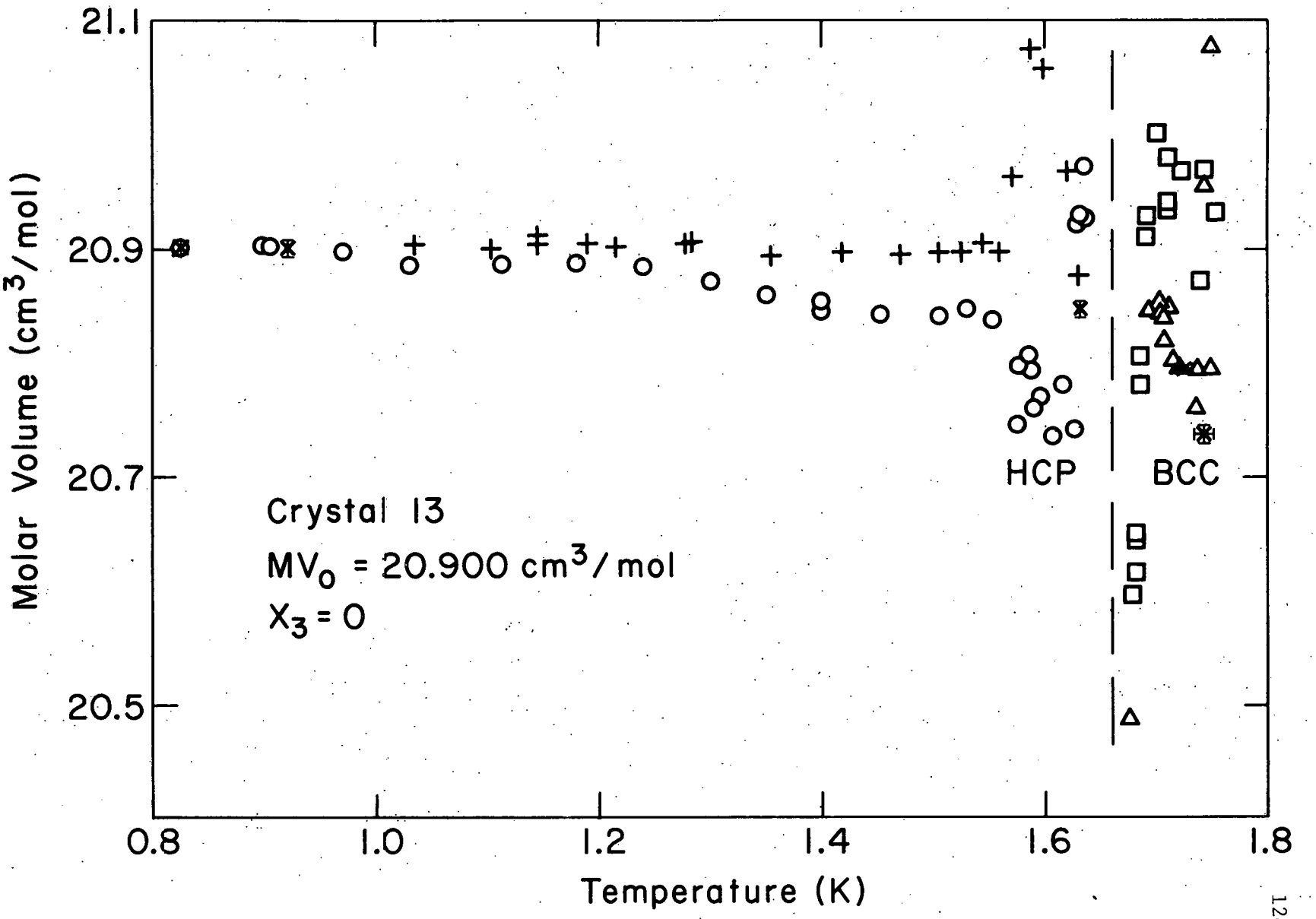
21.1
20.9
20.7
20.5
Molar Volume (cm^3/mol)
0.8
1.0
1.2
1.4
1.6
1.8
Temperature (K)
HCP
BCC
Crystal 13
MV_0 = 20.900 cm^3/mol
X_3 = 0

Figure 26. Crystal 13 hcp phase vacancy measurements. The data shown here were obtained on the cooling run made on crystal 13 in the hcp phase. The data above 1.5 K were excluded because of the anomalies associated with the hcp to bcc transition in this crystal. The solid line is a least squares fit to Equation II-25 in which both e_v and s_v are varied. The dashed line is the fit with s_v=0. See text for a discussion of T_m.

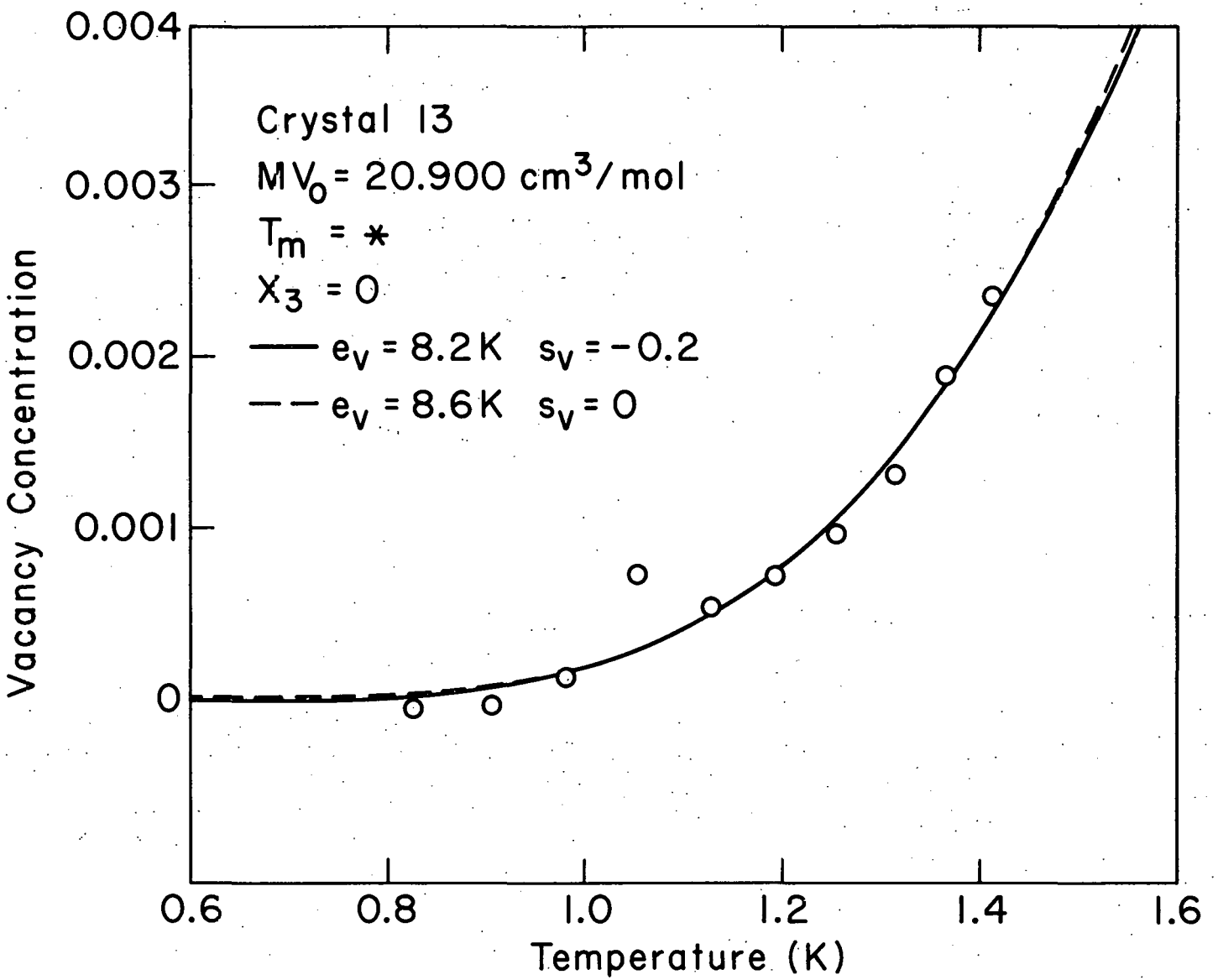
Crystal 13
MV_0 = 20.900 cm^3/mol
T_m = *
X_3 = 0
e_v = 8.2K s_v = -0.2
e_v = 8.6K s_v = 0
Vacancy Concentration
0.004
0.003
0.002
0.001
0
0.6
0.8
1.0
1.2
1.4
1.6
Temperature (K)

Figure 27. Crystal 14 lattice parameter measurements. These data were obtained on the initial cooling run on the crystal. The high temperature and low temperature absolute lattice parameters (x) were measured before and after the cooling run. The error bars on the absolute measurements correspond to 300 ppm in lattice parameter.

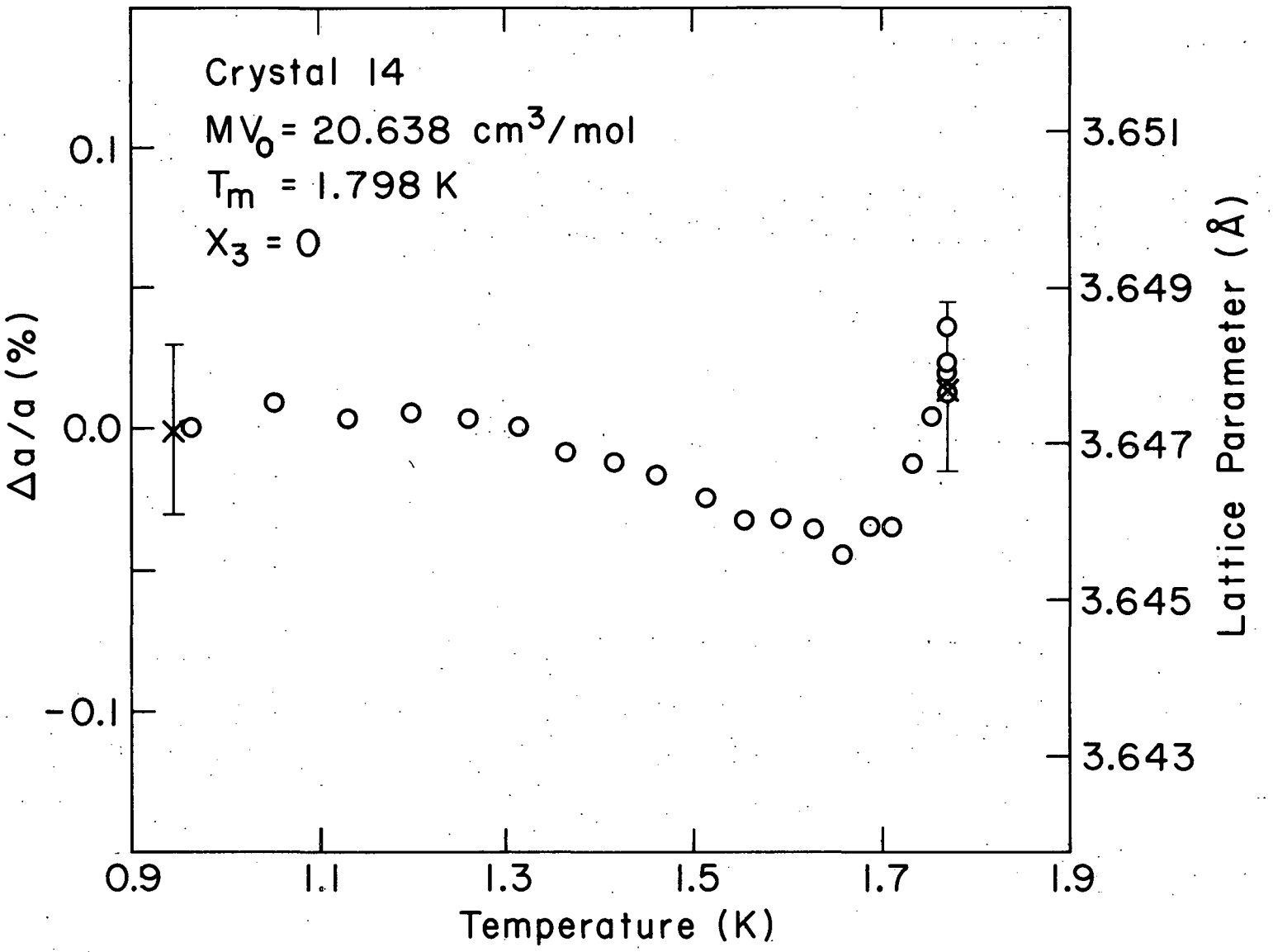
Crystal 14
MV0 = 20.638 cm3/mol
Tm = 1.798 K
X3 = 0
0.1
0.0
-0.1
Δa/a (%)
3.651
3.649
3.647
3.645
3.643
Lattice Parameter (Å)
0.9
1.1
1.3
1.5
1.7
1.9
Temperature (K)

Figure 28. Crystal 14 vacancy measurements. The data were obtained on warming. The solid line is a least squares fit to Equation II-25 in which both e_v and s_v are varied. The dashed line is the fit with s_v=0.

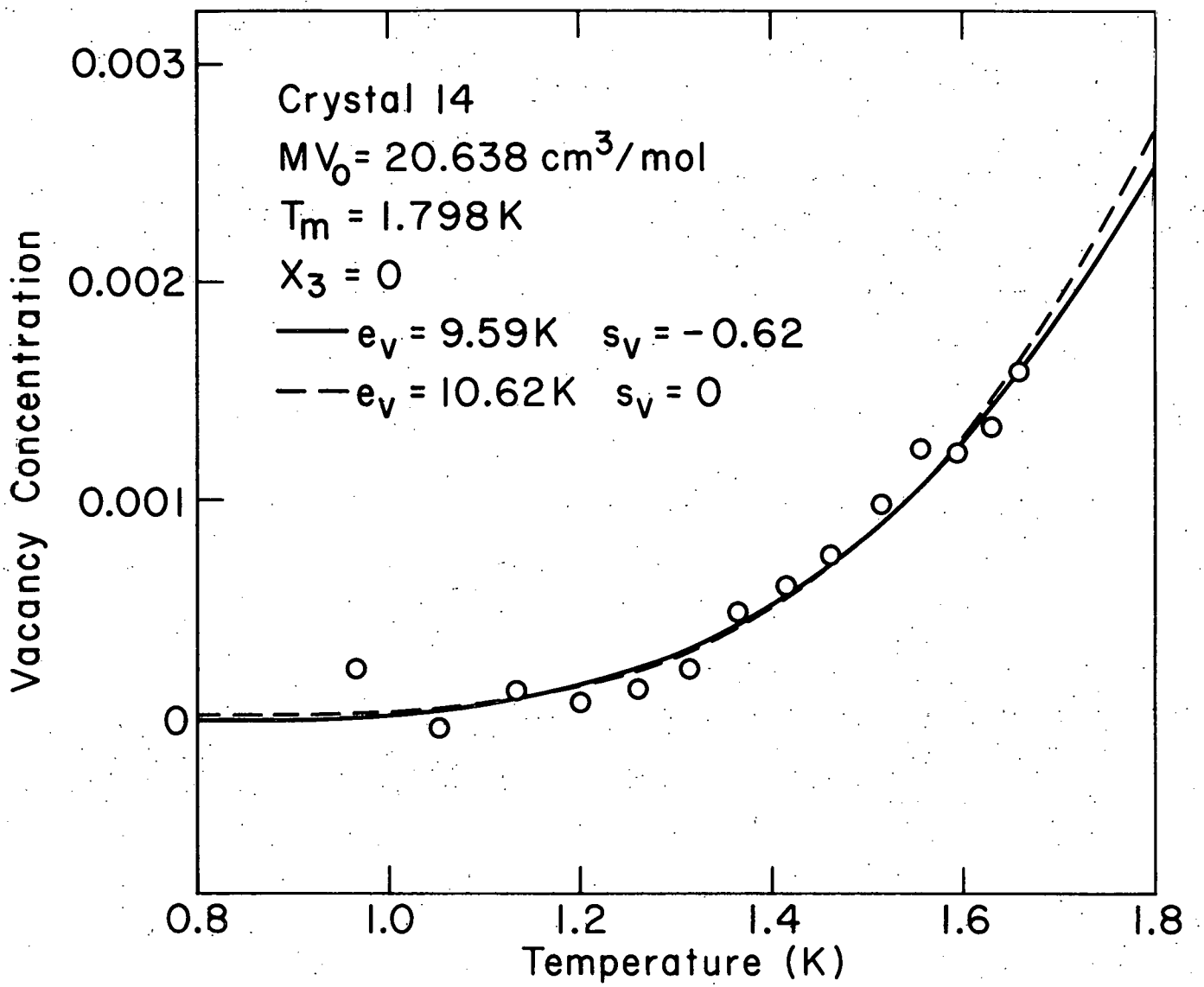
Crystal 14
MV_0 = 20.638 cm^3/mol
T_m = 1.798 K
X_3 = 0
e_v = 9.59K s_v = −0.62
e_v = 10.62K s_v = 0
Vacancy Concentration
0.003
0.002
0.001
0
0.8
1.0
1.2
1.4
1.6
1.8
Temperature (K)

Finally, the Bragg peak was monitored as the crystal was warmed through the melting temperature with the fill line still plugged. The lattice parameter stopped decreasing and abruptly started increasing as the crystal was warmed through T_m, with the change occurring within 2 mdeg of T_m. The peak showed few shape changes up to a temperature of 1.86 K, where the fill line was unplugged and the crystal disappeared. This behavior is similar to that seen in the bcc phase data from crystal 13.

5. Crystal 16

Crystal 16 was grown in order to facilitate comparisons between the present mixture data and the ^{3}He measurements of Heald. The melting pressure of about 3 MPa also makes the molar volume of this crystal very large, so that possible anomalous behavior of the vacancies at high molar volumes could be checked. Inspection of Fig. 29, which displays all the data obtained on crystal 16, shows no lack of anomalous behavior. The first cooling run (circles in Fig. 29) follows an absolute lattice parameter measurement which confirms the unexpected increasing lattice parameters of the highest temperature points. These three points are excluded from the vacancy analysis of the cooling run which is shown in Fig. 30.

After a lattice parameter measurement at the end of the cooling run, the crystal was cooled to 0.186 K. As is seen in Fig. 29, below 0.3 K the lattice parameter increased, and then sharply began to decrease at about 0.208 K as the crystal was cooled. This behavior was repeated on warming with very little hysteresis. There was no change of peak shape during either cooling or warming. This effect is probably due to cooling through the lower melting point of the crystal, as discussed in Chapter V.

Figure 29. Crystal 16 lattice parameter measurements. The absolute lattice parameter (x) at 0.504 K was obtained after crystal growth was completed. The cooling vacancy measurements (circles) were then done, followed by the absolute measurement at 0.280 K. The cooling run (circles) then continued to low temperatures. The return warming run is the crosses. A third absolute measurement at 0.303 K was performed, followed by the final warming vacancy run (squares). The error bars on the absolute measurements correspond to 300 ppm in lattice parameter.

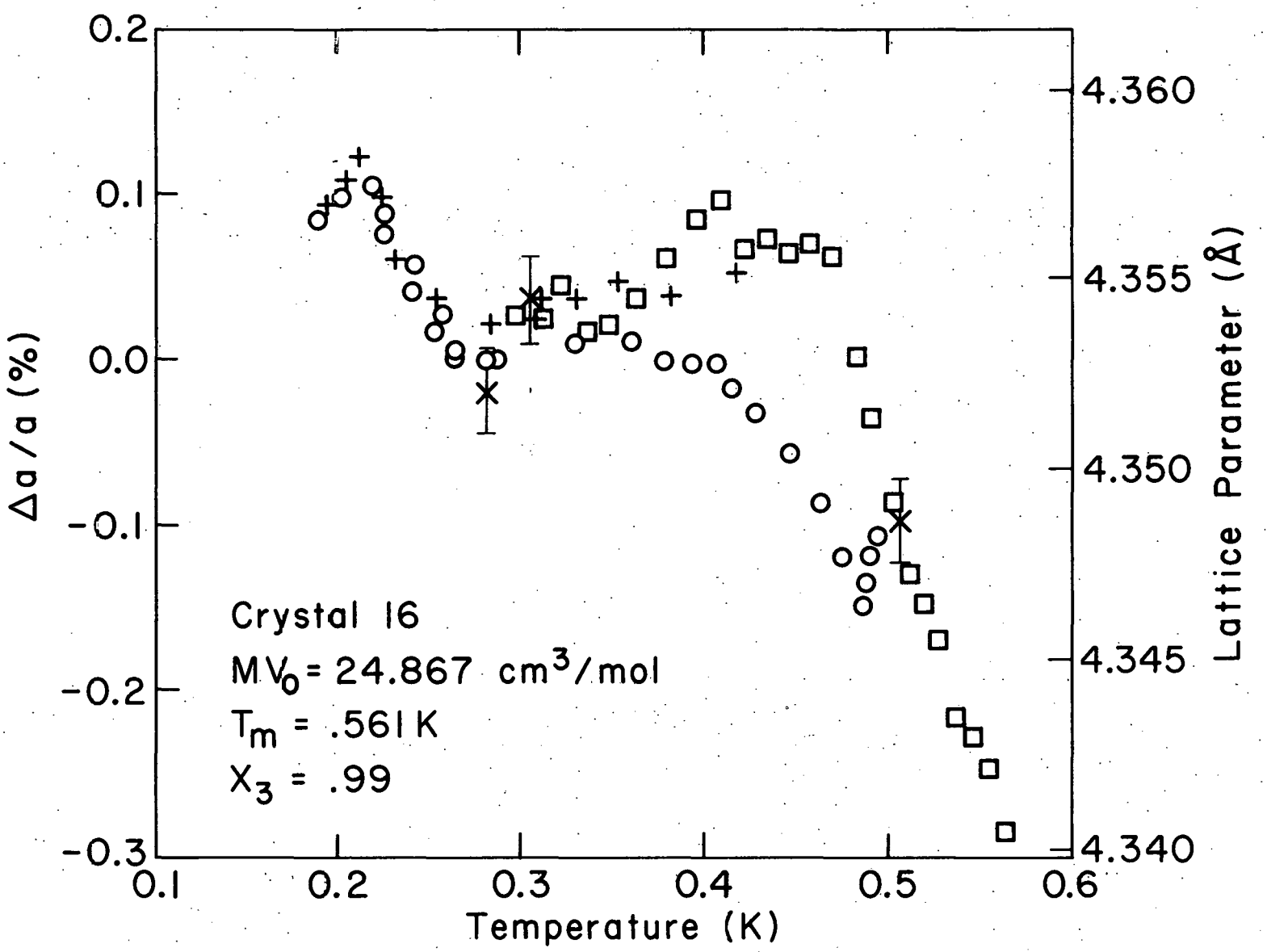
0.2
0.1
0.0
-0.1
-0.2
-0.3
Δa/a (%)
4.360
4.355
4.350
4.345
4.340
Lattice Parameter (Å)
0.1
0.2
0.3
0.4
0.5
0.6
Temperature (K)
Crystal 16
MV0 = 24.867 cm3/mol
Tm = .561 K
X3 = .99

Figure 30. Crystal 16 vacancy measurements taken on cooling. These data were obtained on the initial cooling of this crystal. The solid line is a least squares fit to Equation II-25 in which both e_v and s_v are varied. The dashed line is the fit with s_v=0.

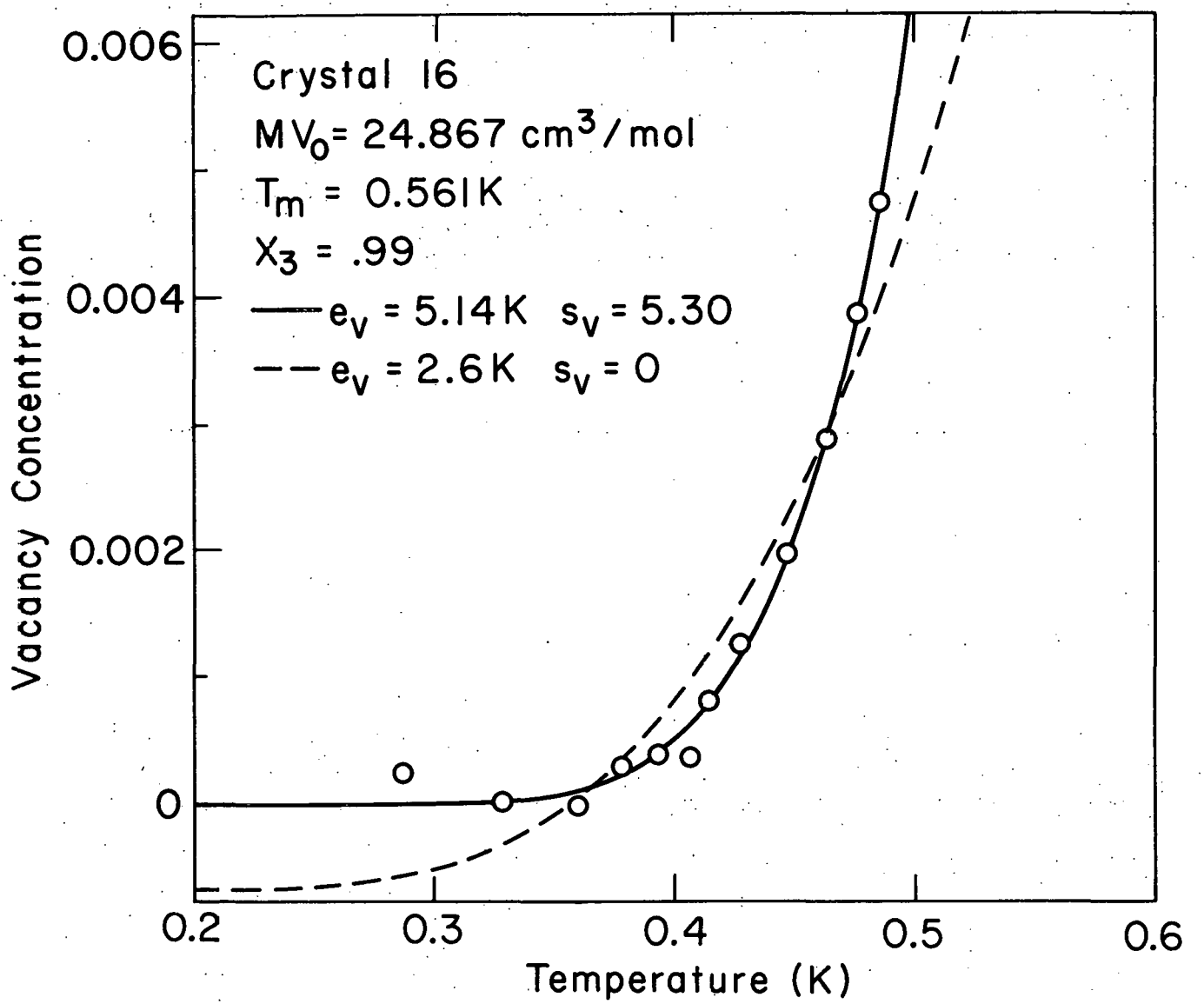
Crystal 16
MV_0= 24.867 cm^3/mol
T_m = 0.561K
X_3 = .99
e_v = 5.14K s_v = 5.30
e_v = 2.6K s_v = 0
Vacancy Concentration
0.006
0.004
0.002
0
0.2
0.3
0.4
0.5
0.6
Temperature (K)

Another measurement of the lattice parameter after warming back to 0.3 K showed a small change in lattice parameter which could be due to the excursion below the lower melting point.

A warming run was made after the lattice parameter measurement at about 0.3 K. These data are shown in Fig. 31, and are the squares in Fig. 29. Several interesting points should be noted. The data were taken right up to the melting temperature, 0.561 K. At low temperatures, there is an apparent dip in the vacancy concentration as the crystal is warmed, after which the change in lattice parameter is very steep. This dip had been observed by Heald in pure ^{3}He at high molar volumes, but he thought it was due to scatter in the data. This is clearly not the case here: two points were taken at each temperature, with close agreement. The final point to be made is that even though the cooling run (Fig. 30) and the warming run (Fig. 31) have so many differences, both give almost exactly the same results for $e_v(s_v=0)$, e_v, and s_v. It thus appears that the exponential fits to the data are useful in describing the vacancy content in general, independent of details in the temperature dependence.

6. Crystal 17

The data obtained on crystal 17 are shown in Fig. 32. All the data shown were obtained on warming, except the absolute lattice parameter measurement at 1.961 K, which was done immediately after growth of the crystal. The cooling run which was done between the lattice parameter measurement and the data which are shown here qualitatively agrees with the warming run, although experimental problems caused excessive scatter. On the warming run, two points were taken at each temperature. This allowed a correction to be

Figure 31. Crystal 16 vacancy measurements taken on warming. These data were obtained on warming after the crystal had been cooled below its lower melting temperature. The solid line is a least squares fit to Equation II-25 in which both e_v and s_v are varied. The dashed line is the fit with s_v=0.

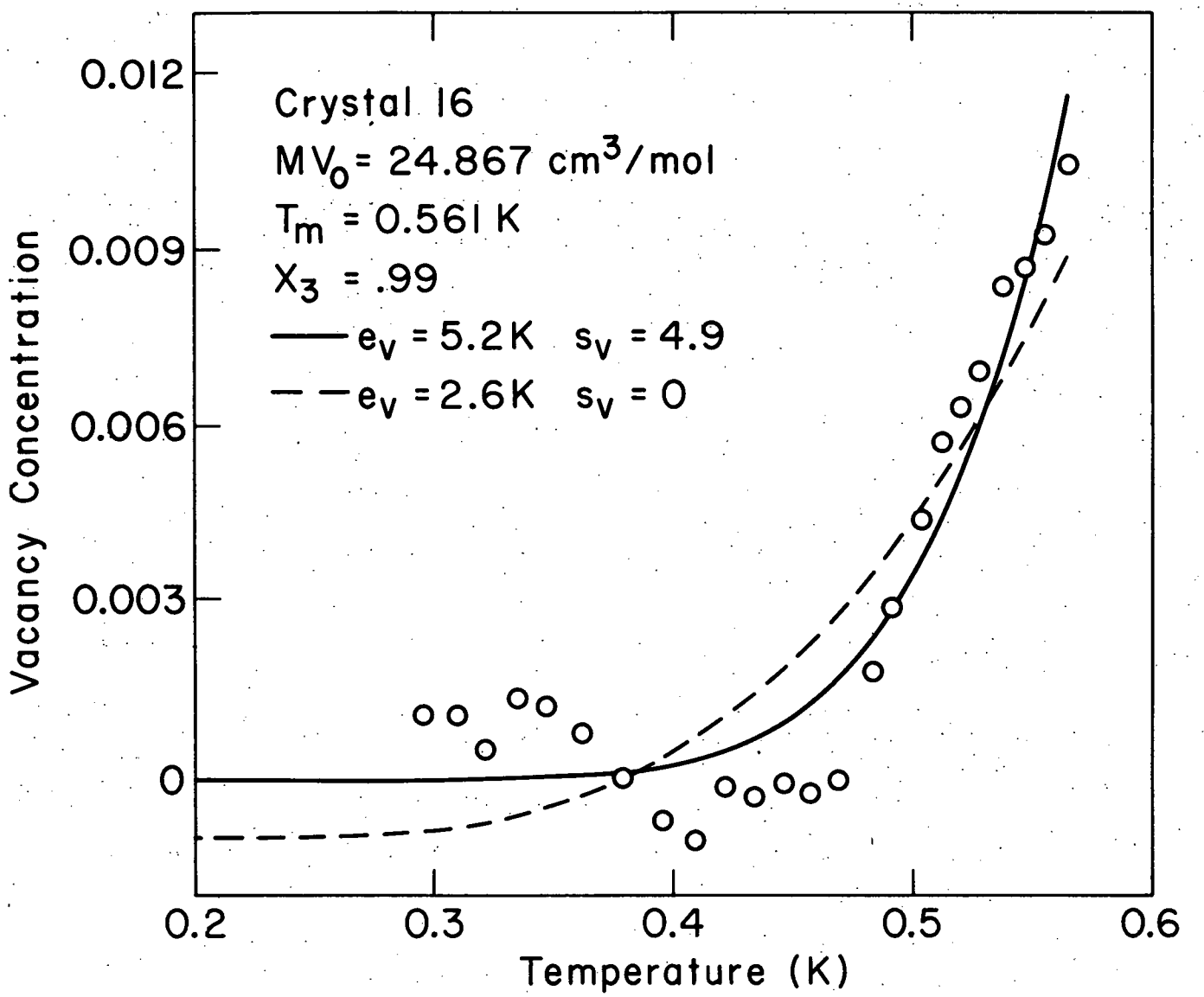
Crystal 16
MV_0 = 24.867 cm^3/mol
T_m = 0.561 K
X_3 = .99
e_v = 5.2K s_v = 4.9
e_v = 2.6K s_v = 0
Vacancy Concentration
0.012
0.009
0.006
0.003
0
0.2
0.3
0.4
0.5
0.6
Temperature (K)

Figure 32. Crystal 17 vacancy and absolute lattice parameter measurements. The vacancy data shown here were obtained on warming and have been corrected as described in the text. The solid line is a least squares fit to Equation II-25 in which both e_v and s_v are varied. The dashed line is the fit with s_v=0. The absolute lattice parameter (x) at 1.961 K was measured immediately after crystal growth, and the absolute measurement at 1.090 K was performed before the warming run which is shown here. The error bars correspond to 300 ppm in the lattice parameter.

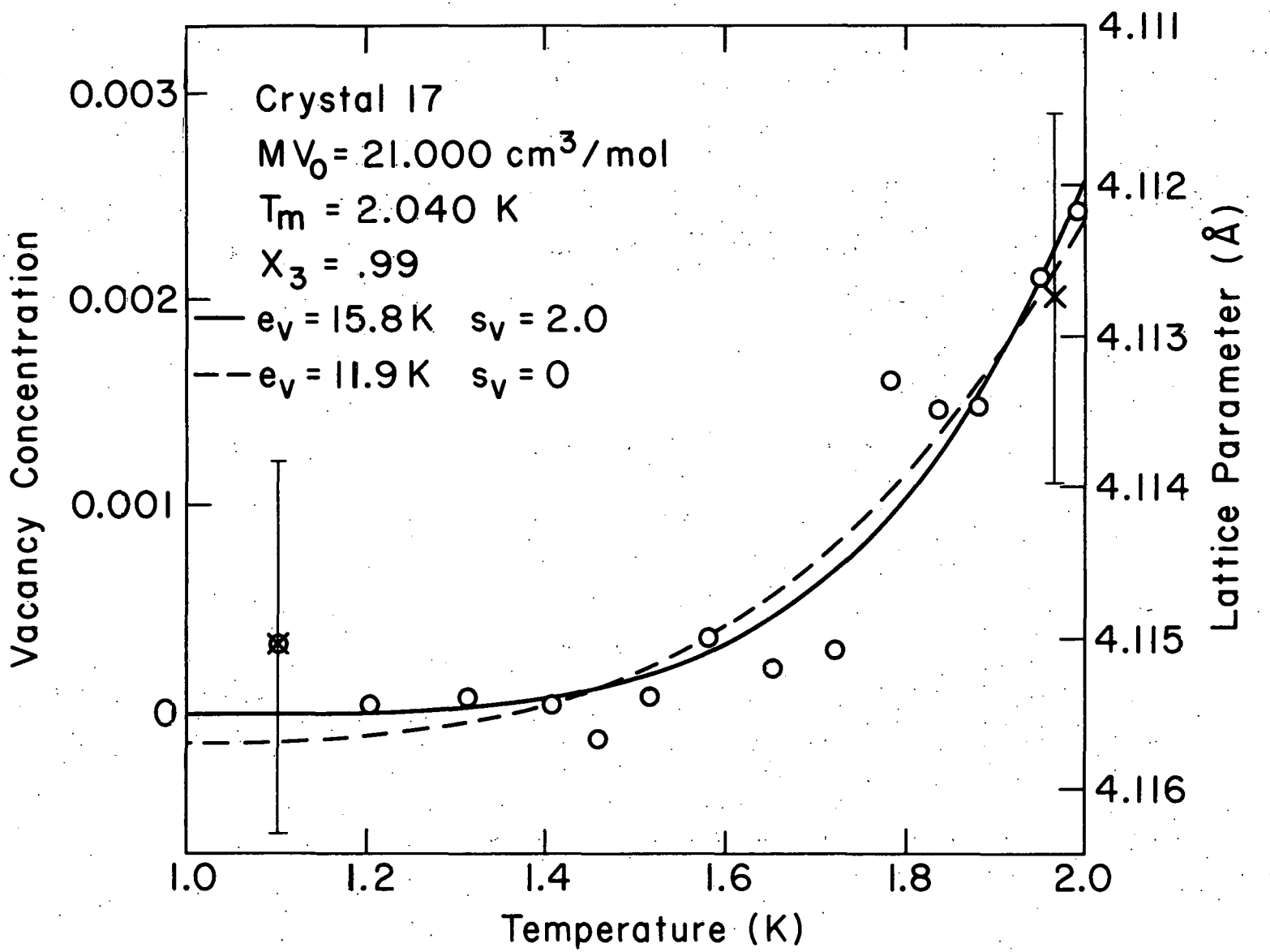
Crystal 17
$MV_0 = 21.000\ cm^3/mol$
$T_m = 2.040\ K$
$X_3 = .99$
$e_v = 15.8\ K \quad s_v = 2.0$
$e_v = 11.9\ K \quad s_v = 0$
Vacancy Concentration
0.003
0.002
0.001
0
Lattice Parameter (Å)
4.111
4.112
4.113
4.114
4.115
4.116
1.0
1.2
1.4
1.6
1.8
2.0
Temperature (K)

made for drift in the "mca" data (which was probably due to insufficient gas flow in the PSD). The agreement of the lattice parameter and vacancy data, as shown in Fig. 32, confirms the validity of the correction.

7. Specimen 18

No data are shown for specimen 18 because the crystal became bi-crystalline as it was cooled. However, there are several interesting points to be mentioned. At temperatures near 2 K, the specimen was a good quality single crystal. However, after it was cooled to below 1.84 K, the peak split into two peaks. The interesting point is that even through this transformation, the present method of data collection still provided consistent measurement of the lattice parameter changes. The combination of ω scans over the crystal mosaic with the centroid determination of the peak positions is very effective in removing the dependence of the data on peak shape. Scans were also done at the top, middle, and bottom of the cell, to check the z motion of the diffractometer. The lattice parameters at the three heights agreed within the normal scatter associated with ω scan measurements.

8. Crystal 19

The data obtained on crystal 19 are shown in Fig. 33. This warming run was also corrected for detector drift. Two points were taken at each temperature, as usual, to check for drift. As with crystal 17, the cooling run was not useful.

9. Specimens 20 and 21

Specimens 20 and 21 were the first attempts at growing crystals with the x_3=0.51 mixture. Crystal growth is very difficult in the

Figure 33. Crystal 19 vacancy and absolute lattice parameter measurements. The vacancy data were obtained on warming, and were corrected as described in the text. The solid line is a least squares fit to Equation II-25 in which both e_v and s_v are varied. The dashed line is the fit with s_v=0. The absolute lattice parameter measurement (x) at 1.923 K was done immediately after crystal growth. The absolute measurement at 1.163 K was done before the warming run which is shown here. The error bars on the absolute measurements are 300 ppm.

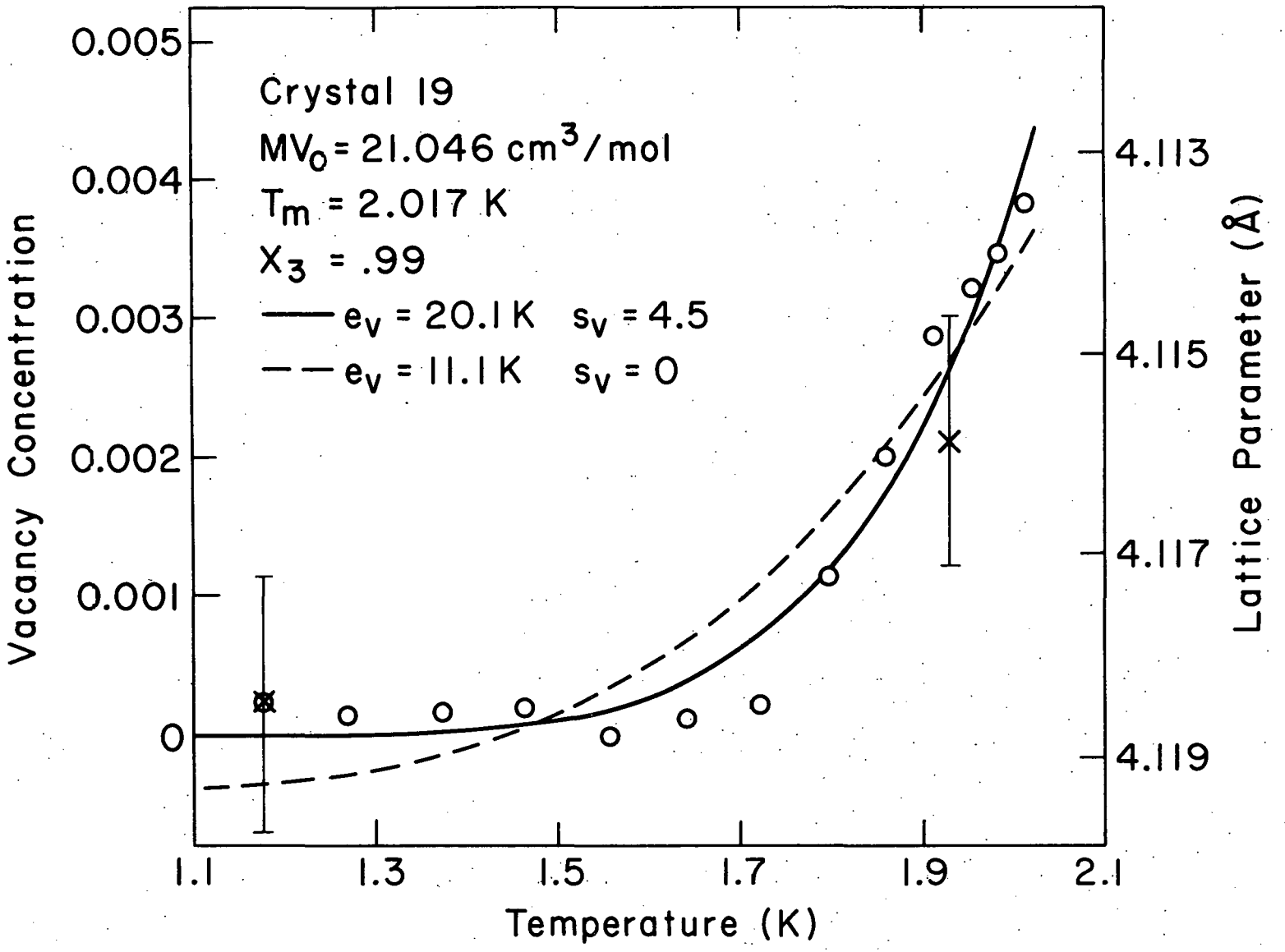
Crystal 19
$MV_0 = 21.046\ cm^3/mol$
$T_m = 2.017\ K$
$X_3 = .99$
$e_v = 20.1\ K \quad s_v = 4.5$
$e_v = 11.1\ K \quad s_v = 0$
Vacancy Concentration
0.005
0.004
0.003
0.002
0.001
0
Lattice Parameter (Å)
4.113
4.115
4.117
4.119
1.1
1.3
1.5
1.7
1.9
2.1
Temperature (K)

concentrated mixtures, as is discussed in Section III-E-2. Absolute lattice parameter measurements were made on both specimen 20 and specimen 21 at several different heights in the cell. The goal was to see if there was a concentration gradient in the specimen which was making growth of single crystals difficult. Both specimens had many grains, and were bad quality, but the measurements indicate no change in lattice parameter with height in the cell. This is especially interesting because specimen 21 was melted back, and regrown again very slowly (over a 48 hour period) while the progress of growth was seen by monitoring the Bragg peak intensity as a function of height in the cell. The crystal was of good quality near the apparent liquid-solid interface, but was a poorer quality behind the interface.

This slow regrowth method may have caused a concentration gradient in the crystal, since apparently there was still liquid in the bottom of the cell at temperatures more than 0.4 deg below the "melting" temperature at which growth started. Qualitative examination of published $T=x_3$ phase diagrams[30/] (see Fig. 4) would lead to the expectation of a concentration gradient of tens of percent for this apparent depression of the solidification temperature. If this gradient was present in this crystal, there was no evidence of it in the lattice parameter measurements.

10. Crystal 23

The vacancy data obtained on crystal 23 are shown in Fig. 34. These measurements were made on warming. It was necessary to use a different cutoff than usual when calculating the centroids of the "sca" peaks because there was a small grain at the base of the peak which was changing shape somewhat. The cutoff was changed from 90% to 70% of the peak during this vacancy run.

Figure 34. Crystal 23 vacancy measurements. The data were obtained on warming. The solid line is a least squares fit to Equation II-25 in which both e_v and s_v are varied. The dashed line is the fit with s_v=0.

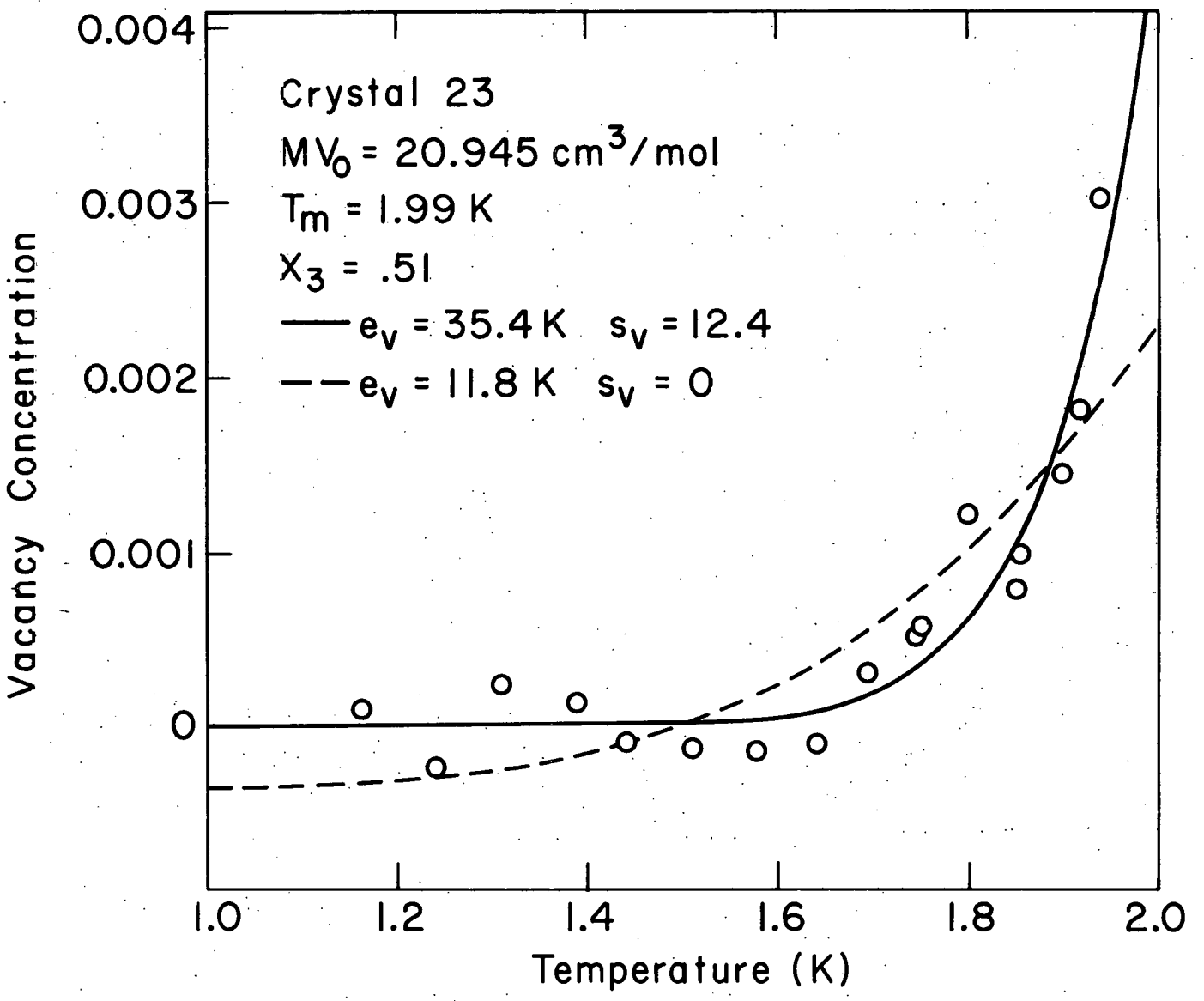
Crystal 23
MV_0 = 20.945 cm^3/mol
T_m = 1.99 K
X_3 = .51
—— e_v = 35.4 K s_v = 12.4
– – e_v = 11.8 K s_v = 0
Vacancy Concentration
0.004
0.003
0.002
0.001
0
1.0
1.2
1.4
1.6
1.8
2.0
Temperature (K)

The data taken on the crystal as it was cooled, and then warmed back through the phase separation temperature T_{ps}, are shown in Fig. 35. These changes in lattice parameter are calculated from the "mca" data only, since the "sca" data become very unreliable below T_{ps}. The vacancy measurements from Fig. 34 are not shown in Fig. 35, for clarity. The lattice parameter measurements which are shown were taken during the vacancy measurements. There is a pronounced dip in the lattice parameter before phase separation. The lattice parameter then quickly rises as soon as the temperature gets below T_{ps}.

The lattice parameter changes seen on warming back through T_{ps} show much different behavior than the cooling data. This is not time dependent behavior. The points taken on warming at 0.435 K were separated by more than 12 hours, and show no hint of annealing or returning to the pre-phase separation lattice parameter as a function of time. This difference of behavior between warming and cooling is seen also in Fig. 36, which is a plot of the width of the "mca" and "sca" peaks on cooling and warming near T_{ps}. The width of the "mca" peak, which measures the width of the Bragg peak, is seen to show no hysteresis at all. This is very different from the "sca" peak width, which is a measure of the width of the crystal mosaic. This width does not decrease to its pre-phase separation width until after the crystal has been warmed to fairly near the melting temperature, where the damage done to the crystal structure by phase separation can be repaired.

11. Crystal 24

Shown in Fig. 37 are the vacancy data obtained on crystal 24. The vacancy data obtained below 0.5 K are not included in the figure or the fits

Figure 35. Crystal 23 lattice parameter measurements. The circles were obtained on cooling, and the crosses on warming. The vacancy measurements from Fig. 34 are not shown on this figure for clarity. The absolute lattice parameters (x) are shown with 300 ppm error bars.

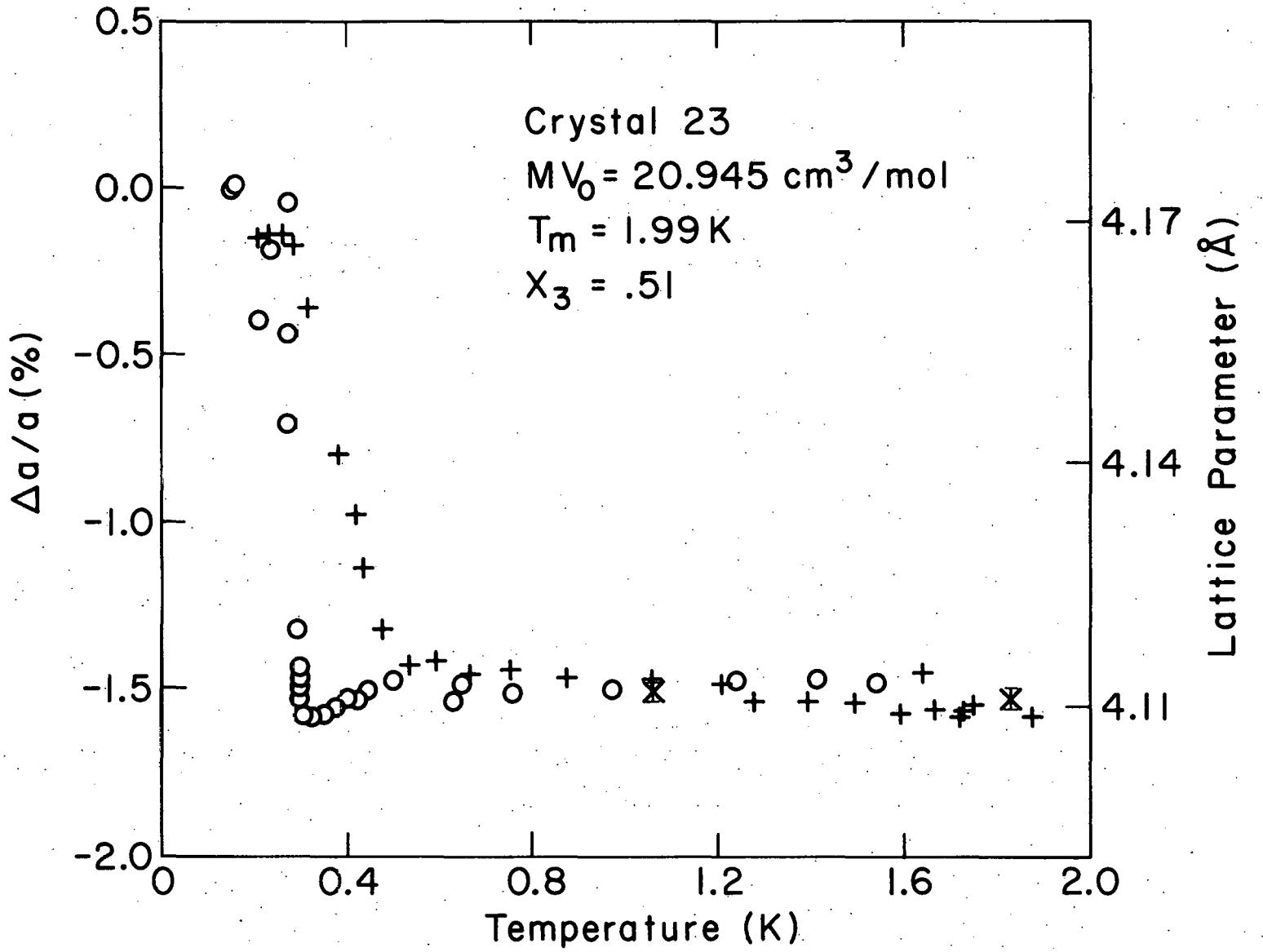
Crystal 23
MV_0 = 20.945 cm^3/mol
T_m = 1.99 K
X_3 = .51
0.5
0.0
-0.5
-1.0
-1.5
-2.0
Δa/a (%)
4.17
4.14
4.11
Lattice Parameter (Å)
0
0.4
0.8
1.2
1.6
2.0
Temperature (K)

Figure 36. Crystal 23 peak widths at phase separation on cooling and warming. The mosaic ("sca") peak width is plotted versus temperature for crystal 23 near T_{ps}. The inset shows the width of the Bragg ("mca") peak in the same temperature range. The circles are points obtained on cooling, and the crosses are warming points.

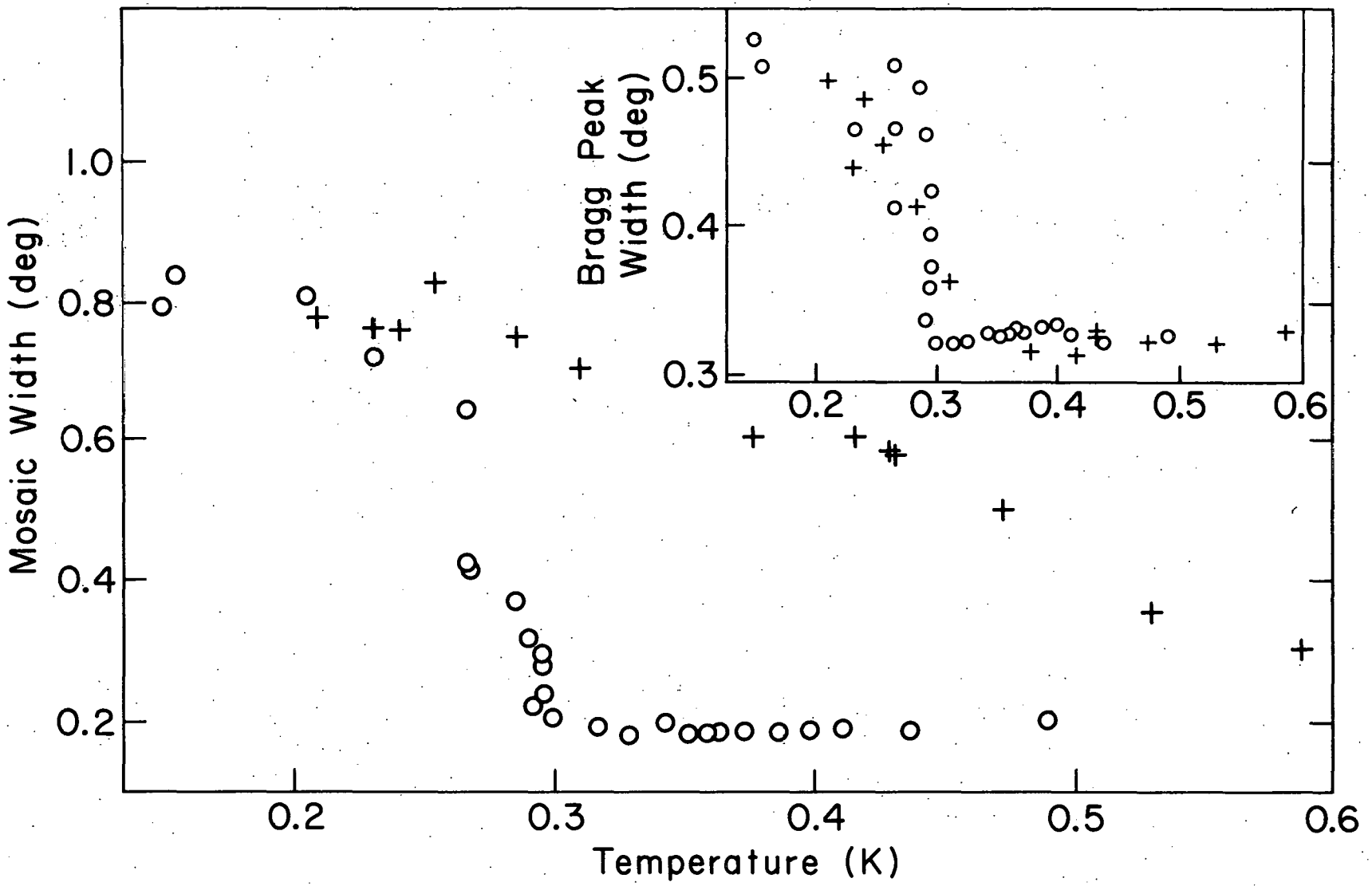
Mosaic Width (deg)
1.0
0.8
0.6
0.4
0.2
0.2
0.3
0.4
0.5
0.6
Temperature (K)
Bragg Peak Width (deg)
0.5
0.4
0.3
0.2
0.3
0.4
0.5
0.6

Figure 37. Crystal 24 vacancy measurements. The data were obtained on cooling. The solid line is a least squares fit to Equation II-25 in which both e_v and s_v are varied. The dashed line is the fit with s_v=0.

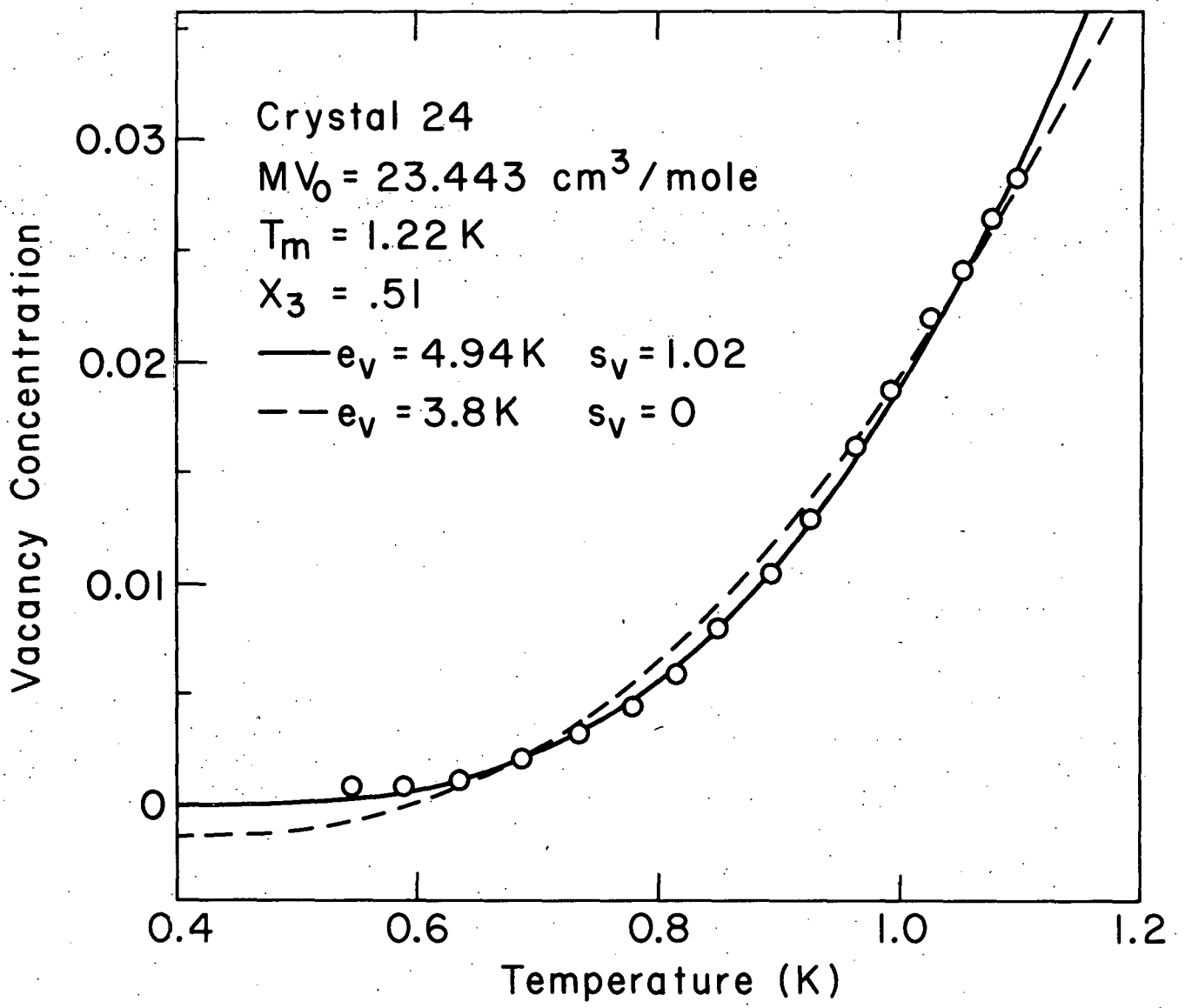
Crystal 24
MV_0 = 23.443 cm^3/mole
T_m = 1.22 K
X_3 = .51
e_v = 4.94 K s_v = 1.02
e_v = 3.8 K s_v = 0
Vacancy Concentration
0.03
0.02
0.01
0
0.4
0.6
0.8
1.0
1.2
Temperature (K)

because there was a decrease in a, perhaps due to phase separation which occurs at 0.4 K. It is not obvious, however, that the lattice parameter decrease at low temperatures (above T_{ps}) is not similar to the anomalous behavior seen in crystal 16 and other high molar volume crystals.

The vacancy measurements discussed above, the single absolute lattice parameter measurement, and all the data taken on cooling and warming through phase separation are shown in Fig. 38. The lattice parameter (a) definitely starts decreasing before the phase separation temperature T_{ps} is reached. There is a large decrease in a as phase separation occurs, the total change in lattice parameter between T_{ps} and 0.15 K being about 4 percent. The gap in the cooling data at about 0.37 K is due to a 9 hour anneal. A 17 hour anneal occurred between the last cooling run point and the lowest temperature point, during which the lattice parameter increased somewhat. As warming was begun, the lattice parameter increased by about 5 percent, and then slowly decreased back toward the expected value. This type of behavior was seen in several of the mixtures studied.

The behavior above T_{ps} on warming is different than that seen in crystal 23 because the lattice parameter is very different from that found on cooling. A small part of the difference is perhaps due to time effects: during a nine hour anneal at 0.56 K the lattice parameter increased 0.4%. A final point should be noted. A qualitative extrapolation of the cooling curve and the warming curve to the melting temperature shows that the two curves apparently meet at the melting temperature.

12. Crystal 26

Crystal 26 was grown at a slightly higher pressure than crystal 24 to check the amazing concentration of vacancies seen in crystal 24 near

Figure 38. Crystal 24 lattice parameter measurements. The circles are data obtained on cooling, and the crosses were obtained on warming. The error bars on the absolute lattice parameter measurement (x) correspond to 300 ppm, and are barely visible.

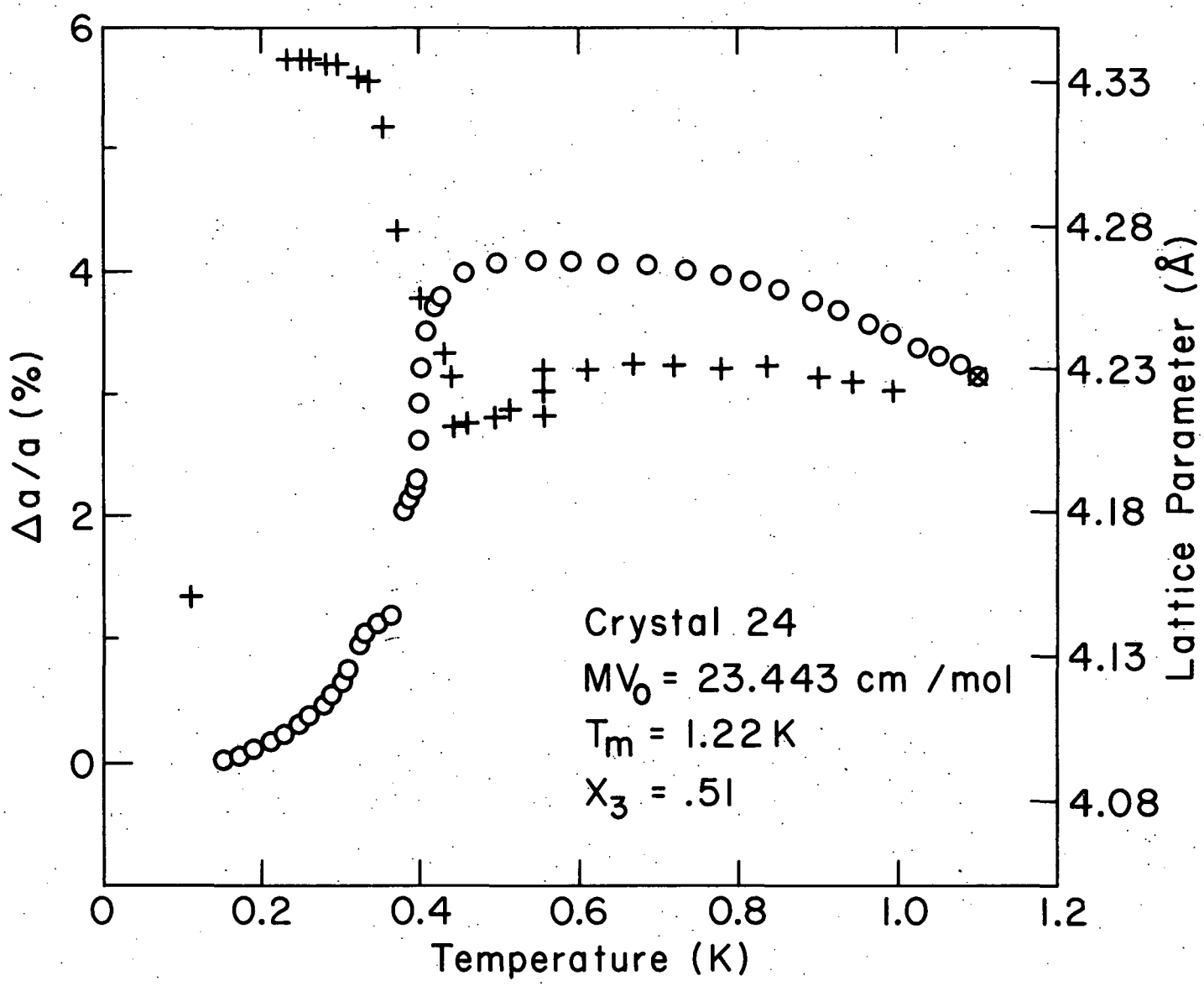
Crystal 24
MV0 = 23.443 cm /mol
Tm = 1.22 K
X3 = .51
Δa/a (%)
Lattice Parameter (Å)
Temperature (K)
0
2
4
6
0.2
0.4
0.6
0.8
1.0
1.2
4.08
4.13
4.18
4.23
4.28
4.33

melting (more than 3% at a temperature more than 0.1 deg below the melting temperature!). The vacancy data on crystal 26, shown in Fig. 39, completely confirm the large number of vacancies. As with all the vacancy data, two scans were taken at each temperature to insure against equipment difficulties. The two data points at each temperature agree very well over the whole temperature range of the vacancy measurements.

All of the measurements on crystal 26 are shown in Fig. 40. The behavior of this crystal at phase separation is qualitatively different from that of crystal 24, even though the two were grown at pressures different by only 0.5 MPa. Below phase separation, crystal 26 shows two distinct peaks. The two lattice parameters obtained from the two peaks are shown in Fig. 40. The small lattice parameter peak has very small intensity immediately after phase separation, and the intensity increases as the temperature is lowered. While this is happening, the intensity of the large lattice parameter peak goes to zero. This transition is illustrated by Figs. 41 and 42 , which show the Bragg ("mca") and mosaic ("sca") peaks, respectively, as the phase separation proceeds. The gap between the small lattice parameter peak data and the lattice parameter before phase separation is due to the fact that the emerging peak cannot be separated distinctly from the larger lattice parameter peak until it is at a different enough lattice parameter for the two to be resolved. This can easily be seen in Fig. 41. The mosaic peak in Fig. 42 is included as an example of the degradation of the crystal quality as phase separation proceeds.

The crystal sat at 0.35 K for 7 hours after the separation into two peaks, after which only the smaller lattice parameter peak was left. There was little change in the lattice parameter of that peak, but as can be seen

Figure 39. Crystal 26 vacancy measurements. The data were obtained on cooling. The solid line is a least squares fit to Equation II-25 in which both e_v and s_v are varied. The dashed line is the fit with s_v=0.

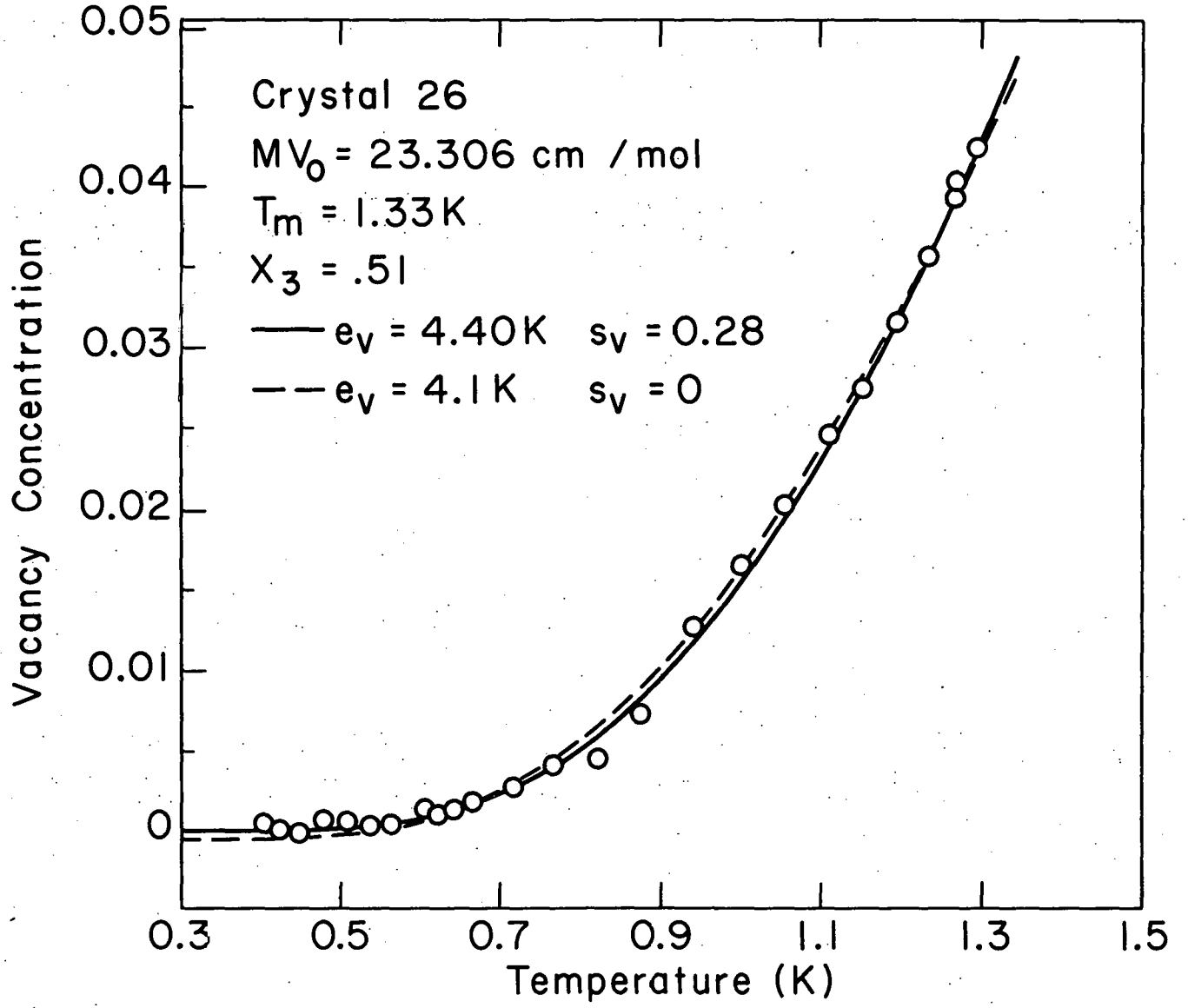
Crystal 26
MV0 = 23.306 cm /mol
Tm = 1.33K
X3 = .51
ev = 4.40K sv = 0.28
ev = 4.1K sv = 0
Vacancy Concentration
0.05
0.04
0.03
0.02
0.01
0
0.3
0.5
0.7
0.9
1.1
1.3
1.5
Temperature (K)

Figure 40. Crystal 26 lattice parameter measurements. The circles were obtained on cooling, and the crosses on warming. The error bars on the absolute lattice parameter measurement (x) correspond to 300 ppm, and are barely visible.

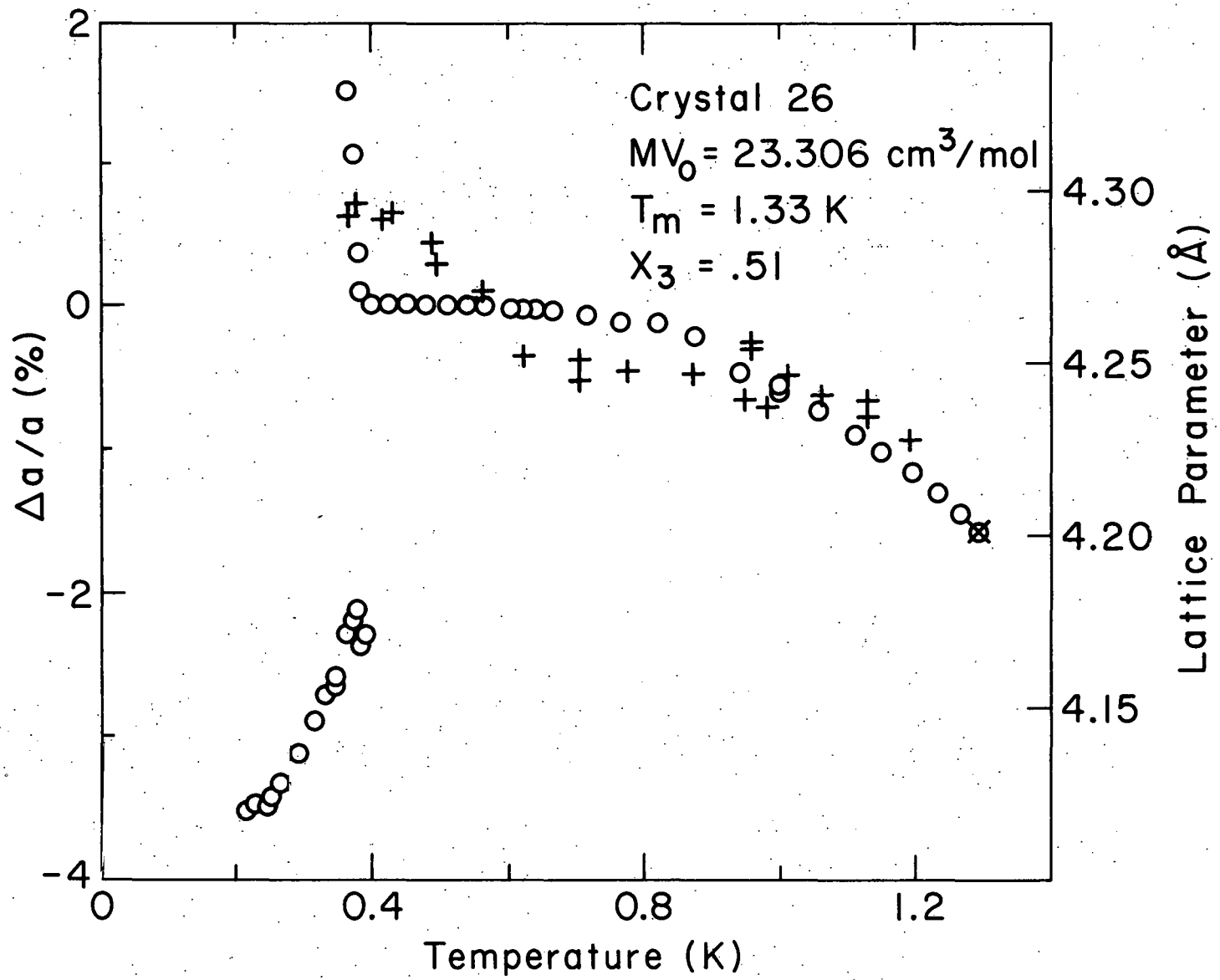
Crystal 26
MV0 = 23.306 cm3/mol
Tm = 1.33 K
X3 = .51
Δa/a (%)
Lattice Parameter (Å)
Temperature (K)
2
0
-2
-4
0
0.4
0.8
1.2
4.30
4.25
4.20
4.15

Figure 41. Bragg ("mca") peak during phase separation. The Bragg peak is shown as crystal 26 phase separates. Counts per channel in the MCA are plotted versus channel number. One degree corresponds to 101.3 channels on the PSD. The evolution of the two separate peaks (which were seen in crystals 26, 27, and 28) is clearly visible.

For clarity, only one set of actual data is shown (curve C), as an example of the method used to determine the other curves. The temperatures at which the various peaks were obtained are: (A) 0.393 K, (B) 0.387 K, (C) 0.381 K, (D) 0.377 K, (E) 0.370 K, (F) 0.359 K.

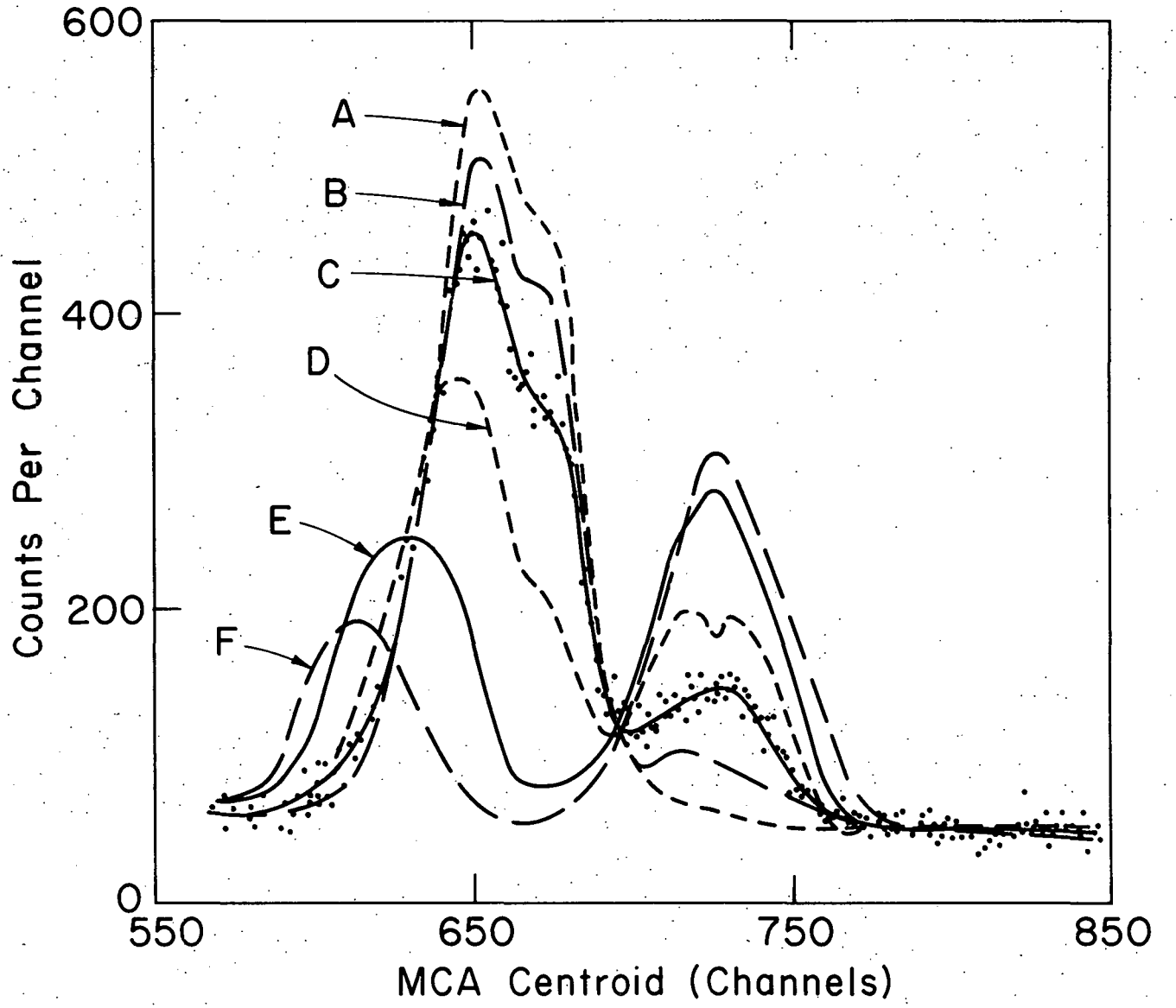
600
400
200
0
Counts Per Channel
550
650
750
850
MCA Centroid (Channels)
A
B
C
D
E
F

Figure 42. Mosaic ("sca") peak during phase separation. The degeneration of the mosaic structure of crystal 26 as it phase separated is shown here as a function of temperature. The total number of counts into the PSD per unit time is plotted versus Bragg angle.

For clarity, only one set of actual data are shown (curve D), as an example of the method used to determine the other curves. The temperatures at which the data were obtained are: (A) 0.393 K, (B) 0.387 K, (C) 0.381 K, (D) 0.377 K, (E) 0.370 K, (F) 0.359 K.

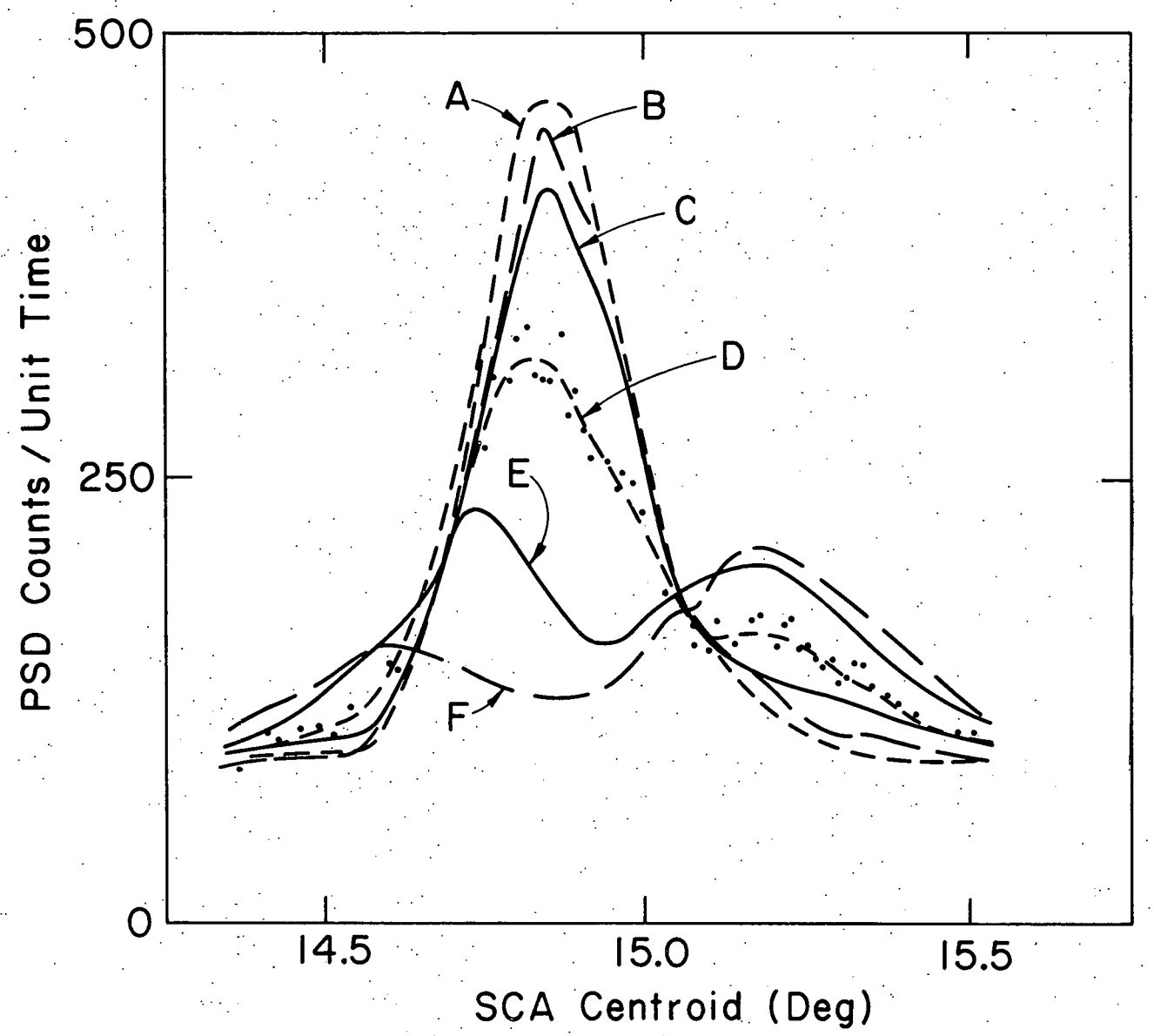
500
250
0
PSD Counts / Unit Time
14.5
15.0
15.5
SCA Centroid (Deg)
A
B
C
D
E
F

in Fig. 21, the width of the mosaic had returned to its pre-phase separation value. As the crystal was cooled further, the width again increased. Nothing unusual was observed as the crystal was cooled to 0.21 K: the mosaic ("sca") peak degenerated as expected, but the Bragg ("mca") peak shape remained basically the same. After 10 hours at 0.22 K, both peaks were totally gone. Warming to 0.27 K caused the return of the "mca" peak, although with little intensity. As warming continued, both peaks grew in intensity, although the mosaic ("sca") peak was really only a bunch of crystallites spread over about 5 degrees. Note that on warming the general behavior of the lattice parameter (as obtained from the "mca" peak, since the "sca" peak is unreliable after phase separation) for this crystal was qualitatively the same as that of crystal 24.

13. Crystal 27

Two vacancy data runs were obtained for crystal 27. The data displayed in Fig. 43 were obtained on a cooling run. The data obtained below 1.25 K were excluded from the vacancy analysis because of clearly anomalous behavior in the data below this temperature. This increase in lattice parameter can be seen in Fig. 44, which is a plot of all the crystal 27 data. This behavior has been tentatively identified with the transition from the pure bcc phase to a mixed hcp and bcc phase. The decrease in lattice parameter at 0.77 K is the result of an 11 hour anneal.

The data shown in Fig. 45 are vacancy measurements from a warming run done after the crystal recovered from phase separation. Inspection shows much more scatter of the data below 1.0 K than above it. This is about the same temperature at which the mixed phase was identified in the

Figure 43. Crystal 27 vacancy measurements before phase separation. The data were obtained on cooling, with the data below 1.25 K excluded because of the entry into the mixed phase. The solid line is a least squares fit to Equation II-25 in which both e_v and s_v are varied. The dashed line is the fit with s_v=0.

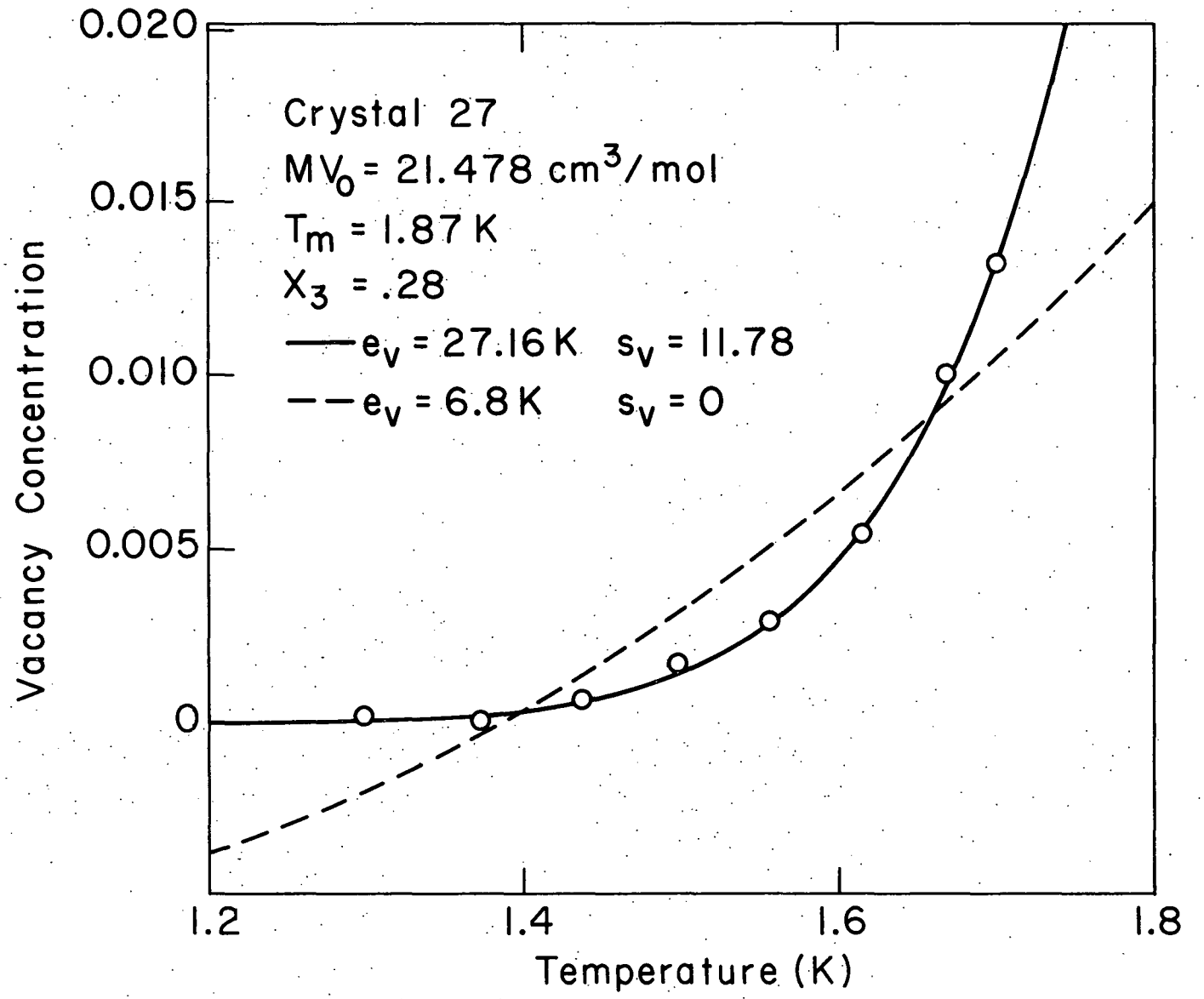
Crystal 27
MV_0 = 21.478 cm^3/mol
T_m = 1.87 K
X_3 = .28
—— e_v = 27.16 K s_v = 11.78
– – e_v = 6.8 K s_v = 0
0.020
0.015
0.010
0.005
0
Vacancy Concentration
1.2
1.4
1.6
1.8
Temperature (K)

Figure 44. Crystal 27 lattice parameter measurements. The circles were obtained on cooling, and the crosses on warming. The error bars on the absolute lattice parameter measurement (x) correspond to 300 ppm, and are barely visible.

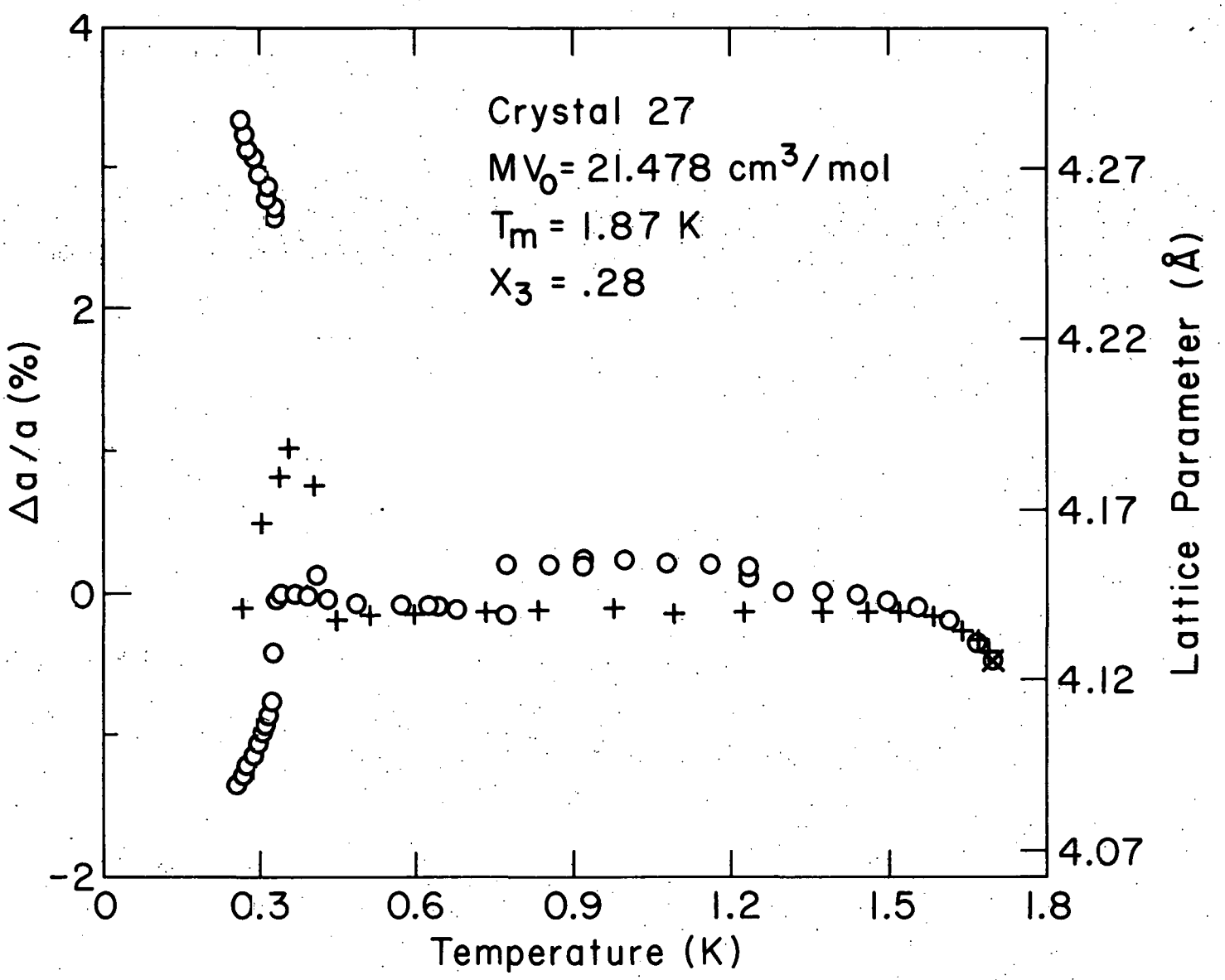
Crystal 27
MV0 = 21.478 cm3/mol
Tm = 1.87 K
X3 = .28
Δa/a (%)
Lattice Parameter (Å)
Temperature (K)
4
2
0
-2
4.27
4.22
4.17
4.12
4.07
0
0.3
0.6
0.9
1.2
1.5
1.8

Figure 45. Crystal 27 vacancy measurements after phase separation. The data shown here were obtained on warming after the crystal was cooled into the phase separation region. The solid line is a least squares fit to Equation II-25 in which both e_v and s_v were varied. The dashed line is the fit with s_v=0.

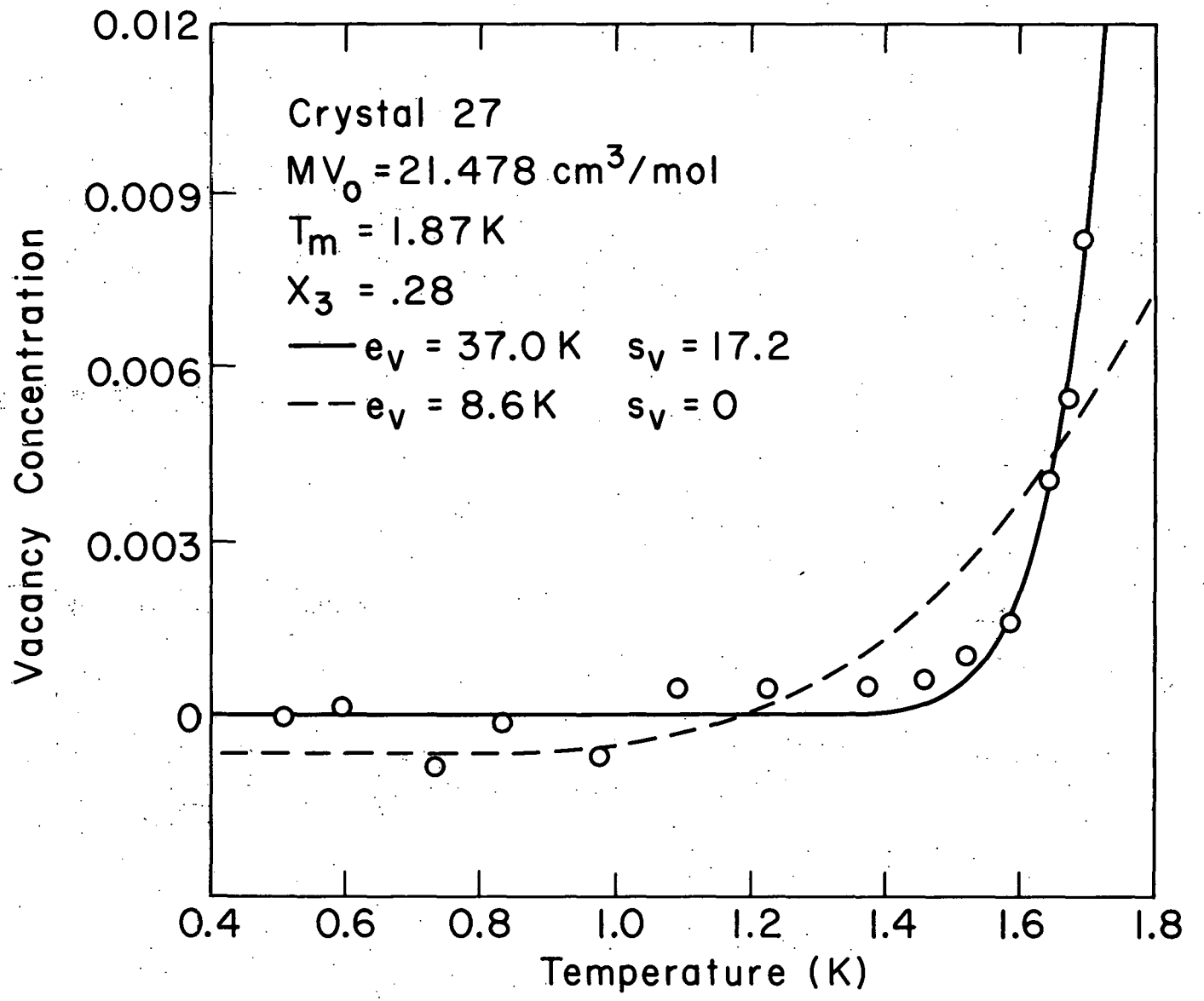
Crystal 27
MV$_0$ = 21.478 cm^3/mol
T$_m$ = 1.87 K
X$_3$ = .28
e$_v$ = 37.0 K s$_v$ = 17.2
e$_v$ = 8.6 K s$_v$ = 0
Vacancy Concentration
0.012
0.009
0.006
0.003
0
0.4
0.6
0.8
1.0
1.2
1.4
1.6
1.8
Temperature (K)

cooling data. The difference in the fit parameters between the warming and cooling runs is in large part caused by the different ranges of temperature covered by the data.

Several points of interest are obvious in Fig. 44 , which shows all the data obtained on crystal 27. The lattice parameters of both components are again visible in the figure below T_{ps}. Unlike crystal 26, however, the small peak which splits off from the main peak is at larger lattice parameter this time. After cooling to 0.255 K, the peaks appeared to be going away completely, so the crystal was warmed. The warming data shown below T_{ps} are not from either of the peaks seen on cooling, but are from the centroid of the two peaks as they coalesced. The quality of both the Bragg ("mca") and mosaic ("sca") peaks nearly returned to its original pre-phase separation value after a 9 hour anneal at about 0.4 K (above T_{ps}). It was possible to perform the vacancy warming run after phase separation because the crystal did not sit in the separated region for more than about 6 hours, thus minimizing the damage to the crystal structure. It is interesting to note that, as before, near the melting temperature the pre-phase separated lattice parameter agrees with that found after phase separation. There is also a fair amount of agreement between the warming and cooling data between 0.4 and 0.8 K.

14. Crystal 28

The vacancy data on crystal 28 are shown in Fig. 46. They were obtained on cooling, and show an interesting decrease in lattice parameter (increase in vacancy concentration) at low temperatures. All of the data from crystal 28 are displayed in Fig. 47. The by-now usual behavior below phase separation is seen, although this time the larger lattice parameter

Figure 46. Crystal 28 vacancy measurements. The data were obtained on cooling. The solid line is a least squares fit to Equation II-25 in which both e_v and s_v are varied. The dashed line is the fit with $s_v=0$.

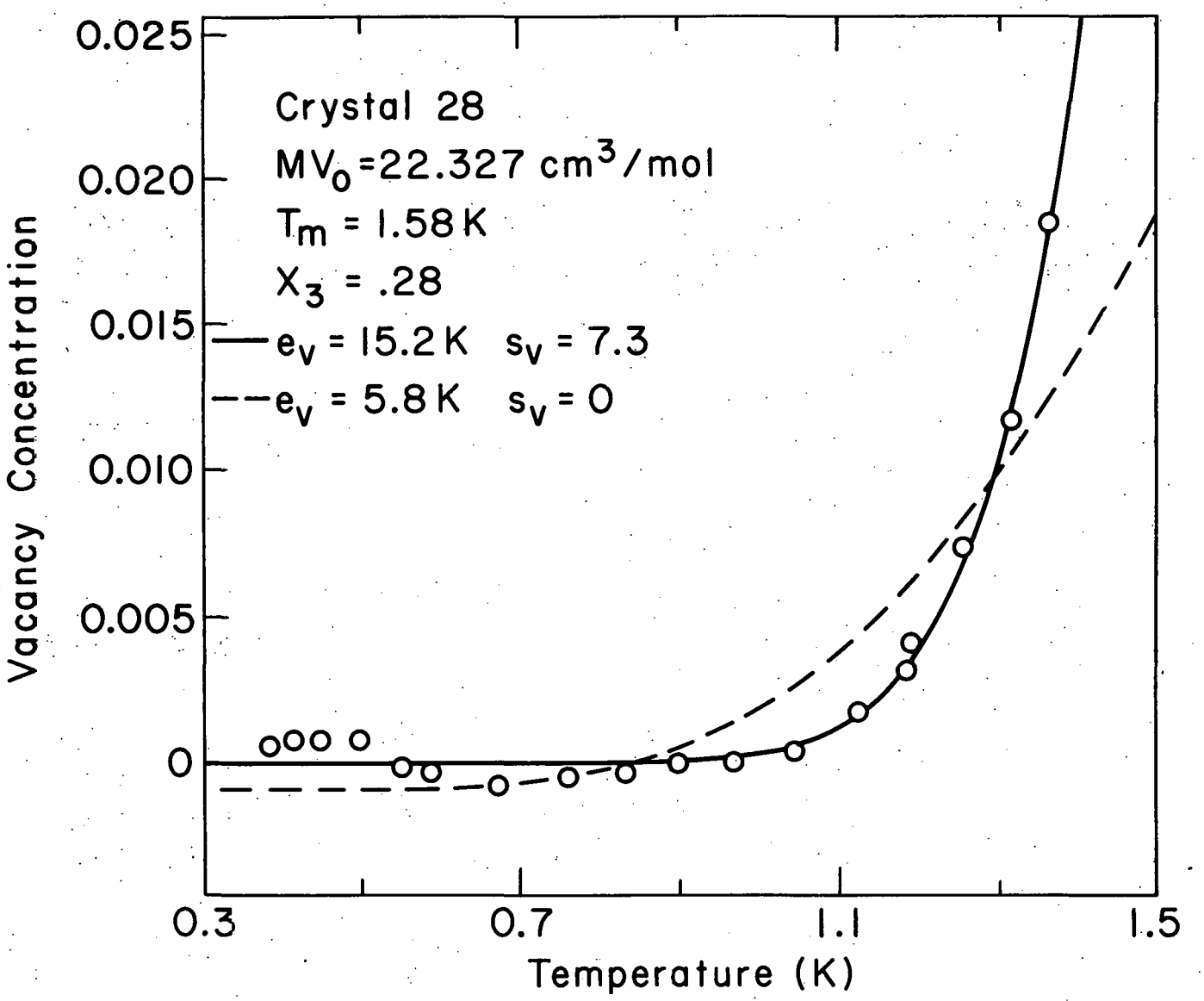
Crystal 28
MV0=22.327 cm3/mol
Tm = 1.58 K
X3 = .28
ev = 15.2 K sv = 7.3
ev = 5.8 K sv = 0
Vacancy Concentration
0.025
0.020
0.015
0.010
0.005
0
0.3
0.7
1.1
1.5
Temperature (K)

Figure 47. Crystal 28 lattice parameter measurements. The circles were obtained on cooling, and the crosses on warming. The absolute lattice parameter (x) was obtained before the cooling run. The error bars on the absolute measurement correspond to 300 ppm, and are barely visible.

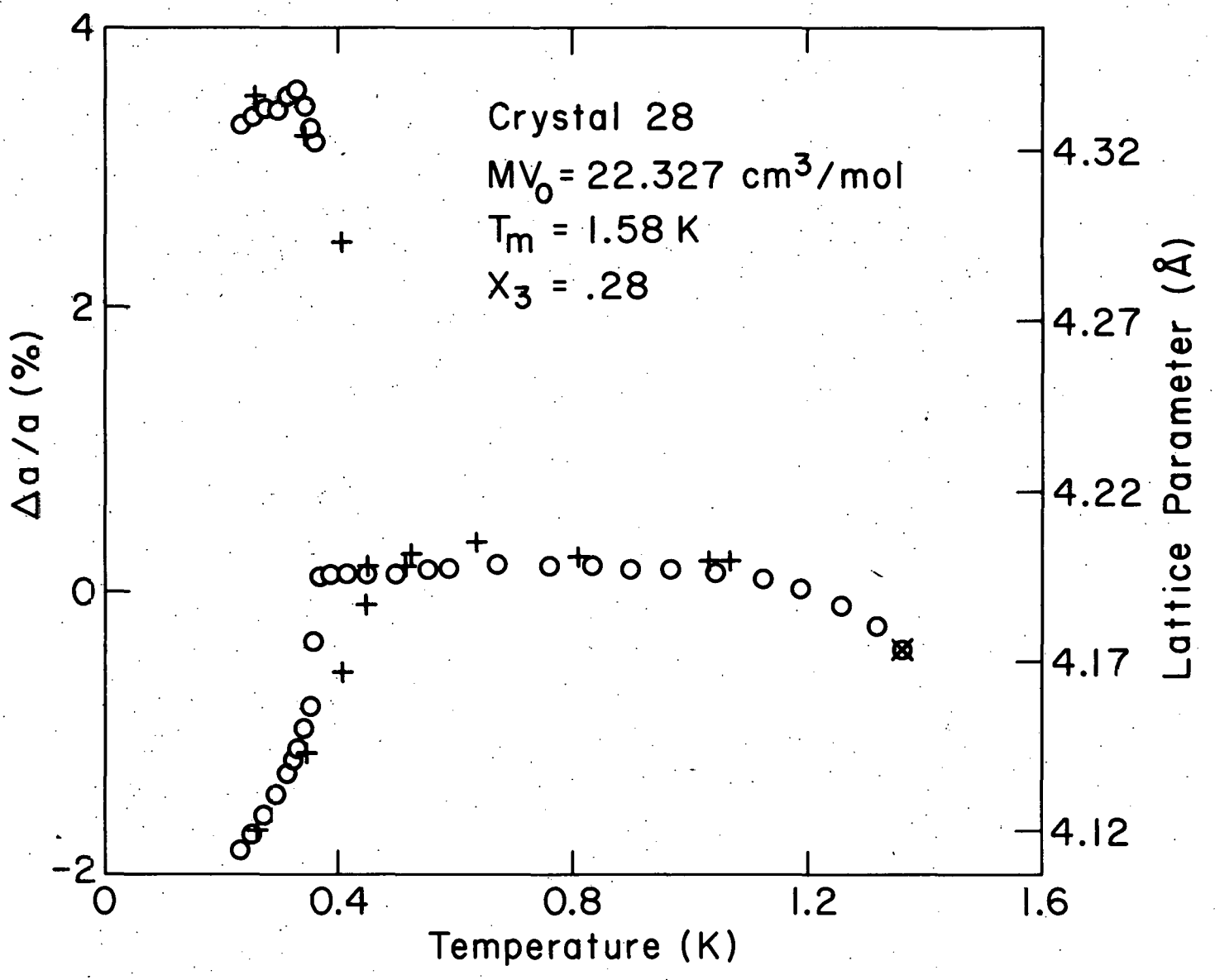
Crystal 28
MV0 = 22.327 cm3/mol
Tm = 1.58 K
X3 = .28
Δa/a (%)
Lattice Parameter (Å)
Temperature (K)
4
2
0
-2
4.32
4.27
4.22
4.17
4.12
0
0.4
0.8
1.2
1.6

peak started shifting rapidly to smaller lattice parameter. This was taken to be the transition of one of the separated phases from bcc to hcp, so the crystal was warmed back above T_{ps}. It was hoped that the crystal quality would be regained. Although the warming data show the usual reluctance to return along the cooling curve near phase separation, at slightly higher temperatures the lattice parameters do agree. This agreement is apparently due to the fact that the crystal was below T_{ps} for only 5 hours.

15. Crystal 29

The data obtained on the first warming and cooling runs on crystal 29 are shown in Fig. 48. Also shown are two lattice parameter measurements, one obtained at the beginning of the cooling-warming cycle, and the other at the end. The agreement between the $\Delta a/a$ and absolute lattice parameter measurements confirms that the strange behavior found on cooling was real. The jump in lattice parameter from $\Delta a/a = 0.02$ to -0.05 at 0.82 K occurred during a 9 hour anneal. The drop in lattice parameter near 0.27 K is due to phase separation. The behavior at phase separation for both crystals (29 and 30) with $x_3=0.12$ is qualitatively different than that seen before. While the changes in peak shape were fairly small, at T_{ps} in crystal 29 the intensity of the peak increased by more than a third.

Crystal 29 was not allowed to go very far into the phase separation region due to the need to make more vacancy measurements. The warming run which followed phase separation is shown in Fig. 49. Two succeeding runs were also made on the crystal, and were found to agree qualitatively with this warming run. The vacancy measurements from the first warming run were

Figure 48. Crystal 29 lattice parameter measurements. The circles were obtained on cooling, and the crosses on warming. The absolute lattice parameter measurements (x) were made before and after the cooling-warming cycle which is shown here. The error bars correspond to 300 ppm in lattice parameter.

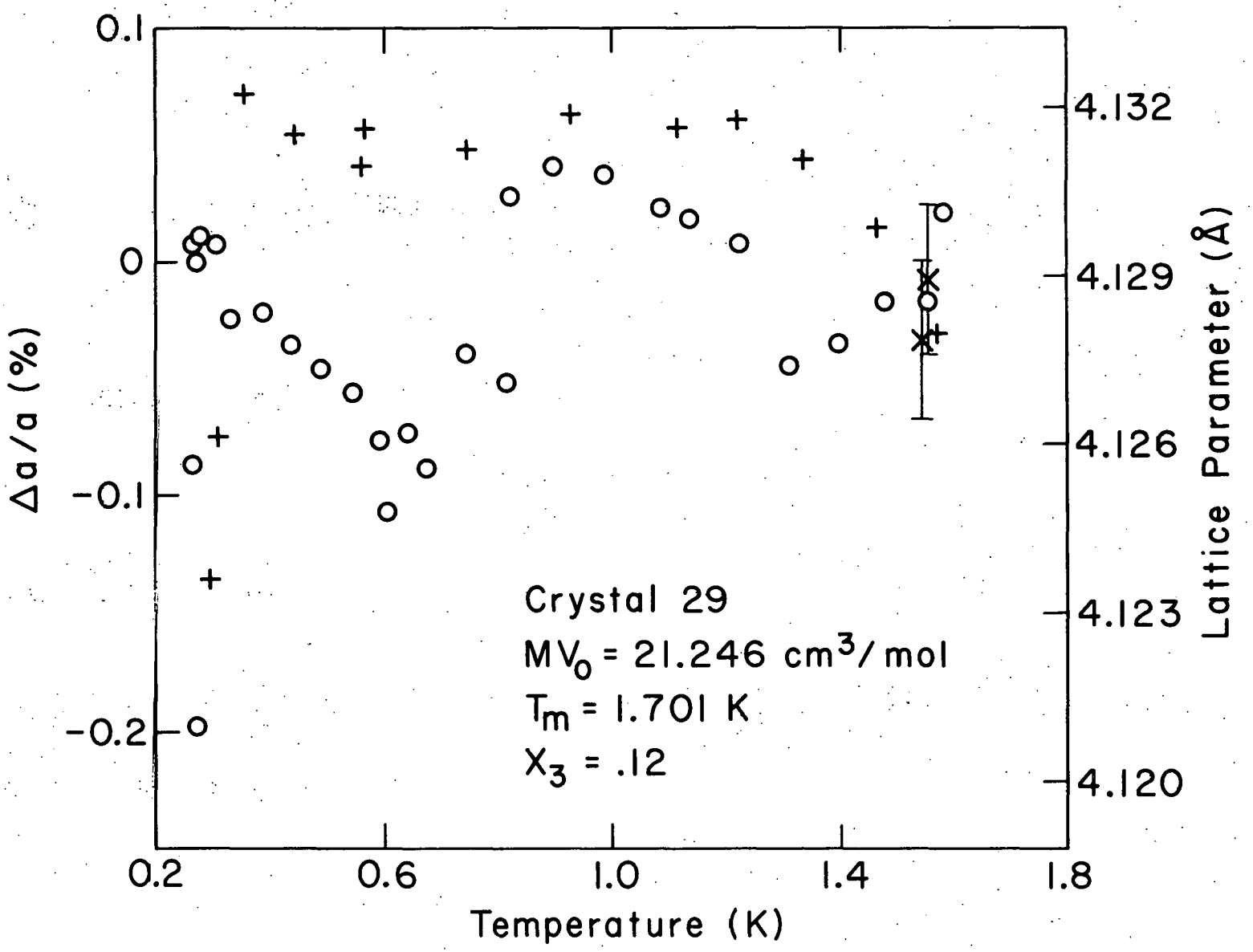
0.1
0
-0.1
-0.2
Δa/a (%)
4.132
4.129
4.126
4.123
4.120
Lattice Parameter (Å)
0.2
0.6
1.0
1.4
1.8
Temperature (K)
Crystal 29
MV0 = 21.246 cm3/mol
Tm = 1.701 K
X3 = .12

Figure 49. Crystal 29 vacancy measurements. The data were obtained on warming. The solid line is a least squares fit to Equation II-25 in which both e_v and s_v are varied. The dashed line is the fit with s_v=0.

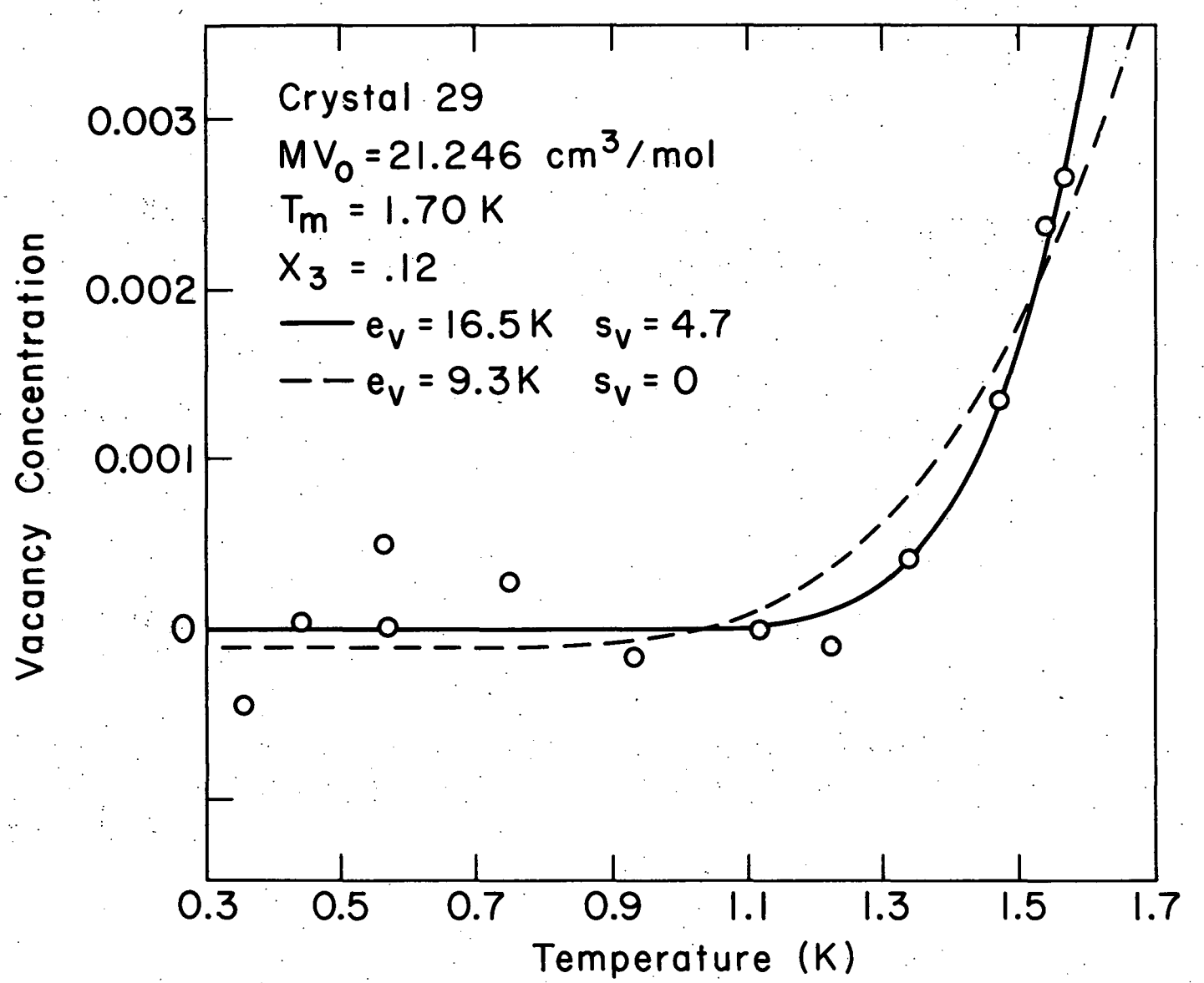
Crystal 29
MV0 = 21.246 cm3/mol
Tm = 1.70 K
X3 = .12
ev = 16.5 K sv = 4.7
ev = 9.3 K sv = 0
0.003
0.002
0.001
0
Vacancy Concentration
0.3
0.5
0.7
0.9
1.1
1.3
1.5
1.7
Temperature (K)

used to determine the low temperature x-ray molar volume for crystal 29 which is listed in Table 4.

16. Crystal 30

The data on crystal 30 are shown in Fig. 50. It is interesting that each of the strange features noticed in the crystal 29 data is repeated here. The anomaly near 0.74 K occurs after a 11 hour anneal. Phase separation was studied in more detail than with crystal 29. Here the intensity increase on phase separation was about 30%. There are no useful vacancy data for this crystal.

Figure 50. Crystal 30 lattice parameter measurements. All the data were obtained on cooling after the one absolute lattice parameter measurement (x). The error bar corresponds to 300 ppm in lattice parameter. There are no useful warming data.

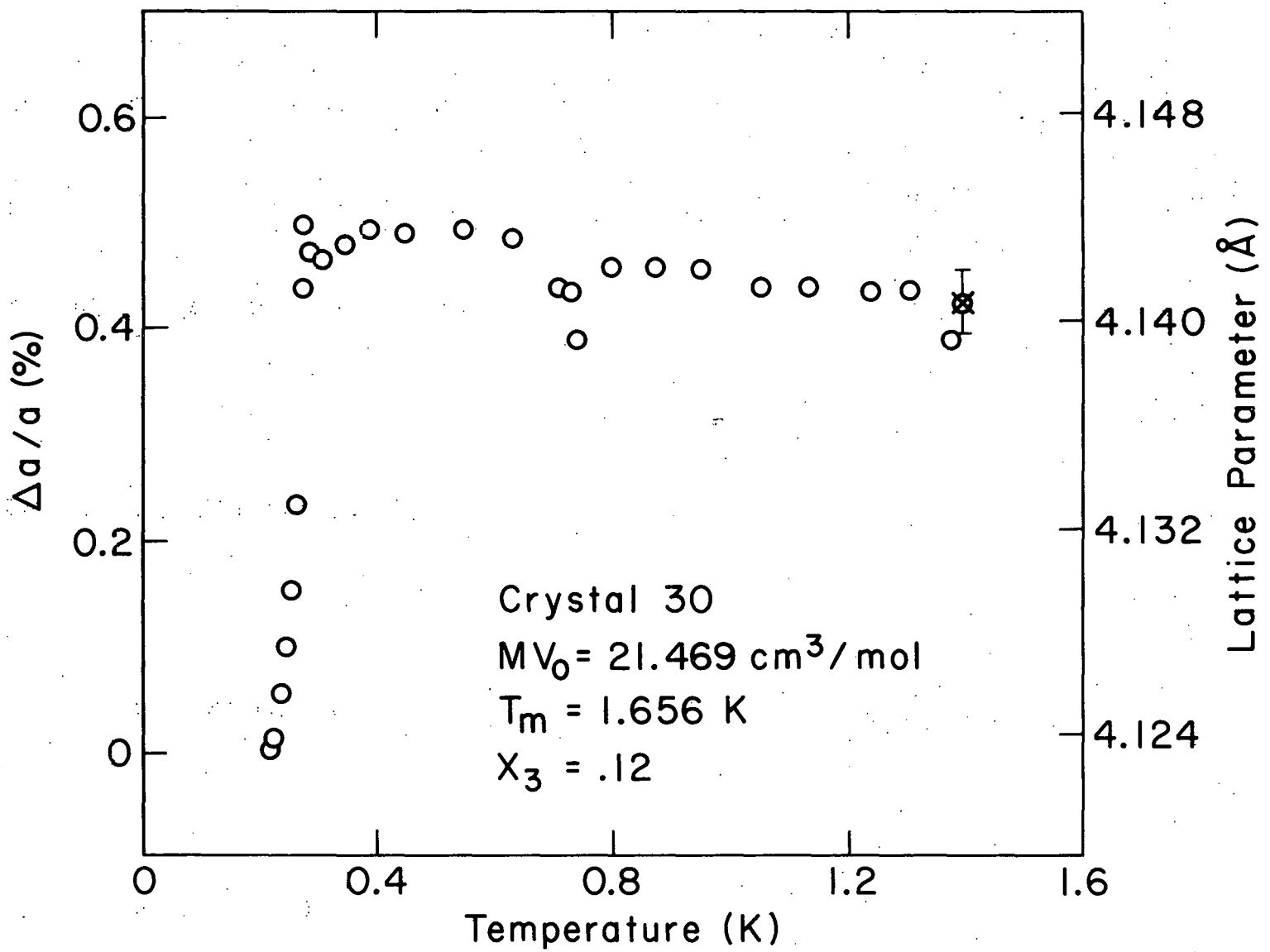
0.6
0.4
0.2
0
Δa/a (%)
4.148
4.140
4.132
4.124
Lattice Parameter (Å)
0
0.4
0.8
1.2
1.6
Temperature (K)
Crystal 30
MV0 = 21.469 cm3/mol
Tm = 1.656 K
X3 = .12

V. ANALYSIS

A. Vacancies

1. General Results

The results of two exponential fits to the vacancy data have been summarized in Table 5. Equation II-25 is used for both fits, but s_v, the apparent formation entropy of the vacancy, is held equal to zero in one. Inspection of the various figures in Chapter IV shows clearly that the $s_v=0$ fit is a poor parameterization of the data in almost each case. However, this fit is very useful, as it allows straightforward comparison of the present results to previous work. None of the previous studies of vacancies in solid helium[12-20,27,62,104] have been able to determine both the formation energy e_v and the formation entropy s_v. Determination of s_v in NMR experiments is difficult because the non-temperature-dependent factor e^{s_v} is buried in a pre-exponential factor which is very model dependent.[19] The entropy s_v is also difficult to obtain from heat capacity measurements. As described in Chapter II, the vacancy contribution to the experimental heat capacity can be obtained by subtracting an estimate of the "normal lattice" heat capacity from the experimental result. The vacancy contributions to the heat capacity are very sensitive to the form taken for the "normal lattice" contribution. This sensitivity makes estimation of anything more than an activation energy very difficult.

Each vacancy formation energy e_v (obtained from the $s_v=0$ fit to the present vacancy measurements) is divided by the respective melting

temperature T_m, and plotted versus molar volume in Fig. 51. The molar volumes are those obtained from PVT measurements (MV_{PVT} in Table 4), because all other workers have used PVT molar volumes for classification of their results. The only published vacancy activation energies for concentrated bcc mixtures have been obtained from NMR experiments. Miyoshi, et al.[27] have made T_1, T_2, and diffusion measurements on mixtures with ^{3}He concentration x_3=0.321, 0.0778, and 0.0194, respectively. Spin diffusion measurements have been done by Grigor'ev, et al.[29] in mixtures with x_3=0.063, 0.0217, and 0.0075, respectively. Most NMR measurements in dilute mixtures concentrate on the low temperature region,[105] where there is much discussion of excitations such as mass fluctuation waves.[106] There are, however, spin diffusion activation energy measurements by Allen and Richards[107] in hcp samples with a ^{3}He concentration $x_3=5\times10^{-4}$. Only data for $x_3>0.06$ are shown in Fig. 51 for reasons of clarity. For comparison, x-ray,[20] NMR,[18,19] and heat capacity[13] results for pure ^{3}He are also shown.

There are three basic points of interest in Fig. 51. First, it appears that below about 20.5 cm^3/mol, the ratios of the vacancy activation energy to T_m in the bcc phase (ϕ/T_m) seem to agree, regardless of isotopic content or experimental technique used. At molar volumes larger than 20.5 cm^3/mol, this is no longer true. ϕ/T_m is much smaller for the concentrated mixtures than for pure ^{3}He. This means that there are a large number of vacancies present. It appears that the large vacancy concentrations seen in the present work have also been seen in the NMR work of Miyoshi, et al.,[27] and Grigor'ev, et al.[29] The possible errors associated with the activation energy determinations in the work of Miyoshi, et al. and Grigor'ev, et al., are as large as 15% of the ϕ/T_m ratio, and could explain the differences

Figure 51. Summary of vacancy activation energies. The activation energy associated with vacancies, divided by the melting temperature T_m, is plotted versus MV_{PVT} for pure ^3He, ^4He, and mixtures. The x-ray activation energies e_v are the results of the s_v=0 fits that are listed in Table 5. Identification of the symbols is given below:

Symbol	x_3	Method	Author	Reference
●	1.0	x-ray	Heald	20
○	1.0	NMR	Sullivan, *et al.*	19
□	1.0	C_v	Greywall	13
+	1.0	NMR	Reich	18
⬢	0.99	x-ray	present	present
◆	0.51	"	"	"
▲	0.28	"	"	"
▼	0.12	"	"	"
■	0	"	"	"
△	0.321	NMR	Miyoshi, *et al.*	27
▽	0.078	"	"	"
◇	0.063	"	Grigor'ev, *et al.*	29

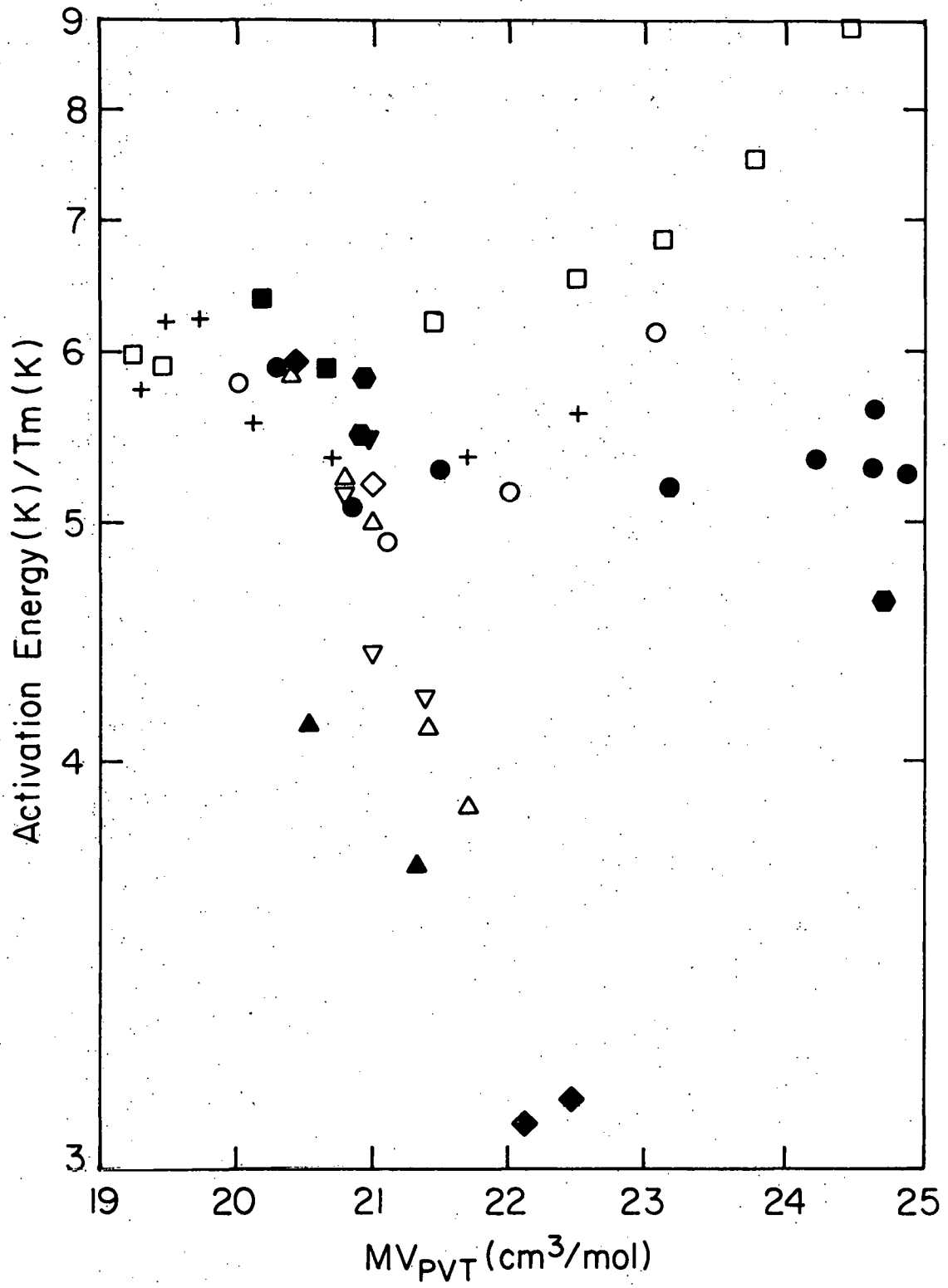
9
8
7
6
5
4
3
Activation Energy (K) / Tm (K)
19
20
21
22
23
24
25
MV$_{PVT}$ (cm^3/mol)

between the various measurements which are seen in Fig. 51. It is interesting to note that while the ϕ/T_m determinations of Allen and Richards[107] for molar volumes between 20.2 and 20.8 cm^3/mol agree very well with the present x-ray results for pure ^4He, their result at 20.95 cm^3/mol is $\phi/T_m=4.2$. This agrees well with the mixture results and not with the pure ^4He results. This is especially surprising because the Allen and Richards data were apparently all taken in the hcp phase. All the pure ^3He hcp phase NMR activation energies are much larger than the activation energy determined with x-rays.[20] Finally, the lowest concentration data from the NMR experiments ($x_3=0.0194$ for Miyoshi, et al.,[27] and 0.0075 for Grigor'ev, et al.[29]) result in somewhat larger ϕ/T_m ratios than expected from Fig. 51. This is difficult to understand since the Grigor'ev, et al. result for $x_3=0.0217$ and the Allen and Richards result at $x_3=0.0005$ both seem to agree with the general trend of the more concentrated mixtures.

Figure 51 highlights one more interesting result. At high molar volume (21 cm^3/mol), the heat capacity[13] and x-ray[20] ϕ/T_m determinations disagree. The measurements on the 99% ^3He mixture in this work were in part done to confirm the previous x-ray results of Heald.[20] Inspection of Fig. 51 shows that the results of Heald have been confirmed both at low and high molar volumes. Unfortunately, there are no NMR data in pure ^3He at larger molar volumes to assist in the understanding of this disagreement. It is interesting to note that the disagreement between the heat capacity and x-ray results for pure ^3He begins at about the same molar volume at which the mixture results start deviating from pure substance values.

The results of the present vacancy measurements are displayed in Fig. 52. The free energy of formation of the vacancy, $f_v=e_v-Ts_v$, is plotted

Figure 52. Temperature dependence of $f_v(T)$ determined in this work. $f_v(T)=e_v-Ts_v$ is plotted versus temperature T, where e_v and s_v are taken from the fits to the vacancy data (from Table 5). The solid lines extend over the temperature interval in which the data were taken for each particular crystal. The short-dashed line is an extrapolation of the solid line to the observed melting temperature. The long-dashed line is a guide to the eye: note that $f_v(T_m)$ for all the crystals (except the 28% mixtures, crystals 27 and 28) lies approximately on the long-dashed line. Plots are identified by crystal number:

Crystal	P_m(MPa)	MV_o(cm^3/mol)	x_3
0	3.710	20.206†	0
13	*	20.900	0
14	3.137	20.638	0
16	3.061	24.867	0.99
17	7.853	21.000	0.99
19	7.812	21.046	0.99
23	6.178	20.945	0.51
24	3.220	23.443	0.51
26	3.565	23.306	0.51
27	4.681	21.478	0.28
28	3.475	22.327	0.28
29	3.240	21.246	0.12

w signifies warming, and c means cooling. *See discussion of crystal 13 for its melting pressure P_m. †MV_{PVT}.

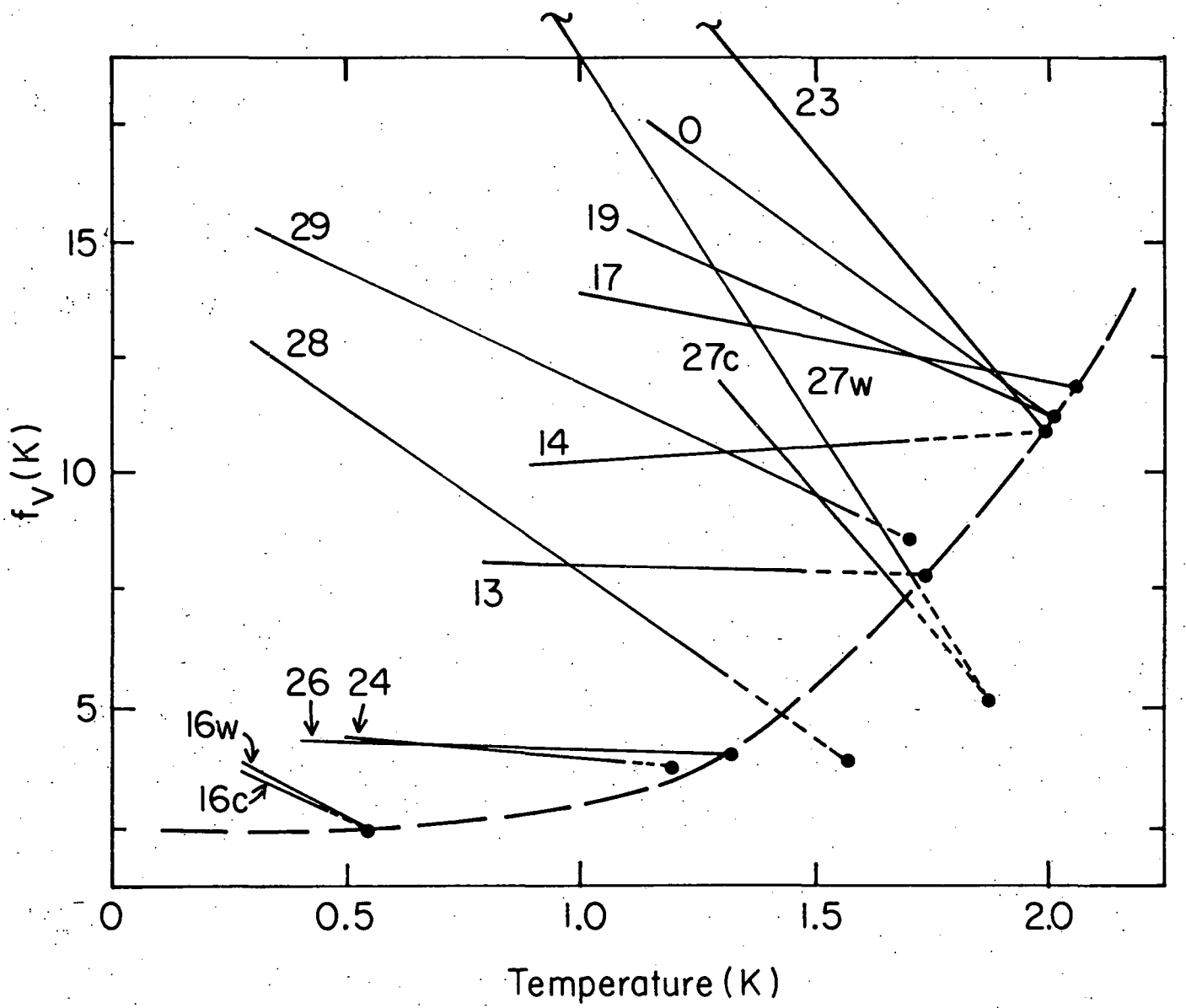
23
0
29
19
17
28
27c
27w
14
13
26
24
16w
16c
15
10
5
0
0.5
1.0
1.5
2.0
f_v(K)
Temperature (K)

versus temperature. The results of the two parameter exponential fit of the data to Eq. II-25 are used, since this is clearly a much better parameterization of the data than the simple one parameter fit discussed above. The free energy f_v is plotted over the temperature range in which data were taken on each particular crystal. f_v is extrapolated to the melting temperature T_m. The low temperature ends of the lines are more uncertain than the high temperature ends, because the vacancy concentration, and hence f_v, are easy to measure at high temperatures since there are many vacancies.

There is one main point of interest in Fig. 52. Qualitative inspection of the figure shows that nearly all the free energy of formation at melting $[f_v(T_m)]$ values fall on the same curve, regardless of mixture concentration. This means that $f_v(T_m)$ is not in general a function of ^{3}He concentration or of molar volume, but is a function only of melting temperature T_m. This conclusion is easily demonstrated for the crystals with $T_m \sim 2.0$ K. In the present study, five crystals were grown with melting temperatures of about 2.0 K. For these crystals, x_3 varied from 0.99 to 0, and the molar volume (MV_o) varied from 20 to 21 cm^3/mol, with basically the same result for $f_v(T_m)$ in each case. This lack of dependence on molar volume, at least, is surprising. It has been generally thought that most properties of solid helium could be explained solely with volume effects.[108,109]

Both crystals (27 and 28) with x_3=0.28 disagree with the trend which is discussed above. The warming and cooling runs for crystal 27 are both shown. Although e_v and s_v for each of these two runs are different, the extrapolation of each line to the melting temperature results in the

same value of $f_v(T_m)$ for each. This value is much lower than the general curve would predict. The other 28% crystal also is in disagreement with the curve. A satisfactory explanation of the disagreement is unlikely as long as the origins of the curve from which the deviations are measured is unclear. One possible hypothesis is that there might be a binding energy between vacancies and ^{3}He atoms in the mostly ^{4}He crystal. This and other complications in the further analysis of the vacancy data are discussed below.

2. Vacancy Entropy of Formation

Although fits to the vacancy data have been made using Eq. II-25, with s_v (the vacancy formation entropy) allowed to vary, to this point the fitted value of s_v has been treated as a parameterization of the data. Knowledge of the actual value of s_v is important because its value can change the vacancy concentration inferred indirectly by other experimental methods. Reference to Table 5 or Fig. 52 shows that nearly all the s_v's determined in this work are positive, and in many cases large. This does not mean that the actual entropy of formation for monovacancies is large and positive. Other important effects, such as vacancy-vacancy binding, vacancy-solute binding (in mixtures), long- and short-range ordering (in mixtures), and vacancy delocalization, can be expected to contribute to the apparent entropy s_v. In the present work, it is clear that the temperature range in which the data are taken affects the fitted values of s_v. For example, the two crystals which have fitted s_v's which are less than zero, 13 and 14, both had anomalies at high temperature so that the vacancy data stop at temperatures 0.3 deg below T_m. The fitted entropies

of these two crystals are therefore rather uncertain due to the lack of high temperature data.

The monovacancy non-configurational entropy has been calculated for normal solids. A typical result (for copper) is an entropy of about +1.5.[110] This result can be compared to the vacancy formation entropy found experimentally for gold (s_p=+1.0)[111] and for solid krypton (s_p = +2.0),[112] where s_p is the entropy of formation at constant pressure. This positive entropy is expected on general grounds in the constant pressure case. If the crystal is treated as a collection of harmonic oscillators, then it is easily seen[110] that the entropy due to a vacancy is just due to the change in phonon frequencies. We have $s = \sum_j \ln(\nu_{ji}/\nu_{jf})$, where ν_{ji} and ν_{jf} are the frequencies of the jth phonon before and after the vacancy is put into the lattice. Because the vacancy allows local expansion of the lattice, the frequencies should drop when the vacancy is considered, thus making s>0.

Application of this argument to solid helium at constant volume is not straightforward. For example, vacancy creation at constant volume causes local compression of the lattice, which should increase the frequencies, and decrease the entropy. The vacancy formation entropy in solid helium has been discussed by Hetherington,[113] Widom, Sokoloff, and Sacco,[114] and Sullivan, et al.[19] The conclusions of Hetherington's general considerations are that a large ($s_v \sim 1$) entropy cannot be ruled out. $s_v \sim 1$ would mean that the vacancy is easily deformed with low-lying excited states, or that it has a degenerate ground state. A zero or negative entropy would mean that there was a single vacancy state. Widom, et al.[114] predict an appreciable negative entropy. The many inconsistencies in their assumptions

and analysis, however, make this prediction questionable. The conclusion of Sullivan, et al.[19] is that the entropy is negligibly small. They believe that the contribution to the entropy from phonons is small because k_BT is always small compared to the phonon frequencies. The only other contribution possible, they claim, is the entropy associated with a lattice relaxation with less symmetry than the perfect lattice. This is unlikely since the energy required is larger than that for a cubic relaxation.

In light of the present data, and the theoretical considerations mentioned above, two usually implicit assumptions concerning the entropy of formation s_v must be questioned. The first assumption is that s_v is temperature independent. Although a temperature independent s_v is in most cases consistent with the present measurements, the complexity of the factors contributing to the vacancy concentrations does not rule out temperature dependence. The second assumption is less quantitative, but is basically the assumption that there exists one "vacancy entropy of formation for helium." It is clear from the present data that there are major differences in s_v which depend on pressure, molar volume, crystalline structure, or isotopic constitution. One definite conclusion that it is possible to make is that many large contributions to the vacancy concentration temperature dependence will have to come from vacancy binding energies and similar sources if the entropy of formation is to be negative.

3. Vacancy Binding Effects

In the present measurements, vacancy-vacancy binding must be considered. In metals such as aluminum, in which the vacancy concentration at melting is only 9×10^{-4},[25] divacancies are believed to be important. We have studied here crystals with vacancy concentrations of more than 4%

at melting. This large number of vacancies means that at least 30% of the vacancies have another vacancy as a near neighbor. A large divacancy binding energy $e_b^{(2)}$ could enhance the large number of vacant sites already present in the crystal.

A definite upper limit of the effect of divacancies on the present measurements can be found by setting the divacancy binding energy $e_b^{(2)}$ equal to the monovacancy formation free energy f_v. Equation II-41 then gives the concentration of vacant lattice sites:

$$x_v^{tot} = e^{-f_v/T} + 8\left(e^{-f_v/T}\right)^2 e^{e_b^{(2)}/T} = x_v^{(1)}\left[1+8x_v^{(1)} e^{e_b^{(2)}/T}\right] . \quad \text{(V-1)}$$

Since the binding energy is equal to the monovacancy formation energy, we have $x_v^{tot}=9x_v^{(1)}$, which is simply equivalent to an increase in the fitted entropy of formation s_v of $\ln(9)=2.2$. A large divacancy binding energy (and by analogy binding energies of larger vacancy clusters) therefore contributes to the apparent s_v obtained from the vacancy data fits. Two final points are clear: (1) even this upper limit does not explain the large values of s_v obtained for many of the crystals, and (2) smaller binding energies, and their contribution to the temperature dependence of the measured x_v, can be part of the fitted values of s_v that have been obtained in the present work.

Bound states of vacancies and solute atoms in mixtures are another possibility that may contribute to the formation energy and entropy for the vacancies in helium mixtures. The general reasoning behind this possibility is described in Section II-B-3. Also in that section the general expression is given for the free energy which is minimized to find the effect of the binding on the vacancy formation energy and entropy. (See Equations

II-42 to II-47). This expression is very complicated for the present case in which both the solute concentration x_3 and the vacancy concentration x_v are too large to allow valid approximations. The dilute mixture limit of this expression, which is given in Eq. II-48, is clearly inapplicable here.

Binding energies have been calculated for the vacancy-^{3}He bound state in almost pure ^{4}He by Locke and Young.[56] The result is an energy of about 0.2 K. This calculation is for the dilute case, and so is not helpful in the present case. In general, one would expect the contribution of the vacancy-solute binding to the observed temperature dependence would be similar to that of the vacancy-vacancy binding. However, due to the large concentrations of solute atoms (^{3}He) in the present mixtures, further quantitative analysis seems inappropriate, because the multiplicative factors in front of the expected $e^{f_b/T}$ term are important and unknown.

A further complication of the situation in the mixtures is the possibility of long- or short-range ordering. It is dangerous to speak of one formation energy in an ordered alloy, because there are two (or more) kinds of vacancies, with their own formation energies, entropies, and lattice sites.[115] A possibility is that ordering will leave many vacant sites of one type (as much as 50% in TiC[116]). The possibility of ordering in the helium mixtures was considered after the fact, but there was no evidence in support of such a contention. All the Laue photographs were inspected for indications of superlattice spots, but none were seen. This is not surprising. One can only reasonably expect to see the possible superlattice lines by orienting the diffractometer and looking carefully in particular places in reciprocal space. This was not done.

Both vacancy-vacancy and vacancy-solute binding apparently cause an additional temperature dependence in the monovacancy concentration (i.e., the fitted s_v is larger). It is therefore interesting to examine the two high molar volume crystals with x_3=0.51 (crystals 24 and 26). The vacancy concentrations at melting are almost 5%, while the fitted values of s_v are very small when compared to the other data. This small s_v apparently disagrees with most of the above discussion. It does, however, agree very well with some results obtained by Mukherjee, Lieberman, and Read[117/] in vacancy measurements on a 50% alloy of gold-zinc. They found: (1) $x_v(T_m)\sim 0.6\%$, which is about ten times the vacancy concentration normally found in the pure substances, (2) an entropy of formation $s\sim 0.01$, which is very much smaller than that for the pure metals, (3) no x-ray evidence of a long-range order-disorder transition or of quenching strain, and (4) a relaxation volume similar to that of the pure substances. All four of these results agree with what was seen in the present 51% mixture measurements. The apparent lack of vacancy-vacancy and vacancy-solute binding, and lack of ordering in these approximately 50% mixtures is not understood.

4. Delocalization

The data on crystal 16 (x_3=0.99, MV_o=24.867 cm^3/mol) were taken in part to investigate some anomalous behavior seen by Heald[20/] in his measurements of pure ^3He at high molar volumes. In several crystals with molar volumes above 24.5 cm^3/mol, Heald saw the vacancy concentration first dip, and then rise sharply as the temperature was raised. The present measurements on crystal 16 confirm that behavior. Two points were taken at each temperature during the warming run shown in Fig. 31, with close agreement.

It is interesting to note that this kind of behavior is most pronounced in warming data, as is seen in this work, and that of Heald. A similar deviation of the vacancy concentration from the expected exponential temperature dependence can be seen by careful inspection of the heat capacity data of Greywall (see Fig. 19b in ref. 13).

The most detailed examination of the effects of vacancy delocalization and band structure on crystal properties, especially heat capacity, is due to Hetherington.[23/] In this work, Hetherington shows that the data of Greywall[13/] are consistent with a finite vacancy band width, but he does not address the vacancy concentration temperature dependence which is discussed here. An attempt was made to use the ideas discussed in Section II-B-4 to explain the crystal 16 temperature dependence, but it failed. The basic effect of Hetherington's approximation[24/] to the band structure is to effectively decrease the observed s_v obtained from the data. This is the opposite of the effect that is needed here.

The present crystal 16 data could be explained by a vacancy band structure with two bands. Since vacancies in ^{3}He are like holes in a metal, they are fermions and can be described by the Fermi distribution function. The two vacancy bands could be arranged so that as the Fermi distribution changes shape when the temperature is raised, the number of filled vacancy states in the bands decreases. At higher temperatures, the number of filled vacancy states would increase with increasing temperature. The large number of adjustable parameters present in such a theory make further study inappropriate here, since there is only one set of data available. When there are more data available, this theory should be investigated further. It is quite possible that the low energy band might

be associated with the existence of so-called zero-point vacancies, which were first suggested by Andreev and Lifshitz,[118] and have been discussed and invoked by many workers.[119]

5. Conclusions

The present vacancy concentration measurements lead to several general conclusions. Vacancy concentrations of almost 5% at melting have been measured in the nearly 50% mixtures of ^{3}He and ^{4}He. These large values of $x_v(T_m)$ are qualitatively confirmed by NMR measurements in concentrated mixtures. Progress has been made toward characterizing the detailed temperature dependence of the vacancy concentration. Large positive apparent vacancy entropies of formation have been found in most of the crystals measured. This addition to the temperature dependence of x_v due to the vacancy formation energy (e_v) comes from many sources, including (1) the actual entropy of formation, (2) vacancy aggregates, such as divacancies, (3) vacancy-solute binding in the mixtures, (4) possible ordering, and (5) delocalization effects.

The qualitative differences observed in the near zero s_v values obtained for the 51% mixture (especially crystals 24 and 26), and the large s_v's obtained in the 28% mixtures (crystals 27 and 28) lead to speculations on the cause of these differences. The large s_v seen in the 28% mixtures suggests that vacancy-^{3}He binding might be important. This is backed up by the deviation of the 28% mixture $x_v(T_m)$ values from the "universal" curve seen in Fig. 52. On the other hand, the very small s_v's obtained for crystals 24 and 26 suggest that most of the contributions mentioned above do not apply to the 51% mixture at low pressures. Since these contributions

are generally expected to be present, the possibility of some ordering in the 51% mixture is not excluded.

B. Molar Volumes and Vacancy Volumes of Formation

Table 4 shows a comparison of MV_o, the low temperature x-ray molar volume, with MV_{PVT}, which is the molar volume determined by comparison of the melting pressure P_m with the bulk molar volume measurements of Grilly.[4,5,8] The large differences between the two molar volume values clearly demonstrate the need for a more detailed examination of the measurements and their meaning.

The low temperature molar volume MV_o is obtained in the present work from the low temperature lattice parameter a_o and Avogadro's number (N_a=6.02252×10^{23}/mol),[120] using the equation

$$MV_o = N_a (a_o)^3 /2$$

for the bcc phase data, and a similar expression for the hcp phase (where c/a is assumed to be 1.633). The c/a ratio was experimentally checked on an hcp ^{4}He crystal with a molar volume of 19.2 cm^3/mol by measuring the lattice spacing d of several different reflections.[121] The results agreed with the assumed value. The low temperature lattice parameter a_o was either measured at a low enough temperature that there were no thermal vacancies present, or the measured value of a was corrected for the vacancy content using $\Delta a/a$ measurements. MV_o is therefore the molar volume of the real crystal, that is, MV_o gives directly the isochore along which this constant volume experiment is done.

The molar volume measured by Grilly along the melting line, MV_{PVT}, is also a measurement of the actual macroscopic volume of the crystal. We should therefore have $MV_o = MV_{PVT}$, if both measurements are made on the same isochore. As can be seen in Table 4, MV_o obtained here, and MV_{PVT} obtained from the melting pressure of the crystal and PVT data, do not agree. In fact, the percentage difference between the two determinations, $(MV_o - MV_{PVT})/MV_o$, approximately scales with the vacancy concentration at melting, $x_v(T_m)$. This phenomenon is not understood. The detailed interpretation of the melting molar volume measurements done by Grilly[4/] is difficult, suggesting that perhaps the reason for the present discrepancy lies in the present interpretation of the PVT data. It should be noted here that similar comparison between MV_{PVT} and MV_o for bcc ^4He, as discussed in Section 4, shows good agreement between MV_o and MV_{PVT}. The reason for this agreement, while all the other measurements disagree, is unclear.

The discussion above depends on the validity of the assumption that the sample cell volume does not change during the experiment. This assumption should be examined, since both thermal expansion of the cell, and expansion of the cell with pressure changes are possible. The temperature dependence of the cell is small: thermal expansion measurements[122/] of Lucite have shown that the volume coefficient of thermal expansion at 1.5 K is 2.4×10^{-8} K^{-1}, which is certainly small enough to ignore here. The effect of pressure on the cell must be considered in more detail.

The compressibility of the Lucite cell is about 1.3×10^{-5} MPa^{-1}.[20/] This is important because vacancy formation at constant volume causes an increase in the pressure of the crystal, and in the present work very large vacancy concentrations were found. The vacancy pressure of formation p_v is

given by Eq. II-33. The total pressure increase due to the changes in vacancy concentration x_v can be calculated using Eq. II-33 and x_v, v_p/v_a, and the compressibility $\chi_T(B_T=1/\chi_T)$. Using representative values of v_p/v_a from Table 7, the measured x_v, and the compressibility data of Straty and Adams[123] for ^{3}He and Jarvis, Ramm, and Meyer[124] for ^{4}He, the total pressure increase due to vacancy formation (ΔP) can be calculated. The results for the pure substances are $\Delta P \sim 0.1$ MPa, while in the mixtures, ΔP can be as large as 1.1 MPa (crystal 27). This large pressure increase causes expansion of the cell, so that the measured result $x_v(\text{meas}) = -3\Delta a/a$ underestimates the number of vacancies actually present. The correction is $x_v = x_v(\text{meas})[1+(\chi_{cell}/\chi_{He})(v_p/v_a)]$. This amounts to about 2% of $x_v(\text{meas})$. The correction can be treated simply as a small (+0.2) contribution to the fitted values of s_v. The correction is also too small to affect the MV_o-MV_{PVT} disagreement much. Therefore detailed corrections are not made to the data.

The large pressure differences calculated above have apparently been measured, although they were not attributed to vacancy formation at the time. Tedrow and Lee[30] have made a detailed study of the phase diagrams of solid helium mixtures. They have seen large pressure differences which apparently correspond to vacancy formation. Data they obtained on a 78% mixture is especially suggestive. Pressure differences between low temperature and T_m of about 0.9 MPa were seen. This compares well with the $\Delta P/=1.1$ MPa calculated for crystal 27 ($x_3=0.28$). The shape of their data is also suggestive. The pressure versus temperature plot of their 78% sample corresponds to an exponential (with a positive entropy term), as found here for the 28% mixtures. The final analogy between the two sets

TABLE 7.--Inferred vacancy volumes of formation. The ratio of the vacancy volume of formation v_p to an atomic volume v_a is listed as obtained by several methods: H-G, elastic theory; α, thermal expansion; χ, compressibility; $\Delta f_v/\Delta V$, volume dependence of x-ray f_v. Also listed are the ^3He concentration x_3 and MV_o. See text for details.

Crystal	x_3	MV_o (cm^3/mol)	v_p/v_a: H-G	α	χ	$\Delta f_v/\Delta V$
16	0.99	24.867	0.22	0.006	0.09	0.60
19	0.99	21.046	0.56	0.52	0.42	
17	0.99	21.000	0.59	0.67	0.49	
24	0.51	23.443	-	-	-	1.1
26	0.51	23.306	-	-	-	
23	0.51	20.945	-	-	-	
28	0.28	22.327	-	-	-	1.2
27	0.28	21.478	-	-	-	
29	0.12	21.246	-	-	-	-
13	0	20.900	1.18	0.29	0.30	1.25
14	0	20.638	1.31	0.51	0.52	1.4
0	0	20.21(PVT)	1.28	0.70	0.61	

of data is the qualitative agreement of the differences between warming and cooling runs.

Table 7 lists vacancy volumes of formation calculated by several methods. The results of compressibility and thermal expansion measurements, when combined with the present vacancy data, can be used in Eqs. II-37 and II-36, respectively, to obtain v_p/v_a. The compressibility and thermal expansion measurements of Straty and Adams[123/] in ^{3}He and of Jarvis, et al.,[124/] for ^{4}He are used. For both cases all of the temperature dependence of each property is attributed to the vacancies. The small derivative terms in Eqs. II-36 and II-37 are ignored. v_p has been calculated from the volume dependence of the vacancy free energy as displayed in Fig. 52, using Eqs. II-28 and II-33. $(\Delta f_v/\Delta V)_T$ is obtained graphically from the figure at the highest possible temperature at which the two crystals which are being compared were measured. The final method of determination is the use of an elastic theory of Holder and Granato.[125/] They find that the defect volume is given by

$$v_p/g_p = G'/G - 1/B \quad , \qquad \text{(V-2)}$$

where g_p ($=f_v$, see Eq. II-30) is the Gibbs vacancy free energy of formation at constant pressure, G and G' are the shear elastic constant and its pressure derivative, respectively, and B is the bulk modulus. The elastic constant data were obtained from Wanner[126/] for ^{3}He, and from Franck and Wanner[127/] for ^{4}He.

The results of all these different calculations show some general trends, although the agreement is clearly not excellent. v_p/v_a generally decreases as the volume increases (pressure decreases). Two of the methods

show that v_p/v_a is larger in ^{4}He, although the χ and α determinations disagree with this tendency. The very low v_p/v_a obtained with the α and χ methods for crystal 16 are probably due only to the lack of adequate data in that region. Finally, it is interesting to note that nearly all the methods agree in low molar volume ^{3}He, while the agreement in ^{4}He is poorer. There do not appear to be any abnormal effects occurring in the mixtures.

Several conclusions can be made on the basis of the analyses found in this section. First, the difference in molar volume found by this work and that found in the bulk measurements of Grilly is unexplained, but possibly related to the vacancy concentration. The volumes of formation calculated using thermodynamic relations are in qualitative agreement, although much work needs to be done here. The large number of vacancies, especially in the mixtures, causes pressure changes of up to 1 MPa. The pressure changes have apparently been measured, although mistakenly identified at the time. The pressure changes cause expansion of the sample cell used in the present work, but this effect does not affect the vacancy measurements enough to merit correction.

C. Phase Separation

1. Experimental Results

The first detailed study of the phase separation in solid helium was made by Edwards, McWilliams, and Daunt in 1962.[35] They displayed their measured phase separation temperatures (T_{ps}) in a plot of T_{ps} versus x_3 at a pressure of 3.63 MPa (where most of their measurements were made). Since that time, it has been traditional[36,39,40] to use the same type of

plot for comparison of different sets of data. Therefore, in Fig. 53 phase separation temperatures (T_{ps}) are shown for several sets of data, including those of the present work. All of the data shown have been corrected to P=3.63 MPa with the pressure dependence of T_{ps} which has been determined in the present work. The actual values of T_{ps} obtained in the present work are listed in Table 6.

To find the pressure dependence of T_{ps}, Eq. II-16 has been used to obtain a value of T_c for each measured T_{ps}. In regular solution theory, T_c is a function of pressure (or volume). The values of T_c obtained from the present work are listed in Table 8, along with the value of T_c (determined by Edwards, et al.[35]) which has generally been used to describe the expected regular solution behavior of the helium mixtures. dT_c/dP has been obtained by a simple linear fit of the present T_c's to the equation $T_c=AP_m+B$, where P_m is the melting pressure, because the pressure at phase separation is not known in the present experiment (or in that of Edwards, et al.). The result for the present data, excluding crystals 29 and 30 because of their anomalous behavior, is $A = dT_c/dP = -34$ mdeg/MPa. Deviations from the linear fit that are listed in Table 8 are well within the probable error of the T_{ps} determinations, and show that $T_c(P)$ is remarkably linear over the pressure range from 3.2 to 6.2 MPa.

The value of dT_c/dP obtained in the present work can be compared to three other determinations. Panczyk, et al.,[36] obtain values of dT_c/dP which range from -15 to -28 mdeg/MPa. These results are calculated from their dP/dT data which were obtained over a wide concentration range and a small (2.9 to 3.9 MPa) pressure range. Arnold and Pipes[39] have recently obtained $dT_c/dP = -46$ mdeg/MPa from their dP/dT data. The pressure range

Figure 53. T_{ps} versus x_3. The phase separation temperature T_{ps} is plotted versus the ^3He concentration x_3. The present results, the heat capacity results of Edwards, et al.,[35] dP/dT data of Panczyk, et al.,[36] dP/dT results of Arnold and Pipes,[39] and the thermal conductivity determination of Burgess and Crooks[128] are shown. All the data are corrected to a pressure of 3.63 MPa as described in the text. The curve is the regular solution curve (Eq. II-16), with T_c determined from the present data. The x-ray data on warming are presented to show the unsuitability of warming measurements. The error bars on the warming points simply show how widely spaced in temperature the data points are.

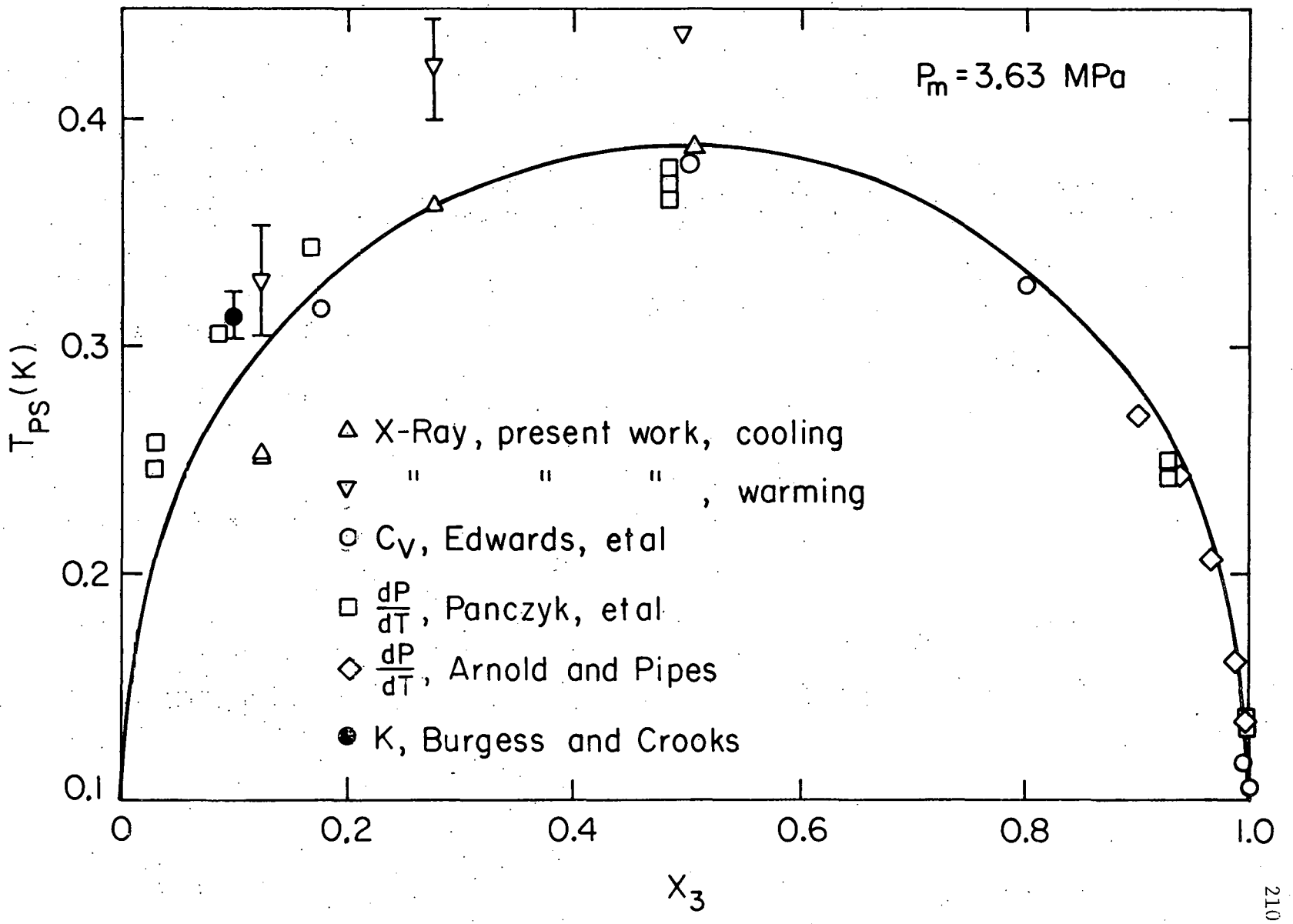
P_m = 3.63 MPa
T_{PS} (K)
0.1
0.2
0.3
0.4
0
0.2
0.4
0.6
0.8
1.0
X_3
X-Ray, present work, cooling
" " " , warming
C_V, Edwards, et al
$\frac{dP}{dT}$, Panczyk, et al
$\frac{dP}{dT}$, Arnold and Pipes
K, Burgess and Crooks

TABLE 8.--Values of T_c obtained from Equation II-16 with the present results are compared to the determination of Edwards, et al.[35] Deviations from a simple linear fit to the pressure dependence of T_c are also listed, along with the melting pressure P_m. Crystal 30 is excluded from the fit.

Crystal	P_m(MPa)	T_c(K)	Deviation (mdeg)	Source
23	6.178	0.299	-1.5	present work
27	4.681	0.354	+3.0	"
26	3.565	0.388	-1.3	"
28	3.475	0.394	+1.8	"
24	3.220	0.399	-2.0	"
30	3.041	0.346	-60.8	"
-	3.63	0.378	+9.8	Edwards, et al.

of their measurements was larger (3.1 to 4.3 MPa), but only concentrations greater than 0.9 were studied. dT_c/dP has been calculated by Trickey, et al.[11] from the $x_3 > 0.99$ data of Henriksen, et al.[37] They find dT_c/dP approaches zero at pressures above 5 MPa. The present determination of dT_c/dP is believed to be the most accurate because the pressure range studied was much larger than in the other studies, and the study was done in concentrated mixtures, where T_c is most nearly equal to T_{ps}.

The derivative dT_c/dP is related to the excess volume v^E by Eq. II-19 (in regular solution theory). The present determination of dT_c/dP therefore confirms two predictions made by Mullin in his microscopic calculation of phase separation effects.[40] His prediction that v^E is independent of pressure is confirmed by the constant dT_c/dP found here. Numerically, $v^E = x(1-x)c$, where Mullin found $c = -0.4$ cm^3/mol, and the present data show that

c = -0.57 cm^3/mol. The general agreement of Mullin's result with the present one is good. The effect of the difference in c on the molar volumes of the mixtures is fairly small: about 0.05 cm^3/mol for a 50% mixture. The effect of this change of MV_{PVT} on the difference between MV_o and MV_{PVT} will not be large enough to qualitatively change the discrepancy, so the values of MV_{PVT} have not been changed.

A detailed discussion of the T_{ps} results which are plotted in Fig. 53 is useful. The present data for the 51% and 28% mixtures fall right on the regular solution curve (Eq. II-16) which was determined using the present values of T_c. The disagreement of the 12% mixture with the curve is not understood. It is interesting to note that the behavior of the x-ray peaks at T_{ps} was qualitatively different at this concentration. Instead of a degeneration of the peak shape at T_{ps}, the intensity increased by more than 30%. It is possible that the T_{ps} disagreement with the regular solution curve and the intensity increases at T_{ps} are due to the proximity of the hcp-bcc mixed phase.

In general, the agreement of different experiments with each other and with the curve in Fig. 53 is good for $x_3 > 0.4$. At these higher concentrations, it is believed that the disagreements are generally explained by experimental errors in the T_{ps} determinations and differences in temperature scales. The corrections to P=3.63 MPa are somewhat uncertain, because the melting pressures are not clearly mentioned in the published reports. The disagreements at low x_3 must be further discussed.

There are several points to be made. First, the pressures given by Panczyk, et al.,[36/] that were used to correct their data to 3.63 MPa are pressures immediately above T_{ps}, not the melting pressures. If the

large pressure changes (due to vacancies) which were discussed in the previous section are invoked, then the melting pressures for the samples of Panczyk, et al., are much higher than their quoted pressures. This would make a positive temperature correction which should be added to the values displayed on this figure. The correction could amount to 30 mdeg for a 1 MPa pressure difference. The Panczyk, et al., data should therefore probably be even further from the regular solution curve than they are.

Second, most of the Panczyk, et al., data were taken on warming, by finding the inflection point in the pressure versus temperature plot.[36/] The present data clearly show that data obtained on warming in the phase separation region are unreliable. Shown in Fig. 53 are T_{ps}'s obtained from the inflection points of the present x-ray measurements on warming. The lattice parameter recovers very slowly after phase separation, although it does go through an inflection point (see Figs. 35, 38, 44, 47, 48). This method of identifying T_{ps} is analogous to that used by Panczyk, et al. The results obtained in this way are incorrect and uncertain, and appear to agree with the Panczyk, et al., and Burgess and Crooks[128/] data. This lack of consistency, and non-equilibrium-type behavior were also noted by Greenberg, Thomlinson, and Richardson[38/] in their NMR work on mixtures with x_3=0.01 and 0.02. They found temperature hysteresis of as much as 0.08 deg. They also noticed non-reproducible behavior after remixing similar to that seen in the present work.

The shape of the T_{ps} versus x_3 curve has been calculated for helium by Mullin,[40/] as discussed in Section II-A-2. He predicts an asymmetric curve which is higher on the small x_3 side. The present data are not in agreement with that prediction, although the anomalous behavior at 12% makes

this statement qualitative rather than quantitative. The above discussion of the Panczyk, et al., results make their use in the discussion of the validity of Mullin's prediction questionable. Thus apparently more work is needed to decide the question of the asymmetry of the T_{ps} versus x_3 curve.

One useful bit of information that can be gleaned from the present data below T_{ps} is an approximate value for the dislocation density D in the crystal. Two estimates of D can be obtained from the mosaic width of the crystal (the width of the "sca" peak). The first estimate is an upper limit on D derived by Auleytner.[129] His result is that $D < (0.479\beta/b)^2$, where β is the full width of the crystal mosaic, and b is the Burgers vector. Using the experimental widths of 0.3 deg (crystal 30) to 0.8 deg (crystal 23), and b equal to the lattice parameter, one finds $D \sim 2\times10^9$ to 1×10^{10} cm^{-2}. If the substructure size t is known, then D can be determined from a formula given by Hirsch.[130] His result is that $D \sim \beta/3bt$. Burgess and Crooks[128] have estimated the domain size in helium below T_{ps} from their thermal conductivity data, and have obtained $t \sim 0.75$ μm. This is in basic agreement with an estimate by Greenberg, Thomlinson, and Richardson[38] due to their NMR work. Their result is $t \sim 2$ μm. Using the approximate result $t \sim 1$ μm in Hirsch's equation, and the same experimentally determined widths β, one obtains $D \sim 4\times10^8$ to 1×10^9 cm^{-2}. These results can be compared with the dislocation densities of 10^5 to 10^6 cm^{-2} which have previously been estimated in isotopically pure solid helium.[131]

2. Phase Diagram Speculations

Use of the T_{ps} versus x_3 data from Fig. 53 makes detailed analysis of the x-ray lattice parameter data which were obtained at temperatures

below T_{ps} worthwhile. The T_{ps}-x_3 curve determines the concentration of both the ^{3}He-rich and ^{4}He-rich components of the mixture at each particular temperature. The molar volume of each component (calculated from the observed lattice parameter) can therefore be plotted against the concentration of that component (inferred from the T_{ps}-x_3 curve and the temperature of the lattice parameter measurement). Therefore, from the lattice parameter versus temperature data taken below phase separation on one mixture, one obtains the molar volume of each component everywhere along the concentration axis. If the pressure is known, these measurements yield P, V, T, and phase information for both phase separated components of the mixture.

The basic purpose of the following discussion is twofold: to understand the present data qualitatively, and to demonstrate that this technique is probably a very useful method of obtaining phase diagram information near the phase separation region. Several cautionary statements must be made. The pressure in the present work is unknown, and can be very different from the melting pressure since there are large vacancy concentrations in the mixture crystals. It is believed that most of the measurements were done at equilibrium, but in some cases this may not be completely assured. The concentrations used in this analysis were obtained from Equation II-16 (the regular solution curve), where the T_c used in the equation was obtained from Table 8. Therefore, it is assumed that the phase separation curve is always symmetrical. This is probably not true, especially at low temperatures (see Fig. 4, for example), where there are univariant lines caused by the meeting of a mixed phase region with the phase separation curve. This difficulty is apparent and useful in the present analysis.

The molar volume versus x_3 data, obtained by the method described above, are plotted in Fig. 54 for crystals 23, 24, 26, 27, 28 and 30. Fig. 55 shows the ratio of the x-ray peak intensity I to I_o, the total intensity at $T > T_{ps}$. I/I_o is plotted versus x_3 (obtained as in Fig. 54). The simplest way to describe the method with which phase diagram information is inferred from this figure is by example. The most straightforward example is the highest pressure crystal, #23 (0). (Plot symbols will be used along with crystal number to help avoid confusion. For simplicity in this discussion, 4 will signify ^{4}He-rich, and 3 will signify ^{3}He-rich, unless otherwise noted.) One can deduce that the 4 phase is totally hcp for this crystal, since no 4 peak was seen. The data on the 3 peak show that the 3 component is solely bcc at concentrations $x_3 > 0.771$, because the cooling data extrapolate to the correct pure ^{3}He molar volume for the presumed pressure of the crystal. The change in slope in the cooling data at $x_3 = 0.771$ is probably the transition from the mixed hcp-bcc phase to the solely bcc phase. This inference is supported by the anomaly in the peak intensity at $x_3 \sim 0.77$ in Fig. 55.

The line through the crystal 23 (0) data with $x_3 > 0.771$ is a linear fit to the data. The pure ^{3}He molar volume (MV_{extrap}) obtained from this extrapolation, and the pressure calculated from MV_{extrap} using PVT data (P_{extrap}) are listed in Table 9 for each crystal. Also shown is the molar volume (determined by P_m of the crystal) which should be compared to MV_{extrap}, the phase inferred from the extrapolation, and the kind of extrapolation that was done. P_{extrap} is expected to be near the pressure that the crystal is experiencing during the measurements now being discussed. This pressure differs from P_m because of the pressure drop associated with the destruction

Figure 54. Molar volume versus inferred concentration below T_{ps}. Molar volumes, calculated from the measured lattice parameters in each phase, are plotted against the concentration x_3 of each of the phase separated components. x_3 is calculated from the temperature as described in the text. The crystal number, melting pressure, and plot symbol for each crystal are shown in the figure. Filled in symbols were obtained on warming, open ones on cooling. A symbol with a circle around it signifies the molar volume and concentration at which phase separation first started for each crystal. The lines in the figure are extrapolations of the data which are described in the text. The molar volume (MV_{PVT}) for each melting pressure is shown as the appropriate symbol and an arrow, both outside the axes. Those for pure ^4He are on the left, while those on the right belong to pure ^3He. See text for detailed interpretation of the data presented here.

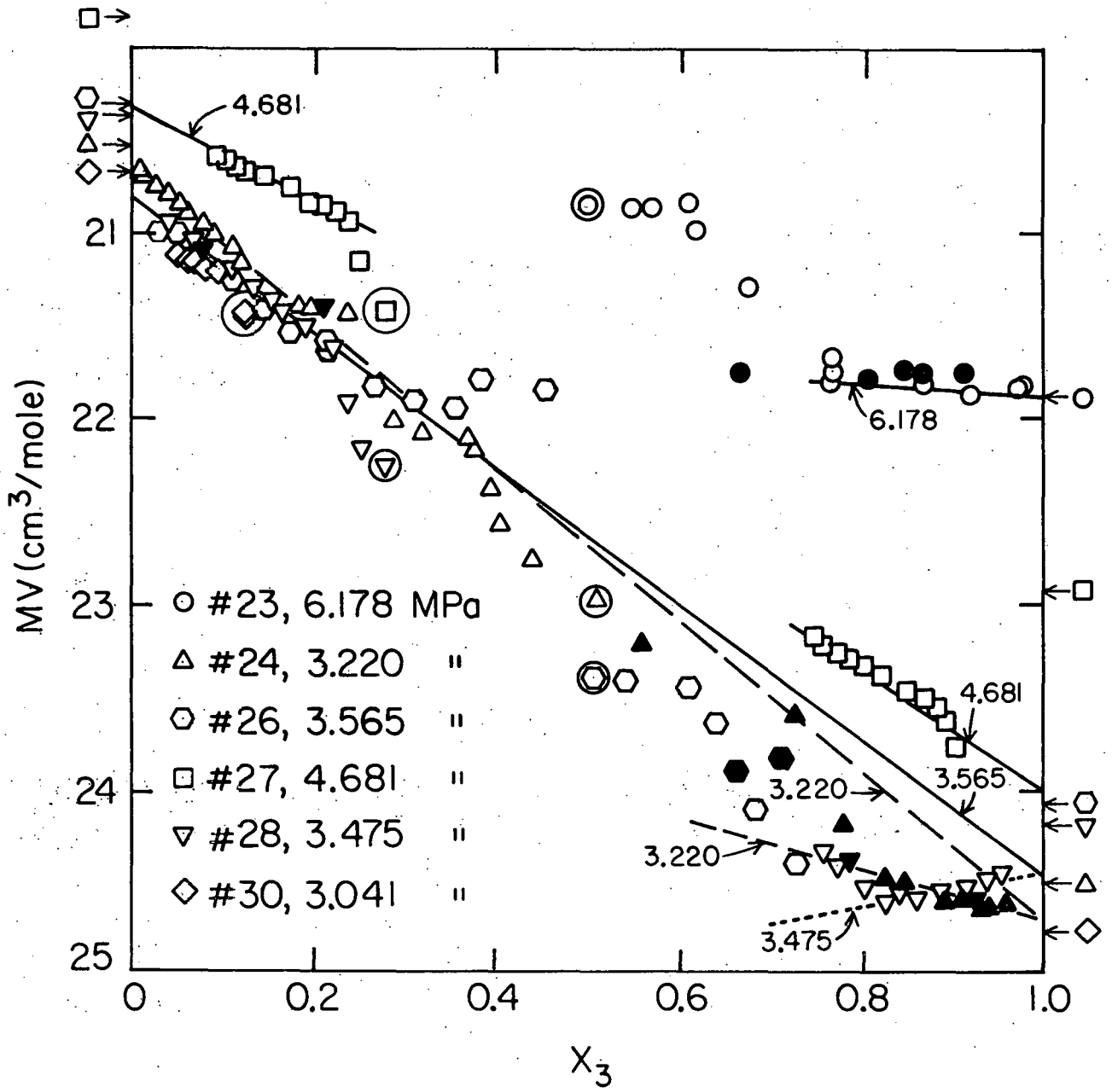
MV (cm³/mole)
21
22
23
24
25
0
0.2
0.4
0.6
0.8
1.0
X3
4.681
6.178
4.681
3.565
3.220
3.220
3.475
#23, 6.178 MPa
#24, 3.220 "
#26, 3.565 "
#27, 4.681 "
#28, 3.475 "
#30, 3.041 "

Figure 55. X-ray peak intensity versus x_3. The x-ray intensity I is plotted versus concentration x_3, which is determined as described in Fig. 54 and the text. I_o is the total intensity immediately above T_{ps}. Symbols are the same as those of Fig. 54. Open symbols are cooling data, solid symbols are warming data.

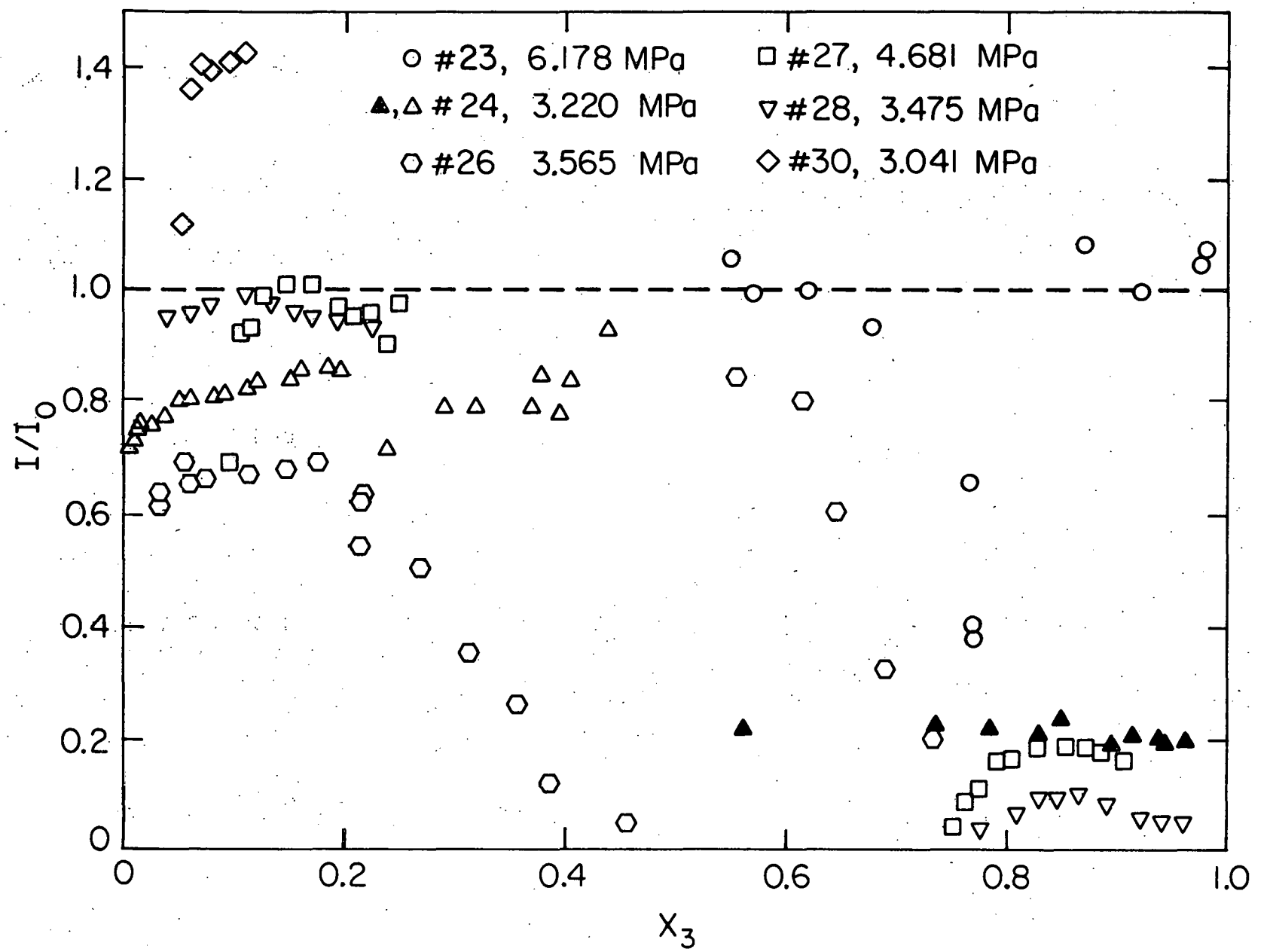
○ #23, 6.178 MPa
□ #27, 4.681 MPa
▲,△ #24, 3.220 MPa
▽ #28, 3.475 MPa
⬡ #26 3.565 MPa
◇ #30, 3.041 MPa
1.4
1.2
1.0
0.8
0.6
0.4
0.2
0
I/I_0
0
0.2
0.4
0.6
0.8
1.0
X_3

TABLE 9.--Phase diagram information obtained from x-ray data in the phase separated region. From 4 means extrapolated from the ^{4}He-rich phase and To 4 means extrapolated to the pure ^{4}He phase; 3 is analogous. All molar volumes (MV) are in cm^3/mol, and pressures (P) are in MPa. See text for further explanation. Plot symbols from Figs. 54 and 55 are also shown.

Crystal	P_m	From	To	MV(pure,P_m)	MV_{extrap}	P_{extrap}	Phase
23 ○	6.178	4	4	19.15	-	-	^{4}hcp
		3	3	21.88	21.88	6.18	^{3}bcc
27 □	4.681	4	4	19.86	20.37	3.43	^{4}bcc
		3	3	22.97	24.00	3.65	^{3}bcc
26 ⬡	3.505	4	4	20.29	20.86	3.01	^{4}bcc
		4	3	24.10	24.47	3.26	^{4}bcc-^{3}liq-^{3}bcc
28 ▽	3.475	4	4	20.35	20.77	∿3.0	^{4}bcc
		3	3	24.20	24.45	3.28	^{3}bcc-^{3}liq
24 △	3.220	4	4	20.51	20.66	∿3.0	^{4}bcc
		3	3	24.53	24.74	3.07	^{3}bcc-^{3}liq
		4	3	24.53	24.72	3.08	^{4}bcc-^{3}liq-^{3}bcc
30 ◇	3.040	4	4	20.63	20.98	2.83	^{4}bcc
		3	3	24.78	-	-	^{3}liq

of the vacancies as the crystal is cooled from high temperatures. From the various results of this analysis, the pressure, concentration, temperature, and molar volume of various transitions can be inferred. These speculations for the various crystals are listed in Table 10. It must be reiterated that these numbers are indicative of the possibilities of the method of analysis, but are not to be taken too seriously.

The analysis of the crystal 27(□) data is fairly clear cut. Both the 4 component and 3 component are bcc, since both x-ray peaks are visible (see Fig. 44). The 4 data stop at x_3=0.095 because the 4 component transforms to hcp. This conclusion is reinforced by the decrease in I/I_o of the 4 component as x_3 approaches 0.095 (see Fig. 55). Both 4 and 3 components extrapolate to a pressure of approximately 3.5 MPa. This is about 1.1 MPa lower than P_m, which is about the pressure change predicted by the vacancy concentration for this crystal, as discussed in Section B.

The lower pressure data (crystals 24, 26, 28, and 30) are more difficult to distinguish in Fig. 54 than the higher pressure data, because of their similarities. The main result of the data from crystals 24 (Δ), 26 (⬡), and 28 (∇) is the determination of the ^{4}bcc-^{3}bcc-^{3}liq univariant line. (As before, ^{4}bcc means that the ^{4}He-rich component is bcc.) The univariant is a horizontal line on the T-x_3 phase diagram, along which all three phases coexist. This conclusion is the result of two features of the data on the three crystals mentioned. First, at x_3=0.83 for both crystals 24 (▲) (warming data), and 28 (∇), there is a change in slope (see Fig. 54). As x_3 approaches 1.0, both crystals approach reasonable pure ^{3}He melting line values. The P_{extrap} obtained with crystal 24 (▲), 3.07 MPa, agrees with P_{extrap} obtained from the ^{4}He-rich peak of crystal 24 (Δ), 3.08 MPa. This

TABLE 10.--Phase boundaries derived from x-ray data in the phase separated region. P is the extrapolated pressure, x_3 and T the concentration and temperature, and MV the extrapolated molar volume. See text for cautionary notes. The numerical values are not to be taken literally.

Crystal	Phase Boundary	P(MPa)	x_3	T(K)	MV(cm^3/mol)
23 ○	^{3}hcp-^{3}bcc to ^{3}bcc	6.18	0.771	0.269	21.88
27 □	^{4}bcc to ^{4}hcp	3.55	0.095	0.255	20.37
26 ⬡	^{4}bcc-^{3}bcc-^{3}liq univariant	3.26	-	-	24.47
28 ▽	^{4}bcc-^{3}bcc to ^{4}bcc-^{3}bcc-^{3}liq	3.28	0.831	0.328	24.45
24 △	"	3.08	0.830	0.333	24.73 20.66
30 ◇	^{4}bcc to ^{4}hcp	2.83	0.052	0.214	20.98

agreement means that the bcc ^{4}He-rich peak must be in contact with both bcc ^{3}He, and liquid ^{3}He. These three phases can only coexist along a univariant line. The extrapolations of the ^{4}He-rich data of crystal 26 (⬡) and the ^{3}He-rich data of crystal 28 (∇) to pure ^{3}He show the same features as crystal 24 (Δ). The results of these extrapolations are shown in Table 9. The agreement of the different determinations of the position of the ^{4}bcc-^{3}bcc-^{3}liq univariant and the ^{4}bcc-^{3}bcc to ^{4}bcc-^{3}bcc-^{3}liq phase boundary in Table 10 reinforce the validity of these arguments.

The data obtained on crystal 30 (◇) also yield some interesting results. The data extend only from x_3=0.11 to 0.052. This lower limit is the hcp to bcc transition, as can clearly be seen in Fig. 55. The intensity of the peak is constant until about x_3=0.06, where it falls off dramatically. The fact that no ^{3}He-rich peak is observed implies that the ^{3}He is all liquid. The extrapolated pressure of 2.8 MPa is in agreement with that result. The one unexplained feature of the crystal 30 (◇) data is the increase of the peak intensity at phase separation. I/I_o is larger than 1.4. Perhaps the contact with the liquid which occurs below phase separation allows some annealing to take place. Crystal 30 (◇) was also apparently in the mixed hcp-bcc phase above phase separation, which may have caused difficulties in the crystal structure. A slight increase in I/I_o is seen in crystal 23 (○) after it makes the mixed to pure phase transition.

Aside from the explanation of all the bizarre behavior seen in Figs. 54 and 55, this analysis allows some general speculations about the low temperature mixture phase diagram to be made. Comparison of the inferred phase boundaries found in Table 10 with the phase diagram (P=3.0 MPa) of Tedrow and Lee[30/] (see Fig. 4) shows a basic incompatibility. Figure 4 shows that the mixed bcc-hcp phase meets the phase separation curve at a

higher temperature than that at which the mixed bcc-liq phase (at high x_3) meets the phase separation curve. This does not agree with the present inferences, which show the coexistence of ^{4}bcc-^{3}bcc-^{3}liq. A phase diagram which qualitatively agrees with the present data is shown in Fig. 56. It must be emphasized that this diagram is schematic only. The relationship of the two univariants shown in this picture, ^{4}bcc-^{3}bcc-^{3}liq and ^{4}bcc-^{4}hcp-^{3}liq, is reinforced by the fact that the ^{4}bcc and ^{3}bcc x-ray peaks existed to temperatures lower than those possible if Fig. 4 were correct. It should be noted once more that the data in the phase separation region of Fig. 4 are determinations of T_{ps} only, and have nothing to do with crystallographic transformations.

Three other comments about the schematic phase diagram in Fig. 56 should be made. First, the width of the two phase regions as they meet the phase separation curve is not determined. From the present work, it is suspected that the ^{4}bcc-^{4}hcp mixed phase width is very small, while the liquidus-solidus region due to the lower melting temperature of pure ^{3}He is probably wider, since the distortion of the MV versus x_3 picture (Fig. 54) is so much more obvious. Second, the reflexive behavior of the bcc-hcp mixed phase boundary can explain the crystal 27, 29, and 30 lattice parameter data which show anomalous changes apparently unrelated to vacancies (see Figs. 44,48,49 and 50). Finally, the width of the liquidus-solidus region at high temperatures has probably been exaggerated here. The single solidus data point in Fig. 4 is probably incorrect, since the pressure changes in that 78% sample of Tedrow and Lee[30/] are probably due to vacancies.

Other results in Table 10 seem reasonable also. The mixed hcp-bcc to pure bcc transition seen at 6.1 MPa in crystal 23 (○) agrees qualitatively with an "interpolation" between the published T-x_3 phase diagrams

Figure 56. Schematic T-x_3 phase diagram. This diagram has been drawn to illustrate the qualitative differences between the conclusions of Table 10 and the phase diagram drawn by Tedrow and Lee (see Fig. 4). The results on this diagram are not quantitative. A is the phase separation curve, which is assumed to be nearly regular. B is the ^{4}bcc-^{3}bcc-^{3}liq univariant, while C is the ^{4}hcp-^{4}bcc-^{3}liq univariant. This diagram illustrates that B probably occurs at a higher temperature than does C (and not vice versa, as shown in Fig. 4). The reflexive behavior of the bcc-hcp mixed phase is also shown.

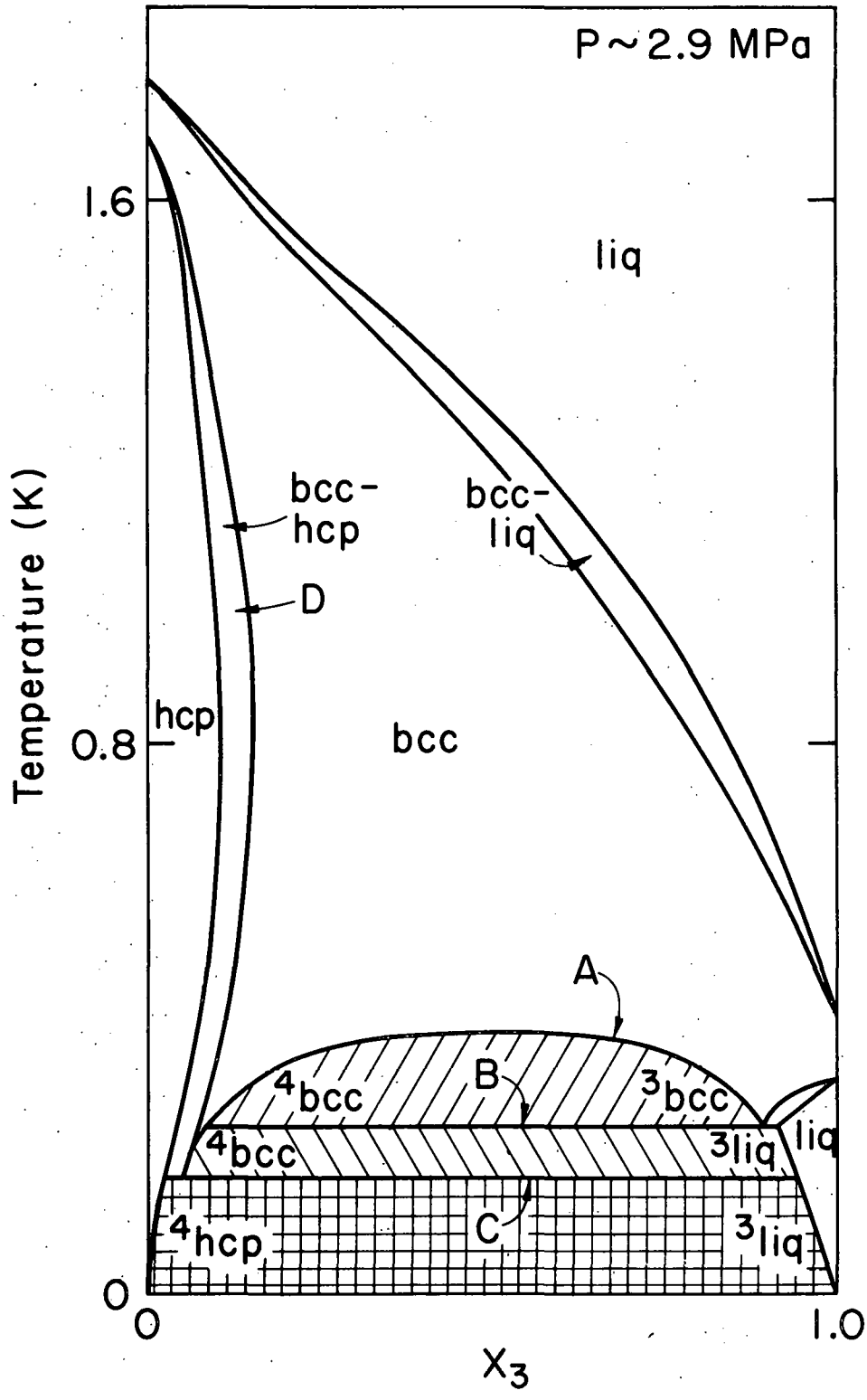
P ~ 2.9 MPa
1.6
0.8
0
Temperature (K)
liq
bcc-
hcp
bcc-
liq
D
hcp
bcc
A
B
4bcc
3bcc
4bcc
3liq
liq
4hcp
C
3liq
0
1.0
X3

at 4.7 MPa[32/] and 11.5 MPa.[31/] The hcp-bcc boundaries in these diagrams are apparently guesses by the authors, but are expected to be qualitatively correct. The qualitative agreement of the crystal 27 (□) conclusions with the published phase diagrams at 3.2 MPa[32/] and 4.5 MPa[31/] is also clear. The present conclusions certainly fulfill the present need for an explanation of the observed behavior. A more systematic investigation of this technique also seems in order to quantify the present speculations.

D. Bcc ^{4}He and Other Analysis

Discussion of the pure ^{4}He bcc phase data from crystal 13 is useful. As shown in Fig. 23, the present data show the crystal melted at 1.735 K, while the transition from bcc to mixed bcc-hcp occurred at 1.70 K. In this small temperature range the change in lattice parameter was $\Delta a/a \sim 1.3\times10^{-3}$, while the measured molar volume was about 20.79 cm^3/mol. These results give some useful information when compared with bulk PVT data, such as that of Hoffer, Gardner, Waterfield, and Phillips.[132/]

The molar volumes obtained by Hoffer, et al., are tied to the results of Grilly,[8/] and so the same discussion of MV_{PVT} versus MV_o that was applied to the Grilly PVT data in Section B applies to the work of Hoffer, et al. The molar volume (MV_{PVT}) can be determined for the present case from the observed melting temperature T_m and the bcc to mixed bcc-hcp phase transition temperature T_b. Using the data of Hoffer, et al., the present T_m=1.735 K implies that MV_{PVT}=20.903 cm^3/mol, while T_b=1.70 K gives MV_{PVT}=20.906 cm^3/mol. The agreement of the two molar volumes means that the transition temperatures were correctly identified.

Comparison of the MV_{PVT} values should now be made to the molar volumes obtained in the present work. Two numbers are important: MV_o, which

is obtained at low temperatures in the hcp phase, and MV_x(bcc), which is the x-ray molar volume obtained in the bcc phase. The same relationship between MV_o and MV_{PVT} as described in Section B should hold here also, even though a crystallographic transformation is involved. The only variable which is important in this argument is the volume of the isochore which is followed during this experiment. The bcc-hcp transformation causes a pressure change of only 0.28 MPa, which means that the cell expansion amounts to $\Delta V/V \sim 3.6\times10^{-4}$ (too small to affect the present discussion). The agreement of MV_o=20.900 cm^3/mol with the MV_{PVT} results of 20.90 cm^3/mol is surprisingly good. The discrepancy discussed in Section B does not seem to be present here. The molar volumes of Hoffer, et al.,[132/] are tied to those of Grilly,[8/] so that there is no simple difference apparent between this case and the other data discussed in Section B.

The difference between MV_o and MV_x(bcc) can also give the number of vacancies. The relation used is simply $x_v = -3\Delta a/a = -\Delta V/V$. Using MV_x(bcc)= 20.79 cm^3/mol, the vacancy concentration inferred is 5.3×10^{-3}. This implies $f_v(T_m)$ = 9.1 K. This vacancy concentration at melting agrees with that found by Heald[20/] for most of his pure ^{3}He crystals. The x-ray molar volume determinations thus seem reasonably consistent in the bcc ^{4}He case, so that the discrepancy between MV_o and MV_{PVT} in the other crystals is not understood.

The transition from bcc to hcp in ^{4}He is puzzling. The main point of interest is that the lattice parameters obtained on several different runs through the bcc to mixed transition agree with each other. This reproducibility is surprising because the lattice parameters obtained at the hcp to mixed phase transition on different runs disagree dramatically. The fact that a good quality hcp crystal was present after the transformation

of the bcc crystal to hcp is also surprising, since there is no simple relationship between the two lattices.

One final point worthy of some attention is the lower melting point of crystal 16. As can be seen in Fig. 29, below about 0.3 K, the lattice parameter of crystal 16 begins to increase, and then sharply turns over and decreases. This is not due to phase separation, because T_{ps} (for x_3=0.989 and P $\sim$ 3.0 MPa) is 0.186 K, and no peak shape changes were seen near the transition point, 0.208 K. The decrease in lattice parameter is the result of melting of the crystal at the lower melting temperature of this mixture. For comparison, the melting temperature for pure ^{3}He at the appropriate pressure ($\sim$ 2.95 MPa) is 0.20 K.[4/] The melting point hypothesis is reasonable because (1) the decrease in lattice parameter below T_m corresponds to compression of the solid by the newly forming liquid in the plugged cell, and (2) the exact shape of the melting curve for the 99% mixture is unknown.

VI. SUMMARY

For the study of thermal vacancies and of phase separation phenomena in ^3He-^4He solid mixtures, a new position sensitive detector-x-ray diffractometer system has been developed. The system has many advantages over the diffractometer previously used for studies of helium crystals. Absolute lattice parameters are measured with an accuracy of 300 ppm, and the system is capable of much better accuracy if crystal centering problems are overcome. Vacancy ($\Delta a/a$) measurements are considerably more stable and reproducible than in the past. The sensitivity of the helium vacancy data to crystal quality, rotation, and Bragg peak shape changes has been dramatically reduced. Detailed information about the mosaic structure of the crystal is available from each scan of the Bragg peak which is being studied. The diffractometer-PSD system is completely controlled by an LSI-11 microcomputer, allowing much flexibility in possible scan modes. The LSI-11 also makes immediate analysis and storage of the data possible.

The most remarkable result of the present study of vacancies in ^3He-^4He mixtures is that the concentration of vacancies in several of the mixed crystals was almost 5% near the melting temperature. The character of the temperature dependence of the vacancy concentration was different in the 51% and 28% ^3He mixtures. The large apparent entropy of formation that was found for the 28% mixture crystals suggests that vacancy clusters and vacancy-^3He binding effects could be important. The large molar volume 51% mixture crystals, on the other hand, show a very small apparent entropy of formation. This surprising result suggests that ordering or vacancy

delocalization may be more important in this mixture than the expected vacancy cluster and vacancy-^{3}He binding effects. Vacancy measurements in a high molar volume nearly pure ^{3}He crystal lead to speculations about vacancy delocalization and band structure effects. The first direct measurements of vacancies in hcp ^{4}He are reported. The hcp ^{4}He data are in basic agreement with the bcc results in pure ^{3}He and mixtures.

Absolute lattice parameters of most of the crystals studied here have been measured with an accuracy of 300 ppm. In conjunction with the $\Delta a/a$ measurements, the low temperature lattice parameter has been determined, from which the molar volume of the vacancy-free crystal, MV_o, has been obtained. Several methods are used to obtain the vacancy volume of formation v_p. Analysis of the pressure increases caused by vacancy formation at constant volume shows that there are large pressure drops in the mixtures as the large number of vacancies are destroyed on cooling. These pressure changes have apparently been measured in the past, and explained incorrectly. The comparison of MV_o to the high temperature x-ray molar volume for the bcc ^{4}He crystal measured here results in an estimate of 5×10^{-3} for the vacancy concentration at melting. $\Delta a/a$ measurements in bcc ^{4}He have also shown that it is possible to obtain useful vacancy information, even though there is a very limited temperature range available.

The present diffractometer-PSD system has also made possible a detailed x-ray study of the solid phase separation in the mixtures. This is the first phase separation study in concentrated mixtures in which a microscopic probe was used. The phase separation temperature T_{ps} was determined from crystals grown over a wide range of concentration and pressure. From these T_{ps} measurements, the pressure dependence of T_c (related to the energy

of mixing) was determined to be linear in pressure, with $dT_c/dP=-34$ mdeg/MPa. This value is believed to be more accurate than any previous determination. From dT_c/dP one obtains the excess volume of the mixture, $v^E=-0.57\ x_3(1-x_3)$ cm^3/mol. The calculation of v^E by Mullin[40/] is shown to be in qualitative agreement with the present result. The asymmetry of the T_{ps} versus x_3 phase separation curve predicted by Mullin is not supported, and the data of Panczyk, et al.,[36/] which do support Mullin's prediction, are shown to be questionable.

Analysis of the lattice parameter data obtained during phase separation suggests the use of the present method to make a detailed study of the low temperature phase diagram (near phase separation) of helium mixtures. The present data allow several qualitative conclusions and speculations about the form of the low temperature phase diagram. One conclusion that is backed by several different types of evidence is that the bcc ^{4}He-rich phase exists to much lower temperatures than claimed in published phase diagrams.[30/] The present data in the phase separated region also suggest that study of the kinetics of the phase separation process may be possible: for example, the apparent dominance of the returning Bragg peak by the ^{3}He-rich domains, as the phase separated solid is warmed, can be studied by the present techniques.

The increased sensitivity, accuracy, and flexibility of the new diffractometer-PSD system make several subjects attractive for further study. Pure bcc ^{3}He at high molar volumes is still a candidate for further study, especially to substantiate further the complex temperature dependence of the vacancy concentration. For comparison, bcc ^{4}He could be studied further with the techniques developed here. ^{3}He-^{4}He mixtures are also an inviting

subject, (1) for further study of phase separation and the low temperature phase diagram, and (2) because of the large number of vacancies in the mixtures, and their apparently qualitatively different behavior in different mixtures.

APPENDIX A

CAPACITIVE STRAIN GAUGE

A capacitive strain gauge was built to measure the pressure of the crystal. The design, which is shown in Fig. 57, was constrained by the need to grow single crystals, and not obstruct the access of the x-rays to the crystal. The size of the capacitor plates, 1.6×0.25 cm, was perhaps the biggest difficulty with the design. Because they were so small, the capacitance of the gauge was only about 10 pf. The capacitance of the coaxial cable between the inductor and the gauge was about 50 pf, so the sensitivity of the gauge to pressure changes was smaller than its desired value.

The electronics used to measure the capacitance changes are shown in Fig. 58. A tunnel diode oscillator is the basis of the circuit, in which the capacitor (strain gauge) is part of an LC tank circuit. The oscillator circuit is similar to that used by Van Degrift[133/] and Boghosian, Meyer, and Rives.[134/] As the capacitance changes the frequency of the resonant circuit changes. This is detected by the frequency counter. In the configuration shown in Fig. 58, the oscillator was stable to one part in 10^5 in frequency. However, this was not good enough to allow pressure measurements with the strain gauge. With a larger capacitance in the gauge, the parameters of the various components in the oscillator circuit would not be so critical. In this case the oscillations would be more easily stabilized.

Figure 57. Strain gauge design. Shown here is an exploded view of the capacitive strain gauge, mounted on the Lucite sample cell (F). The movable capacitor plate (E), the fixed plate (D), and the mounting blocks (C) are Lucite. Plate (E) and blocks (C) are attached to the Lucite cell with Clearwell Lucite Cement. Gold was evaporated on the two plates (D and E), with a thickness of 210 Å on the fixed plate (D) and 600 Å on the moving plate (E). Electrical connection to the coaxial cable (B) (Lake Shore Cryotronics Type A ultraminiature coax) is made with Uniset Conducting Adhesive (Polymer Products Div., Omicon Corp.). The 0.025 mm Mylar spacers (G) are used to assure that the two plates are not shorted together when the strain gauge is assembled by screwing the plate (D) onto the mounting blocks (C) with the nylon 1-72 screws (A). The capacitance of the assembled gauge is about 10 pf.

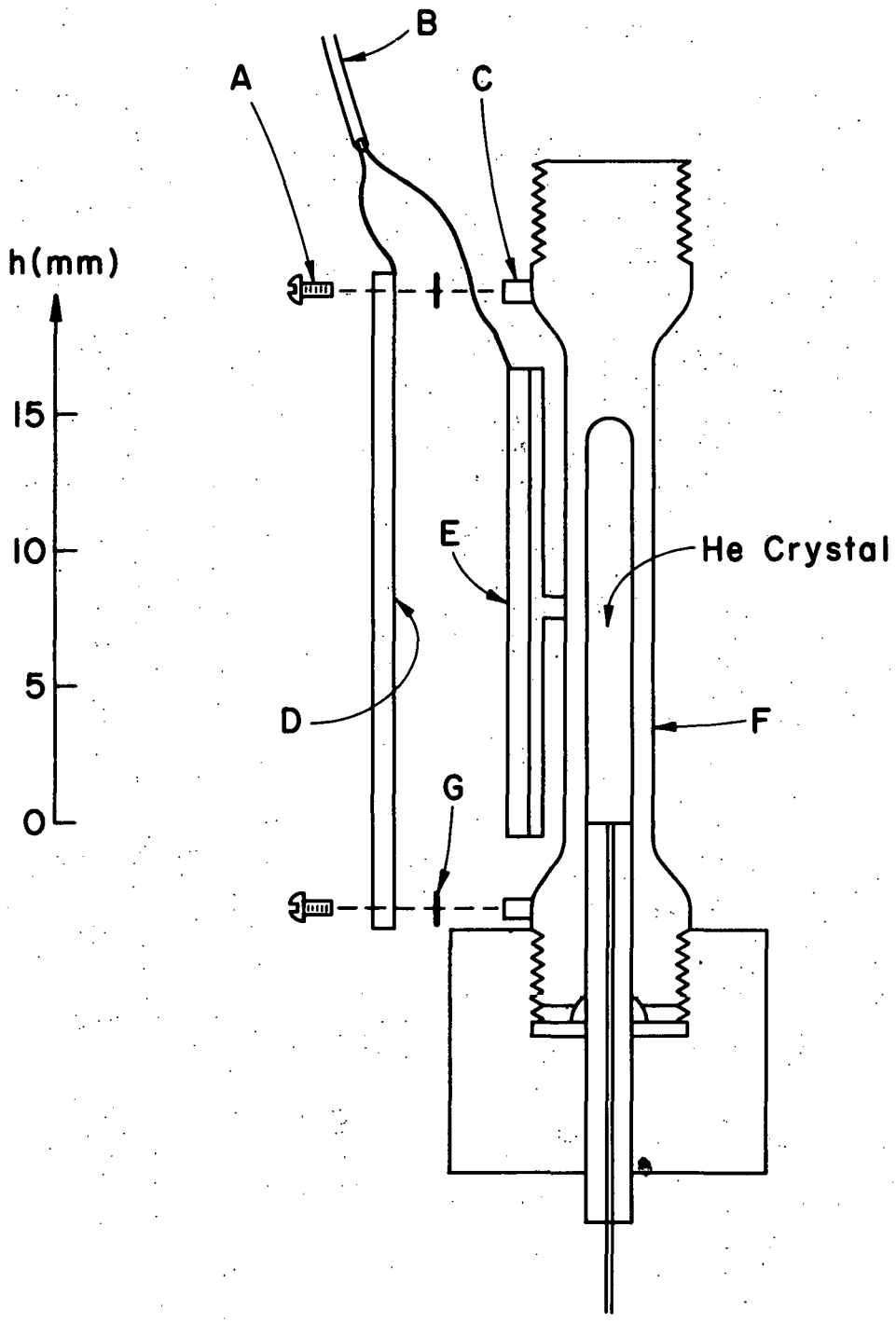
B
A
C
h(mm)
15
10
5
0
E
He Crystal
D
F
G

Figure 58. Strain gauge electronics. The tunnel diode oscillator is shown in the lower left corner. The diode D is a General Electric BD-6 tunnel diode. C is the strain gauge, while L is a tapped inductor (x is 2 turns on the 0.6 cm diameter teflon core, y is 15 turns). R_p limits the power into the resonant circuit, and is 75 Ω here. The ratio of R_1 to R_2 determines the biasing of the diode. R_1 is 26.1 KΩ, R_2 is 2.15 KΩ, C_1 is 20 pf, and C_2 is 2000 pf.

The bias supply is shown inside the dashed line. The batteries B are Eveready E42N 1.35 v mercury cells. The rf filter components L_3 and C_3 are 50 μh and 22 μf respectively. The bias current can be measured (Bias Meas.).

The rf signal (∿15 MHz) is analyzed with the electronics shown on the right. The preamp is an Arulab PA-620 tunable preamplifier, the amp is an Arulab WA-600E Wide Band Amplifier, and the frequency counter is a Fluke 1900A Multi-Counter. The interface, Blox, LSI-11, and chart recorder are discussed in Appendix C.

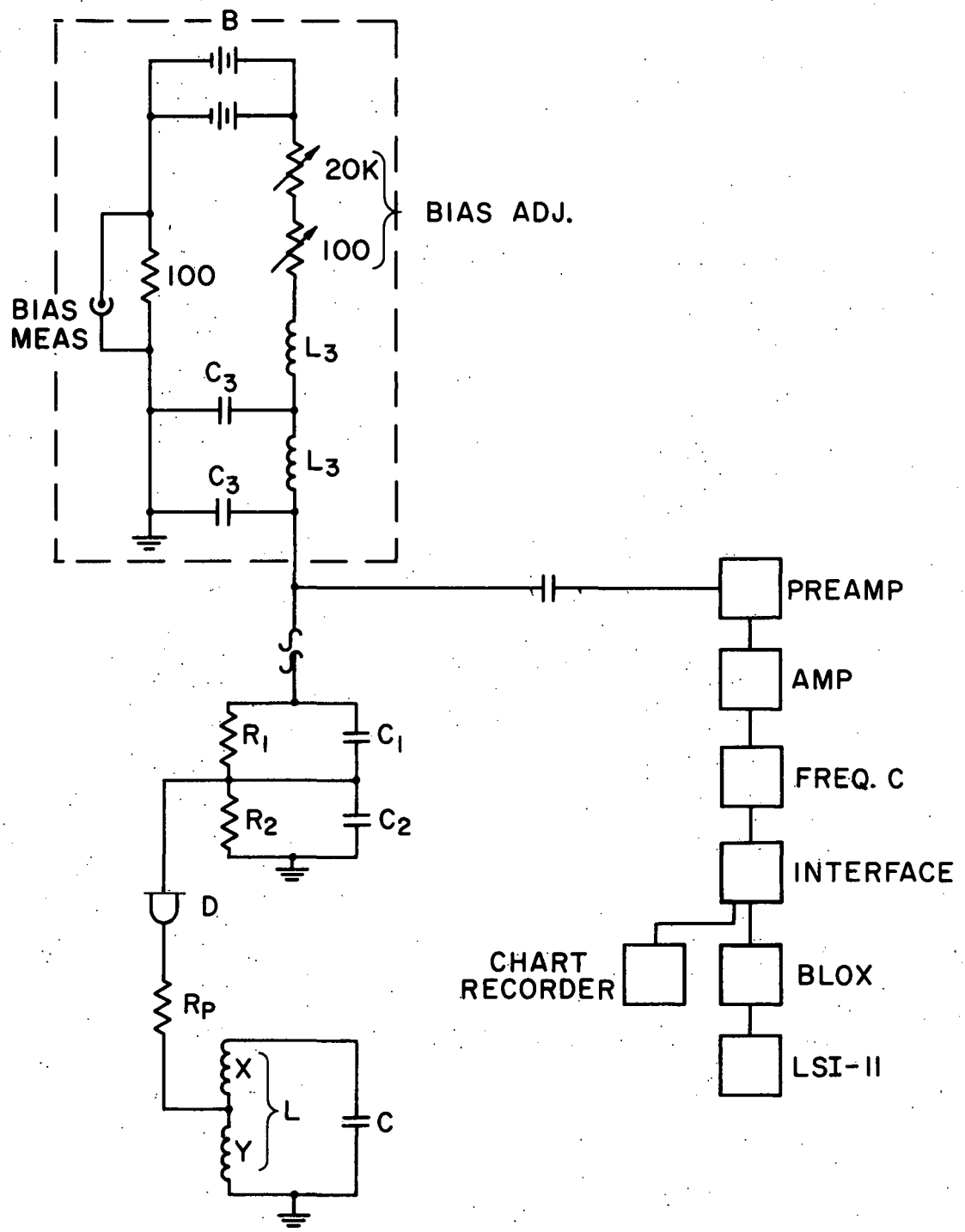
B
20K
100
BIAS ADJ.
100
BIAS
MEAS
L3
C3
L3
C3
PREAMP
AMP
FREQ. C
INTERFACE
BLOX
LSI-11
CHART
RECORDER
R1
C1
R2
C2
D
RP
X
Y
L
C

APPENDIX B

MACHINE LANGUAGE PROGRAMS

Several machine language (macro) programs were written to facilitate communication between the LSI-11 microcomputer and the Blox and MCA. READER.MAC and WRITER.MAC are macro subroutines which are called by the Fortran programs used on the LSI-11, and which read and write, respectively, to any module in the Blox. MCASUB.MAC is a macro subroutine which reads the data from the MCA at 3000 baud (through the interface and Blox), and stores it in a file on the floppy disk in a specific ASCII format. A listing of these programs follows this discussion.

READER.MAC and WRITER.MAC are all that is needed to perform any communication with any Blox module. READER.MAC is called in the Fortran program with "CALL READER(J,K,L)," where J is the Blox module number (decimal), K is the result of the read (in octal), and L is 0 if a read was tried 1000 times, and failed. The call for WRITER.MAC is similar: "CALL WRITER(J,K)," where J is the module number, and K is the information to be written (in decimal).

MCASUB.MAC performs several functions, allowing the data from the MCA to be read into the LSI-11 very quickly. The MCA transmits 4 bits to the computer at one time, and these 4 bits are part of the usual 7 bit ASCII code. The four bits do not give an unambiguous definition of the characters transmitted, and so careful attention must be payed to the format in which the data are transmitted. This difficulty is the explanation for all the format counters involved in the 4 bit to ASCII translation part of

the program. The data are stored in the file FD1:MCATEM.DAT on the floppy disk, in ASCII, in the same format as that obtained from the MCA when the teletype output (110 baud) is used. The data in this file are then analyzed later in the Fortran program which called MCASUB.MAC as a subroutine. No extra parameters are needed by the subroutine.

READER.MAC

```
        .GLOBL  READER
        .MCALL   .REGDEF,..V2..,.PRINT,.EXIT
        ..V2..
        .REGDEF
        DRCSR=177510
;
;GET ARGUMENTS FROM MAIN PROGRAM
;
READER: MOV     (R5)+,R3        ;GET # ARGUMENTS,R5 NOW POINTS
                                ; TO MOD ADDR
        CLR     R2              ;CLEAR READ TRY COUNTER
        INC     R2              ; INCREMENT COUNTER
;
;MAKE SURE BB READY, THEN READ
;
FIRST:  MOV     #DRCSR,R1       ;PUT ADDRESS IN R1
        TST     (R1)            ;IS BIT 15 1?
        BMI     FIN1            ;LEAVE, INTERRUPT PENDING
        TSTB    (R1)            ;DONE?
        BPL     FIRST           ;IF NOT TRY AGAIN
        CLR     (R1)            ;DROUT TO CR, ST TO DRIN
        MOV     @(R5)+,2(R1)    ;GET MOD ADDR AND READ THERE IN
                                ;BB, R5 PTS TO RESULT
SECOND: TSTB    (R1)            ;DONE?
        BPL     SECOND          ;IF NOT TRY AGAIN
        TST     4(R1)           ;IS TRANSMISSION OK?
        BMI     THIRD           ;IFNOT, BIN NOT DONE, TRY AGAIN
;
;READ IS OK, SO FIX ARGS
;
        INC     (R1)            ;RBUF TO DRIN
        MOV     4(R1),@(R5)     ;MOVE DRIN TO ARG LIST
        MOV     R2,@2(R5)       ;MOVE # OF READ TRYS TO ARG LIST
        RTS     PC              ;RETURN TO MAIN PROGRAM
;
;TRY ANOTHER READ OF BB
;
        INC     R2              ;INCREMENT READ TRY COUNTER
        CMP     #1000,R2        ;IS READ TRY COUNT 1000?
        BPL     FIRST           ;IF NOT GO TRY AGAIN
        MOV     #0,@4(R5)       ;MOVE 0 TO READ TRY ARG
        RTS     PC
FIN1:   .PRINT  #MSG2
        .EXIT
FIN2:   .PRINT  #MSG3
        .EXIT
MSG2:   .ASCIZ  /INTERRUPT PENDING/
MSG3:   .ASCIZ  /TRANSMISSION NOT OK, WRONG BIN?/
MSG6:   .ASCIZ  /READ TRY 10/
        .END    READER
*
```

WRITER.MAC

```
        .GLOBL  WRITER
        .MCALL   .REGDEF,..V2..,.EXIT,.PRINT
        ..V2..
        .REGDEF
        DRCSR=177510
;
;GET ARGUMENTS FROM MAIN PROGRAM
;
WRITER: MOV     #DRCSR,R1          ;DRCSR INTO R1
        MOV     (R5)+,R3           ;R3=# OF ARGS, R5 PTS TO ARG1
        MOV     @(R5)+,R2          ;MOD # TO R2
;
; IS BB READY FOR A WRITE?
;
        TST     (R1)               ;TEST DRCSR
        BMI     FIN3               ;BRANCH IF INTERRUPT PENDING
        TSTB    (R1)               ;DONE?
        BPL     WRITER             ;IF NOT TRY AGAIN
;
; PUT DATA INTO BB
;
        MOV     #2,(R1)            ;DROUT TO WBUF, ST TO DRIN
        MOV     @(R5),2(R1)        ;WRITE THE DATA TO BBX
SECOND: TST     (R1)               ;READ DRCSR
        BMI     FIN3               ;BRANCH IF INTERRUPT PENDING
        TSTB    (R1)               ;BUSY?
        BPL     SECOND             ;YEP, TRY AGAIN
        CLR     (R1)               ;0 TO DRCSR
;
; WRITE TO THE MODULE IN BB
;
        ADD     #100000,R2         ;MAKES IT EASIER TO WRITE
        MOV     R2,2(R1)           ;LOAD MOD ADDR IN BBX,THEN WRITE
THIRD:  TST     (R1)               ;READ DRCSR
        BMI     FIN3               ;BRANCH IF INTERRUPT PENDING
        TSTB    (R1)               ;DONE?
        BPL     THIRD              ;NOPE,TRY AGAIN
        TST     4(R1)              ;STATUS OK?
        BMI     FIN                ;NOPE, GO TO FIN
        RTS     PC
FIN3:   .PRINT  #MSG3
        .EXIT
FIN2:   .PRINT  #MSG1
        .EXIT
FIN:    .PRINT  #MSG2
        .EXIT
MSG1:   .ASCIZ  /STATUS NOT OK,BUSY?/
MSG2:   .ASCIZ  /TRANSMISSION NOT OK/
MSG3:   .ASCIZ  /INTERRUPT PENDING/
        .END    WRITER
*
```

MCASUB.MAC

```
;THIS PROGRAM IS A MODIFICATION OF UPDOWN.MAC
;THIS PROGRAM READS 4 BITS PARALLEL FROM THE MCA DIRECTLY
;INTO ASCII.  DRCSR IS THE ADDRESS OF THE PARALLEL BOARD USED
;BY THE BLACK BOX, C IS THE ADDRESS OF THE DECWRITER SERIAL
;BOARD.  REPEAT: IS VERY IMPORTANT.  ITHIS TIME DELAY IS
;NEEDED TO KEEP PROGRAM FROM READING CHARACTERS TWICE, AND ALSO
;FROM MISSING A PERCENTAGE.  IF STEPS ARE ADDED IN THE READ
;PART OF THE PROGRAM, WILL PROBABLY HAVE TO CHANGE THIS
;NUMBER.  LOOK AT TRL AND TGATE OUT OF THE MCA AND IF TGATE
;IS NOT LOW FOR ABOUT 3.5 MSEC AFTER TRL GOES LOW, THEN MORE
;DELAY IS NEEDED.  IF USE #100 INSTEAD OF 300, THE BAUD
;RATE IS ABOUT 1000 INSTEAD OF THE PRESENT 3000.
        .GLOBL  MCASUB
        .MCALL   .REGDEF,..V2..,.PRINT,.CSIGEN,.WAIT,.CLOSE
        .MCALL  .WRITC,.EXIT,.READW,.CSTAT
        ..V2..
        .REGDEF
        ERRWRD=52
        C=177560
        DRCSR=177510
;
;THIS SECTION CREATES OR OPENS FD1:MCATEM.DAT, INTO WHICH
;THE DATA GOES.  ALSO SETS UP COUNTERS AND FLOPPY BUFFERS.
;
MCASUB: MTPS    #0                  ;ALLOW PROCESSOR INTERRUPTS
        MOV     #100,@#C            ;ALLOW CONSOLE INTERRUPTS
        .CSIGEN #DEVSPC,#DEFEXT,#FILADD ;FILADD IS FILNAM ADDR
        BCC     TEMP3               ;JUMP NEXT STATEMENT IF OK
        .PRINT  #MSG5               ;OOPS
        TSTB    @#ERRWRD            ;TEST ERROR WORD
        BNE     TEMP1               ;BRANCH IF ERROR IS BAD DEVICE.
        .PRINT  #MSG3               ;ERROR IS FILENAME, ETC.
TEMP3:  .CSTAT  #CAREA,#0,#CADDR
        BCS     NOCHAN              ;CHANNEL NOT OPEN
        CLR     @#C                 ;STOP CONSOLE INTERRUPTS
        CLR     BLOCK               ;ZERO BLOCK NUMBER FOR NEW FILE
        CLR     R4                  ;ZERO COUNTER
        MOV     #BUF1,R2            ;PUT BUF1 ADDRESS IN POINTER
        MOV     #BUFND1,R3          ;R3 NOW POINTS TO END OF BUF1
DOIT3:  .WAIT   #0                  ;IS CHANNEL #0 OPEN?
        BCC     DOWNLD              ;IF SO THEN DOWNLD
TEMP1:  JMP     ERR1                ;IF NEITHER OPEN,RTN TO ERR1
NOCHAN: .PRINT  #MSG14
        .EXIT
FILADD: .ASCIZ  "FD1:MCATEM.DAT="
        .EVEN
;
```

```
;
;THIS SECTION FILS FLOPPY BUFFERS.  IT IS CALLED
;FROM LATER PARTS OF THE PROG. LIKE A SUBROUTINE.
;
DOWNLD: JSR     PC,FILL          ;FILL BUF1 FROM MODEM
        TST     FINFLG           ;HAS BUF2 BEEN LOADED YET?
        BNE     1$               ;IF NOT SEND ERROR MESSAGE
        INC     FINFLG           ;SET FINFLG FOR WRITING
        .WRITC #AREA,#0,#BUF1,#400,#FIN,BLOCK ;WRITE BUF1 TO FD
        INC     BLOCK            ;COUNT NEXT BLOCK TO BE WRITTEN
        MOV     #BUF2,R2         ;PUT BUF2 ADDRESS IN POINTER
        MOV     #BUFND2,R3       ;R3 NOW POINTS TO END OF BUF2
        JSR     PC,FILL          ;FILL BUF2 FROM MODEM
        TST     FINFLG           ;HAS BUF1 BEEN LOADED YET?
        BNE     1$               ;IF NOT SEND ERROR MESSAGE
        INC     FINFLG           ;SET FINFLG FOR WRITTING
        .WRITC #AREA,#0,#BUF2,#400,#FIN,BLOCK ;WRITE  BUF2 TO FD
        INC     BLOCK            ;COUNT NEXT BLOCK TO BE WRITEN
        MOV     #BUF1,R2         ;PUT BUF1 ADDRESS IN POINTER
        MOV     #BUFND1,R3       ;R3 NOW POINTS TO END OF BUF1
        BR      DOWNLD           ;GO BACK AND FILL BUF1
1$:     JMP     ERR4             ;RELAY A BRANCH
;
;READ THE NEW CHARACTER FROM BB
;
FILL:   MOV     #DRCSR,R1        ;R1 POINTS TO BB DRCSR
        MOV     #77000,R4        ;COUNT # OF READ TRIES
FIRST:  INC     R4               ;ANOTHER READ TRY
        BMI     FINISH           ;IF R4 HAS BIT 15 =1, GO FINISH
        TST     (R1)             ;IS BIT 15 1?
        BMI     FIN1             ;LEAVE, INTERRUPT PENDING
        TSTB    (R1)             ;DONE?
        BPL     FIRST            ;IF NOT TRY AGAIN
        CLR     (R1)             ;DROUT TO CR,ST TO DRIN
        MOV     #66,2(R1)        ;MOD ADDRESS, READ THERE IN BB
SECOND: TSTB    (R1)             ;DONE?
        BPL     SECOND           ;IF NOT TRY AGAIN
        TST     4(R1)            ;IS BUSY OR FLAG ON?
        BMI     FIRST            ;IF YES, TRY READ AGAIN
```

```
;
;THIS SECTION TRANSLATES EACH 4 BITS INTO ASCII
;
        INC     (R1)            ;RBUF TO DRIN, RESULT AT 4(R1)
        MOV     4(R1),R4        ;DATA INTO R4
        COM     R4              ;COMPLEMENT DATA
        MOV     #177760,R5      ;R5 IS MASK FOR 1ST 4 BITS
        BIC     R5,R4           ;RESULT IN R4 IS MCA 4 BITS
        CMPB    #12,R4          ;IS IT A LINE FEED?
        BEQ     DOIT6           ;IF SO DOIT5
        CMPB    #15,R4          ;IS IT A CARRIAGE RETURN?
        BEQ     DOIT6           ;IF SO DOIT6
        CMPB    #0,R4           ;IS IT A 0 OR SPACE?
        BEQ     SIXTY           ;IF SO SIXTY
        ADD     #60,R4          ;R4 IS NOW AN ASCII #
        TSTB    R0              ;IS R0 0(LAST CHAR IN #)?
        BEQ     DOIT10          ;IF SO DOIT10
        TST     R0              ;IS BIT 15 1?
        BMI     DOIT7           ;IF SO DOIT7
        ADD     #100000,R0      ;MAKE BIT 15 1
        BR      DOIT7           ;GO TO DOIT7
DOIT10: MOV     #7,R0           ;SET FORMAT COUNTER FOR NEW #
        BR      DOIT7           ;GO TO DOIT7
DOIT6:  MOV     #4,R0           ;SET FORMAT COUNTER FOR CHAN #
        BR      DOIT5           ;GO TO DOIT5
SIXTY:  MOV     #40,R4          ;CHAR. IS NOW A SPACE
        TSTB    R0              ;IS R0 0(LAST CHAR. OF #)?
        BEQ     DOIT8           ;IF SO DOIT8
        TST     R0              ;IS BIT 15 1(IN MIDDLE OF #)?
        BMI     DOIT9           ;IF YES THEN DOIT9
        BR      DOIT7           ;GO TO DOIT7
DOIT8:  MOV     #7,R0           ;SET UP R0 FOR NEXT #
DOIT9:  MOV     #60,R4          ;CHAR IS A 0
DOIT7:  DEC     R0              ;DEC FORMAT COUNTER FOR NXT CHAR
```

```
;
;CHARACTER IS ASCII NOW, SO PUT IT INTO FLOPPY BUFFER AND
;GO GET NEXT CHARACTER
;
DOIT5:  MOVB    R4,(R2)+        ;PUT CHARACTER IN BUFFER
        CLR     R5              ;CLR R5 FOR USE AS DELAY COUNTER
REPEAT: ADD     #300,R5         ;DELAY,100 TOO SMALL,500 TOO BIG
        BCC     REPEAT          ;IF CARRY NOT SET THEN REPEAT
GOON:   MOVB    -1(R2),SAVE     ;SAVE CHARACTER IN CASE ITS IN
                                ; PREVIOUS BUFFER
        CMP     R2,R3           ;ARE WE AT BUFND?
        BLO     FIRST           ;IF NOT THEN GO GET NEXT CHAR
        RTS     PC              ;RETURN TO DOWNLD IF BUFFER FULL
FIN:    CLR FINFLG              ;SET FLAG TO ZERO
        ROR     R0              ;MOV BIT 0 TO CARRY
        BCS     FLOP            ;IF I/O ERROR THEN GIVE UP
        RTS     PC              ;RETURN TO PROGRAM
FLOP:   TST     (SP)+           ;CORRECT (SP) FOR UNCONDITIONAL
                                ;BRANCH FROM A SUBROUTINE
        BR      ERR6            ;SEND I/O ERROR MESSAGE
;
;FINISHED, ARRANGE PARAMETERS FOR RETURN TO FORTRAN PROG
;
FINISH: MOV     #3,-1(R2)       ;PUT AN EOF AT END OF FILE
ZERO:   CLRB    (R2)+           ;CLEAR BUFFER
        CMP     R2,R3           ;IS POINTER AT BUFFER END?
        BLO     ZERO            ;IF NOT THEN KEEP ZEROING BUFFER
        SUB     #1000,R3        ;RETURN BUFFER POINTER TO FIRST
                                ; BYTE
        TST     FINFLG          ;HAS LAST BUF LOADED YET?
        BNE     ERR4            ;IF NOT THEN SEND ERROR MESSAGE
        .WRITC  #AREA,#0,R3,#400,#FIN,BLOCK  ;WRITE LAST BLOCK
                                ;TO FLOPPY DISK
        .CLOSE  #0                ;CLOSE FILE
        MTPS    #0              ;ALLOW PROCESSOR INTERRUPTS
        MOV     #100,@#C        ;ALLOW CONSOLE INTERRUPTS
        TST     (SP)+                ;RESET STACK POINTER
        TST     (SP)+
        RTS     PC
FIN1:   .PRINT  #MSG2
        .EXIT
ERR1:   .PRINT  #MSG1
        .EXIT
ERR4:   .PRINT  #MSG4
        .CLOSE  #0
        .EXIT
ERR6:   .PRINT  #MSG6
        .CLOSE  #0
        .EXIT
```

```
MSG3:    .ASCIZ  /BAD SEP,ILLIGAL FILENAME,ETC./
MSG5:    .ASCIZ  /OOPS/
MSG14:   .ASCIZ  /CSTAT CHANNEL NOT OPEN/
MSG2:    .ASCIZ  /INTERRUPT PENDING/
MSG1:    .ASCIZ  /CHANNEL NOT OPEN/
MSG9:    .ASCIZ  /FOR NEW FILE  TYPE FD1:NAME.EXT=/
MSG4:    .ASCIZ /BUFFER FAIL-NO FLOPPY OR BAUD RATE TOO HIGH/
MSG6:    .ASCIZ /IO ERROR DURING WRITE/

.EVEN

SAVE:    .WORD   0
DELAY:   .WORD   0
BUF1:    .=.+1000
BUFND1:  .
BUF2:    .=.+1000
BUFND2:  .
FINFLG:  .WORD   0
BLOCK:   .WORD   0
CAREA:   .BLKW   5
CADDR:   .BLKW   6
DEFEXT:  .WORD   0,0,0,0
AREA:    .BLKW   10
DEVSPC=.
         .END    MCASUB
*
```

APPENDIX C

X-RAY DIFFRACTOMETER INTERFACE SCHEMATICS

The interface is broken into three sections. The first section is the Read Section, which is shown in Fig, 59. Each of the five functional blocks of Fig. 59 is then shown in detail in Fig.60 through 64 . It is with the Read Section that the 6 digit BCD numbers from the encoder, frequency counter, digital voltmeter, and the 4 bits from the multichannel analyzer (MCA) are read into the LSI-11, 16 bits at a time.

The second section is the Encoder Translation Section. This section translates the grey binary code obtained from the shaft encoder into 5 BCD digits. This information is then read into the computer with the Read Section, and it is also displayed on the front of the interface box with LED's. A general diagram of the section is given in Fig. 65, and details are shown in the two block diagrams Figs. 66 and 67.

The third section is the 3 Digit D to A Section. This was designed for use with the strain gauge electronics. It allows any of four sets of digits from the frequency counter to be displayed on a chart recorder. Digits 543, 432, 321, and 21- (where - is nothing) can be displayed. Which of the combinations is used is determined in the Selection Block, Fig. 68. The output of this block goes to the D to A Block, Fig. 69, where the BCD to binary and digital to analog conversions are done. The output from this block then goes to the chart recorder.

Figure 59. Block diagram of interface read section. This diagram shows the relationship of each of the different functional blocks in the read section of the interface. Information generally flows from the top of the diagram to the bottom. Signals which interconnect the different blocks are labeled. Inputs are: (E), 5 BCD digits from the encoder translation section of the interface; (F), 6 BCD digits from a Fluke 1900A frequency counter; (V), 6 BCD digits from a Vidar 520 digital voltmeter; (X) unassigned 32 bit inputs; 7 control lines from a Blox module REG306; and 3 control lines and 4 data lines from the MCA (Tracor-Northern TN-1706). Outputs are: 16 bits and 2 control lines to a Blox module REG312; 3 lines to a Blox module REG309; and 3 control lines to the MCA. The five functional blocks, shown in the next five figures, are: (I) Data Input Block, (II) Read Control Block, (III) MCA Block, (IV) Data Select Block, and (V) MCA Control Block.

A symbol, followed by a number in parenthesis, means that there are that many bits of information being transmitted, i.e., E (32) means that there are 32 separate lines from the encoder being represented by the one line drawn in the schematic. This notation holds throughout this appendix. Also, integrated circuits are labeled by small letters in circles, and their numbers[135/] are listed at the bottom of each figure caption.

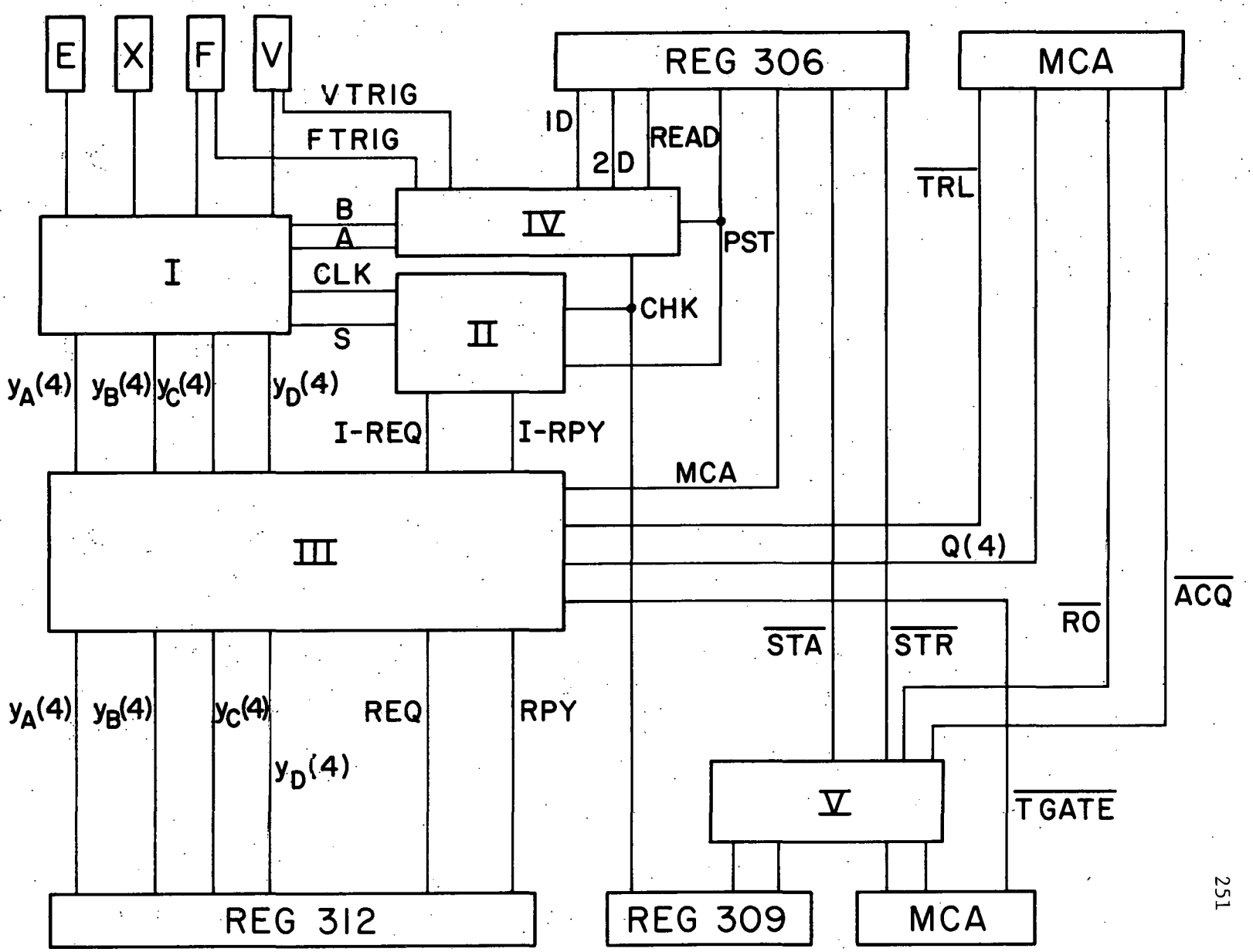
E
X
F
V
VTRIG
FTRIG
REG 306
MCA
ID
2D
READ
TRL
B
A
IV
PST
I
CLK
II
CHK
S
$y_A(4)$
$y_B(4)$
$y_C(4)$
$y_D(4)$
I-REQ
I-RPY
MCA
III
Q(4)
ACQ
RO
STA
STR
$y_A(4)$
$y_B(4)$
$y_C(4)$
REQ
RPY
$y_D(4)$
V
TGATE
REG 312
REG 309
MCA

Figure 60. Data Input Block (I). This block connects one of the four input data sets (E, F, V, or X) to the 16 output bits (Y_i(1,2,4, or 8), i=A,B,C,D). Which of the four input sets is chosen is determined by input lines A and B. The (a) chips therefore are just switches, of which there are 8 sets (of 2 each). The notation for the input lines is: $^{q}_{jk}$, where q is E, F, V, X; j=digit number; k=1,2,4, or 8th bit. For each two a chips (hence one BCD digit), there is a latch (b) which stores the data Z_i(1,2,4, and 8), where i is 1 through 8. This store happens when a pulse occurs on CLK. In this way all 8 digits can be stored into the latches (b) at the same time. Next, either the first four digits (Z_i(4), i=1,2,3,4), or the second four digits (Z_i(4), i=5,6,7,8) are connected to the 16 lines out from this section (Y_i(4), i=A,B,C,D) through the multiplexers (c). These multiplexers are controlled by S.

This system is necessary because only 16 bits can be read into the REG312 and the LSI-11 at one time. One must be sure that all 32 bits of the input data were obtained at the same time, even though only 16 are read at one time. The latches (b) , which store all 32 bits, solve this problem.

(a) Dual 4 → 1 Multiplexer (74153)

(b) 4 Bit Latch (7475)

(c) Quad 2 → 1 Multiplexer (74157)

I

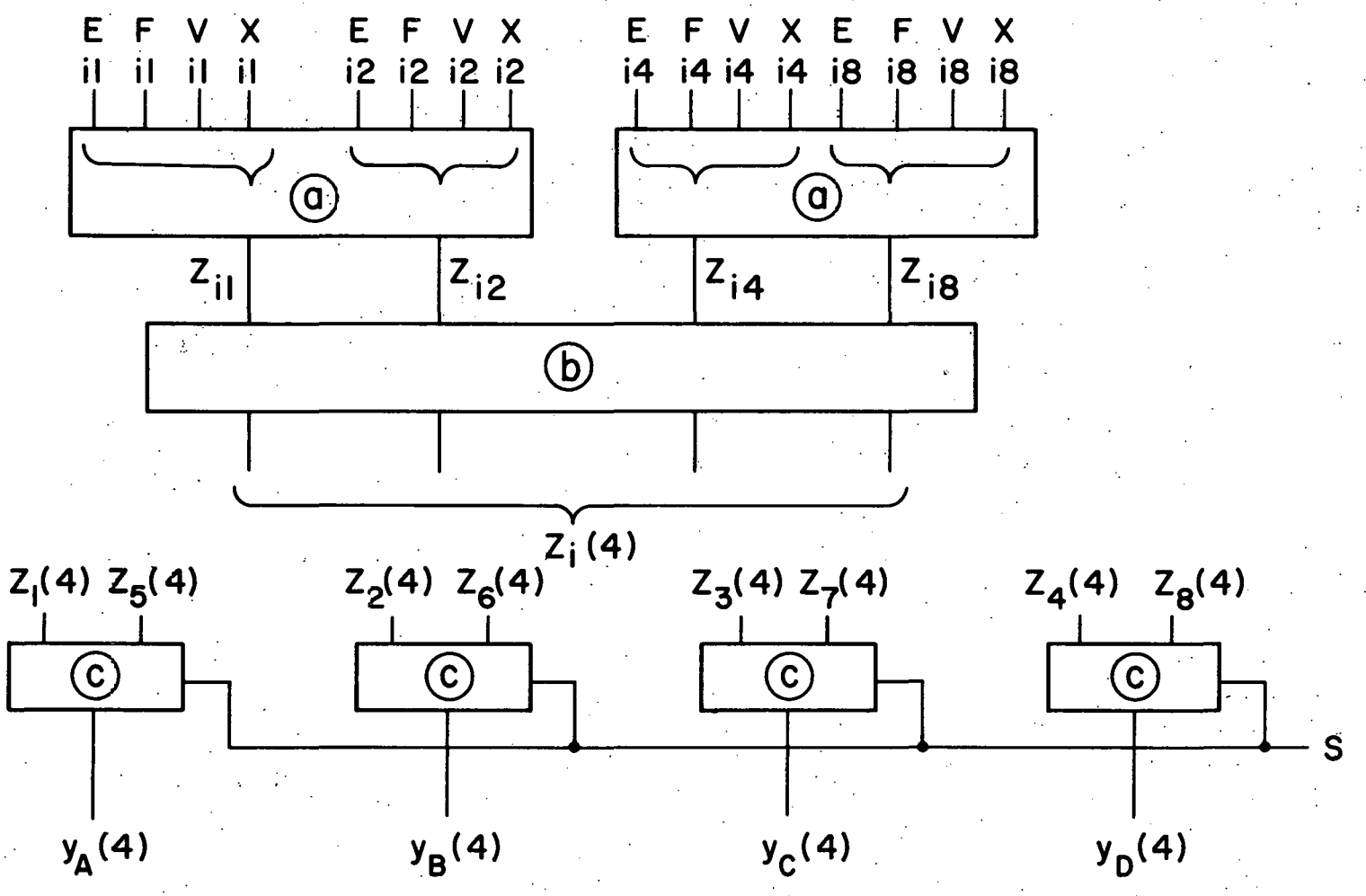
E F V X
i1 i1 i1 i1
E F V X
i2 i2 i2 i2
E F V X E F V X
i4 i4 i4 i4 i8 i8 i8 i8
a
a
Z_{i1}
Z_{i2}
Z_{i4}
Z_{i8}
b
$Z_i(4)$
$Z_1(4)$ $Z_5(4)$
$Z_2(4)$ $Z_6(4)$
$Z_3(4)$ $Z_7(4)$
$Z_4(4)$ $Z_8(4)$
c
c
c
c
S
$y_A(4)$
$y_B(4)$
$y_C(4)$
$y_D(4)$

Figure 61. Read Control Block (II). All the critical timing that controls the reading occurs in this section. PST going high sets up the logic for a read sequence. CHK goes high when READ is allowed through the logic in block IV. This causes a pulse (CLK) from monostable (e) 82 which latches the data in block I. It also causes I-REQ to go low. This tells Blox module REG312 that the data are ready to be read. Finally, the CLK pulse sets S low so that the first set of 16 bits is read (see block I). When the Blox REG312 starts reading, I-RPY goes low. This sets I-REQ high again. When the read is finished, I-RPY goes high. This sets S high, so that the second set of digits will be read, and it sets I-REQ low so that another read by the Blox REG312 will occur. I-RPY again goes low during the read, which sets I-REQ high again. I-RPY goes high at the completion of this read, but since both sets of 4 digits have been read, nothing else happens.

(d) Dual flip-flop (7474)

(e) Monostable (74121)

II

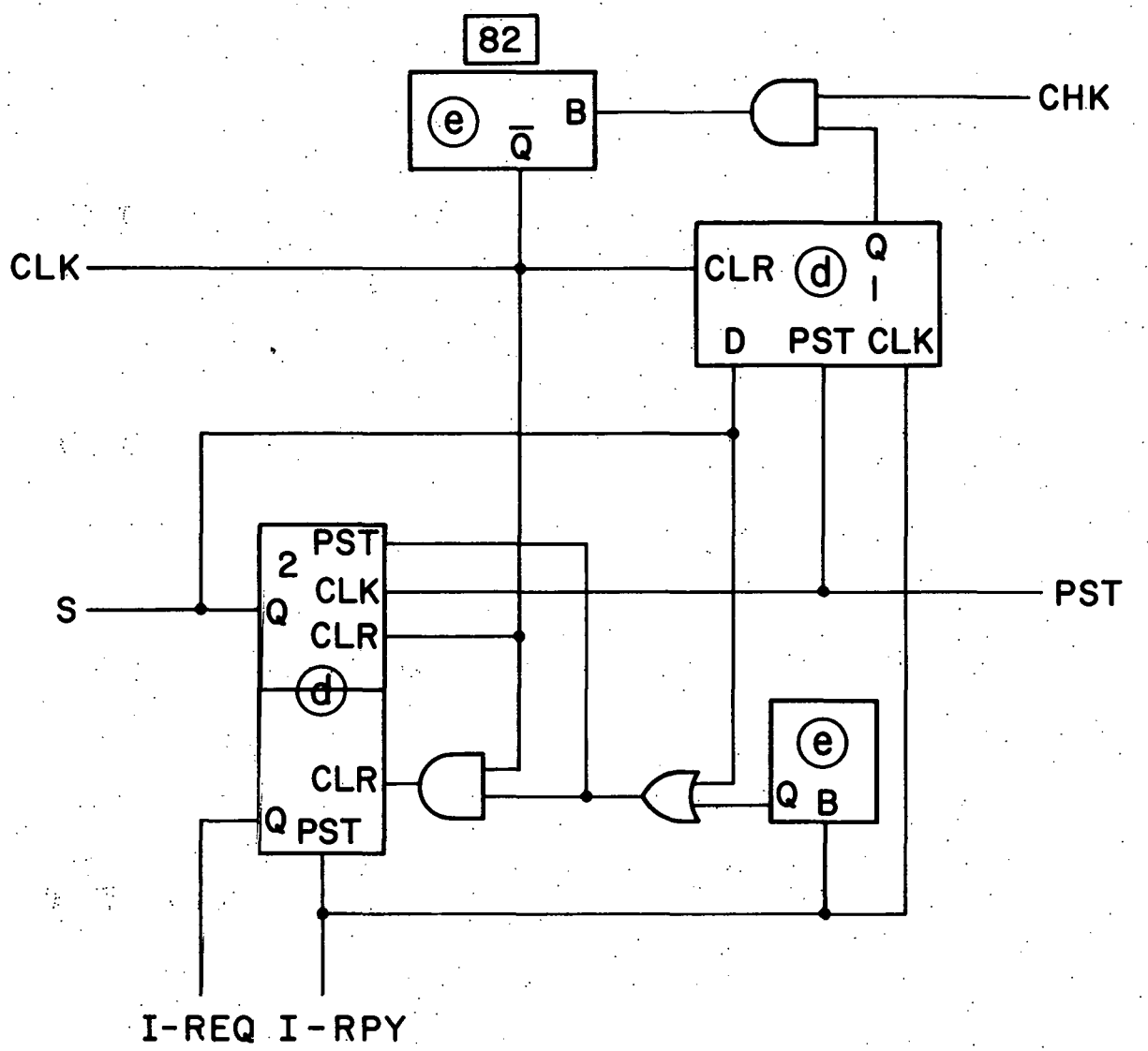
82
e
B
Q̄
CHK
CLK
CLR
d
Q
1
D
PST
CLK
S
2
Q
PST
CLK
CLR
d
CLR
Q
PST
e
Q
B
PST
I-REQ
I-RPY

Figure 62. MCA Block (III). This block switches the MCA 4 bits onto the same lines used to read the other data (encoder, frequency counter, etc.) into Blox module REG312. It also relays the MCA I/O controls between the MCA and the interface. M is set high when the MCA is read, switching the MCA data and controls onto the output lines (y_A) and the control lines REQ and RPY. Q_1, Q_2, Q_4, Q_8 are the 4 data bits from the MCA. It was originally thought that another 4 bits (L_5-L_8) would be needed, and so that wiring is in place, although presently unused. REQ and RPY work as before (see block II), but now they are connected to $\overline{TRL}$ and $\overline{TGATE}$ through a flip-flop ((d)). $\overline{TRL}$ goes high when the MCA is ready with 4 bits to be transmitted. This causes REQ to go low, causing a read by the REG312. That makes RPY go low, which sets REQ high. REQ makes $\overline{TGATE}$ low, which keeps the MCA from getting a new character ready. When the read is completed, RPY goes high, causing $\overline{TGATE}$ to go high, allowing the MCA to start the next cycle.

(d) Dual Flip-flop (7474)

III

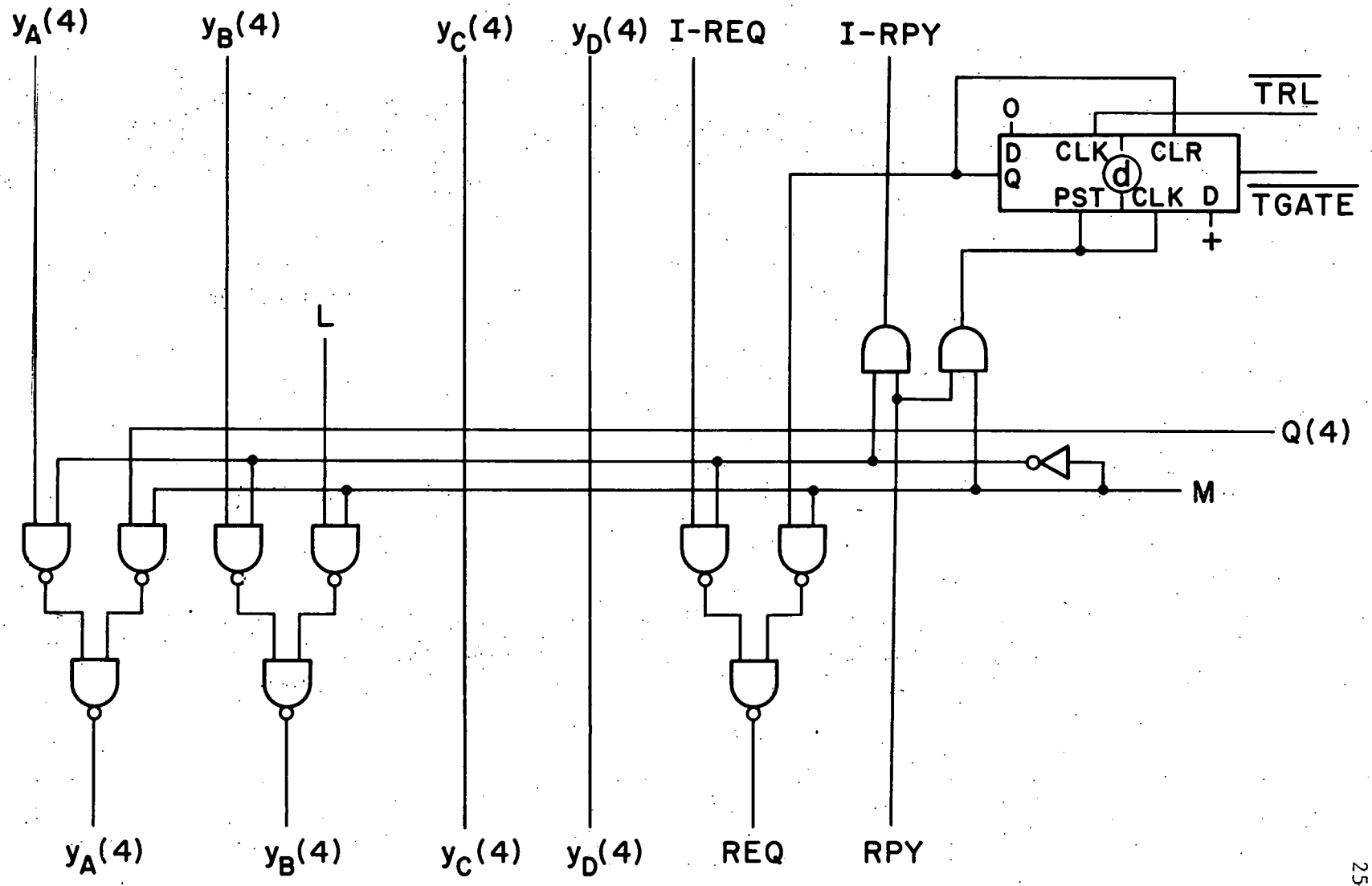
$y_A(4)$
$y_B(4)$
$y_C(4)$
$y_D(4)$
I-REQ
I-RPY
$\overline{TRL}$
O
D
Q
CLK
CLR
d
PST
CLK
D
+
$\overline{TGATE}$
L
Q(4)
M
$y_A(4)$
$y_B(4)$
$y_C(4)$
$y_D(4)$
REQ
RPY

Figure 63. Data Select Block (IV). This block has two functions, (1) to set up the logic for block I so that the correct data set is read, and (2) to prevent reads when the external equipment is not ready. (1) is accomplished simply by a flip-flop ((d)) which saves inputs 1D and 2D (from REG306) as A and B (which are used in block I) when PST goes high. If the notation 1=high, 0=low, (A,B) is used, then the code for the different input data sets is E(0,0), F(1,0), V(0,1), and X(1,1).

Function (2) involves the input READ, from REG306. This is set high when a read sequence is desired. The output, CHK, only becomes high after the READ signal has made it through the trigger logic. If the data set desired is F or V, then the READ level will only be passed after FTRIG or VTRIG goes to the correct level. This assures that the frequency counter and DVM are not read while their output is changing. The output CHK is also read by Blox module REG309, so that the LSI-11 can wait for the FTRIG or VTRIG to be correct before it continues with the read sequence program.

(d) Dual Flip-flop (7474)

IV

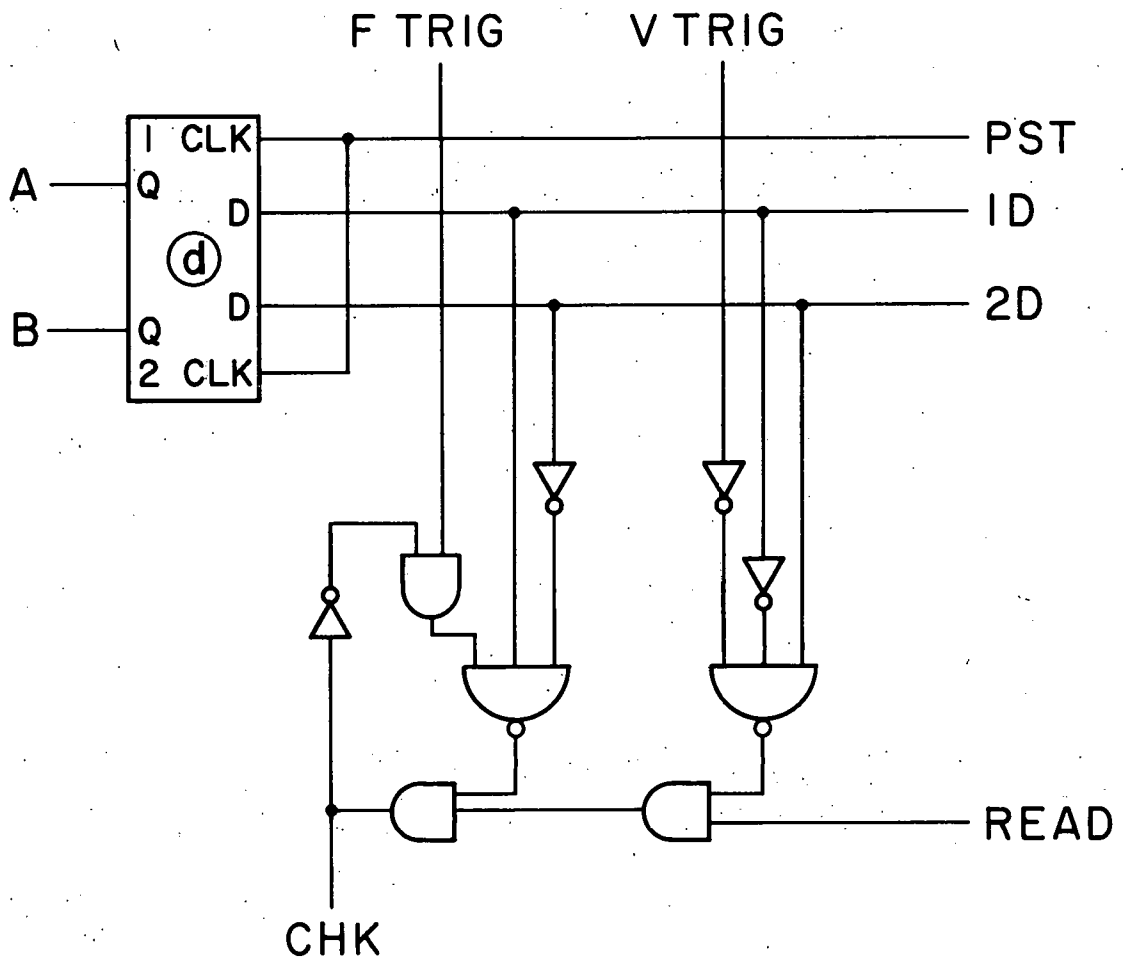

Figure 64. MCA Control Block (V). This block uses 555 timers (f) to make control signals from REG306 compatible with the controls of the TN-1706 MCA. The pulses which control the I/O ($\overline{STR}$) and acquire ($\overline{STA}$) functions of the MCA need to be longer than 15 μsec. This requires 555 timers. $\overline{RO}$ gives the status of the MCA I/O function, while $\overline{ACQ}$ gives the status of the MCA acquire function.

(f) Timer (LM555)

V

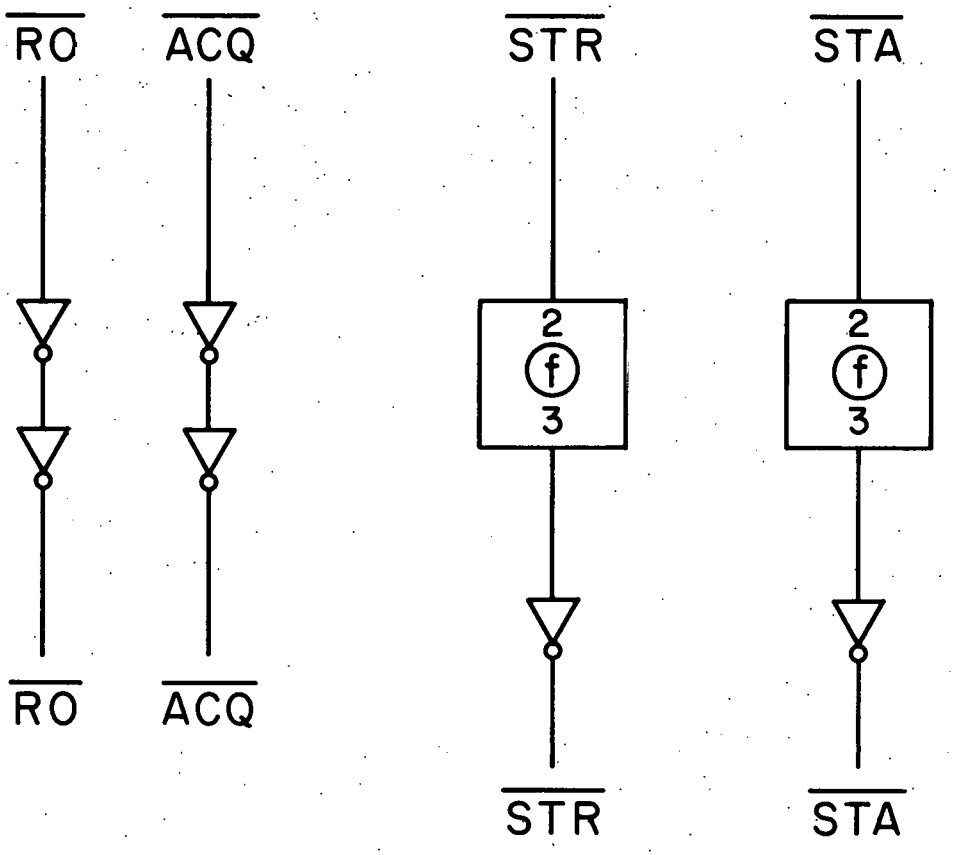
$\overline{RO}$
$\overline{ACQ}$
$\overline{STR}$
$\overline{STA}$
2
f
3
2
f
3
$\overline{RO}$
$\overline{ACQ}$
$\overline{STR}$
$\overline{STA}$

Figure 65. Encoder Translation Section. This figure shows the interconnection of the various parts of the translation section. Although the grey-BCD translation block (Block VI, see Figure 66) is the same for each digit, the grey code forces much interconnection between digits. The inputs (see Fig. 67 for details) are U_i, where U is units and i is A,B,C, or D, with A being the least significant bit. T is tens, H hundreds, TH thousands, and TTH ten thousands. Outputs are in the notation used previously (see Fig. 59). For the TH and TTH inputs there are two sets of inputs, for example T_{A_1} and T_{A_2}. These are known respectively as lead and lag. Only one set, either lead or lag, is used at any one time. See Fig. 67, (Block VII) for details. The 5 BCD digits which result from the translation are the E input set to the Read Section (Fig. 59), and are also connected to an LED display on the front of the interface.

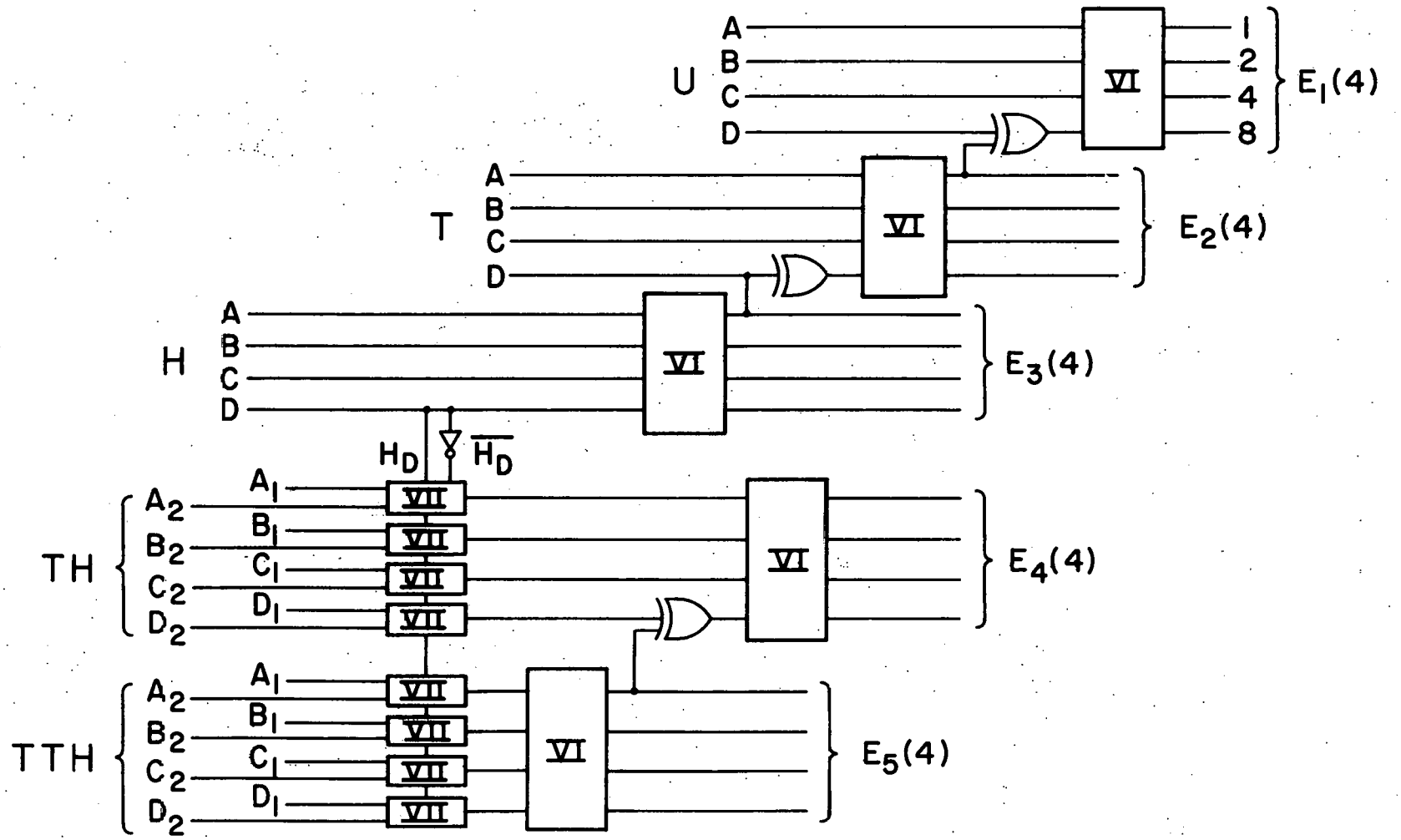
U
A
B
C
D
VI
1
2
4
8
E1(4)
T
A
B
C
D
VI
E2(4)
H
A
B
C
D
VI
E3(4)
HD
HD
TH
A2
B2
C2
D2
A1
B1
C1
D1
VII
VI
E4(4)
TTH
A2
B2
C2
D2
A1
B1
C1
D1
VII
VI
E5(4)

Figure 66. Grey to BCD Translation Block (VI). The grey to BCD translation block is the same for each digit. The parity checker ((g)) gives a high output when the number of high inputs is even. The logic employed here will become obvious with study of a sample of the grey code which is obtained by counting from 0 to 9.

Decimal	A	B	C	D
0	1	0	0	0
1	1	1	0	0
2	0	1	0	0
3	0	1	1	0
4	0	0	1	0
5	0	0	1	1
6	0	1	1	1
7	0	1	0	1
8	1	1	0	1
9	1	0	0	1

The next ten numbers are obtained by incrementing the least significant bit of the next higher digit by one, and then counting back from 9 to 0. The advantages of this code are that only one bit changes between any two consecutive numbers, and that the combinations 0000 and 1111 are not used, and are therefore useful in checking for open or short circuits.

(g) Parity Checker (74180)

VI

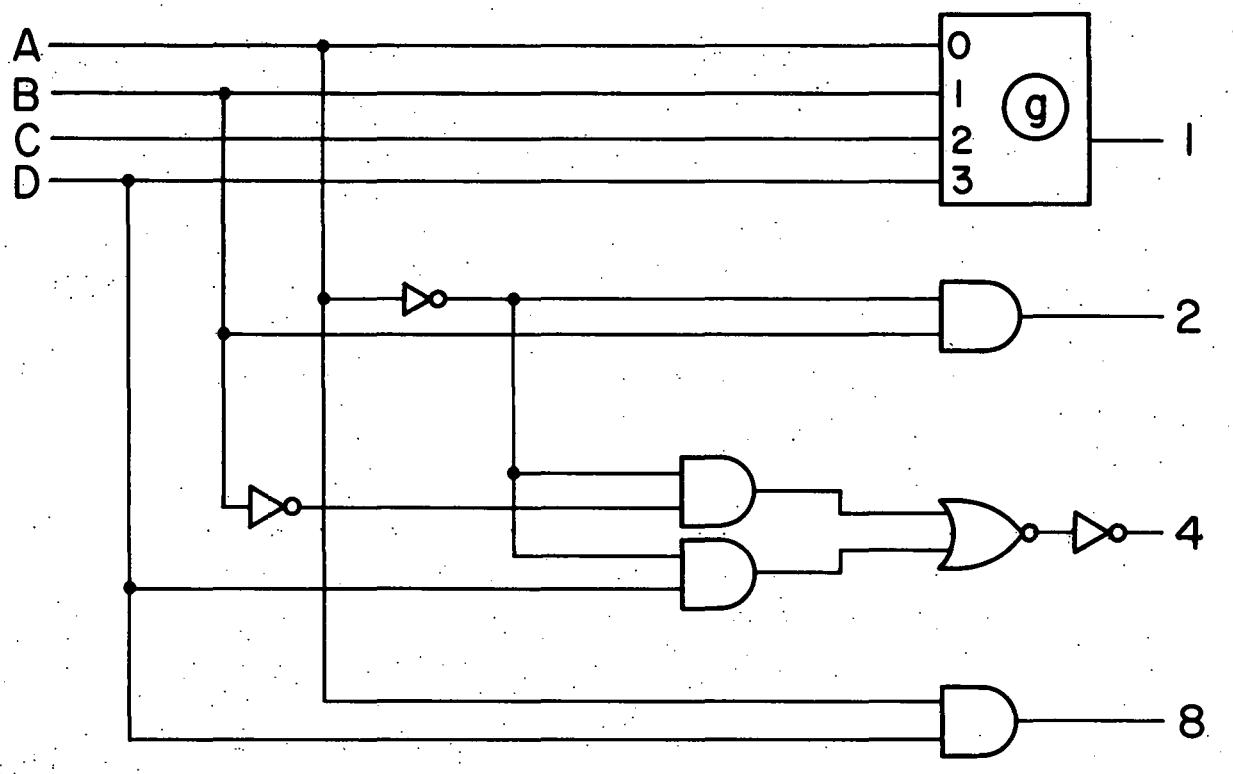

Figure 67a. Lead-Lag Selection Block (VII). The selection of either the lead bits or the lag bits for the thousands or ten thousands inputs for the encoder is done by the most significant of the hundreds bits, H_D. When the hundreds digit is between 2 and 7, the lead bits are chosen (H_D is low), while the opposite is true between 8 and 1. This is necessary because this encoder is actually two encoders, a high speed encoder and a low speed encoder. The lead-lag design is used to alleviate possible problems due to alignment between the two encoders, and it prevents any possible ambiguities in data between the high speed and low speed encoders.

b. Encoder Input. The encoder itself is just a set of switches. The present scheme uses a 10 KΩ pull-up resistor attached to the 5 volt supply. When the switch is open, the input to the inverter is high, while if the switch is closed, the input to the inverter is grounded.

VII

a)

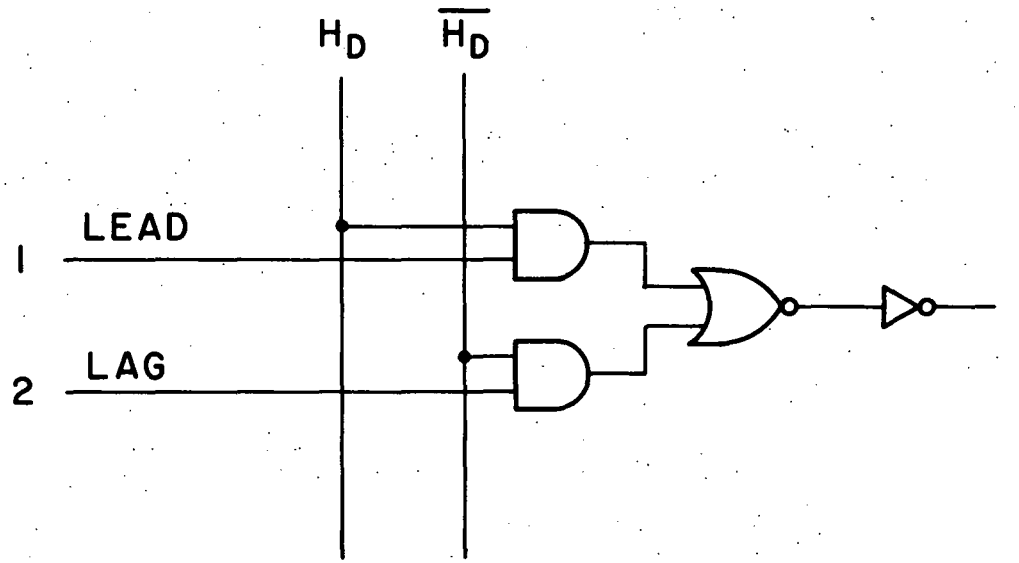

b)

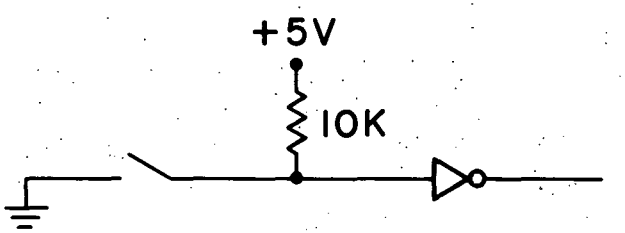

Figure 68. 3 Digit D to A Digit Selection Block. In this block, which of 4 possible combinations (three digits each) from the frequency counter (input data set F) will be displayed on a chart recorder is chosen. Digit 6 is the most significant digit (msd). Possible combinations of digits are 543, 432, 321, and 21-. Six multiplexers ((a)) are used to select the correct bits that are input to the next block (Fig. 69). The notation for the inputs to the multiplexers is ij, where i is the digit number, and j is the bit number (either 1,2,4, or 8). The outputs are labeled Z_i, where i=1 is the least significant bit (lsb).

(a) Dual 4 → 1 multiplexer (74153)

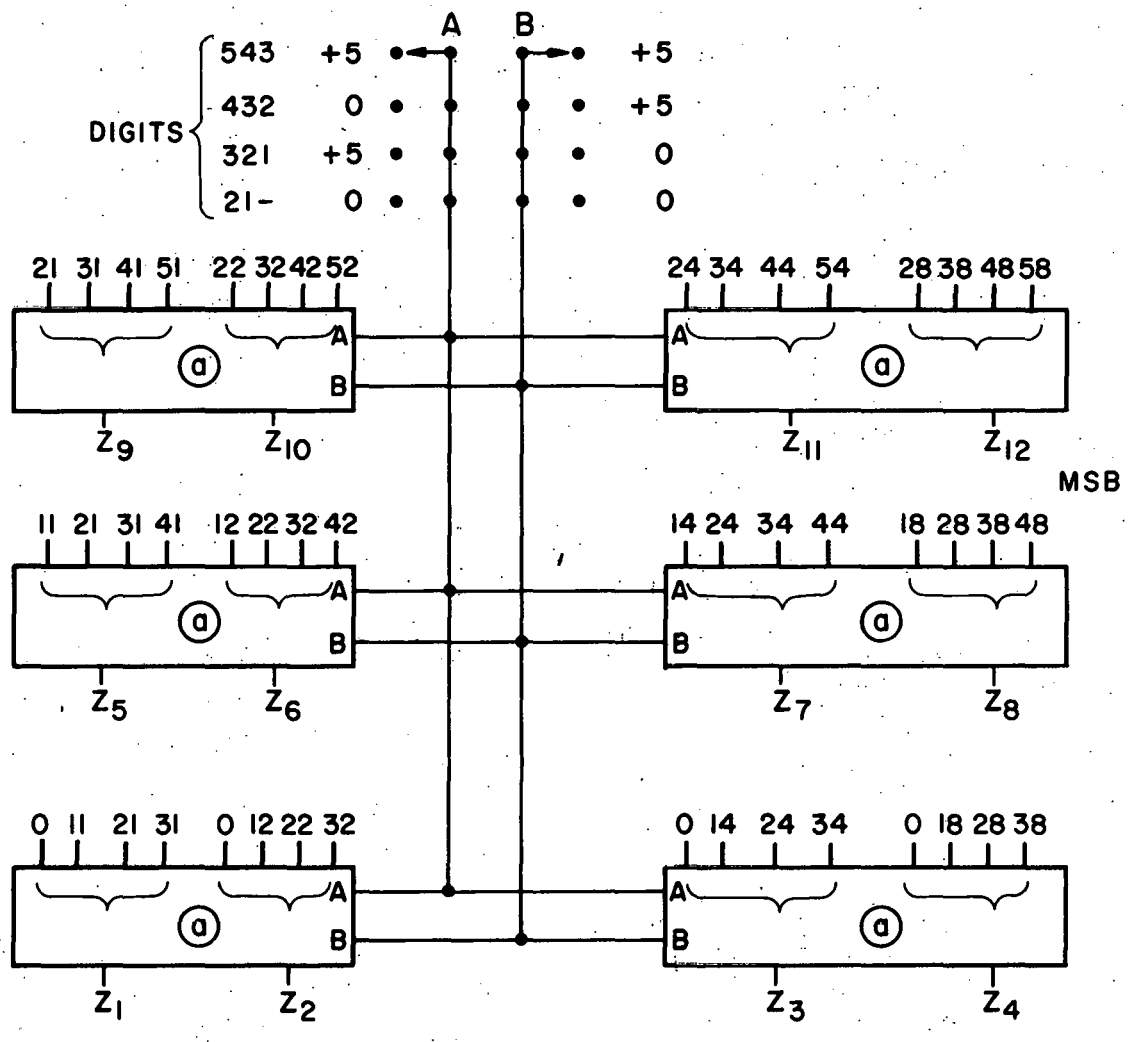
A
B
DIGITS
543 +5 +5
432 0 +5
321 +5 0
21- 0 0
21 31 41 51 22 32 42 52
24 34 44 54 28 38 48 58
11 21 31 41 12 22 32 42
14 24 34 44 18 28 38 48
0 11 21 31 0 12 22 32
0 14 24 34 0 18 28 38
a
A
B
Z9 Z10
Z11 Z12
Z5 Z6
Z7 Z8
Z1 Z2
Z3 Z4
MSB

Figure 69. D to A Block. The 12 bits obtained from the digit selection block are converted to binary by this array of BCD to BIN converters ((h)). The 10 bits thus obtained are converted to an analog signal by the D/A converter ((i)). The output is displayed on a strip chart recorder.

(h) BCD to BIN converter (74184)

(i) Analog Devices MP 1812 D/A

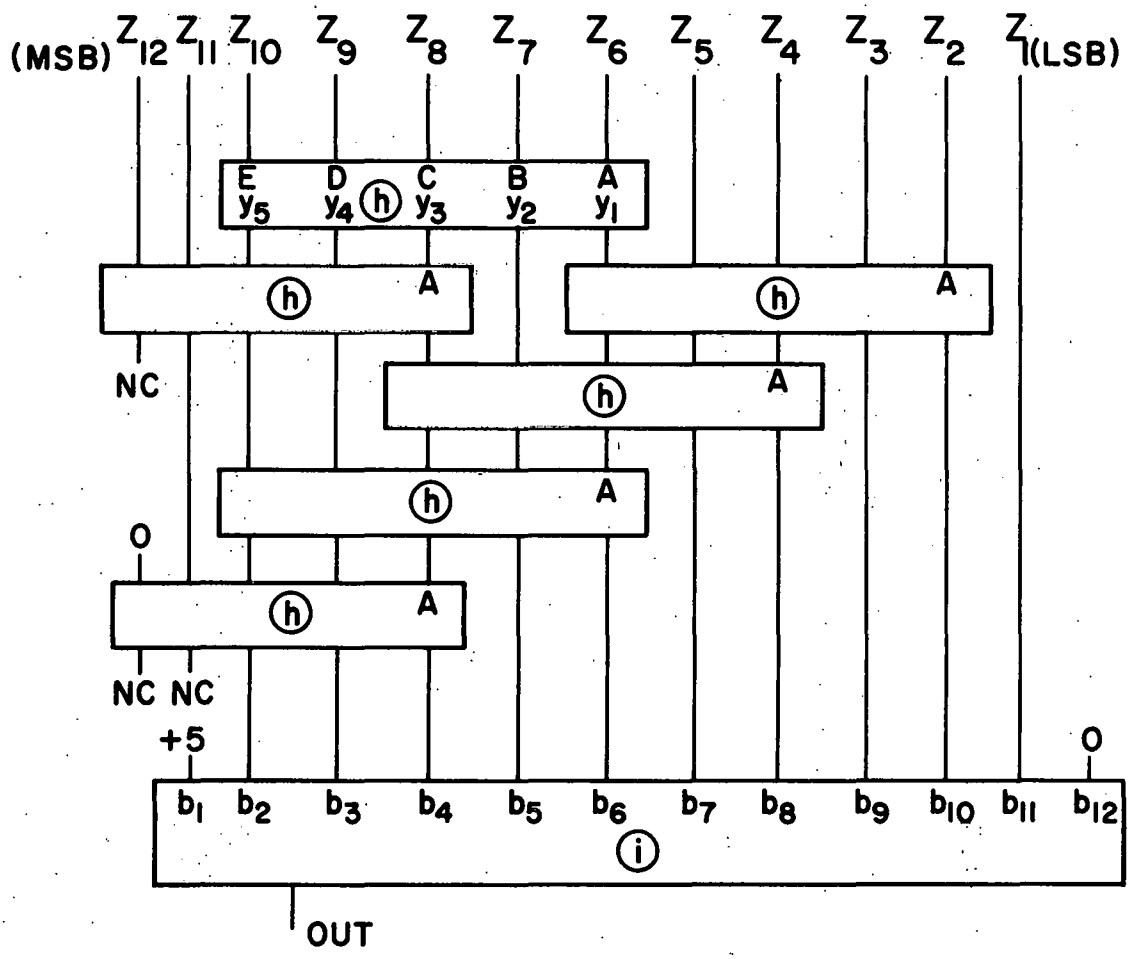
(MSB) Z12 Z11 Z10 Z9 Z8 Z7 Z6 Z5 Z4 Z3 Z2 Z1 (LSB)
E y5
D y4
h
C y3
B y2
A y1
h
A
h
A
NC
h
A
h
A
0
h
A
NC NC
+5
0
b1 b2 b3 b4 b5 b6 b7 b8 b9 b10 b11 b12
i
OUT

REFERENCES

1. H. R. Glyde, in Rare Gas Solids, Vol. I, ed. M. L. Klein and J. A. Venables, (Academic Press, New York, 1976), Chapter 8.

2. L. H. Nosanow, Phys. Rev. 146, 120 (1966).

3. R. A. Guyer, R. C. Richardson, and L. I. Zane, Rev. Mod. Phys. 43, 532 (1971).

4. E. R. Grilly, J. Low Temp. Phys. 4, 615 (1971).

5. E. R. Grilly and R. L. Mills, Annals of Physics 8, 1 (1959).

6. G. C. Straty and E. D. Adams, Phys. Rev. 150, 123 (1966).

7. J. S. Dugdale and J. P. Franck, Phil. Trans. Royal Soc. 257, 1 (1964).

8. E. R. Grilly, J. Low Temp. Phys. 11, 33 (1973).

9. W. P. Halperin, F. B. Rasmussen, C. N. Archie, and R. C. Richardson, J. Low Temp. Phys. 31, 617 (1978).

10. W. P. Halperin, C. N. Archie, F. B. Rasmussen, R. A. Buhrman, and R. C. Richardson, Phys. Rev. Lett. 32, 927 (1974).

11. S. B. Trickey, W. P. Kirk, and E. D. Adams, Rev. Mod. Phys. 44, 668 (1972).

12. S. H. Castles and E. D. Adams, J. Low Temp. Phys. 19, 397 (1975).

13. D. S. Greywall, Phys. Rev. B15, 2604 (1977).

14. E. C. Heltemes and C. A. Swenson, Phys. Rev. Lett. 7, 363 (1961).

15. D. O. Edwards, A. S. McWilliams, and J. G. Daunt, Phys. Lett. 1, 218 (1962).

16. R. C. Pandorf and D. O. Edwards, Phys. Rev. 169, 222 (1968).

17. H. H. Sample and C. A. Swenson, Phys. Rev. 158, 188 (1967).

18. H. A. Reich, Phys. Rev. 129, 630 (1963).

19. N. Sullivan, G. Deville, and A. Landesman, Phys. Rev. B11, 1858 (1975).

20. S. M. Heald, Ph.D. Dissertation, University of Illinois at Urbana-Champaign (1976).

21. J. H. Hetherington, Phys. Rev. 176, 231 (1968).

22. R. A. Guyer, J. Low Temp. Phys. 8, 427 (1972).

23. J. H. Hetherington, J. Low Temp. Phys. 32, 173 (1978).

24. J. H. Hetherington, private communication. See also ref. 20.

25. R. O. Simmons and R. W. Balluffi, Phys. Rev. 117, 52 (1960).

26. J. H. Vignos and H. A. Fairbank, Phys. Rev. 147, 185 (1966).

27. D. S. Miyoshi, R. M. Cotts, A. S. Greenberg, and R. C. Richardson, Phys. Rev. A2, 870 (1970).

28. R. Berman and S. J. Rogers, in Low Temperature Physics-LT9, ed. J. G. Daunt, D. O. Edwards, F. J. Milford, M. Yaqub, (Plenum Press, New York, 1965), p. 262.

29. V. N. Grigor'ev, B. N. Esel'son, and V. A. Mikheev, Sov. J. Low Temp. Phys. 1, 1 (1975).

30. P. M. Tedrow and D. M. Lee, Phys. Rev. 181, 399 (1969).

31. N. G. Bereznyak, I. V. Bogoyavlenskii, and B. N. Esel'son, Sov. Phys. JETP 18, 335 (1964).

32. C. Le Pair, K. W. Taconis, R. de Bruyn Ouboter, E. de Jong, and J. Pit, in Low Temperature Physics-LT9, ed. J. G. Daunt, D. O. Edwards, F. J. Milford, M. Yaqub, (Plenum Press, New York, 1965), p. 234.

33. K. N. Zinov'eva, Sov. Phys. JETP 17, 1235 (1963).

34. G. K. Walters and W. M. Fairbank, Phys. Rev. 103, 262 (1956).

35. D. O. Edwards, A. S. McWilliams, and J. G. Daunt, Phys. Rev. Lett. 9, 195 (1962).

36. M. F. Panczyk, R. A. Scribner, J. R. Gonano, and E. D. Adams, Phys. Rev. Lett. 21, 594 (1968).

37. P. N. Henriksen, M. F. Panczyk, and E. D. Adams, Solid State Comm. 8, 735 (1970).

38. A. S. Greenberg, W. C. Thomlinson, and R. C. Richardson, J. Low Temp. Phys. 8, 3 (1972).

39. R. H. Arnold and P. B. Pipes, private communication.

40. W. J. Mullin, Phys. Rev. Lett. 20, 254 (1968).

41. I. Prigogine, Molecular Theory of Solutions, (North-Holland Publishing Co., Amsterdam, 1957), p. 7.

42. P. M. Tedrow, Ph.D. Dissertation, Cornell University (1966).

43. E. A. Guggenheim, Mixtures, (The Clarendon Press, Oxford, 1952).

44. R. A. Swalin, Thermodynamics of Solids, (John Wiley and Sons, New York, 1972).

45. J. W. Cahn and J. E. Hilliard, J. Chem. Phys. 28, 258 (1958).

46. J. H. Hetherington, W. J. Mullin, and L. H. Nosanow, Phys. Rev. 154, 175 (1967).

47. J. H. Vignos and H. A. Fairbank, Phys. Rev. Lett. 6, 265 (1961), and Proc. 8th Int. Conf. on Low Temp. Physics, (Butterworths, Washington, 1963), p. 31.

48. C. Le Pair, K. W. Taconis, R. de Bruyn Ouboter, P. Das, and E. de Jong, Physica 31, 764 (1965).

49. J. L. Baum, D. F. Brewer, J. G. Daunt, and D. O. Edwards, Phys. Rev. Lett. 3, 127 (1959).

50. R. Haase and H. Schönert, Solid-Liquid Equilibrium, (Pergamon Press, Oxford, 1969), p. 17.

51. W. E. Schoknecht, private communication.

52. F. W. de Wette, L. H. Nosanow, and N. R. Werthamer, Phys. Rev. 162, 824 (1967).

53. K. F. Stripp and J. G. Kirkwood, J. Chem. Phys. 22, 1579 (1954).

54. N. H. March and J. S. Rousseau, Cryst. Latt. Defects 2, 1 (1971).

55. A. C. Damask and G. J. Dienes, Point Defects in Metals, (Gordon and Breach, New York, 1963).

56. D. P. Locke and R. A. Young, J. Low Temp. Phys. 23, 177 (1976).

57. A. B. Lidiard, Phil. Mag. 5, 1171 (1960).

58. M. Lomer, in Vacancies and Point Defects in Metals and Alloys, (The Institute of Metals, London, 1958), p. 79.

59. A. Eikum and G. Thomas, J. Phys. Soc. Japan 18, Suppl. III, 98 (1963).

60. A. F. Andreev, Sov. Phys. JETP Lett. 24, 564 (1976).

61. M. G. Richards, J. Hatton, and R. P. Giffard, Phys. Rev. 139, A91 (1965).

62. R. Balzer and R. O. Simmons, in Low Temperature Physics-LT13, Vol. 2, ed. K. D. Timmerhaus, W. J. O'Sullivan, E. F. Hammel, (Plenum Press, New York, 1972), p. 115.

63. S. M. Heald and R. O. Simmons, Rev. Sci. Instrum. 48, 316 (1977).

64. A. C. Anderson, Rev. Sci. Instrum. 41, 1446 (1970).

65. Stycast 2850GT, Emerson and Cumming Inc., 3450 Commercial, Northbrook, IL 60062.

66. G. C. Straty and E. D. Adams, Rev. Sci. Instrum. 40, 1393 (1969).

67. L. G. Rubin and Y. Golahny, Rev. Sci. Instrum. 43, 1758 (1972).

68. J. W. Ekin and D. K. Wagner, Rev. Sci. Instrum. 41, 1109 (1970).

69. Analog Devices model 153 J.

70. PAR model HR-8 Lockin Amplifier, with Type D Preamp.

71. E. P. Roth, J. R. Matey, A. C. Anderson, and D. A. Johns, Rev. Sci. Instrum. 49, 813 (1978).

72. National Bureau of Standards Standard Reference Material 767, Superconducting Thermometric Fixed Point Device.

73. R. J. Soulen, Jr., J. F. Schooley, and G. A. Evans, Jr., Rev. Sci. Instrum. 44, 1537 (1973).

74. J. F. Schooley, R. J. Soulen, Jr., and G. A. Evans, Jr., National Bureau of Standards Certificate, SRM 767.

75. M. Durieux, D. N. Astrov, W. R. G. Kemp, and C. A. Swenson, Metrologia 15, 57 (1979).

76. Model GR-200A-30, Lake Shore Cryotronics, P. O. Box 29876, Columbus, OH 43229.

77. Metrologia 15, 65 (1979).

78. B. A. Fraass, S. M. Heald, and R. O. Simmons, J. Cryst. Growth 42, 370 (1977).

79. E. B. Osgood, V. J. Minkiewicz, T. A. Kitchens, and G. Shirane, Phys. Rev. A5, 1537 (1972).

80. ^{4}He: Veeco type SC-4 Sensitivity Calibrator. ^{3}He: Hastings model OM-8HE3 Calibrated Leak.

81. C. J. Borkowski and M. K. Kopp, Rev. Sci. Instrum. 39, 1515 (1968).

82. C. J. Borkowski and M. K. Kopp, Rev. Sci. Instrum. 46, 951 (1975).

83. Dag 154, Acheson Colloids Co., Port Huron, MI 48060.

84. Carl M. Zvanut Co., 14 Chetwynd Rd., Paoli, PA 19301.

85. A. R. Faruqi, IEEE Nucl. S. NS22, 2066 (1975).

86. J. L. C. Ford, Jr., P. H. Stelson, and R. L. Robinson, Nucl. Instrum. and Methods 98, 199 (1972).

87. C. J. Borkowski and M. K. Kopp, IEEE Nucl. S. NS17, 340 (1970).

88. F. N. Kabat, Ph.D. Dissertation, University of Illinois at Urbana-Champaign (1971).

89. AMPCO 8 (8% Al Bronze), Copper and Brass., 6555 E. Davison St., Detroit, MI 48212.

90. Worm and gear cut by A. Bart Gear and Machine Co., 4830 W. 16th St., Chicago, IL 60650.

91. W. L. Bond, Acta Cryst. 13, 814 (1960).

92. M. M. Umanskii, D. M. Kheiker, and L. S. Zevin, Sov. Phys. Crystallography 2, 505 (1958).

93. J. Ladell, W. Parrish, and J. Taylor, Acta Cryst. 12, 561 (1959).

94. A. Taylor and H. Sinclair, Proc. Phys. Soc. 57, 108 (1945).

95. J. B. Nelson and D. P. Riley, Proc. Phys. Soc. 57, 160 (1945).

96. D. N. Batchelder and R. O. Simmons, J. Chem. Phys. 41, 2324 (1964).

97. D. N. Batchelder and R. O. Simmons, J. Appl. Phys. 36, 2864 (1965).

98. W. Parrish, Acta Cryst. 13, 838 (1960).

99. H. A. McKinstry, Ph.D. Dissertation, Pennsylvania State University (1960).

100. J. S. Shah and M. E. Straumanis, Z. Anorg. Allg. Chem. 391, 79 (1964).

101. International Tables for X-Ray Crystallography, Vol. III, ed. C. H. MacGillavry and G. D. Rieck, (Kynoch Press, Birmingham, 1962), p. 122.

102. P. M. Bronsveld, S. M. Kumra, and J. C. Stryland, Can. J. Phys. 51, 25 (1973).

103. A. Segmüeller, in Advances in X-Ray Analysis, Vol. XIII, ed. B. L. Henke, J. B. Newkirk, G. R. Mallet, (Plenum Press, New York, 1970), p. 455.

104. D. Marty and F. I. B. Williams, J. de Physique 34, 989 (1973).

105. See for example M. G. Richards, J. Pope, P. S. Tofts, and J. H. Smith, J. Low Temp. Phys. 24, 1 (1976).

106. W. Huang, H. A. Goldberg, M. T. Takemori, and R. Guyer, Phys. Rev. Lett. 33, 283 (1974).

107. A. R. Allen and M. G. Richards, in International Quantum Crystals Conference Proceedings, ed. J. Sites, (Colorado State University Press, Ft. Collins, Colorado, 1977), p. C-83.

108. I. Prigogine, R. Bingen, and A. Bellemans, Physica 20, 633 (1954).

109. P. G. Klemens and A. A. Maradudin, Phys. Rev. 123, 804 (1961).

110. H. B. Huntington, G. A. Shirn, and E. S. Wajda, Phys. Rev. 99, 1085 (1955).

111. R. O. Simmons and R. W. Balluffi, Phys. Rev. 125, 862 (1962).

112. D. L. Losee and R. O. Simmons, Phys. Rev. 172, 934 (1968).

113. J. H. Hetherington, Sov. J. Low Temp. Phys. 1, 295 (1975).

114. A. Widom, J. B. Sokoloff, and J. E. Sacco, Phys. Rev. B18, 3293 (1978).

115. Y. Quéré, Défauts Poctuels Dans Les Métaux, (Masson et Cie, Paris, 1967), p. 175.

116. C. Kittel, Introduction to Solid State Physics, (John Wiley and Sons, New York, 1971), Fourth Edition, p. 641.

117. K. Mukherjee, D. S. Lieberman, and T. A. Read, J. Appl. Phys. 36, 857 (1965).

118. A. F. Andreev and I. M. Lifshitz, Sov. Phys. JETP 29, 1107 (1969).

119. See for example A. Widom and J. B. Sokoloff, J. Low Temp. Phys. 21, 463 (1975); A. Widom and D. P. Locke, J. Low Temp. Phys. 23, 335 (1976); and refs. 22, 60, 114.

120. Handbook of Chemistry and Physics, ed. R. C. Weast, (Chemical Rubber Co., Cleveland, 1972), p. F-70.

121. P. R. Granfors, private communication.

122. K. Lyon, G. L. Salinger, and C. A. Swenson, Phys. Rev. B19, 4231 (1979).

123. G. C. Straty and E. D. Adams, Phys. Rev. 169, 232 (1968).

124. J. F. Jarvis, D. Ramm, and H. Meyer, Phys. Rev. 170, 320 (1968).

125. J. Holder and A. V. Granato, Phys. Rev. 182, 729 (1969).

126. R. Wanner, Phys. Rev. A3, 448 (1971).

127. J. P. Franck and R. Wanner, Phys. Rev. Lett. 25, 345 (1970).

128. A. E. Burgess and M. J. Crooks, Phys. Lett. 39A, 183 (1972).

129. J. Auleytner, X-Ray Methods in the Study of Defects in Single Crystals, (Pergamon Press, Oxford, 1966), p. 169.

130. P. B. Hirsch, in Progress in Metal Physics-6, ed. B. Chalmers and R. King, (Pergamon Press, London, 1956), p. 282.

131. R. Wanner, I. Iwasa, and S. Wales, Solid State Comm. 18, 853 (1976).

132. J. K. Hoffer, W. R. Gardner, C. G. Waterfield, and N. E. Phillips, J. Low Temp. Phys. 23, 63 (1976).

133. C. T. Van Degrift, Rev. Sci. Instrum. 46, 599 (1975).

134. C. Boghosian, H. Meyer, and J. E. Rives, Phys. Rev. 146, 110 (1966).

135. The Integrated Circuits Catalog, Texas Instruments, Inc.

VITA

Benedick Andrew Fraass was born on [redacted] He received his secondary education at Corona del Mar High School, in Newport Beach, California. In September 1970, he entered Stanford University, and he obtained his Bachelor of Science degree in Physics in June 1974. He joined the Physics Department of the University of Illinois as a graduate student in September 1974, and held a teaching assistantship the first year, and a research assistantship thereafter. In August 1975, he received his Master of Science degree in Physics. He is a member of the American Physical Society.

In June 1973, he married Wendy Elaine Brockett of Newport Beach, California.

Publications:

"Growth of Several Quantum Crystals: CD_4, ^4He, and ^3He," B. A. Fraass, S. M. Heald, and R. O. Simmons, J. Cryst. Growth 42, 370 (1977).

"Thermal Vacancies in Solid Helium," International Quantum Crystals Conference Proceedings, B. A. Fraass, S. M. Heald, and R. O. Simmons, ed. J. Sites, (Colorado State Univ. Press, Ft. Collins, Colorado, 1977), p. C-73.

"Lattice Parameters and Thermal Expansion of Solid CD_4," D. R. Baer, B. A. Fraass, D. H. Riehl, and R. O. Simmons, J. Chem. Phys. 68, 1411 (1978).

"The Structure Transition in Hydrogen Below 1 K," J. V. Gates, P. R. Granfors, B. A. Fraass, and R. O. Simmons, J. de Physique 39, C6-103 (1978).

"X-Ray Study of the Crystallographic Transformation in Hydrogen Below 1.5 K," J. V. Gates, P. R. Granfors, B. A. Fraass, and R. O. Simmons, Phys. Rev. B19, 3667 (1979).